U.PORTO
FEUP FACULDADE DE ENGENHARIA
UNIVERSIDADE DO PORTO

DEPARTAMENTO DE ENGENHARIA MECÂNICA

POWER LOSS IN ROLLING BEARINGS AND GEARS LUBRICATED WITH WIND TURBINE GEAR OILS

CARLOS MIGUEL DA COSTA GOMES FERNANDES

2015

CARLOS MIGUEL DA COSTA GOMES FERNANDES

POWER LOSS IN ROLLING BEARINGS AND GEARS LUBRICATED WITH WIND TURBINE GEAR OILS

A THESIS SUBMITTED TO THE
FACULDADE DE ENGENHARIA DA UNIVERSIDADE DO PORTO
FOR THE *PROGRAMA DOUTORAL EM ENGENHARIA MECÂNICA*

Supervisor: Doctor Ramiro C. Martins
Co-supervisor: Professor Jorge H. O. Seabra

DEPARTAMENTO DE ENGENHARIA MECÂNICA
FACULDADE DE ENGENHARIA
UNIVERSIDADE DO PORTO

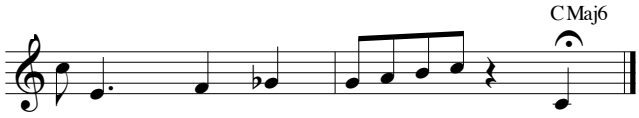

To the memory of my late grandparents Maria and Manuel

Abstract

The present work is intended to study power loss in rolling bearings and gears, in particular lubricated with wind turbine gear oils. It will be shown that the oil formulation, as well as the gears and rolling bearings geometry have a very significant influence on the power loss of gearboxes.

The most important experimental work that supports this thesis is:

- The physical characterization of different fully formulated wind turbine gear oils;
- The traction coefficient and film thickness measurements in a ball-on-disc contact;
- The power loss measurement on a wide range of conditions with different oil formulations and rolling bearing geometries;
- The power loss measurement of FZG gearboxes with different oil formulations and gear geometries.

The work is complemented by several analytical and numerical models for:

- The calibration of a rolling bearing power loss model;
- The characterization of the average coefficient of friction of the meshing gear;
- The development and validation of a gearbox power loss model.

The findings clearly show that the efficiency of a gearbox can be improved by modifying the oil formulation, the gear geometry, the rolling bearing geometry and the operating conditions.

Resumo

O presente trabalho destina-se ao estudo da perda de potência em rolamentos e engrenagens, em particular quando lubrificadas por óleos para caixas de engrenagens de turbinas eólicas. Como se demonstrará, a formulação do lubrificante assim como a geometria das engrenagens e rolamentos tem um grande impacto na perda de potência de caixas de engrenangens.

O presente trabalho assenta em torno dos seguintes tópicos fundamentais de carácter experimental:

- A caracterização das propriedades físicas de diferentes óleos para caixas de engrenagens the turbinas eólicas totalmente formulados;
- A medição do coeficiente de atrito e espessura de filme num contacto bola disco;
- A medição da perda de potência em rolamentos de diferentes geometrias lubrificados com óleos de engrenagens;
- A medição da perda de potência de caixas de engrenagens FZG utilizando diferentes geometrias de dentado.

O trabalho numérico apresentado assenta nos seguintes pilares:

- A calibração de um modelo de perda de potência para rolamentos;
- A caracterização do coeficiente de atrito nos dentes das engrenagens;
- A construção de um modelo de perda de potência para caixas de engrenangens devidamente calibrado e validado.

Os resultados apresentados demonstram claramente que a eficiência de uma caixa de engrenagens pode ser melhorada modificando a formulação do lubrificante, a geometria de engrenagens e rolamentos assim como escolhendo condições de funcionamento adequadas.

Résumé

L'objectif de ce travail est d'étudier la perte de puissance des roulements et des engrenages lubrifiés avec huiles d'engrenages utilisés dans les multiplicateurs des éoliennes. En effet, la formulation de l'huile, aussi bien que la géométrie des engrenages et des roulements ont une influence très significative sur ces pertes de puissance.

Plusieurs travaux expérimentaux ont été réalisés qui constitue la base de cette thèse:

- La caractérisation physique et chimique de plusieurs huiles, entièrement formulés, pour les engrenages d'éoliennes;
- La détermination du coefficient de traction et de l'épaisseur de film, mesurés dans le contact bille-sur-disque;
- Mesure de la perte de puissance pour différentes géométries de roulements, lubrifiés avec les huiles des multiplicateurs des éoliennes, pour une large gamme de vitesses et charges appliquées;
- Mesure de la perte de puissance pour différentes géométries d'engrenages, lubrifiés avec les huiles des multiplicateurs des éoliennes, pour une large gamme de vitesses et couples appliquées.

Les pertes de puissance dans les roulements, dans les engrenages et dans les transmissions par engrenages (boîte de vitesses et multiplicateurs) ont été modélisées par des outils numériques, notamment:

- Validation et calibration d'un modèle de perte de puissance des roulements, basée sur le modèle de SKF;
- Validation et calibration d'un modèle de perte de puissance des engrenages;
- Validation des paramètres lubrifiant (XL) dans l'équation du coefficient de frottement moyen entre les dents des engrenages;
- Validation d'un modèle de perte de puissance pour les transmissions par engrenages.

Les résultats obtenus montrent, clairement, que le rendement d'une transmission par engrenages peut être améliorée par l'optimisation simultanée de la formulation d'huile, de la géométrie des engrenages et de la géométrie des paliers à roulements, en tenant compte des conditions de fonctionnement en vitesse et couple transmis.

Keywords

Power loss
Wind turbine gear oils
Rolling bearings
Low loss gears

Palavras chave

Perda de potência
Óleos de engrenagens para turbinas eólicas
Rolamentos
Engrengens de baixa perda de potência

Mots-clés

Perte de puissance
Huiles pour engrenages d'eóliennes
Roulements
Engrenages á faibles pertes

Acknowledgements

I would like to express my gratitude to Professor Jorge Seabra and to Professor Ramiro Martins for their patient guidance and support throughout the realisation of this work. Without their help, this work would be impossible. They taught me important lessons about engineering, science and about life.

I would also like to acknowledge and give my sincere thanks to a few people without whom this thesis couldn't have been possible: Armando Campos, Beatriz Graça, Pedro Marques, David Gonçalves, Jorge Castro, José Brandão, Luís Magalhães, André Gama. They are my fellow colleagues at CET IB and I want to thank their constant help and support but also for the great moments we spent.

A special thank to Tiago Cousseau that didn't return to Brazil without teach me a lot of things about rolling bearing friction torque models.

I would like to thank to the Master Science students that worked with me in order to complete all the work. Namely: Pedro Amaro, Albano Marinho, Ricardo Machado and Maroi Hammami.

My sincere thanks to the Faculdade de Engenharia da Universidade do Porto and its staff, for their contribution in time and resources to my work.

My sincere thanks to the INEGI and its staff, for their contribution in time and resources to my work.

I would like to thank my family for all the help and support.

A special acknowledgement for my girlfriend for the love and support even during the toughest times, that were very few.

I wish to express my gratitude to Repsol for the ICP analysis of the wind turbine gear oils and Evonick for the piezoviscosity measurements.

I wish to express my gratitude to FCT for the financial support given through the projects: "High efficiency lubricants and gears for windmill planetary gearboxes", with research contract PTDC / EMEPME / 100808 / 2008 and "Modelização e ensaio da perda de potência e do desgaste em engrenagens helicoidais. Influência do material e da geometria da engrenagem", with research contract EXCL / EMSPRO / 0103 / 2012.

Contents

List of Figures

List of Tables

List of Symbols

α	Pressure viscosity or piezoviscosity coefficient [Pa^{-1}]
α_t	Thermal expansion coefficient [-]
α_z	Gear pressure angle [°]
α_{bl}	Pressure exponent for boundary conditions according to Doleschel [-]
α_{cond}	Conduction heat transfer coefficient [W/m°K]
α_{conv}	Convection heat transfer coefficient [W/m°K]
α_{EHD}	Pressure exponent for full film conditions according to Doleschel [-]
α_{rad}	Radiation heat transfer coefficient [W/m°K]
α_{ztw}	Gear transverse working pressure angle [°]
α_{zt}	Gear transverse pressure angle [°]
β_L	Lubricant thermoviscosity coefficient [$°K^{-1}$]
β_R	Seals friction torque exponent of a rolling bearing [-]
β_z	Gear helix angle [°]
β_{bl}	Speed exponent for boundary conditions according to Doleschel [-]
β_{EHD}	Speed exponent for full film conditions according to Doleschel [-]
β_{zb}	Gear base helix angle [°]
$\dot{\gamma}$	Shear rate [s^{-1}]
$\dot{Q}_e$	Oil jet flow [m^3/s]
ϵ	Emission ratio of housing surface [-]
ϵ_1	Addendum contact ratio of pinion [-]
ϵ_2	Addendum contact ratio of wheel [-]

ϵ_α	Transverse contact ratio [-]
ϵ_β	Overlap contact ratio [-]
ϵ_γ	Total contact ratio [-]
η	Dynamic viscosity [mPas]
η_0	Dynamic viscosity at atmospheric pressure and reference temperature [Pas]
η_S	Efficiency of FZG slave gearbox [−]
η_T	Efficiency of FZG test gearbox [−]
η_z	Gearbox efficiency [%]
$\eta_\%$	Representative factor to calculate dynamic viscosity [mPas]
η_{global}	Global efficiency of FZG gearboxes [−]
η_R	Reference viscosity according to Doleschel [-]
γ	Centrifugal acceleration [m/s^2]
γ_{EHD}	Viscosity exponent for full film conditions according to Doleschel [-]
κ	Viscosity ratio [-]
κ_{ISO}	Viscosity ratio according to ISO 281 [-]
Λ	Specific film thickness [-]
$\lambda(\mu)$	Dimensionless loss factor [-]
λ_{wand},λ_{oil}	Gearbox geometric factors to calculate the windage losses [-]
μ_1	Load dependent coefficient of friction of a rolling bearing [-]
μ_{bl}	Boundary coefficient of friction [-]
μ_{EHD}	Elasto-Hydrodynamic coefficient of friction [-]
μ_{mZ}	Average coefficient of friction along the path of contact [-]
$\mu_{R,bl}$	Reference coefficient of friction for boundary conditions according to Doleschel [-]

$\mu_{R,EHD}$	Reference coefficient of friction for full film conditions according to Doleschel [-]
μ_{sl}	Sliding coefficient of friction [-]
ν	Kinematic viscosity [cSt]
ν_0	Reference kinematic viscosity [1000 cSt]
ϕ_{bl}	Lubrication weighting factor of rolling friction torque [-]
ϕ_{ish}	Inlet shear heating factor of rolling friction torque [-]
ϕ_{rs}	Replenishement/starvation factor of rolling friction torque [-]
ϕ_T	Thermal reduction factor [-]
ρ	Density [kg/m^3]
ρ_0	Density at reference temperature [kg/m^3]
ρ_{redC}	Equivalent contact radius on the pitch point [mm]
Σ_C	Composite contact roughness [m]
τ	Shear stress [Pa]
τ_{rep}	Representative shear stress [mPa]
θ	Temperature [°C]
θ_0	Reference temperature [°C]
θ_∞	Ambient temperature [°C]
θ_{base}	Temperature of FZG machine base plate [°C]
θ_{oil}	Oil temperature [°C]
$\vartheta_{stab,base}$	Stabilization temperature of the FZG machine base plate [°C]
ξ	Portion of boundary lubrication [-]
ξ_V	Gearbox loss degree [%]
a	Gear centre distance [mm]
A_{base}	Base area of the gearbox [m^2]

A_{ca}	Area of the gearbox [m^2]
A_c	Contact area [m^2]
A_h	Horizontal area of the gearbox [m^2]
a_H	Hertz half-width [m]
A_v	Vertical area of the gearbox [m^2]
B	Rolling bearing width [mm]
b	Gear face width [mm]
c_f	Conduction factor [-]
C_m	Dimensionless drag group of churning losses [-]
C_0	Ellipticity influence parameter [-]
C_{ch}	Churning torque loss [Nm]
Ca	Tip relief coefficient [-]
COF	Coefficient of friction [-]
D	Rolling bearing outside diameter [mm]
d	Rolling bearing bore diameter [mm]
d_1	Reference pitch diameter of the pinion [mm]
d_2	Reference pitch diameter of the wheel [mm]
d_m	Mean diameter of a rolling bearing [mm]
d_{sh}	Shaft diameter [m]
d_s	Rolling bearing seal counter-face diameter [mm]
da_1	Addendum diameter of the pinion [mm]
da_2	Addendum diameter of the wheel [mm]
db_1	Base diameter of the pinion [mm]
db_2	Base diameter of the wheel [mm]
E^*	Equivalent Young Modulus [Pa]

F	Resultant force [N]
F_a	Axial force [N]
F_D	Viscosity effect factor to calculate seal losses [-]
F_N	Local load per unit length [N/mm]
F_r	Radial force [N]
f_0	Load dependent friction torque constant [-]
f_1	Load dependent friction torque constant [-]
F_{bn}	Normal force to tooth flank [N]
F_{bt}	Transverse force to tooth flank [N]
Fr	Froude number [-]
G	Material influence parameter [-]
g	Gravitational acceleration [9.8 m/s^2]
g_1	Length of path of addendum contact of pinion [mm]
g_2	Length of path of addendum contact of wheel [mm]
g_α, $\overline{AE}$	Length of path of contact [mm]
G_{rr}	Rolling friction torque constant of a rolling bearing [-]
G_{sl}	Sliding friction torque constant of a rolling bearing [-]
H	Rolling bearing oil level [mm]
h	Gear submersion height [m]
h_t	Tooth height [m]
$H_V^{Buckingham}$	Gear loss factor according to Buckingham [-]
$H_V^{Henriot}$	Gear loss factor according to Henriot [-]
$H_V^{Niemann}$	Gear loss factor according to Niemann [-]
$H_V^{Ohlendorf}$	Gear loss factor according to Ohlendorf [-]
h_{0C}	Corrected central film thickness [nm]

h_0	Central film thickness [nm]
h_{ca}	Height of gear unit housing [m]
h_m	Minimum film thickness [nm]
H_p	Modified Hersey number [-]
h_{t0}	Reference tooth height [m]
H_{VL}	Local gear loss factor using rigid load distribution [-]
i	Gear transmission ratio [-]
k_0	Dimensionless position of pitch point on base plane [-]
k_L	Lubricant thermal conductivity [W/m°K]
k_V, b_V, c_V	Vogel's equation constants to calculate kinematic viscosity [-]
k_z	Addendum shortening coefficient [-]
K_{FZG}	FZG load stage [-]
$K_L,\ K_Z$	Drag friction torque constants of a rolling bearing [-]
$K_{S1},\ K_{S2}$	Seals friction torque constants of a rolling bearing [-]
l	Roller element width [m]
L^*	Thermal parameter of the lubricant [-]
$l^i(x)$	Single contact line length [mm]
l_{ca}	Width of gear unit housing [m]
LP	Lubricant Parameter [s]
m	Gear normal module [mm]
M_0	Load independent friction torque of a rolling bearing [Nmm]
M_1	Load dependent friction torque of a rolling bearing [Nmm]
m_A, n_A, a_A	ATSM D341 constants to calculate kinematic viscosity [-]
M_{drag}	Drag friction torque of a rolling bearing [Nmm]
M'_{rr}	Rolling friction torque of a rolling bearing [Nmm]

M_{seal}	Seals friction torque of a rolling bearing [Nmm]
M_{sl}	Sliding friction torque of a rolling bearing [Nmm]
M_t	Total friction torque of a rolling bearing [Nmm]
M_t^{exp}	Experimental total friction torque of a rolling bearing [Nmm]
n	Rotational speed [rpm]
n_1	Pinion rotational speed [rpm]
n_2	Wheel rotational speed [rpm]
p	Pressure [Pa]
p_0	Hertz contact pressure [Pa]
p_S	Contact seal pressure [Pa]
p_{ca}	Depth of gear unit housing [m]
P_{IN}	Gearbox input power [W]
P_M	Mesh power on the planetary tooth contacts [W]
p_R	Reference pressure according to Doleschel [1000 MPa]
P_{VD}	Shaft seals power loss [W]
P_{VL}	Rolling bearings power loss [W]
$P_{VZ0,acceleration}$	Power loss due to ventilation due to oil acceleration [W]
$P_{VZ0,squeeze}$	Power loss due to squeeze or pocketing [W]
$P_{VZ0,ventilation}$	Power loss due to ventilation [W]
P_{VZ0}	Load independent meshing gears power loss [W]
$P_{VZP,rolling}$	Meshing gears rolling power loss [W]
P_{VZP}	Load dependent meshing gears power loss [W]
P_V	Gearbox total power loss [W]
P_V^{exp}	Gearbox total power loss measured [W]
Q_T	Total heat dissipated [W]

Q_{cond}	Heat dissipated by conduction [W]
Q_{conv}	Heat dissipated by convection [W]
Q_{rad}	Heat dissipated by radiation [W]
r_1	Pitch radius of the pinion [mm]
r_2	Pitch radius of the wheel [mm]
R_a	Average absolute surface roughness (DIN 4768) [μm]
R_q	Root mean square average surface roughness (DIN 4768) [μm]
R_z	Mean peak-to-valley height (DIN 4768) [μm]
R_{max}	Maximum peak-to-valley height (DIN 4768) [μm]
R_X	Equivalent radius in rolling direction [m]
Re	Reynolds number [-]
Re_c	Critical Reynolds number [-]
S	Slide-to-Roll ratio [-]
s, t	Gold equation constants to calculate pressure viscosity coefficient [-]
s_a	Distance from gears to the wall in axial direction [m]
S_m	Submerged are of the gear [m^2]
S_p	Modified Hersey number [-]
s_r	Distance from gears to the wall in radial direction [m]
s_z	Distance from gears to the wall in height direction [m]
S_F	Gears bending stress safety factor [-]
S_g	Gear geometric parameter [-]
S_H	Gears surface stress safety factor [-]
S_S	Gears scuffing safety factor [-]
SRR	Slide-to-Roll ratio [%]
T	Absolute temperature [°K]

t_S	Contact seal width [m]
T_1	Pinion torque [Nm]
T_2	Wheel torque [Nm]
$T_\%$	Direct measurement on Rheomat 115 [-]
T_∞	Absolute ambient temperature [°K]
T_{IN}	Pinion static torque [Nm]
T_L	Gearbox total torque loss [Nm]
T_{oil}	Absolute oil temperature [°K]
T_W	Wheel static torque [Nm]
U	Speed influence parameter [-]
U_S	Entrainment speed [m/s]
U_{bob}	Bob rheometer speed [m/s]
U_{disc}	Disc speed [m/s]
V_0	Gearbox oil volume [m^3]
v_e	Entrainment speed according to Xu [m/s]
v_g	Sliding speed [m/s]
V_M	Drag loss factor [-]
v_o	Oil jet velocity [m/s]
v_r	Rolling velocity [m/s]
v_t	Absolute tangential speed on the pitch point [m/s]
$v_{\Sigma C}$	Sum of the rolling velocities on the pitch point [m/s]
$v_{R,bl}$	Reference speed for boundary conditions according to Doleschel [m/s]
$v_{R,EHD}$	Reference speed for full film conditions according to Doleschel [m/s]
v_{tb}	Absolute tangential speed on the base plane [m/s]
W	Load influence parameter [-]

x	Coordinate along the gear path of contact [mm]
X_L	Coefficient of friction lubricant parameter [-]
x_z	Gear profile shift [-]
y	Coordinate along the gear width [mm]
z_1	Number of teeth of pinion [-]
z_2	Number of teeth of wheel [-]
${d_1}'$	Working pitch diameter of the pinion [mm]
${d_2}'$	Working pitch diameter of the wheel [mm]
${v_t}'$	Relative tangential speed on the pitch point [m/s]

Chapter 1.

Introduction

1.1. Problem statement

As proven source of clean and affordable energy, wind resources clearly have a vital role to play in energetic sustainability [1]. To make wind energy competitive with other power plants in the near future, enhancements on availability, reliability and lifetime will be required.

Gearboxes have plagued the wind power industry. Wind turbine failures can be extremely costly in terms of repair costs, replacement parts and lost power, and the gearbox is the most likely component to have a major effect on the turbine availability. Often placed in hostile environments, wind turbines have premature bearing and gear failures; the performance of the gear oils plays an important role in the gearbox reliability. Combined with the high repair costs, the downtime due to gearbox failure is usually far greater than any other component failure. This leads to high operational costs and it has become a plague for wind power industry [2–5].

New solutions like the direct drive wind turbines have emerged which in fact also have specific problems like geared drive turbines [6].

Wind turbine gearbox problems start with the operating temperature of the oil. According to DIN recommendations the best viscosity and anti-scuffing properties are reached for oil operating temperatures above 80 °C. In wind turbine gearboxes such temperature does not exceed 60 °C, the anti-scuffing class tends to drop, resulting in a worst start-up behaviour and larger amount of wear debris produced [7].

A high rate of wind turbine gearbox failures that are rooted to the rolling bearings has been reported in the literature [2–5, 8]. The authors claim that the gearbox failures start in the bearings. Jean Van Rensselar [9] has a different opinion and believes that rolling bearings are just the component that indicates damage at an early stage. The most significant fatigue wear phenomena found are micropitting and smearing caused by large amounts of sliding in situations in which specific film thickness (Λ) is low, leading to high stresses and temperatures in the contact [10–13]. Other failure mode reported is the white structure flaking (WSF) that is thought to be

driven by hydrogen release and diffusion into bearing steel, sourced by lubricating oil or water contamination, or transient conditions that are not fully understood [14–19]. The industry, as well as the science in general, have been studying the bearing failure modes in order to solve these problems.

While the main focus of researchers and engineers for the wind turbine applications is yet the gearbox failures, the energetic efficiency of such large machines should not be overlooked.

When talking about the car or the bus of our daily life, the gearbox efficiency is often considered very high and the power loss problem is mainly centred on the engine and vehicle weight [20, 21]. However, in wind turbine gearboxes, handling with several mega watt, even a small efficiency increase can save energy, useful for several more households.

If the efficiency of a 1 MW wind turbine gearbox is increased by 1% something like 10 kW of additional power would be available in only one machine. The 1 MW wind turbines are very rare nowadays, since the current output power is in some cases more than 5 MW.

The power loss reduction has a direct influence on lubrication quality because increased efficiency means lower heat dissipation and lower oil operating temperature. Lowering the operating temperature minimizes oil oxidation and degradation, which has a large impact on the lubrication quality and consequently on the surface protection against failures. Höhn showed that reducing the oil temperature also reduces the risk of failure [22]. Even in the case of gearboxes without failure problems overtime, the oil change will be less frequent contributing for the reduction of the maintenance costs, related to the cost of fresh oil, but also to the cost of replacing it in a wind turbine.

1.2. Background and purpose

Very often efficiency is not considered as a primary requirement in gearbox design, compared to mechanical resistance, production cost or fatigue life. This work will try to put into evidence the improvement that can be achieved in a gearbox by adding efficiency criteria at the design stage. The oil formulation will be treated as a machine element that should not be overlooked.

The main purpose goal of this thesis is to understand the influence of the tribological behaviour of different wind turbine gear oils on the power loss performance of a gearbox. The second goal is to understand the influence of gear and bearing design on the efficiency of a gearbox.

In order to achieve these objectives, specific experimental and modelling work was developed, concerning the power loss of rolling bearings, gears and gearboxes.

As a final outcome, it is intended to demonstrate that it is possible to improve the energetic efficiency of a gearbox, without reducing its operating life, using more efficient lubricants and optimal gearbox design.

1.3. Research approach

The research presented in this thesis is mainly based on experimental results. Therefore, this manuscript is based on more than 2000 hours of experimental work that are be resumed in Table 1.1. Other experimental work was done that is not included on the thesis, because is slightly out of the purpose of the thesis. However, that information complemented some of the conclusions that will be presented.

Table 1.1.: Total hours spent on production of experimental work.

Task	Time [h]
Wind turbine gear oils characterization	≈ 100
Film thickness measurement	≈ 30
Traction coefficient measurement	≈ 30
Rolling bearings friction torque measurement	≈ 400
Gears torque loss measurement	≈ 1440
Total time	≈ 2000

1.3.1. Scientific publications

The work that will be presented on behalf of this thesis was yet been published on scientific journals or conference proceeding, or is under a peer-review process-or under a peer-review process.

As author

Paper I. C. Fernandes, R. Martins and J. Seabra
Friction torque of thrust ball bearings lubricated with wind turbine gear oils
Tribology International (**2013**), 58, 47-54
DOI: 10.1016/j.triboint.2012.09.005

Paper II. C. Fernandes, R. Martins and J. Seabra
Friction torque of cylindrical roller thrust bearings lubricated with wind turbine gear oils

Tribology International (**2013**), 59, 121-128
DOI: 10.1016/j.triboint.2012.05.030

Paper III. C. Fernandes, P. Amaro, R. Martins and J. Seabra
Torque loss of thrust ball bearings lubricated with wind turbine gear oils at constant temperature
Tribology International (**2013**), 66, 194-202
DOI: 10.1016/j.triboint.2013.05.002

Paper IV. C. Fernandes, P. Amaro, R. Martins and J. Seabra
Torque loss of cylindrical roller thrust bearings lubricated with wind turbine gear oils at constant temperature
Tribology International (**2013**), 67, 72-80
DOI: 10.1016/j.triboint.2013.06.016

Paper V. C. Fernandes, R. Martins and J. Seabra
Torque loss of type C40 FZG gears lubricated with wind turbine gear oils
Tribology International (**2014**), 70, 83-93
DOI: 10.1016/j.triboint.2013.10.003

Paper VI. C. Fernandes, P. Marques, R. Martins and J. Seabra
Gearbox power loss. Part I: Losses in rolling bearings.
Tribology International (**2015**), In Press
DOI: 10.1016/j.triboint.2014.11.017

Paper VII. C. Fernandes, P. Marques, R. Martins and J. Seabra
Gearbox power loss. Part II: Friction losses in gears.
Tribology International (**2015**), In Press
DOI: 10.1016/j.triboint.2014.12.004

Paper VIII. C. Fernandes, P. Marques, R. Martins and J. Seabra
Gearbox power loss. Part III: Application to a parallel axis and a planetary gearbox
Tribology International (**2015**), In Press
DOI: 10.1016/j.triboint.2015.03.029

Paper IX. C. Fernandes, P. Marques, R. Martins and J. Seabra
Film thickness and traction curves of wind turbine gear oils
Tribology International (**2015**), In Press
DOI: 10.1016/j.triboint.2015.01.014

Paper X. C. Fernandes, P. Marques, R. Martins and J. Seabra
Influence of gear loss factor on the power loss prediction
Mechanical Sciences (**2015**), under review

As co-author

Paper XI. D. Gonçalves, C. Fernandes, R. Martins and J. Seabra
Torque loss in a gearbox lubricated with wind turbine gear oils
Lubrication Science (**2013**), 25, 297-311
DOI: 10.1002/ls.1222

Paper XII. P. Marques, C. Fernandes, R. Martins and J. Seabra
Power losses at low speed in a gearbox lubricated with wind turbine gear oils with special focus on churning losses
Tribology International (**2013**), 62, 186-197
DOI: 10.1016/j.triboint.2013.02.026

Paper XIII. P. Marques, C. Fernandes, R. Martins and J. Seabra
Efficiency of a gearbox lubricated with wind turbine gear oils
Tribology International (**2013**), 71, 7-16
DOI: 10.1016/j.triboint.2013.10.017

1.4. Thesis outline

Chapter 2, entitled **Wind turbine gear oils**, summarizes, briefly, the importance of lubrication in wind turbine gearboxes and gives a general presentation of different base stocks. The typical physico-chemical properties and rheological response of five fully formulated gear oils is presented, as well as a chemical characterization using FTIR and ICP methods.

Chapter 3, entitled **Film thickness and traction coefficient of wind turbine gear oils**, film thickness measurements, carried out on a ball-on-disc contact lubricated with wind turbine gear oils, will be presented. Film thickness predictions are discussed and compared with the experimental results. The friction behaviour of the oils was also measured in a wide range of operating conditions. Test procedures, pre and post-test analyses are also presented. This work is published in Paper IX.

Chapter 4, entitled **Gearbox power loss model**, presents a literature review about the different sources of power loss occurring in gearboxes. Several models will be presented and compared for gear, rolling bearing and seal losses. The model proposed, as well as several parameters necessary to calculate gear power loss (coefficient of friction and gear loss factor) will be presented. This work is published in Papers VI, VII, VIII and X.

Chapter 5, entitled **Power loss in rolling bearings**, presents the friction torque measurements in rolling bearings with different wind turbine gear oil formulations. The new SKF friction torque model is explored in order to be a valid tool to predict

friction torque of rolling bearings in gearboxes. The friction torque device, the testing procedures and pre and post testing analyses are also presented. This work is published in Papers I, II, III, IV and VI.

Chapter 6, entitled **Power loss in FZG gearboxes**, presents the torque loss measurements on FZG gears lubricated with wind turbine gear oils. The results allowed the calibration of the FZG machine for each oil formulation, allowing to perform tests with different gear geometries other than the spur gears used in a FZG slave gearbox. The influence of the gear oil will be presented and a power loss model will be calibrated. To do that the coefficient of friction of the meshing gears will be determined based on experimental results and correlated with formulas from the literature. This work is published in Paper V and VII.

Chapter 7, entitled **Low loss gears**, presents the 'low loss' concept for the design of efficient gear pairs. The state of art is analysed and experimental results will be presented, showing combination of gear design and oil formulation can promote a v ery significant improvement on gear efficiency. A parametric study of the influential design variables of a gear will be done allowing to find the most efficient gear set for a given situation. This work is published in Paper VII.

Chapter 8, entitled **Testing and prediction of power loss in multi-stage gearboxes**, presents an overview of testing procedures and experimental results of multi-stage gearboxes, both parallel and planetary. A power loss simulation for a full wind turbine gearbox with two planetary stages and a helical final stage will be presented applying all the knowledge described in the previous chapters. This work is published in Papers XI, XII and XIII.

Chapter 9, entitled **Conclusions and future work**, presents the final conclusions of the thesis and suggests possible future work.

Chapter 2.

Wind turbine gear oils

2.1. Introduction

The most important function of lubricants is the reduction of friction and wear, to provide smooth running and a satisfactory life for machine components. The use of lubricants is as old as mankind, although the scientific focus on lubricants and lubrication technology is relatively new [23, 24].

Theoretically, any substance interposed between two surfaces in relative movement is a potential lubricant. However, the urge to have a lubricant that promotes good film formation, good thermal conductivity, good oxidation and corrosion protection is always desirable. A particular focus on the environmental problems should also be paid during the formulation of a lubricant.

Apart from important applications in internal combustion engines, vehicle and industrial gearboxes, compressors, turbines or hydraulic systems, there are a vast number of other applications which mostly require specifically tailored lubricants [23]. The wind turbine gearboxes are an example of a very specific application because the lubricants must withstand extraordinary demands in terms of temperatures, bearing wear and load [9].

In a wind turbine both grease and oil are used. Greases are used to lubricate the blade root bearings, the main shaft bearings and the yaw bearings. The gearbox is oil lubricated and it is the nechanical component where significant savings in energy loss can be attained and where most failures took place [9]. These are the main reasons to focus this study on the wind turbine gearbox.

The ever-increasing performance requirements made on wind turbine gears have led to higher loads and temperatures in a smaller space. Therefore, nowadays wind turbine gearboxes are generally lubricated with synthetic oils. In this context it needs to be observed that different base oils (polyalphaolefin, polyglycol or biodegradable ester) can be used to formulate these gear oils. In spite of the excellent advances that the oil industry has been achieving, the mineral base oils are widely used due to economic reasons. However, what was once a commodity selected on the basis

of price is now considered by many to be a machine element, carefully specified in much the same way that gears and other components are specified [25].

In this Chapter, a brief description of the different base oils usually found in wind turbine lubrication is done and the requirements of wind turbine gear oils are discussed. In elastohydrodynamic lubrication, the most usual mode of oil lubrication, the lubricant properties change with time due to contact pressure as well as large shear rates. As a consequence the oil temperature rises influencing the physical of the lubricant.

The selected wind turbine gear oil formulations were characterized in order to quantify the rheological properties, as well as other physical properties such as the pressure-viscosity and density. Additionally, a chemical analysis was performed using ICP and FTIR techniques.

2.2. Wind turbine gear oil requirements

According to ANSI/AGMA/AWEA 6006-A03 standard [26], several requirements are needed to formulate a wind turbine gearbox oil. Additional requirements of the lubrication system should also be specified as the type of lubricant, viscosity grade, method of lubrication, operating conditions and system maintenance.

Most wind turbine gearbox manufacturers, like Flender and Hansen Transmissions, compiled new lubrication specifications. These specifications are more stringent than those for industrial gear applications, and are more representative of the true operating conditions. Nowadays, it is very common to find wind turbine gear oils that come with seal of approval Flender and it is a requirement of all gearbox manufacturers that all wind turbine gear oils should meet the standard DIN 51517 Part 3.

The gears operate under low to moderate pitch line velocity and high to very high contact load, demanding anti-scuffing and micro-pitting protection. The base oil of these lubricants should be highly refined mineral oils, full synthetic fluids, or semi-synthetic blends.

The viscosity at the operating conditions of temperature, load and velocity has direct impact on gearbox performance and durability. The oil must be formulated keeping in mind the existence of a cold start-up and, after the initial phase, the high operating temperatures for the oil are a reality. The correct viscosity at cold start-up is important to achieve adequate lubricant flow to all critical surfaces without channelling or creating excessive viscous forces that produce power losses. The correct viscosity at operating temperature is required to minimize metal to metal friction and wear but without contributing to excess losses through gear churning or drag loss of bearings.

Table 2.1.: Required oil cleanliness for wind turbine gearboxes [29].

Oil condition	Required cleanliness per ISO 4406:1999
New oil after blending	16/14/11
Oil after factory testing	17/15/12
Gearbox oil during service	18/16/13

Wind turbine gearboxes are submitted to severe temperature cycles, from very low to significantly high temperaturtes, resulting in condensation problems, requiring that the oil must have good stability in the presence of water. The presence of water put in evidence the necessity for a good rust and corrosion protection.

Wind turbines in desert and mountain environments are exposed to airborne particles and moisture during the rainy season. The offshore turbines are constantly exposed to moisture [27]. The gearbox assembly also can be a source of contamination as well as maintenance operations usually introduces some particles. Sayles and Macpherson [28] showed that rolling element bearing life can be increased up to seven times by changing from a 40 μm filter to a 3 μm filter. In spite of the use of a filter, the oil cleanliness must be according to ISO 4406:1999 standard [29] resumed in Table 2.1.

After performance, the base oil also defines the price as well as the operation life, as presented in Figure 2.1. This should be taken into account by the costumers as well as by gearbox manufacturers that expect for an oil with some specific characteristics that last at least more than 3 years [27]. The efficiency of a fully formulated oil can play a role on the process of increasing life since a base oil generating higher power losses, increases the operating temperature, which is a cause of oxidation of the lubricant. Byproducts of oxidation include residue-forming material, such as varnish and sludge, that can plug filters and small oil passages (eg. oil spray nozzles) and deposit on critical surfaces.

In order to meet all the specifications requirements previously presented, the wind turbine gear oils are fully formulated products and the additive package usually includes: anti-foam agents, corrosion inhibitors, detergents and dispersant's, antioxidants, viscosity index improver's, anti-wear and EP additives [26, 30].

2.3. Base oils

Base oil is the name given to lubrication grade oils initially produced from refining crude oil (mineral base oil) or through chemical synthesis (synthetic base oil). The American Petroleum Institute (API) presently categorizes base stocks into five groups

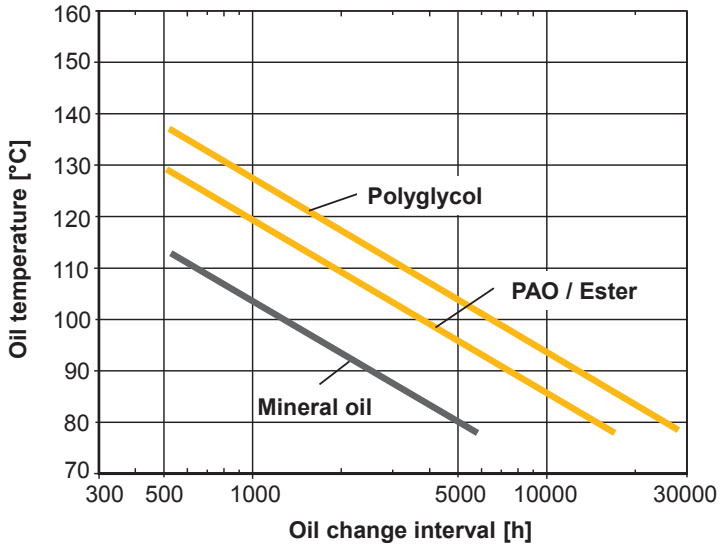

Figure 2.1.: Achievable oil change intervals [25].

Table 2.2.: API categorisation of base oils [23].

Category	Saturates (%)	Sulphur (%)	Viscosity index
Group I	< 90	≥ 0.03	≥ 80, <120
Group II	≥ 90	0.03	≥ 80, <120
Group III	≥ 90	0.03	≥ 120
Group IV	All PAO's		
Group V	All base stocks not included in the other groups		

Table 2.3.: Price of each base stock type in relation to mineral Group I and II [23].

	Mineral (III)	PAO	PAG	Ester
Price of mineral oil Group I and II	1.5 ×	3 – 5 ×	6 – 10 ×	4 – 10

depending on their physical and compositional properties according to Table 2.2 [23].

Base oils are the most important component of lubricants [23] representing the largest influence on the total price of a final product. Before any discussion about the benefits and drawbacks of each base stock, it is important to put the things in economic perspective and the price of each base oil in comparison to the price of mineral Group I and II is presented in Table 2.3.

The costumers main focus, in the case of wind farms, is to produce “green" energy but the kW price should not be influenced by the most overlooked gearbox element: the oil. Because of this, the oil selection is always a economical decision which in

fact will affect the lubricant life and gearbox life.

2.3.1. Mineral

As stated before, the first three groups of API standard [31] are dedicated to the mineral base stocks. Groups I, II, and III represent base stocks typically refined from crude oil and are differentiated by the Viscosity Index (VI), the saturates content, and the sulphur content.

The process of converting crude oil into a finished base oil is referred to as refining. As far as base oil manufacturing is concerned, the actual refining process begins only after the distillation stages. API Group I is normally achieved through solvent refining or separation processing, whereas, API Groups II and III are produced either directly from conversion or hydro-processing technology or from an integration of solvent and hydro-processing technologies [32].

In spite of the continuous introduction in the market of new base stocks, the mineral oil has a lot of characteristics that should keep its use in the future. The lowest price, absolutely out of reach by the other base stocks. The compatibility between mineral formulations and paintings, rubber or plastic components is not a problem. As drawbacks, the mineral oil has poor resistance to oxidation associated with low Viscosity Index (mainly Group I and II) than the other Groups.

2.3.2. Polyalphaolefin

Polyalphaolefin, better known as PAO, are the most commonly used synthetic base fluids in lubricants. Polyalphaolefins are similar to mineral oil hydrocarbons in their chemical structure and are therefore also known under the name of synthetic hydrocarbons. They are manufactured by the catalytic oligomerisation of linear-olefins having six or more carbon atoms. In the case of low molecular weight products they are manufactured by polymerisation. [32, 33].

The rapid growth and acceptance of this type of base fluids are easily explained by their characteristics. According to Shubkin [34] the most significant are:

- A wide operational temperature range;
- Good viscometrics (high VI);
- Thermal stability;
- Oxidative stability;
- Hydrolytic stability;
- Biodegradability (for low viscosity grades);

- Shear stability;
- Low corrosivity;
- Compatibility with mineral oils;
- Compatibility with various materials used on machines;
- Low toxicity;
- Manufacturing flexibility that allows "tailoring" products to specific end-user requirements.

2.3.3. Ester

The esters are of great interest for wind turbine gear applications, in particular the polyols that are manufactured according with the reaction: acid + alcohol = ester + water.

The ester bases are very polar molecules which have direct impact on the lubricant performance. The high polarity makes esters excellent solvents which are usually used to flush other lubricants like polyalkylene glycol. Esters' high polarity also attracts them to metal oxide layers making them good boundary lubricants and friction modifiers.

The strong dipole moments of ester molecules causes them to be attracted to each other. Greater energy is therefore required to overcome these forces and transfer a lubricant molecule from the vapor liquid to the gaseous state. Esters are therefore excellent vacuum pump lubricants. This properties results in low vapor pressures, low volatilities, and high flashpoints. The ester linkage has excellent thermal stability. The reverse reaction of esterification is hydrolysis so the ester fluids has very good hydrolytic stability. They are hygroscopic: water molecules are attracted to the polar ester bond.

2.3.4. Polyalkylene Glycol

Polyalkylene glycol (PAG) based lubricants only represent about 10% of the total industrial market. PAG are very particular among synthetic lubricants due to their high oxygen content and consequent polarity. The polarity of the molecules can also be adjusted through the monomer choice. This capacity allows to modify the solubility in water and hydrocarbons. In general, they provide rather low coefficients of friction suitable mainly for applications with high sliding speeds [32].

The PAG bases have interesting characteristics like: high viscosity index (typically > 200); good temperature stability; reduced wear characteristics and good EP

performance and high hydrolytic stability. In spite of the advantages of using PAG based lubricants, some kind of 'stigma' associated with these products make their penetration into the market quite challenging, according to S. Lawford [32].

Some drawbacks are known about PAG base fluids. Poor compatibility with mineral and PAO base oils due to the high oxygen content, that is, contamination of a PAG with other oil (or vice versa) may create a two phase system and in severe cases gellation. The compatibility with paint and elastomers (seals) is usually an issue, and so the effect of a PAG fluid on a painting should always be assessed before use. According to Lawford [32] the thermal and oxidative stability of PAG is slightly worse than mineral and PAO base oils.

2.4. Additives

The base fluids, both mineral and synthetic, in majority of the cases cannot satisfy high performance requirements without the aid of additives. Additives are chemical compounds added to the oil blend in order to enhance or add some specific properties to the finished oil [23]. The additives can be separated into two different groups according with effects on the lubrication system. They can affect the physical and chemical properties of the base oil, but they can also influence the contacting surfaces, affecting their physicochemical properties.

Usually, the concentration of additives on the blend go from few ppm up to 50% depending on the function of the additive. The multifunctional aptitude of the additives in general reduces the possibility of negative interaction between them. In spite of the good effects that can be obtained with the additives, it is required the use of good quality base oils. In Appendix A the most usual additives are briefly presented.

2.5. Fully-formulated wind turbine gear oils

In order to get an overview of the wind turbine gear oils generally available for use, 5 fully formulated gear oils were selected, also commercially available. It was interesting to cover a good range of possible products, mainly in terms of base oil. In that sense a mineral (MINR), a polyalpholephin (PAOR), a biodegradable ester (ESTR), a polyalkylene glycol (PAGD) and also a hydro-processed group III mineral with polyalkyl methacrilate as viscosity index improver (MINE) are included for this analysis.

All wind turbine gear oils selected have the same viscosity grade, ISO VG 320, and are expected to have 320 cSt ($\pm$ 10 %) at 40 °C.

According to the manufacturer, the mineral based oil (MINR) is formulated with an EP additive system providing anti-foam, oxidation and dispersant properties as well. It complies to DIN-51517 part 3 (CLP); Flender Industrial Gear and ISO 12925-1 CKD quality standards.

The ester based oil (ESTR) is formulated with highly-saturated esters and it is highly biodegradable.

The polyaphaolephin based oil, PAOR, is constituted by 90% of PAO and also with a significant amount of ester used to increase additive solubility and avoid haze. The additive package has primarily EP function. The lubricant meet the requirements of DIN-51517 part 3 (CLP), Flender Industrial Gear, AGMA 9005-E02 EP, ISO 6743/6 CKT and U.S. Steel 224.

The mineral oil with PAMA viscosity modifier, MINE, is about 55% of hydro-processed group III mineral and 40% of PAMA viscosity modifier additivation to improve the high temperature viscosity. About 5% of the formulation is an additive package.

The polyalkylene glycol based oil (PAGD) is a fully formulated oil developed to work under corrosive media and also to be compatible with paintings, a common problem of this type of oil.

2.6. Physical characterization of fully formulated wind turbine gear oils

2.6.1. Rheometry

The first goal of rheometry is a search for stress versus deformation relationships for various technological and engineering materials in order to solve macroscopic problems related to continuum mechanics of these materials. The second goal consists of establishing relationships between rehological properties of a material and its molecular composition content.

The measurements were performed with a Rheomat 115 rotational viscometer operating according to the “Searle” or “Couette” principle.

The measuring bob rotates in the measuring substance driven by an electromotor. The braking torque thereby exerted on the bob by the substance is measured in the measuring head of RHEOMAT 115. The shearing speed prevailing in the substance is a function of the bob’s rotational speed, and the shear stress is a function of the braking torque.

The geometry of the rheometer used is a coaxial cylinder, as presented in Figure 2.2. The coaxial cylinders are referred by the diameter of the inner bob. The diameter of the cup is in proportion to the bob size, as defined DIN 53019 [35]

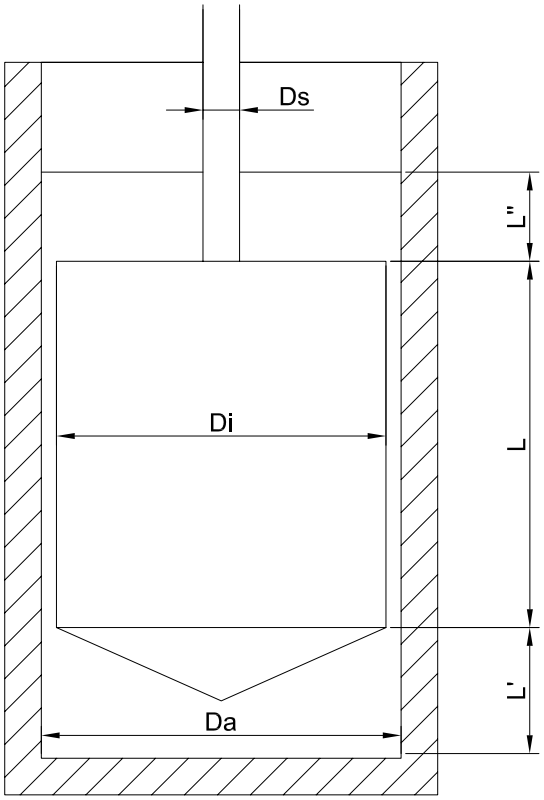

Figure 2.2.: Scheme of a rotary viscosmeter with coaxial cylinders.

standard.

The shear rate ($\dot{\gamma}$) of the fluid tested in the rotary viscometer can be calculated considering the velocity of the bob (U_{bob}) and the characteristic geometry (Da=48.8 mm and Di=45 mm) as expressed in equation (2.1).

$$\dot{\gamma} = \frac{du}{dy} = \frac{U_{bob}}{Da - Di} \tag{2.1}$$

The representative dynamic viscosity is calculated using the representative shear stress divided by the shear rate, as presented in equation (2.2). The value of τ_{rep}=195.5 mPa using the Measuring System MS-DIN 145.

$$\eta_{\%} = \frac{\tau_{rep}}{\dot{\gamma}} \tag{2.2}$$

The Rheomat 115 viscometer measures a dimensionless value ($T_{\%}$) that allow to calculate the dynamic viscosity according to equation (2.3).

$$\eta = \eta_{\%} \cdot T_{\%} \tag{2.3}$$

Five wind turbine gear oils presented in Section 2.5 were submitted to a rheologic measurement according to the procedure described before. The oils were tested at

different operating temperatures: 40, 70 and 100 °C. The shear rate ranged from the minimum allowed value of the rheometer (6.4 s^{-1}) to the maximum of 967 s^{-1} . In some cases due to the limitation in the power of the motor that accelerates the bob on the cup (Figure 2.2), the boundary limits were not achieved.

The dynamic viscosity against the shear rate results are presented in Figure 2.3. The behaviour of the oils can be considered Newtonian, which was expected for this range of shear rate. The rotary viscometer used has some difficulty in keeping the temperature constant when the speed (or shear rate) is increased. For example at 100 °C the oils show a dilatant behaviour as presented in Figure 2.3. However this increase of dynamic viscosity with the shear rate is due to the increase of heat dissipation through convection for the room resulting in lower oil temperature and consequently higher dynamic viscosity.

Comparing the dynamic viscosity of the different formulations it was observed that PAGD has the highest dynamic viscosity, no matter the temperature considered. At 40 °C the MINR and the synthetic fluids have similar dynamic viscosities, but when the temperature rises the MINR has significantly lower dynamic viscosity than the other formulations, as suggested by its low VI.

2.6.2. Engler viscometry

An Engler viscometer was used to measure the kinematic viscosity of the different oils. The ENGLER viscometer (see IP 212/92 standard), is composed by a recipient where the lubricant sample is introduced, which has a calibrated hole in the bottom that is obstructed or cleared through the use of a wood stick. In order to warm up and maintain the lubricant at the desired temperature, the recipient is placed inside another recipient containing a fluid (water or oil) that is heated by an electric resistance. These two recipients are supported by a tripod that allows the levelling of the device. Two thermometers are available to control the temperature (one for the bath and the other for the lubricant).

In the case of an Engler viscometer, the time taken to flow through the hole is proportional to the kinematic viscosity according to equations (2.4) and (2.5).

$$^{\circ}Engler = \frac{fluid\ flow\ time\ (200\ ml)}{water\ flow\ time\ at\ 20\ ^{\circ}C\ (200\ ml)} \tag{2.4}$$

$$cSt = k_1 \times^{\circ} Engler + \frac{k_2}{^{\circ}Engler + k_3} \tag{2.5}$$

with,

$$\begin{cases} ^{\circ}Engler < 3 \ \rightarrow \ k_1 = 14.867;\ k_2 = 75,568;\ k_3 = -6,198; \\ ^{\circ}Engler \geq 3 \ \rightarrow \ k_1 = 7,624;\ k_2 = -2,717;\ k_3 = -1,522; \end{cases}$$

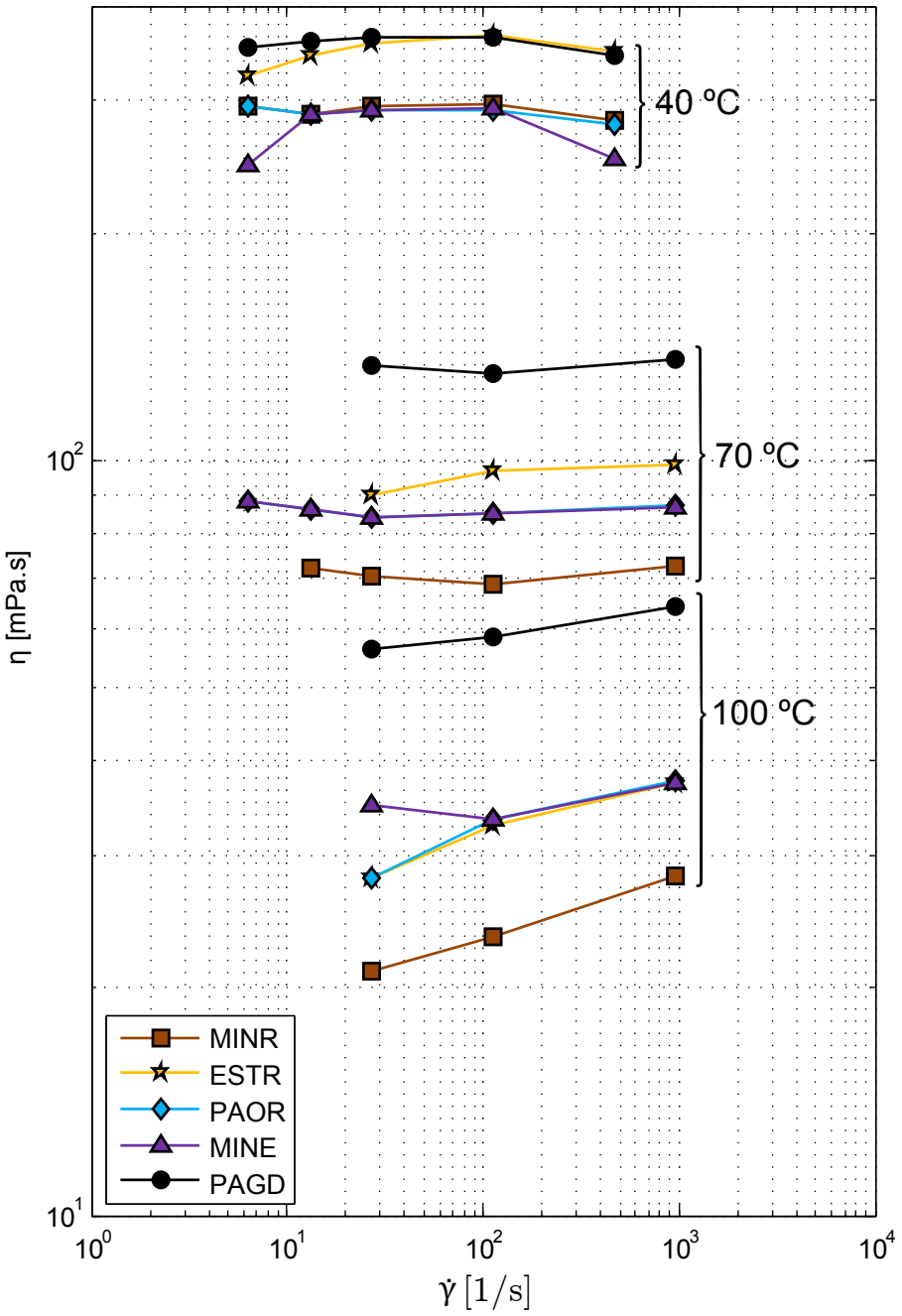

Figure 2.3.: Dynamic viscosity vs. shear rate at 40, 70 and 100 °C.

Table 2.4.: Kinematic viscosity (ν), ASTM constants (m_A, n_A); Vogel constants (k_V, b_V, c_V) and viscosity index (VI) for the wind turbine gear oils.

Parameter	Unit	MINR	ESTR	PAOR	MINE	PAGD
ν @ 40 °C	$[cSt]$	319.22	302.86	313.52	328.30	290.26
ν @ 70 °C	$[cSt]$	65.81	77.48	84.99	93.19	102.33
ν @ 100 °C	$[cSt]$	22.33	34.85	33.33	37.13	51.06
m_A	[/]	9.066	7.582	7.351	7.048	5.759
n_A	[/]	3.473	2.880	2.787	2.664	2.151
k_V	[/]	0.082	1.606	0.188	0.203	1.507
b_V	[/]	1051.82	446.22	1043.23	1072.49	638.49
c_V	[/]	87.129	45.129	100.556	105.173	81.336
VI	[/]	85	165	153	172	252

Tests at 40, 70 and 100 °C were performed in order to measure the kinematic viscosity of all the wind turbine gear oils. The kinematic viscosity measurements are presented in Table 2.4, showing that all the oils are in the range acceptable for an ISO VG 320 grade oil 320 ±32 cSt as expected by the standard. In Appendix B the limits for the ISO VG viscosity grades may be found.

Using ASTM D341 [36] equation (2.6) it was possible to calculate the ASTM constants m_A and n_A keeping the constant value of a_A=0.7 for all the oils.

$$log\ log(\nu + a_A) = n_A - m_A \cdot log(T) \tag{2.6}$$

The equation (2.7), also known as Vogel's equation, was also used to determine the viscosity-temperature dependence of the oils tested. The constants k_V, b_V and c_V were determined and are presented in Table 2.4.

$$\nu = k_V \cdot e^{\left(\frac{b_V}{\theta + c_V}\right)} \tag{2.7}$$

2.6.3. Density

The density was measured with an Anton Par densimeter, a portable unit. The range of temperature available goes from 15 up to 40 °C which is enough to know the density of a fluid under ambient temperature conditions. It is known that the density depends on the temperature [37]. However, the influence of the pressure on the density is much more important than the influence of the temperature as explained in Appendix B.

Table 2.5.: Density (ρ) and thermal expansion coefficient (α_t) for the wind turbine gear oils.

Parameter	Unit	MINR	ESTR	PAOR	MINE	PAGD
ρ @ 15 °C	$[g/cm^3]$	0.902	0.915	0.859	0.893	1.059
$\alpha_t \times 10^{-4}$	[/]	5.8	8.1	5.5	6.7	7.1

The density was measured at 15 °C, which is the reference temperature (θ_0) and the values are presented in Table 2.5. Additional measurements were performed up to the limit temperature of the densimeter. The values measured were used to evaluate the thermal expansion coefficient (α_t), according to equation (2.8).

$$\rho = \rho_0 \cdot (1 + \alpha_t \cdot [\theta_0 - \theta]) \tag{2.8}$$

The results show that MINR, ESTR and MINE have similar densities, between 0.89 and 0.92, while PAOR shows a lower value. PAGD has a significantly high density (higher than water and the other formulations).

2.6.4. Pressure-viscosity

Under elastohydrodynamic lubrication conditions, the formation of the lubricating film is strongly dependent on the pressure viscosity behaviour of a lubricating oil, as shown in literature [37]. The pressure-viscosity coefficient is described in Appendix B and its use in film thickness calculations is presented in Appendix C.

The kinematic viscosities measured and presented in Table 2.4 may be used to determine the pressure-viscosity coefficient using Gold's equation (2.9). The pressure-viscosity coefficient can be determined for a pressure of 0.2 GPa, usual value of the pressure in the inlet zone of the contact, where the film formation occurs [37]. Depending on the base oil, the s and t values are provided by Gold *et al.* [38].

$$\alpha = s \cdot \nu^t \times 10^{-8} \tag{2.9}$$

The pressure-viscosity coefficient can be calculated with some degree of confidence for MINR (mineral naphtenic), ESTR (ester), PAOR (polyalphaolephin) and PAGD (polyalkylene glycol) using equation (2.9). However, for MINE oil, which is a mixture of Mineral and PAMA viscosity modifier in a concentration close to 40 %, the pressure-viscosity coefficient is expected to follow a different behaviour of a fully formulated oil with more than 90 % of mineral base oil like MINR.

To measure the pressure-viscosity coefficient, an high pressure viscometer was used to perform tests at 25, 50 and 80 °C, varying the pressure form 0 up to 10 000 bar.

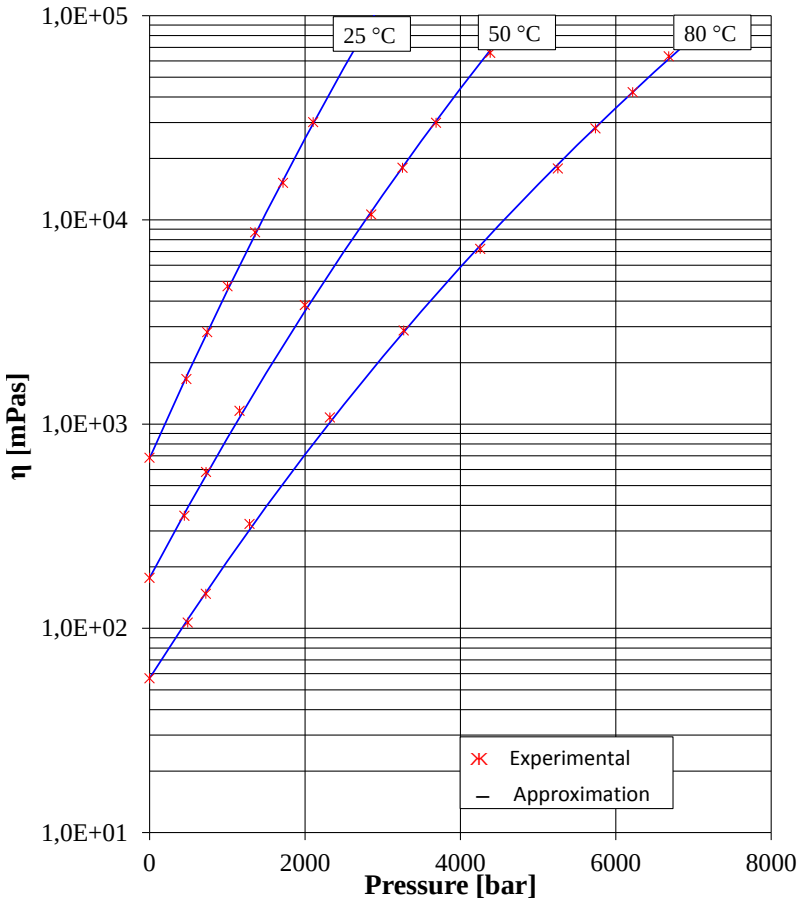

Figure 2.4.: Viscosity measurements vs. pression and "Modulus-Equation" approximation for MINE oil.

The experimental results are presented in Figure 2.4, as well as an approximation of the results using Barus equation (see Appendix B). The "Modulus-Equation" constants determined using equation (2.10) for the oil are presented in Table 2.6.

$$\eta = K \cdot e^{\left[\frac{B}{\nu+C}\right]} \cdot e^{\left[\frac{p}{a_1+a_2\nu+(b_1+b_2\nu)p}\right]} \tag{2.10}$$

The approximation of the "Modulus-Equation" to experimental results allow us to have the dynamic viscosity at 0.2 GPa or 2000 bar for the MINE oil. With the values at a given pressure it is possible to calculate the pressure-viscosity coefficient

Table 2.6.: "Modulus-Equation" constants for MINE oil.

K [mPas]	B [°C]	C [°C]	a1 [bar]	a2 [bar/°C]	b1 [-]	b2 [1/°C]
0.1122	1200.7739	113	403.0987	4.0138	0.0221	0.0002

Table 2.7.: Constants of Gold equation for different base oils at 0.2 GPa.

	MINR	ESTR	PAOR	MINE	PAGD
s	0.9904	0.6605	0.7382	0.5421	0.5489
t	0.1390	0.1360	0.1335	0.1739	0.1485

Table 2.8.: Pressure-viscosity coefficient (α) calculated at 80 °C for the fully formulated wind turbine gear oils.

Oil	MINR	ESTR	PAOR	MINE	PAGD
$\alpha \times 10^{-8}$ [1/Pa]	1.677	1.158	1.279	1.125	1.061

using equation (2.11).

$$\alpha\,(p,T) = \frac{ln\ \eta - ln\ \eta_0}{p - p_0} = \frac{1}{a_1 + a_2 \cdot T + (b_1 + b_2 \cdot T) \cdot p} \tag{2.11}$$

In Section 2.6.2 the kinematic viscosities were measured at different temperatures, which now can be used to calculate s and t constants using equation (2.9). The process follow the principle presented in equation (2.12).

$$s \cdot \nu^t = \frac{ln\ \eta - ln\ \eta_0}{p - p_0} \tag{2.12}$$

With the "Gold" constants s and t determined for MINE and previously published for the other base oils [38] (see Table 2.7), the pressure-viscosity coefficients can be calculated at different temperatures. Table 2.8 shows the α values for all wind turbine gear oils at 80 °C. It is possible to verify that the oils have the following behaviour: $\alpha_{MINR} > \alpha_{PAOR} > \alpha_{ESTR} > \alpha_{MINE} > \alpha_{PAGD}$.

Mia *et al.* [39] determined the pressure-viscosity coefficient from high-pressure rheology for a Mineral oil and different PAO wind turbine oil formulations. The values found are slightly lower than those calculated through Gold's equation. Mia *et al.* values are 15 % lower in the case of mineral oil and 9 % lower in the case of the PAO.

2.7. Chemical characterization of fully formulated wind turbine gear oils

2.7.1. Inductively coupled plasma atomic emission spectrometry (ICP-AES)

Inductively Coupled Plasma - Atomic Emission Spectrometry (ICP-AES) is a technique described in ASTM D5185 [40].

The Atomic Emission Spectrometry was performed for all wind turbine gear oils, and the results are presented in Table 2.9. The elements identified are: Zinc, Magnesium, Phosphorus, Calcium, Boron and Sulphur. Using only ICP, it is almost impossible to understand which particular compounds are present in the fully formulated products, but it can be very useful to monitor lubricant condition, and to verify the additive depletion or contamination by metal particles due to wear.

The sulphur is a constituent of the mineral based oils, but the concentration is not greater than 300 ppm, as previously explained in Section 2.3. The concentration of sulphur in MINR, MINE and PAOR is very high, which can be explained by the presence of EP additives that are sulphur and phosphorous compounds [41–43]. As suggested by the AGMA standard [26], a wind turbine gear oil should primarily be an EP gear oil, but it is clear that PAGD has a different additive package. It is documented that EP oils usually have values of phosphorus greater than 200 ppm and boron can reach 25 ppm [44], which is verified for MINR, MINE and PAOR. The inclusion of EP additives is advised by the manufacturers of the referenced products. The phosphorus concentration on PAGD is much higher than on the other formulations, the high concentration is associated with synthetic oils with anti-wear additives [44], which is also claimed by PAGD manufacturer.

ESTR is a biodegradable product, thus showing much lower sulphur concentration, as expected for biodegradable fluids with low toxicity.

Calcium is commonly associated with the detergent and dispersant additives [41–43] and the ICP result shows that only ESTR has a significant concentration of calcium. In terms of zinc the ESTR and PAOR have much higher content than other oils that can be called zinc-free.

2.7.2. Fourier Transform Infra Red spectroscopy (FTIR)

FTIR is an analytical tool that can be used to provide an indication of the quality of a particular lubricant before, during and after its expected service life.

The spectra of the wind turbine gear oils were evaluated through Infra-Red Spectroscopy (FTIR). The measurement was done on an Agilent Cary 630 FTIR device, using ATR (Attenuated Total Reflectance) accessory. All the spectra shown

Table 2.9.: Chemical composition in ppm of the wind turbine gear oils through ICP analysis.

Parameter	Unit	MINR	ESTR	PAOR	MINE	PAGD
Sulphur (S)	[ppm]	11200	406	5020	6750	362
Phosphorus (P)	[ppm]	354.3	226.2	415.9	460	1100
Boron (B)	[ppm]	22.3	1.7	28.4	36	1.0
Calcium (Ca)	[ppm]	2.5	14.4	0.5	2	0.8
Zinc (Zn)	[ppm]	0.9	6.6	3.5	< 1	1
Magnesium (Mg)	[ppm]	0.9	1.3	0.5	< 1	1.4

here were taken directly from the device's software without smoothing or any type of modification. Since the ATR device does not allow the sample thickness to be controlled, all spectra were normalized to the same peak's height at 1460 cm^{-1}.

FTIR was performed to document each wind turbine gear oil spectra, mainly in the fingerprint zone (<1000 cm^{-1}). The spectra of the fresh oil can be of great importance to monitor the lubricant during its service life. The additive depletion, oxidation or possible contamination can be easily determined comparing the fresh and the used oil.

With this technique one can determine the differences in the spectra of each fully formulated oil in terms of additive package. However, the base oil spectra should be known in advance which is not the case for these particular formulations.

The "fingerprint zone" is presented in Figure 2.5 where the main differences can be observed. However, without a known spectra of the base oil, it is a daunting task to figure out which additive compounds are present in the formulations.

All spectra are presented in Figure 2.6, which include the functional group region (4000 – 100) and finger print region (<1000 cm^{-1}).

A strong absorption band from $\approx$ 2800 to 3000 cm^{-1} is seen in MINR, ESTR, PAOR and MINE oils. It represents the C-H asymmetric stretch of CH_2 and CH_3 molecules that are hydrocarbon structures, present on base oil of the lubricants. The peak's around 1740-1750 cm^{-1} represent the C=O bonds in which the exact position depends on the type of carbonyl. The PAOR and ESTR show the peak exactly at 1446 cm^{-1}, which is expected because PAOR includes ester in the formulation [45,46].

2.8. Closure

The main requirements of a wind turbine gear oil were described in this chapter and possible alternatives for base oils were discussed. Five fully formulated wind

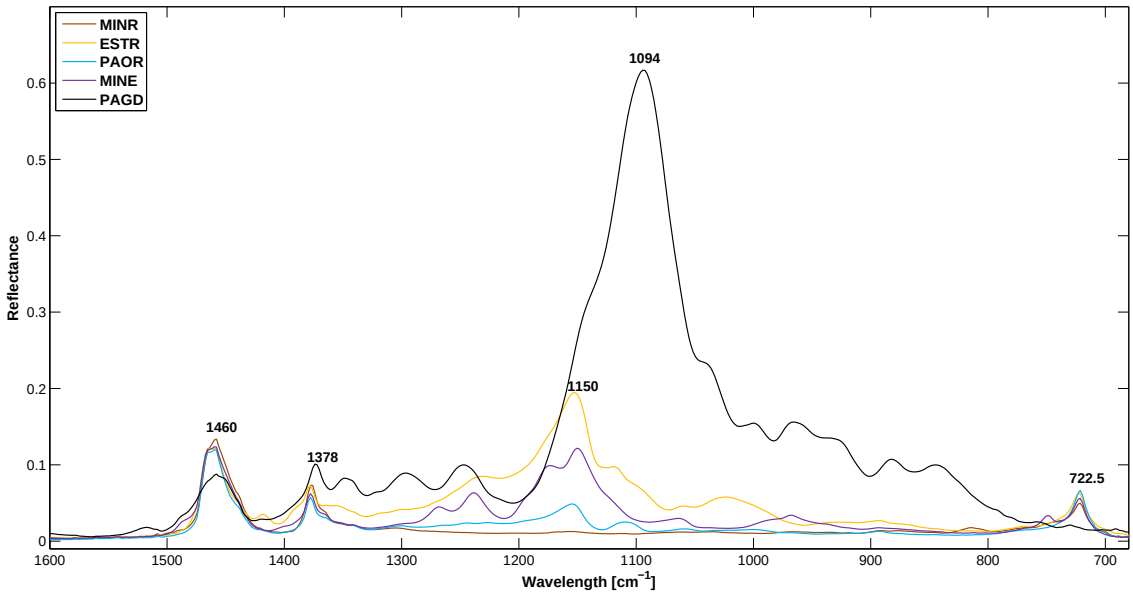

Figure 2.5.: FTIR spectra on finger print zone of all wind turbine gear oils.

turbine gear oils were selected and a physical characterization was done in order to know the dynamic viscosity, kinematic viscosity and density. In the case of MINE, the pressure-viscosity was measured and related with Gold's equation [38].

The results confirm the ISO VG 320 grade of the oils, in spite of the differences verified in the Viscosity Index of the different formulations. The oils show Newtonian behaviour for the conditions tested.

The chemical characterization confirm that the oils are formulated with different additive packages but the exact content is impossible to be identified with ICP and FTIR analysis.

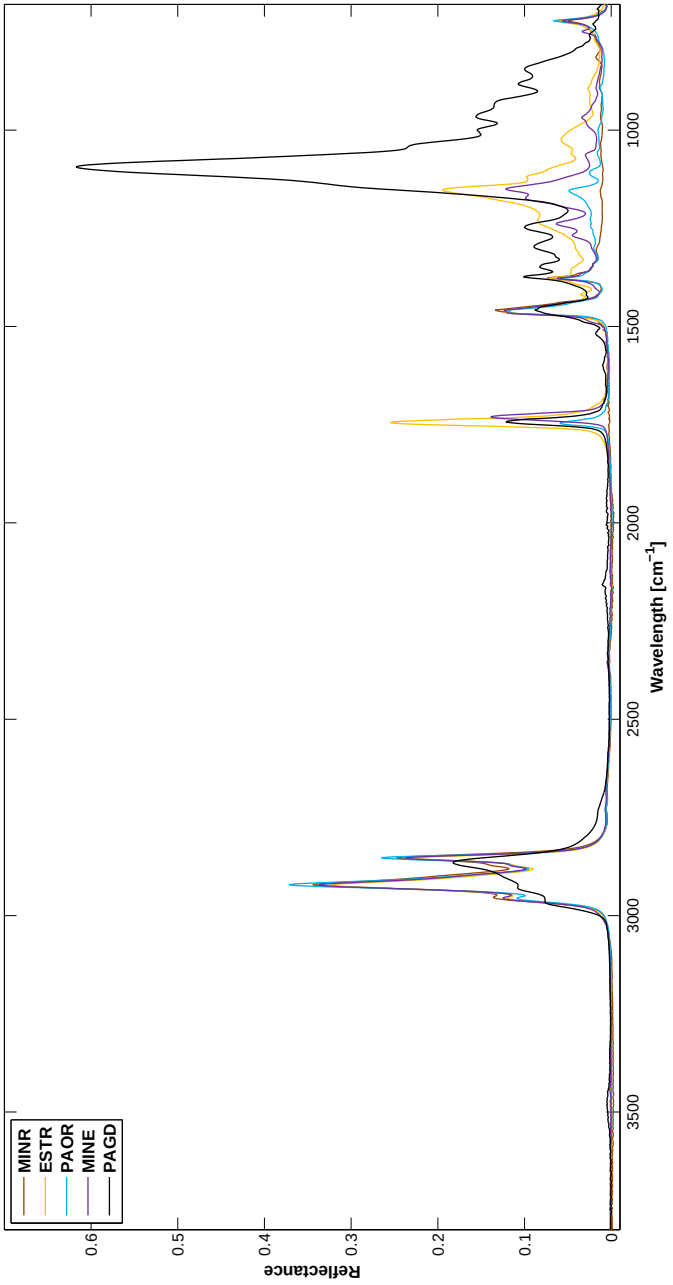

Figure 2.6.: FTIR spectra of all wind turbine gear oils.

Chapter 3.

Film thickness and traction coefficient of wind turbine gear oils

3.1. Introduction

The main focus of EHL researchers has been the prediction of the film thickness and of the traction coefficient in concentrated EHL line and point contacts found in mechanical components such as gears, cams, rolling bearings, etc [47].

In the 1960s Dowson and Higginson [37] performed a series of numerical simulations assuming isothermal Newtonian fluid model and exponential pressure-viscosity to develop the well known minimum film thickness equation in EHL line contacts, presented in Appendix C.

The *"traction coefficient"* or *"coefficient of friction"* depends on the low shear viscosity, the limiting shear modulus and the limiting shear stress the lubricant can withstand. Understand the traction properties of the gear oils is of great interest for their development and for the selection of a lubricant for a given application [48, 49].

In the case of wind turbine gear oils, the published studies are very scarce. This chapter intends to characterize the ability of a wind turbine gear oil to generate a lubricating film. The film thickness prediction is also discussed and related to experimental results. Traction coefficient curves as well as Stribeck curves will be presented to characterize the tribological behaviour of fully formulated wind turbine gear oils.

Figure 3.1.: EHD2 ball-on-disc test apparatus from PCS Instruments.

3.2. Film thickness

3.2.1. Materials and methods

Film thickness measurements were performed on ball-on-disc test apparatus (EHD2 machine, from PCS Instruments) equipped with optical interferometry, as presented in Figure 3.1. This device allow the measurement by optical interferometry of the lubricant film thickness in the contact between a 3/4″ diameter steel ball and a rotating glass disc in the presence of a lubricant fluid. The lubricant film thickness at any point of the image can be accurately calculated by measuring the wavelength of light at that point. Normally, the system measures the wavelength of the light returned from the central plateau of the contact and hence calculates the central film thickness.

Optical interferometry measurements of lubricant film thickness have already been described by several authors. Details of this technique have been reported elsewhere [50–52] and only a brief description will be given here.

The lubricated contact is formed by the reflective steel ball and the flat surface of the glass disc. The glass disc is coated with a semi-reflecting chromium coating on top of which a spacer layer of SiO_2 is deposited. The load is applied by moving the ball upwards towards the disc. The disc is mounted on a shaft driven by an electric motor and the steel ball is also controlled by an independent electric motor, making it possible to run tests under rolling/sliding conditions.

The method to perform film thickness measurements using the EHD2, is described in 4 steps (see Figure 3.2):

1. The contact is illuminated by a white light source directed down a microscope through a glass disc into the contact.

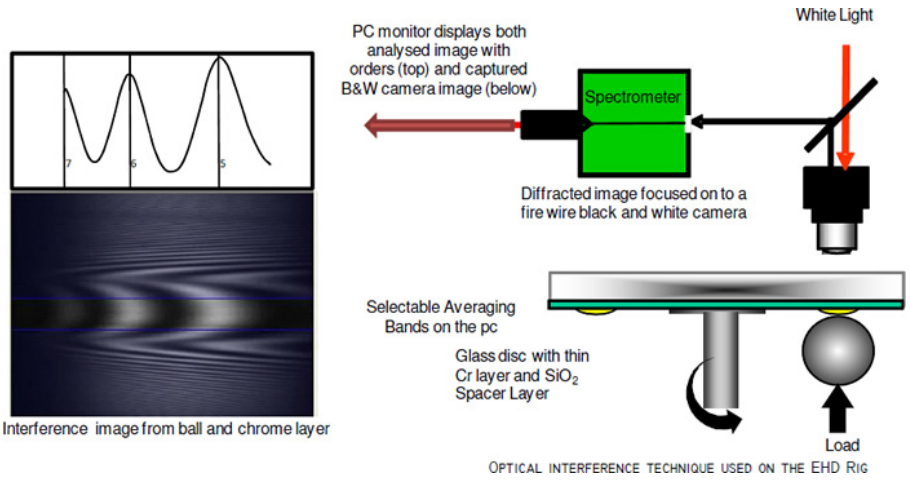

Figure 3.2.: Optical interference technique used in EHD2 test rig.

2. Part of the light is reflected from the Cr layer and part travels through the SiO2 layer and fluid film and is reflected back from the steel ball.

3. Recombining the two light paths forms an interference image that is transferred into a spectrometer and high resolution black and white CCD camera.

4. The camera image is captured by a video frame grabber and analysed by the control software to determine the film thickness.

The method used for translating the optical phase difference map into film thickness has been described by several authors, such as [52–54].

3.2.2. Test Specimens

The standard ball specimen has a 3/4" (19.05 mm) diameter, is made of carbon chrome steel and has a high grade surface finish to ensure good reflectivity. The roughness of the balls and disc is presented in Table 3.1.

The discs are made of glass, coated with approximately 20 nm of chromium and 500 nm of silica. The disc supports a maximum Hertz pressure of approximately 0.7 GPa. The silica spacer layer has a refractive index of 1.4785.

The ball and disc properties are presented in Table 3.1 and the physical properties of the lubricants were described in Chapter 2.

3.2.3. Test procedures

A set of lubricant film thickness measurements were carried out under fully flooded lubrication for all the wind turbine gear oils presented in Section 2.5.

Table 3.1.: Ball and disc data for film thickness measurements supplied by the manufacturer.

	Ball	Disc
Elastic Modulus - E [GPa]	210	64
Poisson Coefficient - ν [-]	0.29	0.2
Radius - R [mm]	19.05	50
Surface roughness - Ra [nm]	20	≈ 5
Spacer layer thickness - [nm]	-	≈ 500
Spacer layer refractive index - [-]	-	≈ 1.4785

The load applied was 50 N, which corresponds to a maximum Hertzian pressure of $p_0 = 0.66$ GPa. Three operating temperatures were used: 50, 80 and 100 °C. Since it is impossible to have pure rolling condition in practice, the tests were carried out with a 3 % slide-to-roll ratio (SRR), defined by equation (3.1).

$$SRR[\%] = 2 \times \frac{(U_{disc} - U_{ball})}{(U_{disc} + U_{ball})} \times 100 \tag{3.1}$$

The entrainment speed range was different for each operating temperature. The highest entrainment speed is always the same and equal to 2 m/s. The lowest value is 0.1 m/s for 50 °C, 0.25 m/s for 80 °C and 0.5 m/s for 100 °C. These conditions generate a measured film thickness above 100 nm, thus ensuring that ball-disc contact does not occur. The largest film thickness that can be measured is around 1000 nm, due to the maximum measuring range of the optical device. Such limitation restricts the maximum entrainment speed used in the tests.

The ball is partially submerged in the lubricant, up to the centre of the ball, and the ball rotation supplies the lubricant to the contact. The lubricant container has got a maximum capacity of 120 ml and the lubricant is heated up to the operating temperature. In this configuration the maximum temperature deviation is ± 1.0 °C.

The temperature oscillations were considered when calculating all the parameters shown in future calculations. For each operating temperature, the film thickness was measured from the highest to the lowest entrainment speed, and then again from lowest up to the highest entrainment speed. This procedure is quite useful to assess the repeatability of the measurements, which was always very good.

3.2.4. Experimental results

The lubricant parameter (LP) defined by the product $LP = \eta \times \alpha$, was calculated using the pressure-viscosity equation (2.9). The corresponding values for all wind

Table 3.2.: Lubricant Parameter ($LP \times 10^{10}$) for the wind turbine gear oils tested.

Temperature	MINR	ESTR	PAOR	MINE
50 °C	32.03	23.30	24.79	25.28
80 °C	6.65	6.52	6.72	6.73
100 °C	3.08	3.38	3.44	3.40

turbine gear oils and for the temperatures of 50, 80 and 100 °C are shown in Table 3.2. At constant temperature the LP values for the different lubricants are very similar.

Figure 3.3 shows the film thickness measurements for a wide range of the entrainment speed and for the temperatures of 50, 80 and 100 °C, for the selected wind turbine gear oils.

Whatever the temperature considered, the film thickness measurements for oils MINR, ESTR and PAOR are always very similar, as presented in Figure 3.3. This is not surprising since for the same temperature these oils have almost the same LP values.

The film thickness of PAOR is about 6% higher than ESTR, which is approximately the same difference found on the LP. In fact, the measurements follow the behaviour of the LP parameter, since for same conditions of speed and geometry, only the dynamic viscosity and the pressure-viscosity (LP) play a role on film thickness.

The MINE oil has higher LP parameter than PAOR and ESTR at 50 and 80 °C, but presented lower film thickness which can be related with shear thinning effects. The viscosity of a mineral oil with 4% of PAMA was measured and a Non-Newotinan behaviour was observed when the shear rate increases, resulting in shear thinning effect [55]. A similar behaviour is expected for a mineral oil with a much higher PAMA content, like MINE.

For all operating temperatures tested, both ESTR and PAOR show similar behaviour. MINE and MINR become close when temperature rises.

3.2.5. Film thickness prediction

In a recent study, Van Leeuwen [56] demonstrated that the centre film thickness values predicted by the equations proposed by Chittenden *et al.* [57] and by Hamrock *et al.* [58] correlated very well ($R^2 > 97$ %) with accurate film thickness measurements for the same operating conditions and for a lubricant with a known pressure-viscosity coefficient (α).

The equations proposed by Chittenden *et al.* and Hamrock *et al.* use the Roelands equation [59] to describe viscosity dependence on pressure and on temperature and

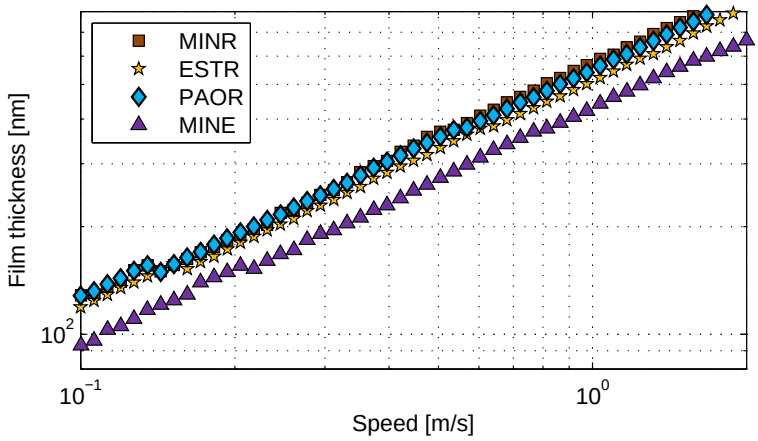

(a) 50 °C.

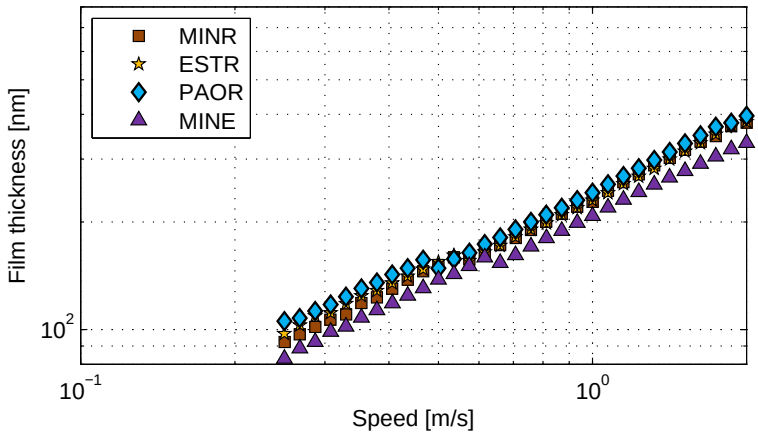

(b) 80 °C.

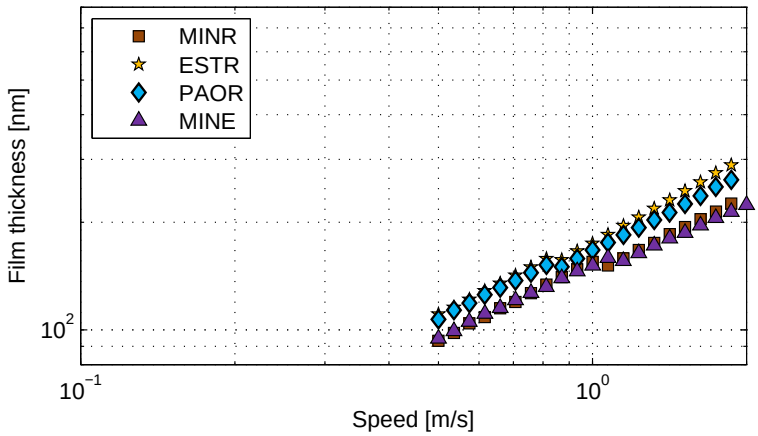

(c) 100 °C.

Figure 3.3.: Film thickness measurements for different wind turbine gear oils.

take into account fluid compressibility according to Dowson and Higginson [37].

Based on the evidence reported by Van Leeuwen [56], equation (3.2) proposed by Hamrock and Dowson [24] will be used in this work to predict the centre film thickness in point contacts. Equation (3.2) is presented in detail in Appendix C.

$$h_0 = 2.69 \cdot R_X \cdot U^{0,67} \cdot G^{0,53} \cdot W^{-0,067} \cdot C_0 \tag{3.2}$$

The corrected equation taking in account the inlet shear heating of the lubricant and corresponding thermal correction (ϕ_T) is presented in equation (3.3).

$$h_{0C} = \phi_T \cdot h_0 \tag{3.3}$$

Thermal correction ϕ_T used was proposed by Gupta *et al.* [60], as shown in equations (3.4) and (3.5).

$$\phi_T = \frac{1 - 13.2 \cdot (p_0/E^*) \cdot (L^*)^{0.42}}{1 + 0.213(1 + 2.23 \cdot S^{0.83}) \cdot (L^*)^{0.64}} \tag{3.4}$$

$$L^* = \frac{\beta_L \cdot \eta \cdot U_S}{k_L} \tag{3.5}$$

Figure 3.4 presents film thickness predicted by equations (3.2) to (3.5) – straight lines and the corresponding experimental measurements – markers. for all gear oils and operating temperatures considered. The correlation between predicted and experimental values is very good for gear oils MINR, PAOR, and ESTR, whatever the entrainment speed and operating temperature. However, such good correlation is not observed in the case of MINE gear oil. In fact, it has been reported in literature [55] that mixtures of mineral or synthetic base oils with polymers, such as gear oil MINE, exhibit a clear non-Newtonian and shear-thinning behaviour. In this case, the film thickness predictions overestimate the film thickness measurements.

The difference between predicted and measured centre film thickness values might be minimized if the pressure-viscosity coefficient is minimized.

The film thickness for all the oils follow the usual trend of the dimensionless velocity group (U) [37], the rate is $h_{0C} \propto U^{0.67}$.

3.2.6. Pressure-viscosity

The difference between the predicted and the measured centre film thickness values might be minimized if the pressure-viscosity coefficient is optimized. Table 3.3 shows the pressure-viscosity coefficients given by Gold's equation [38], α_{Gold}, as well as those resulting the minimization process mentioned above, α_{FTM}.

The values given by Gold's equation are clearly dependent on the lubricant formulation and on the temperature. The α_{FTM} values are, in general, smaller

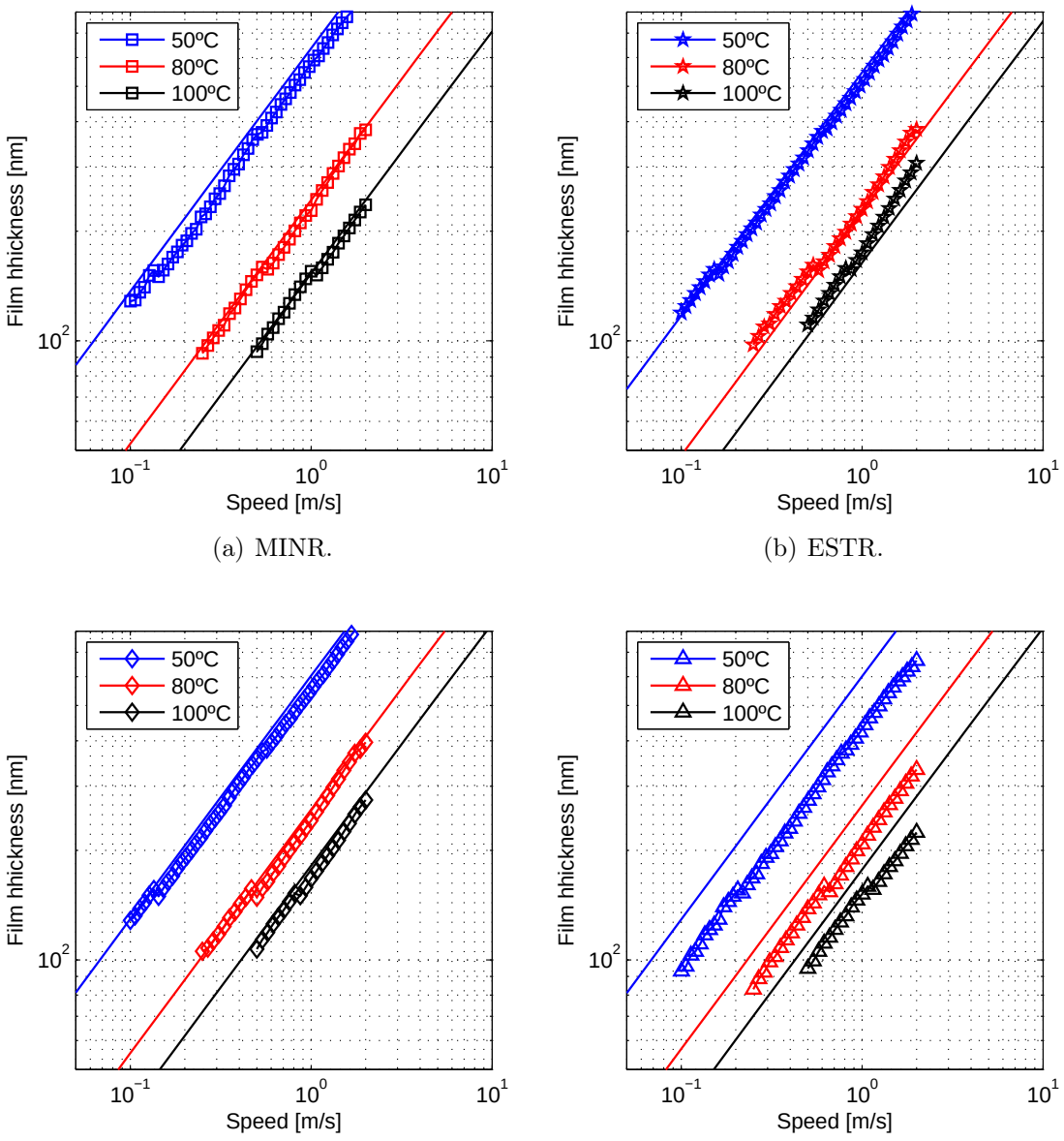

(a) MINR.

(b) ESTR.

(c) PAOR.

(d) MINE.

Figure 3.4.: Film thickness measurements vs predictions for different wind turbine gear oils.

Table 3.3.: Piezoviscosity coefficients determined based on film thickness measurements (α_{FTM}) and Gold's equation (α_{Gold}).

		MINR	ESTR	PAOR	MINE
50 °C	α_{FTM}	1.443	1.092	1.143	0.651
	α_{Gold}	1.995	1.329	1.469	1.346
80 °C	α_{FTM}	1.403	1.038	1.053	0.653
	α_{Gold}	1.667	1.131	1.262	1.112
100 °C	α_{FTM}	1.308	1.139	0.942	0.644
	α_{Gold}	1.526	1.064	1.181	1.011

than the corresponding α_{Gold} values, and such difference is very large in the case of the MINE gear oil (42 % lower). The influence of the temperature also doesn't seem consistent, e.g. $\alpha_{FTM,}$@100°C>α_{FTM}@ 80 °C for ESTR and α_{FTM} @ 40 °C≈α_{FTM}@ 80 °C for MINR.

This indirect prediction of the pressure-viscosity coefficient using film thickness measurements, although very useful, needs further research and these is not a clear consensus in the literature [61, 62].

3.3. Traction curves

3.3.1. Materials and methods

The measurement of the traction coefficients for the wind turbine gear oils were conducted on a ball-on-disc apparatus (Thin Film Measurement System, model EHD2, from PCS Instruments), under controlled temperature. The machine was described in the previous section but a brief description is given here, since the traction measurements require a different arrangement.

During traction measurements the ball runs against the disc and the load is applied by moving the ball upwards towards disc. Both contacting bodies are made of steel and the contact pressure may rise to 1.11 GPa. The remaining conditions related to machine operation capabilities were described in Section 3.2.1.

3.3.2. Test specimens

The ball and disc used are made of carbon chrome steel, with 3/4″ (19.05 mm) and 100 mm diameters, respectively. The ball and disc properties are presented in Table 3.4, and the physical properties of the gear oils were presented in Chapter 2.

Table 3.4.: Ball and disc data supplied by the manufacturer.

	Ball	Disc
Elastic Modulus $-E$ [GPa]	210	210
Poisson Coefficient $-\nu$ [-]	0.29	0.29
Radius $-R$ [mm]	19.05	50
Surface roughness $-\sigma$ [μm]	0.02	0.20

3.3.3. Test procedure

A set of tests were carried out to measure the traction coefficient of the lubricants described in Chapter 2. The traction coefficient of the PAGD oil was not measured because this oil is very aggressive to seals and could damage those of the EHD2 machine.

The load applied was 50 N, which corresponds to a maximum Hertz pressure of $p_0 = 1.11$ GPa. The same operating temperatures were used: 50, 80 and 100 °C. The slide-to-roll ratio varied from 1 to 50 %, for three different entrainment speeds: 0.5, 1 and 2 m/s. In all cases the disc rotated faster than the ball. The temperature control is described in Section 3.2.3.

The test cycle contained several loops where the entrainment speed was kept constant while the SRR was increased from 1 to 50 % and then decrease up to 1% again. The entrainment speed was held at 2 m/s in the first loop and decreased in each loop down to 0.5 m/s.

In order to obtain the Stribeck curves, the SRR was kept constant at 25% and the speed was ranged between 0.01 m/s and 3 m/s. Two different operating temperatures were used: 80 °C and 120 °C. The higher temperature value was used to reach boundary film lubrication conditions.

3.4. Traction coefficient results

The coefficient of friction measurements are presented in Figure 3.5. The relative performance of the oils is almost independent of the temperature and entrainment speed: MINR always generated the highest traction, followed by MINE and PAOR/ESTR have similar behaviour ($COF^{MINR} > COF^{MINE} > COF^{PAOR} \approx COF^{ESTR}$).

When the temperature increases the coefficient of friction decreases, whatever the oil considered. Such behaviour is expected for full film lubrication conditions, as suggested by several authors [63, 64]. To understand the lubrication regime that

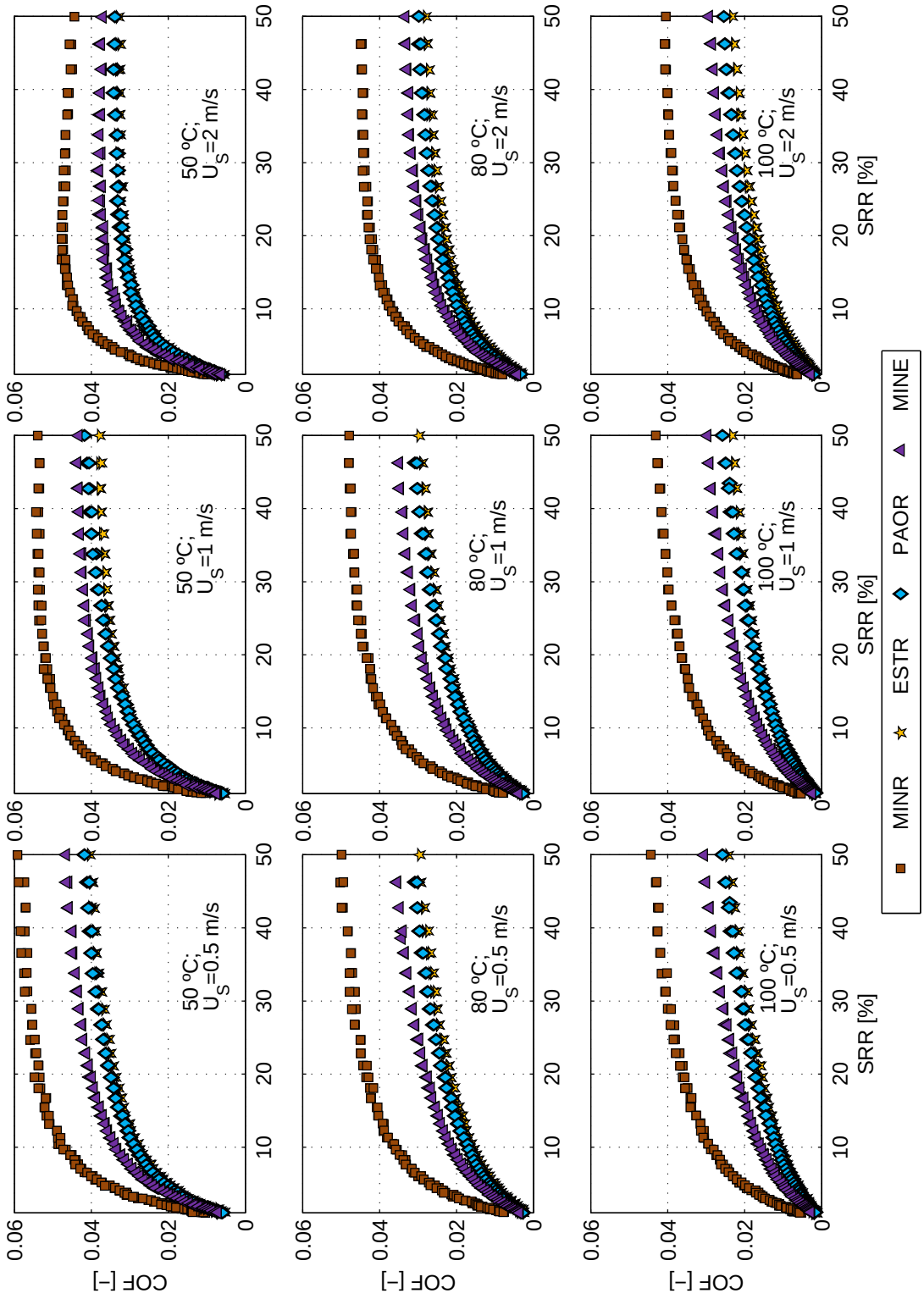

Figure 3.5.: Traction coefficient measurements for different wind turbine gear oils.

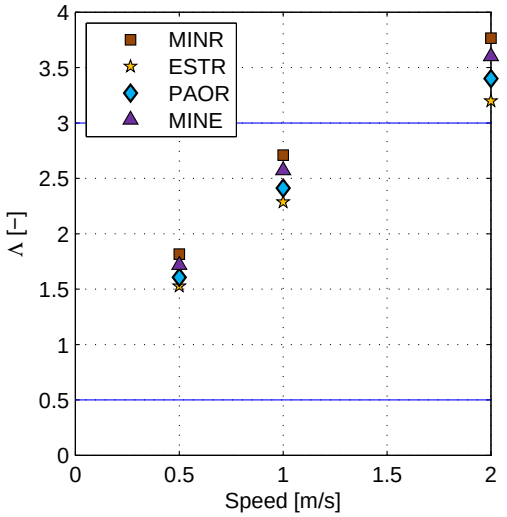

(a) 50 °C.

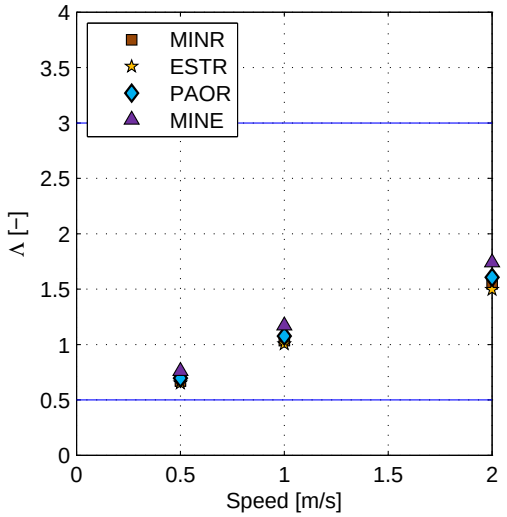

(b) 80 °C.

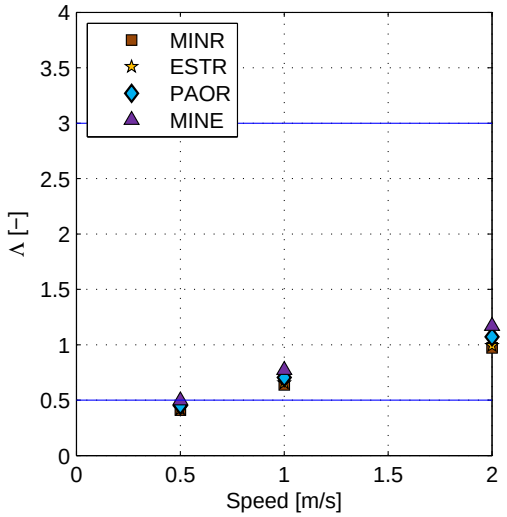

(c) 100 °C.

Figure 3.6.: Specific film thickness predictions for the traction coefficient measurements.

occurs for each test performed, the specific film thickness was calculated for each operating temperature and the results are presented in Figure 3.6. The results confirm that all tests were performed under mixed or full film conditions, since $\Lambda > 0.5$, no matter the operating speed or oil temperature. At 50 °C and U_S=2 m/s, full film conditions are reached and the oils showed a reduction of the coefficient of friction with increasing slide-to-roll ratio.

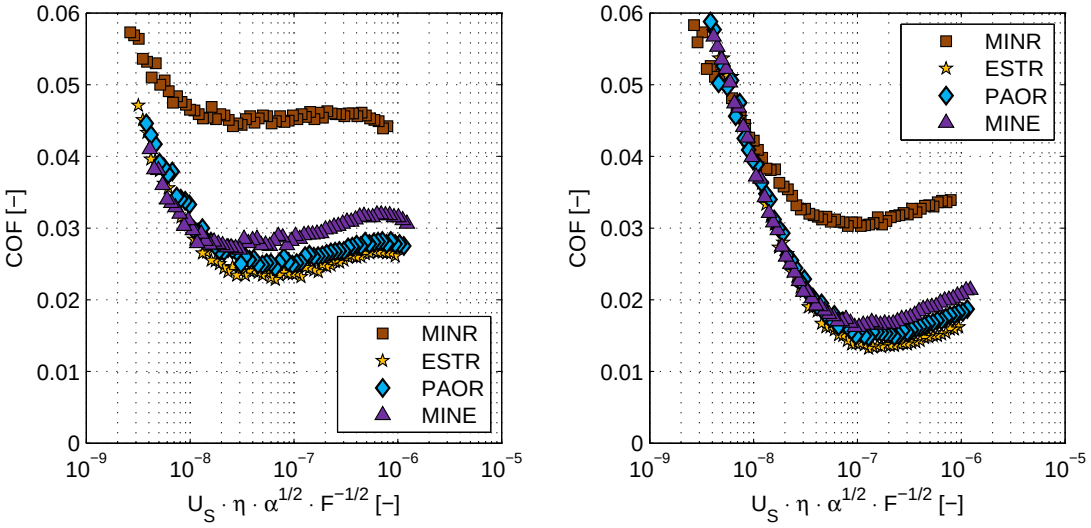

(a) 80 °C.

(b) 120 °C.

Figure 3.7.: Stribeck curves for the wind turbine gear oils at 80 °C and 120 °C.

The coefficient of friction decreases when the speed increases, for all gear oils. However, the oil that appear to be most influenced by speed is MINR, which has the lowest viscosity index.

The results also suggest that the nature of the oil, i.e. the base oil clearly defines the friction behaviour of the lubricant. The oils are fully formulated for gear lubrication. However, the traction coefficient is quite different. So, the base oil appears to be the most important factor for the full film coefficient of friction (μ_{EHD}) [63].

3.5. Stribeck curves results

The Stribeck curves were measured at 80 and 120 °C and are presented in Figure 3.7. The coefficients of friction are presented using the modified Hersey number suggested by Brandão [63] and given by equation (3.6). The original Hersey number (S) is given by equation (3.7).

$$S_p = \frac{\eta \cdot U_S \cdot \alpha^{1/2}}{F^{1/2}} \tag{3.6}$$

$$S = \frac{\eta \cdot U_S}{F} \tag{3.7}$$

Brandão proposed that for a modified Hersey number $S_p < 10^{-9}$, the contact is under boundary film lubrication, while for $S_p > 10^{-7}$ it is under full film lubrication.

The results presented in Figure 3.7 show the expected behaviour for $S_p > 10^{-7}$. Under these conditions the coefficient of friction of the synthetic formulations are very similar for the same temperature and significantly lower than MINR. The influence of the temperature is clear for all the wind turbine gear oils: the coefficient of friction decreases when the temperature increases (see Figures 3.7(a) and 3.7(b)).

At 80 °C, the modified Hersey number never reaches 10^{-9} and so the oils remain under mixed film lubrication for values $S_p < 10^{-7}$.

At 120 °C the oils come closer to the expected boundary lubrication condition, and for these conditions the oils show very similar coefficients of friction, see Figure 3.7(b), whatever the base oil and additive package considered.

For a Hersey number $S_p \approx 10^{-6}$, the oils show the following behaviour: ${\mu_{EHD}}^{MINR} > {\mu_{EHD}}^{MINE} > {\mu_{EHD}}^{PAOR} > {\mu_{EHD}}^{ESTR}$.

3.6. Closure

The film thickness and the traction coefficient was measured for four different wind turbine gear oil formulations, on a ball-on-disc apparatus.

The film thickness tests, clearly show that no substantial differences were found between oils. The MINR oil can generate a lubricating film similar to ESTR and PAOR. MINE show a shear thinning effect and consequently lower film thickness. This behaviour was not expected from the measured properties of MINE.

The traction coefficient tests, performed under full film conditions, allow to understand that the base oil is very important for the friction behaviour of a gear oil under these lubrication conditions. We can observe that a mineral base oil has higher friction coefficient (μ_{EHD}) than a synthetic oil or than a mineral with a viscosity modifier additive in large concentration, as the case of MINE oil. The friction behaviour of the PAO (PAOR) and of the ester (ESTR) are very similar, which has already been reported by Brandão [63]. The traction coefficient decreases with the increasing temperature and decreases with the increasing speed which is coherent with the literature [63].

The Stribeck curves show that the full film coefficient of friction is dependent on the oil formulation and large differences between MINR oil and other formulations were found. However, when the lubrication regime moves towards boundary film lubrication the coefficients of friction are similar at 120 °C for all oil formulations.

Chapter 4.

Gearbox power loss model

4.1. Introduction

Predict the power loss in a gearbox has always been a daunting task. Infinite combinations of rolling bearings, gears, seals, casing geometries, oil formulations and operating conditions can be used, resulting in a large number of variables influencing power loss of a gearbox and making very difficult to model it. However, the power loss models for gearboxes should always be under the focus of tribologists and engineers, because of the increasing importance of improving efficiency and reduce fuel emissions. In alternative, gearbox testing can be used to measure the power loss of a gearbox, but such option is time demanding, quite expensive and in some cases the technical aspects are very difficult to overcome.

It is currently accepted that the different power loss mechanisms acting in a gearbox are those presented in Figure 4.1 [65]. These mechanisms are divided in load dependent and load independent.

The load dependent losses are directly influenced by the applied load torque while the load independent mechanisms depend mainly on the rotational speed, gearbox geometry and oil physical properties, the density and the viscosity [66]. The load dependent losses are due to gears (P_{VZP}) and rolling bearings (P_{VL}). The load independent or no-load losses are due to seals (P_{VD}) as well as rolling bearings (P_{VL}) and gears (P_{VZ0}).

Under the nominal torques and rotational speeds, in an automotive or industrial gearbox, the load dependent gear losses are the main source of energy dissipation followed by the rolling bearing losses [67]. The load independent losses has usually less influence, but may have a large influence when the speed is very high and dip lubrication is used.

This chapter is dedicated to a literature review of the different power loss mechanisms and models present in a gearbox. Afterwards, a basic structure of the gearbox power loss model will be suggested, to be calibrated and validated experimentally.

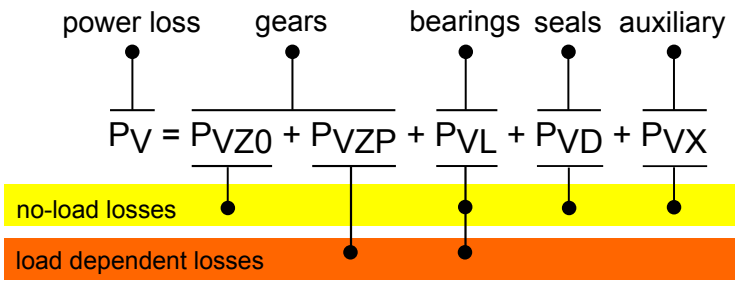

Figure 4.1.: Power loss contributions [65].

4.2. Gear losses

4.2.1. Load independent gear losses or spin power losses

Depending on input power and speed, lubricant characteristics, and gearbox design, the no-load gear power losses (or spin power losses) usually are a very important source of energy dissipation.

Spin power losses are directly related to the type of lubrication method used. Dip lubrication is often used in low to medium speed automotive gearbox or industrial transmission. When the operating gear speeds are relatively high, jet lubrication is preferred.

Under dip lubrication the total spin power losses are divided in two categories: losses due to the interaction between the rotating gears with the fluid and losses due to interaction of the gear at the gear mesh interface. The interaction of the rotating gears can be both with air (windage) or oil (churning). The most relevant losses in the gear mesh interface are the squeezing and pocketing [68].

When jet-oil lubrication is used, the power loss is attributed to windage caused by the rotation of the gears in air/oil-air mixture environments. The losses due to squeezing of compressible air/oil-air mixture on the meshing gears and the drag power losses due to air drag along the teeth and sides of rotating gears are the usual focus on the literature [69].

In both types of lubrication methods (dip or oil jet), the spin losses involve complex hydrodynamic phenomena which are very difficult to describe in analytical formulations. When the majority of the factors involved are taken into account (gearbox and gears design, rotational speed, oil properties, oil level, etc), the nature of the environment surrounding the gears results in a hard task to formulate a fluid-mechanics based model. As result, the works published are based on dimensional analysis or experimental data. This means that such models will only be valid within very limited boundary conditions [70].

The number of published works about no-load power losses under oil jet lubrication is much lower than those published about dip lubrication.

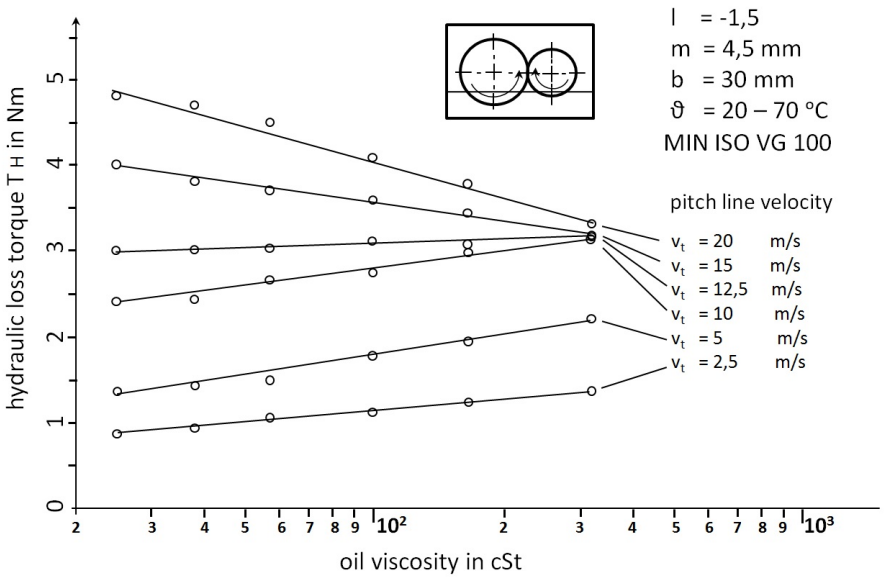

Figure 4.2.: Influence of oil viscosity on gear churning losses [75].

This work is only concerned with lubrication under atmospheric pressure conditions and the pressurized lubrication [71] will not be focused.

Dip lubrication

Many studies have been published to solve the problem of the power loss due to the churning of the gears in an oil bath. Several empiric formulations have been validated with experimental results, the works of Terekhov (1975) [72], Walter (1982) [73], Lauster (1983) [74], Mauz (1987) [75] and Boness (1989) [76] are the most representative of the scientific contribution in this field. All these works are subsequent studies of the formulations proposed by Daily *et al.* (1960) [77] and Mann *et al.* (1961) [78] for the drag torque associated with the circulation and secondary flows induced by rotation of a disk submerged in fluid.

The investigations of Mauz allow to draw some conclusions about the influence of the viscosity on the no-load losses. Mauz showed that increasing viscosity increases churning losses for low speeds and decreases churning losses for high speeds as presented in Figure 4.2 [75]. This behaviour is explained by the fact that less oil volume is in motion at higher viscosities and thus less losses are generated.

Luke and Olver *et al.* (1999) [79] performed many experiments with single and meshed gear pairs under dip lubrication and compared their experimental results with the empirical formulas of Terekhov [72] and Bones [76]. The trends they found are different form those suggested by Boness, and in particular the influence of oil viscosity was significantly lower. Luke and Olver found that, with the accuracy of

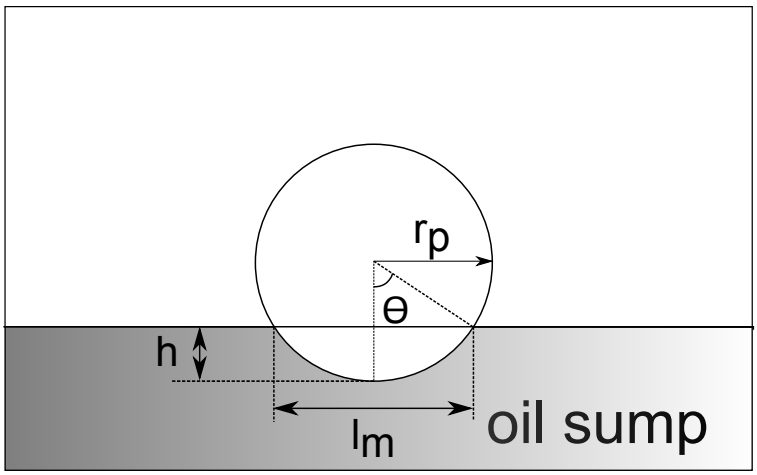

Figure 4.3.: Geometrical data of the gear immersed surface.

these models, and for the same operating conditions, the power loss predicted by Boness' model is more than ten times higher the prediction of the Terekhov's model.

Höhn *et al.* (1996) [66] and Martins *et al.* (2005) [80–82] applied a no-load power loss model that correlated very well with measurements of oil operating temperature under dip lubrication. The model is based on the Walter and Mauz models for churning losses. However, this empiric model is not able to predict the churning losses for gearbox geometries different of that used for those studies (FZG gearboxes).

Later on, Changenet (2007) [83] developed a gear churning loss model based on a dimensional analysis and validated with experimental results. Changenet's model correlates very well with the experimental results within the range of conditions tested. This model was validated for different gearbox geometries with variable distance of the gears to the wall and also includes the aeration effect, which can be a major cause of power loss mainly at very high speed.

Changenet's [83–87] gear churning loss model is given by equation (4.1).

$$C_{ch} = \frac{1}{2} \cdot \rho \cdot \omega^2 \cdot r_1^3 \cdot S_m \cdot C_m \tag{4.1}$$

In equation (4.1), C_m is the drag dimensionless group, S_m the immersed surface of the pinion/wheel (flank and teeth), r_1 the pinion reference radius, ω the angular frequency and ρ the bulk density of the lubricant at the working temperature, considering the general geometry shown in Figure 4.3 [88].

The dimensionless drag group (C_m) was derived from dimensional analysis using the Vashy-Buckingham theorem [88] and is expressed in equation (4.2).

$$C_m = \psi_1 \cdot \left(\frac{h_s}{d_1}\right)^{\psi_2} \cdot \left(\frac{V_0}{d_1^3}\right)^{\psi_3} Fr^{\psi_4} \cdot Re_c^{\psi_5} \cdot \left(\frac{b}{r_1}\right)^{\psi_6} \tag{4.2}$$

The ψ_i coefficients are derived from experimental results. The ψ_i numerical values depend on the working conditions, and four sets of coefficients (depending on the nature of the flow regimes) are used depending on the value of the parameter γ given by equation (4.3) that resembles to a centrifugal acceleration.

$$\gamma = \omega^2 \cdot (r_1 \cdot b \cdot m)^{\frac{1}{3}} \tag{4.3}$$

The Froude (Fr) and the critical Reynolds (Re_c) numbers are defined by equations (4.4) and (4.5).

$$Fr = \frac{r_1 \cdot \omega^2}{g} \tag{4.4}$$

$$Re_c = \frac{r_1 \cdot b \cdot \omega}{\nu} \tag{4.5}$$

The C_m parameter to be used for each one of the flow conditions depends not only on the parameter defined by equation (4.3) but also on the critical Reynolds number defined on equation (4.5), as stated in the following expressions:

- if $\gamma < 750\ m/s^2$ and $Re_c < 4000$

$$C_m = 1.366 \cdot \left(\frac{h}{d_1}\right)^{0.45} \cdot \left(\frac{V_0}{{d_1}^3}\right)^{0.1} \cdot Fr^{-0.6} \cdot Re_c^{-0.21} \cdot \left(\frac{b}{r_1}\right)^{0.21} \tag{4.6}$$

- if $\gamma < 750\ m/s^2$ and $Re_c > 4000$

$$C_m = 0.239 \cdot \left(\frac{h}{d_1}\right)^{0.45} \cdot \left(\frac{V_0}{{d_1}^3}\right)^{0.1} \cdot Fr^{-0.6} \cdot \left(\frac{b}{d_1}\right)^{0.21} \tag{4.7}$$

- if $\gamma > 1250\ m/s^2$ and $Re_c < 4000$

$$C_m = 20.797 \cdot \left(\frac{h}{d_1}\right)^{0.1} \cdot \left(\frac{V_0}{{d_1}^3}\right)^{-0.35} \cdot Fr^{-0.88} \cdot Re_c^{-0.21} \cdot \left(\frac{b}{d_1}\right)^{0.85} \tag{4.8}$$

- if $\gamma > 1250\ m/s^2$ and $Re_c > 4000$

$$C_m = 3.644 \cdot \left(\frac{h}{d_1}\right)^{0.1} \cdot \left(\frac{V_0}{{d_1}^3}\right)^{-0.35} \cdot Fr^{-0.88} \cdot \left(\frac{b}{d_1}\right)^{0.85} \tag{4.9}$$

The model proposed by Changenet [83] was recently used by Marques *et al.* [89] to predict the no-load losses on a multiplier gearbox. The model in the original format was not effective to predict the gear no-load losses of a gearbox with 3 gear pairs. Marques inferred that the model was not able to predict the actual Reynolds number for more complex gearboxes, adjusting the transition between laminar and turbulent flow for the gearbox that was studied.

A physics-based fluid mechanics model to predict the no-load losses of gear pairs due to oil churning and windage was developed by Seetharaman in 2009 and presented very promising results [68].

In recent years, with the increasing computational power of desktop computers, CFD (Computational Fluid Dynamics) is becoming more and more attractive approach to solve this kind of problems. Recently Concli *et al.* [90] proposed a solution for the problem of the churning power loss in a planetary speed reducer which was based in a CFD approach, with promising results.

Oil jet lubrication

Ariura [91] was the first one to investigate the power loss of gears under oil-jet lubrication. The mechanisms that contribute to this energy loss were identified: the acceleration of the injected oil and the oil squeeze by the displacement of the oil in the contact area between the teeth. Ventilation was also identified as a possible source of power loss but with small importance for low speeds.

The contributions to the no-load power loss of gears under oil-jet lubrication, are resumed in equation (4.10).

$$P_{VZ0} = P_{VZ0,acceleration} + P_{VZ0,ventilation} + P_{VZ0,squeeze} \tag{4.10}$$

In his work, Arirura suggested equation (4.11) for the contribution of oil acceleration, which is based on the Euler theorem.

$$P_{VZ0,acceleration} = \begin{cases} \omega \cdot C_x \cdot \rho \cdot \dot{Q}_e \cdot r \cdot (|v_t| - v_o)\,, & for \text{ BO and BU} \\ \\ \omega \cdot C_x \cdot \rho \cdot \dot{Q}_e \cdot r \cdot (|v_t| + v_o)\,, & for \text{ AO and AU} \end{cases} \tag{4.11}$$

Figure 4.4 shows the common oil jet lubrication configurations: constant C_x is 1 for BO and AO cases and 0.9 for BU and AU configurations. The work of Ariura was accepted and confirmed by the subsequent works of Mizutani *et al.* [71] and Akin *et al.* [92].

Mauz proposed equation (4.12) to evaluate the power loss due to squeezing.

$$P_{VZ0,squeeze} = \omega \cdot 4.12 \cdot C_1 \cdot \rho \cdot \dot{Q}_e^{0.75} \cdot r \cdot \left(v_t \cdot b \cdot m \cdot \frac{\nu}{\nu_0} \right)^{0.25} \cdot \left(\frac{h_t}{h_{t0}} \right)^{0.5} \tag{4.12}$$

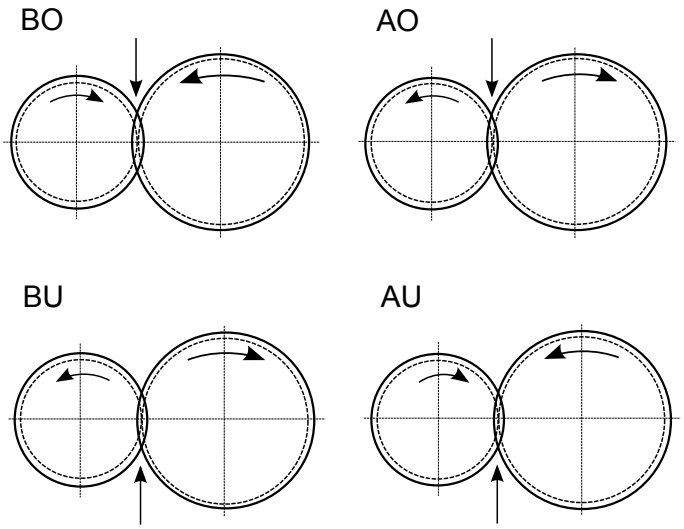

Figure 4.4.: Different configurations of oil jet lubrication [91].

Maurer studied the ventilation problem and defined two sources, the individual gear (ID) and the mating contact area (CA), and resumed the ventilation losses in equation (4.13).

$$P_{VZ0,ventilation} = P_{VZ0,ventilation,ID} + P_{VZ0,ventilation,CA} \tag{4.13}$$

The ventilation losses are then calculated with equations (4.14) and (4.15).

$$P_{VZ0,ventilation,ID} = 1.37 \times 10^{-9} \cdot {v_t}^{1.9} \cdot d^{1.5} \cdot b^{0.52} \cdot m^{0.69} \cdot \lambda_{wand} \cdot \lambda_{oil} \tag{4.14}$$

$$P_{VZ0,ventilation,CA} = 1.17 \times 10^{-6} \cdot {v_t}^{1.95} \cdot d^{1.5} \cdot u^{0.73} \cdot b^{1.37} \cdot \lambda_{wand} \cdot \lambda_{oil} \tag{4.15}$$

The λ_{wand} and λ_{oil} factors account for the influence of the gearbox geometry and are given by equations (4.16) and (4.17), respectively.

$$\lambda_{wand} = 0.763 \cdot s_r^{0.26} \cdot s_a^{-0.0043 \cdot (2 \cdot s_z - 9.53)} \tag{4.16}$$

$$\lambda_{oil} = 0.763 \cdot \dot{Q}_e^{0.163} \tag{4.17}$$

The s_a, s_r and s_z parameters in equation (4.16) are the distance between the gear and wall of the gearbox, in axial, radial and z directions.

While the previous equations were summed by Clemens to calculate the no-load losses under oil jet lubrication, other authors proposed unique equations to calculate the windage losses. The models of Anderson *et al.* [93], Dawson [94], Lord [95], Handschuch [96], Diab [69] and Petry-Jonhson [97] can be found in literature.

4.2.2. Load dependent gear losses

Sliding losses

The contact between meshing teeth is the most important source of power loss in a gear transmission system, mainly in the cases when the velocity is not very high. This is the case in many current applications, such as vehicle gearboxes and industrial transmissions, as in the case of wind turbine gearboxes.

In 1949, the work of Buckingham [98] introduced the first theoretical approach to calculate the efficiency of the meshing gears, which was based on the assumption of constant coefficient of friction (μ_{mZ}) along the path of the contact.

Later on, Ohlendorf (1958) [99] developed the basic formula for the meshing gears power loss presented in equation (4.18).

$$P_{VZP} = P_{IN} \cdot H_V \cdot \mu_{mZ} \tag{4.18}$$

Ohlendorf's equation may be used to deduce a gear loss factor from the efficiency formula of Buckingham, presented in equations (4.19) and (4.20).

$$H_V^{Buckingham} = (1+i)\frac{\pi}{z_1}\epsilon_\alpha(2{k_0}^2 - 2k_0 + 1) \tag{4.19}$$

$$k_0 = \frac{z_1}{2\pi\epsilon_\alpha}\left(\left(\left(\frac{r_{a2}}{r_2}\right)^2 \frac{1}{cos\ {\alpha_{zt}}^2}\right)^{\frac{1}{2}} - tan\ \alpha_{zt}\right) \tag{4.20}$$

Buckingham's and Ohlendorf's loss factors are different, as can be observed comparing equations (4.19) and (4.21).

$$H_V^{Ohlendorf} = (1+i)\frac{\pi}{z_1}\left(1 - \epsilon_\alpha + {\epsilon_1}^2 + {\epsilon_2}^2\right) \tag{4.21}$$

In fact, the tooth geometry implies a variation of the relative velocity of the surfaces along path of contact, as presented in Figure 4.5 [100] and the sliding speed influences the coefficient of friction (see Chapter 3), i.e. the coefficient of friction increases with increasing SRR.

Considering the coefficient of friction constant along the path of contact is a good approximation of the problem, as presented in Figure 4.6 [65]. The coefficient of friction becomes close to zero at the pitch point, but the variation of the coefficient of friction away from the pitch point is very small.

Based on the principle of constant coefficient of friction along the path of contact, Merritt (1971) [101], Henriot (1978) [102], Niemann and Winter (1989) [103] and ISO (2001) [104] introduced alternative approaches for the prediction of load dependent power loss in meshing gears and the corresponding gear loss factors are given by equations (4.21), (4.23), (4.22), with k_0 calculated with equation (4.20).

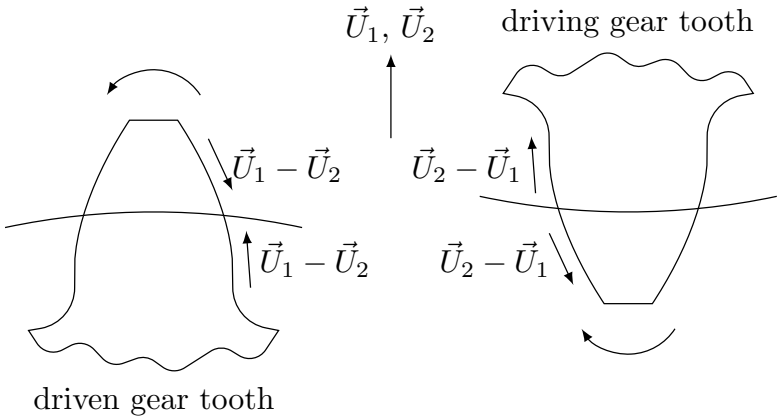

Figure 4.5.: Direction of sliding on a tooth surface [100].

$$H_V^{Henriot} = \left(\frac{1}{r_1} + \frac{1}{r_2}\right) \frac{{g_{a1}}^2 + {g_{a2}}^2}{2\left(g_{a1} + g_{a2}\right) cos\ \alpha_z} \tag{4.22}$$

$$H_V^{Niemann} = (1+i)\frac{\pi}{z_1}\epsilon_\alpha \left(\frac{1}{\epsilon_\alpha} - 1 + \left(2{k_0}^2 - 2k_0 + 1\right)\epsilon_\alpha\right) \tag{4.23}$$

Velex et al. which did no *a priori* assumption on tooth load distribution by using generalized displacements, in order to calculate the efficiency of a meshing gear pair, obtained a closed form solution for the efficiency of a meshing gear pair (constant coefficient of friction was assumed), as presented in equations (4.24), (4.25) and (4.20).

$$\rho = 1 - \mu \cdot (1+i) \cdot \frac{\pi}{z_1} \cdot \frac{1}{\cos\beta_{zb}} \cdot \epsilon_\alpha \cdot \lambda(\mu) \tag{4.24}$$

with

$$\lambda(\mu) = \frac{2k_0^2 - 2k_0 + 1}{1 - \mu \cdot \left(\frac{\tan\alpha_{zt}\cdot(2k_0-1) - \frac{\pi}{z_1}\epsilon_\alpha\cdot(2k_0^2-2k_0+1)}{\cos\beta_{zb}}\right)} \tag{4.25}$$

Ohlendorf's gear loss factor [99] is the most used approach in works related with gear power loss. It was originally formulated based on the the distribution of load along the path of contact for spur gears, as presented in Figure 4.6 and described in equation (4.26). The power loss in each point of the path of contact is given by equation (4.27) which integrated along the path of contact gives the actual power loss as described in equation (4.28).

$$F_N(x,y) = F_{bn} \cdot \frac{1}{\sum_{i=1}^{n} l^i(x,y)} \tag{4.26}$$

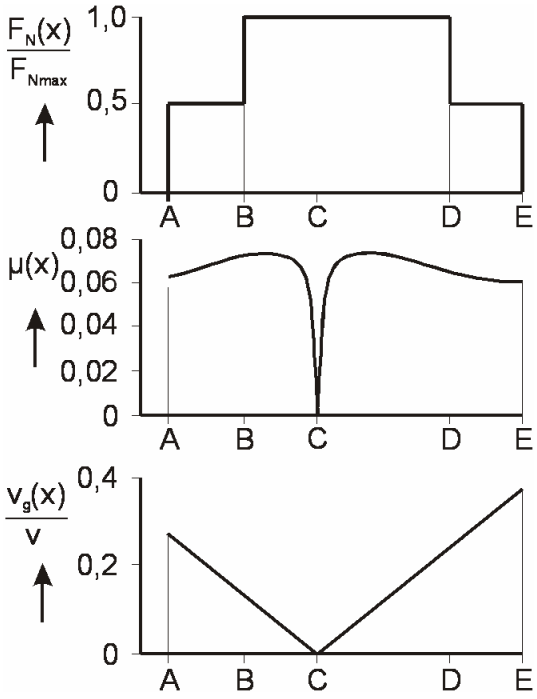

Figure 4.6.: Load, friction coefficient and sliding speed along path of contact [65].

$$P_{VZP}(x) = F_N(x) \cdot v_g(x) \cdot \mu(x) \tag{4.27}$$

$$P_{VZP} = \frac{1}{p_b} \int_A^E P_{VZP}(x) dx \tag{4.28}$$

$$H_V^{Ohlendorf} = \frac{1}{p_b} \int_A^E \frac{F_N(x)}{F_{bt}} \cdot \frac{v_g(x)}{v_{tb}} dx \tag{4.29}$$

Ohlendorf solved equation (4.29) and obtained the gear loss factor for spur gears, equation (4.30).

$$H_V^{Ohlendorf} = (1+i)\frac{\pi}{z_1} \frac{1}{\cos\beta_{zb}} (1 - \epsilon_\alpha + \epsilon_1^2 + \epsilon_2^2) \tag{4.30}$$

All the formulations presented are valid for spur gears without profile shift corrections. In the case of Ohlendorf's approach, equation (4.30) is considered valid for spur gears under the following conditions: $1 \leq \epsilon_\alpha \leq 2$ and $\epsilon_1 \leq 1$ and $\epsilon_2 \leq 1$.

For spur gears the load distribution along the path of contact is shown in Figure 4.7, which is slightly different from the distribution used by Ohlendorf (see Figure 4.6). Under such conditions Wimmer [105] solved the problem and suggested a

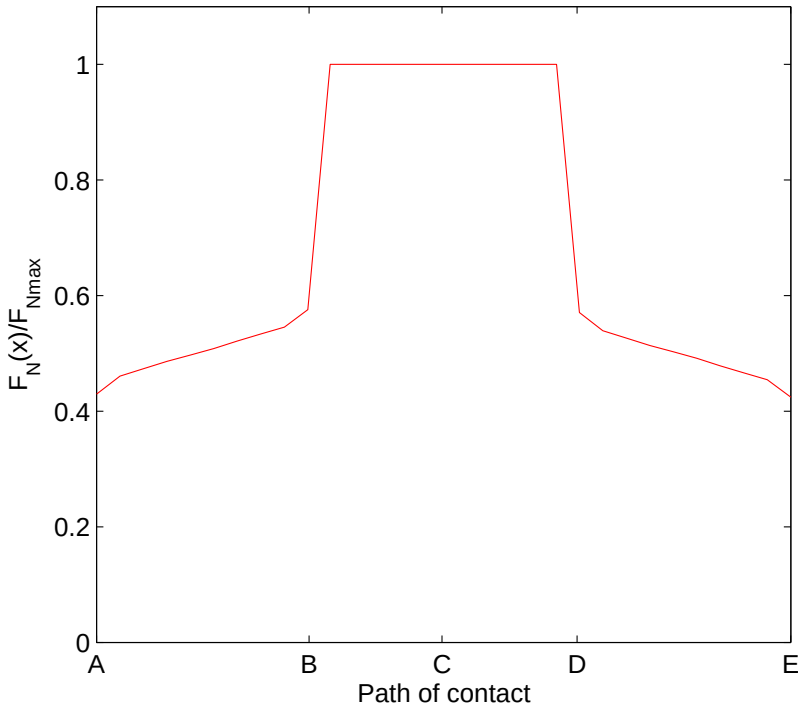

Figure 4.7.: Load distribution of a spur gear considering elastic effects.

solution for a wider range of spur gears, as presented in equation (4.31) and Table 4.1.

$$H_V^{Wimmer} = \frac{\pi(i+1)}{z_1 \cdot i \cdot \cos(\beta_{zb})} \left(a_0 + a_1|\epsilon_1| + a_2|\epsilon_2| + a_3|\epsilon_1|\epsilon_1 + a_4|\epsilon_2|\epsilon_2\right) \tag{4.31}$$

As will be shown later in this study, one of the ways to interfere in the performance of the gears and increase their efficiency is to modify the profile shift and modify the sliding speed behaviour of the gears, generating lower power losses [106]. For these cases of profile modification it is important to have reliable models to predict the power losses. Wimmer used FVA RIKOR to solve equation (4.32) and obtained a gear loss factor for almost every gear geometry, with or without profile shift correction, spur or helical gears. The software solved load distribution problem ($F_N(x,y)$) along the path of contact considering elastic effects. Then, he compared the results of RIKOR with Ohlendorf's approach and observed that, for a helical gear geometry with profile shift, the difference between gear loss factors can be up to 30 % [105].

$$H_{VL} = \frac{1}{p_b} \int_0^b \int_A^E \frac{F_N(x,y)}{F_{bt}} \cdot \frac{v_g(x,y)}{v_{tb}} dxdy \tag{4.32}$$

Profile modifications are desirable since they may reduce the power loss in the

Table 4.1.: Values for the a_i, $(i = 0 : 4)$, coefficients of equation (4.31).

	$\epsilon_\alpha < 1$	$\epsilon_\alpha > 1$ $\epsilon_1 < 1 \vee \epsilon_2 < 1$	$\epsilon_\alpha > 1$ $\epsilon_1, \epsilon_2 > 1$ $l + m = n$	$\epsilon_\alpha > 1$ $\epsilon_1, \epsilon_2 > 1$ $l + m = n + 1$
a_0	0	0	$\frac{2lm}{n}$	$\frac{2(lm-n)}{n-1}$
a_1	0	1	$\frac{l(l-1)-m(m-1)-2lm}{n(n-1)}$	$\frac{l(l-1)+m(m-1)-2(m-1)n}{n(n-1)}$
a_2	0	1	$\frac{-l(l-1)+m(m-1)-2lm}{n(n-1)}$	$\frac{l(l-1)+m(m-1)-2(m-1)n}{n(n-1)}$
a_3	$\frac{1}{\epsilon_\alpha}$	0	$\frac{2m}{n(n-1)}$	$\frac{2(m-1)}{n(n-1)}$
a_4	$\frac{1}{\epsilon_\alpha}$	0	$\frac{2l}{n(n-1)}$	$\frac{2(l-1)}{n(n-1)}$

meshing gears.

In this work a load distribution formulation based only in the geometrical properties of the gears was implemented. The length of contacting lines (l^i) along the plane of action is the final objective in the case of the approach proposed in this work. After determining the length of each contacting line, it is possible to know the sum of all lines, allowing to calculate the load distribution along the plane of action, as presented in equation (4.33).

$$F_N(x, y) = F_{bt} \cdot \frac{1}{\sum_{i=1}^{n} l^i(x, y)} \tag{4.33}$$

The calculation of the length of contacting lines is detailed in Appendix D and an example of the load distribution calculated for an helical gear with profile shift is presented in Figure 4.8.

Rolling losses

The sliding losses are the most important source of load dependent gear losses. However, it should be remarked that gears can produce rolling losses, that are also dependent on the load applied. In almost every case the rolling losses are neglected [70], since an involute gear which is perfectly shaped and has low tooth flexibility has no rolling losses. Anderson and Loewenthal [93,107] proposed equations (4.34) and (4.35), which produce negligible values for current gears.

$$P_{VZP,rolling} = F_R \cdot v_r \tag{4.34}$$

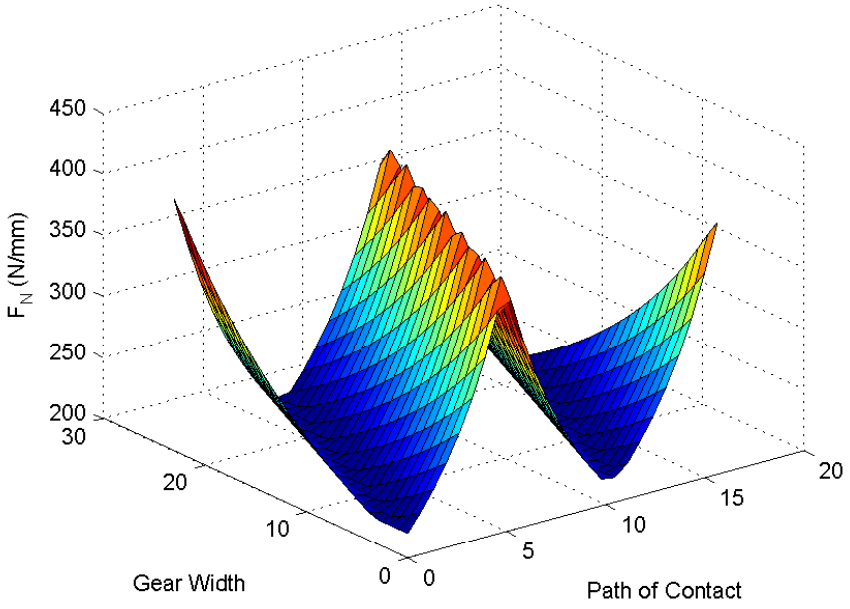

Figure 4.8.: Load distribution under 323 Nm for an helical gear with profile shift (H501).

$$F_R = C_R \cdot h_0 \cdot \phi_T \cdot b \tag{4.35}$$

Anderson *et al.* suggests that C_R=9×10^7 and the film thickness is calculated with Hamrock and Dowson [24] equation.

Comparing gear loss factors

In order to decide which gear loss factor equation is better suited to predict the power loss for different gear geometries, H_V was calculated for eight different gear geometries, in which, both spur and helical gears with profile shift are included (see Table 4.2).

The gear loss factor was also calculated based on the results obtained with the commercial software *"KissSoft"* which accounts for elastic effects.

It is interesting to note that for spur gears the Ohlendorf equation was validated by several authors [66, 80, 105, 108]. In the particular case of C40 gear, Ohlendorf's formula gives the same result of the author's approach. The comparison for a wide range of gears showed that Buckingham, Winter and Velex equations don't follow the expected behaviour of the gears, i.e. increasing the k_0 factor (see Figure 4.9) reduces on the gear loss factor.

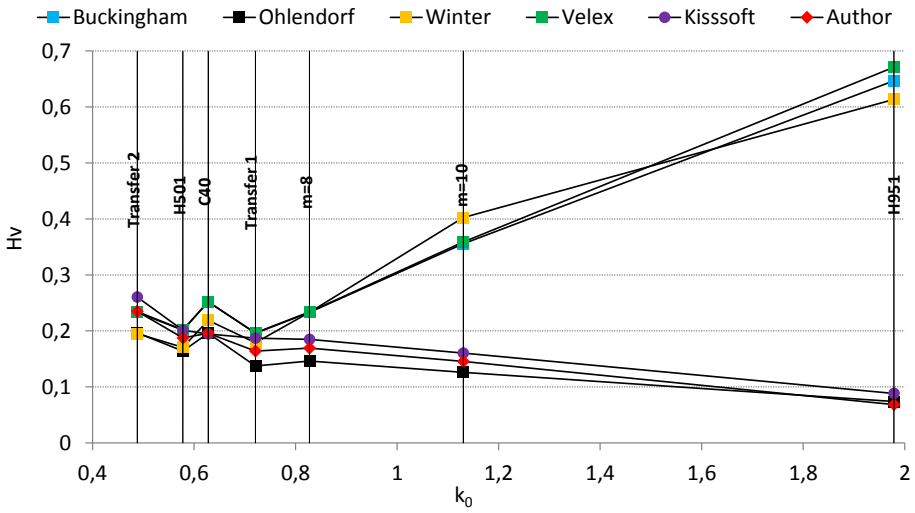

Figure 4.9.: Gear loss factor calculated with different formulas for different gear geometries presented in Table 4.2.

The formulas of Buckingham, Winter and Velex should not be used for helical gears, mainly with profile shift. The other three approaches showed small differences and the author's algorithm generates loss factors higher than Ohlendorf but lower than KissSoft, for helical gears. For spur gears the author's approach gives loss factors lower than KissSoft and equal to Ohlendorf.

In Chapter 7 experimental results with helical gears will be presented and this topic will be discussed again.

Coefficient of friction in meshing gears

The Stribeck work [109–111], published in 1902, showed the influence of the lubrication regime on the coefficient of friction of contacting bodies, as documented in Figure 4.10. The Stribeck curve is still valid today and shows how the coefficient of friction depends on the lubrication regime. Such behaviour is analysed in detail in Appendix C.

Gears very often operated under mixed film lubrication and a large number of empirical formulas for coefficient of friction (in mixed regime mainly) has been published in the literature [70]. Most of the formulas were obtained by curve fitting of measured data collected in twin-disk tests. The equations that have been proposed are based on the following general form [112]:

$$\mu = f(\nu, \eta, v_g, v_r, \rho_{redC}, F_{bt}/b, p_0, Ra, ...) \tag{4.36}$$

Buckingham [98] was the first to introduce a coefficient of friction formula based on experimental results, proposing a coefficient of friction dependent on the oil,

Table 4.2.: Geometrical parameters of the gears.

Gears		Parameters									
		z [/]	m [mm]	a [mm]	α_z [°]	β_z [°]	b [mm]	x [/]	d_a [mm]	ϵ_α [/]	ϵ_β [/]
C40	Pinion	16	4.5	91.5	20	0	40	+0.1817	82.64	1.44	0
	Gear	24						+0.1715	115.54		
H501	Pinion	20	3.5	91.5	20	15	23	+0.1381	80.37	1.45	0.54
	Gear	30						+0.1319	116.57		
H951	Pinion	38	1.75	91.5	20	15	23	+1.6915	76.23	0.93	1.08
	Gear	57						+2.0003	111.73		
Transfer 1	Pinion	32	3.5	105.0	20	20	35	+0.3810	128.45	1.32	1.09
	Gear	23						+0.4150	95.17		
Transfer 2	Pinion	28	4	95.0	20	20	33.5	-0.2400	125.22	1.49	0.91
	Gear	17						+0.0510	80.73		
m=8	Pinion	17	8	355	20	9	124	+0.4965	160.74	1.40	0.77
	Gear	69						+0.3985	580.36		
m=10	Pinion	19	10	500	20	9	175	+0.6500	222.65	1.32	0.87
	Gear	77						+0.8877	814.63		

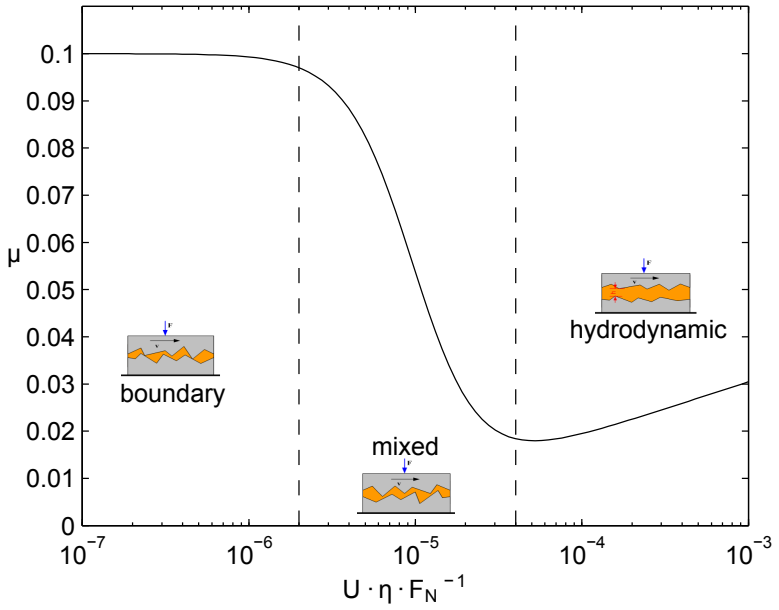

Figure 4.10.: Typical Stribeck curve: influence of the lubrication regime in the coefficient of friction.

speed, load, material and surface finishing, but the formula only considered the sliding speed v_g.

Misharin [113] developed an equation considering the influence of oil viscosity (ν) and surface velocities (v_g, v_r), but disregarded the dependence on the load.

In the same year, Ohlendorf [99] presented an equation that considers the influence of the oil (η), of the applied load (F_{bt}/b) and speed.

Eiselt [114], Cameron [115], Drozdov [116] and Naruse [117] developed several different equations to predict the coefficient of friction, all of them disregarding at least one important parameter of the geometry or of the oil formulation.

DIN 3990 [118] and Michaelis [119] proposed very similar equations that account for the oil viscosity, the load applied, the gear geometry, the velocity and the surface finishing. Schlenk [120] went a little ahead and also included a parameter that takes into account the influence of oil formulation and not only the viscosity of the lubricant. The work of Schlenk was recently included in the ISO standard 14179-2 [104] and his formula for the coefficient of friction gear teeth is the most used one. Schlenck's approach is presented in equation (4.37).

$$\mu_{mZ} = 0.048 \cdot \left(\frac{F_{bt}/b}{\nu_{\Sigma C} \cdot \rho_{redC}} \right)^{0.2} \cdot \eta^{-0.05} \cdot R_a^{0.25} \cdot X_L \tag{4.37}$$

Doleschel (2002) [65] defined the coefficient of friction in a gear mesh as a combination of a boundary coefficient of friction, μ_{bl}, and of a full-film coefficient of friction,

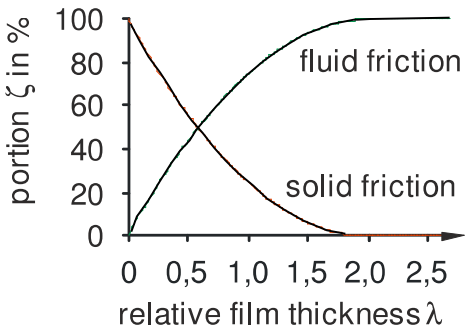

Figure 4.11.: Fluid and solid friction in an EHD contact.

μ_{EHD}. The coefficient of friction in a gear mesh μ_{mZ} is then defined according to equation (4.38). In this equation μ_{mZ} is the coefficient of friction in mixed film lubrication and ξ is the portion of boundary friction, i.e. if ξ=1, μ_{mZ} is equal to μ_{bl}.

$$\mu_{mZ} = \xi \cdot \mu_{bl} + (1 - \xi) \cdot \mu_{EHD} \tag{4.38}$$

In the original work, the boundary film coefficient of friction and the full film coefficient of friction were derived from experimental results in FZG tests [65].

The portion ξ of fluid and solid friction depends on the relative film thickness Λ in the contact, is given by equation 4.39 and is presented in Figure 4.11 [65].

$$\xi = \begin{cases} 0.25 \cdot \Lambda^2 - \Lambda + 1, \ for\ \Lambda < 2 \\ \\ 0, \ for\ \Lambda \geq 2 \end{cases} \tag{4.39}$$

The specific film thickness (or relative film thickness) is defined by equation (4.40) [121].

$$\Lambda = \frac{h_{0C}}{\sqrt{R_{a1}^2 + R_{a2}^2}} \tag{4.40}$$

Recent findings by Matsumoto [122] showed that the equation proposed by Doleschel can correlate very well with experimental results. However, he verified that the load sharing function should be calculated assuming R_z as the relevant surface parameter for the actual portion of solid/liquid coefficient of friction instead of the usual average roughness (R_a). The model of Matsumoto is presented in equations (4.41), (4.42) and (4.43).

$$\mu_{mZ} = \xi \cdot \mu_{bl} + (1 - \xi) \cdot \mu_{EHD} \tag{4.41}$$

$$\xi = 0.5 \cdot \log D \tag{4.42}$$

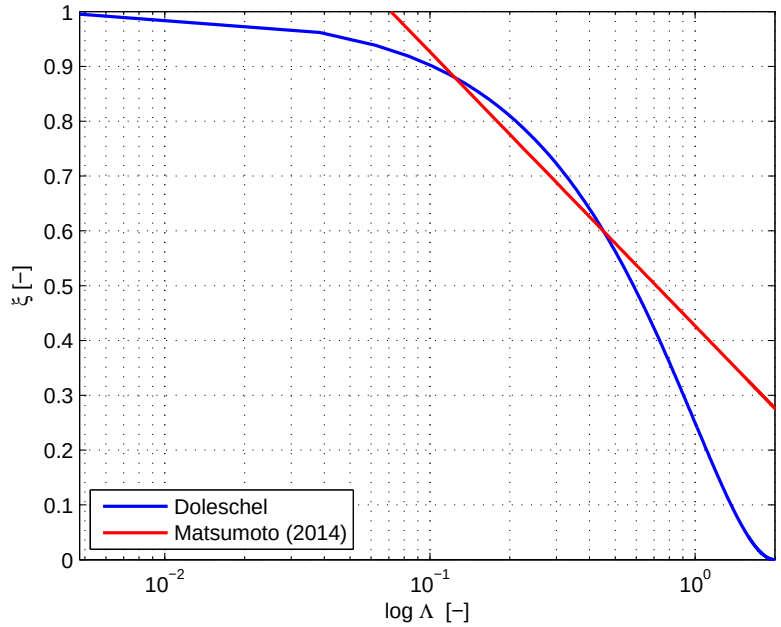

Figure 4.12.: Comparison of load sharing function of Doleschel and Matsumoto for an ISO VG 32 mineral oil without additives with a Type C gear.

$$D = \frac{(R_{z1} + R_{z2})}{h_0} \tag{4.43}$$

Figure 4.12 shows a comparison of the load sharing functions of Doleschel and Matsumoto. In general Matsumoto equation predicts higher coefficients of (μ_{mZ}) higher than Doleschel equation, for the same lubrication regime.

The equations discussed previously were determined assuming constant coefficient of friction along the path of contact. However, it is a simplification of the problem and Bennedict and Kelley [123] introduced an equation that considers the variation of the sliding speed along the path of contact. However, the equation showed a singularity at the pitch point. This equation accounted also for rolling speed, dynamic viscosity and load but disregarded the influence of the radius of curvature.

In 2005, Xu Hai [112] proposed a coefficient of friction based on results obtained with an EHL model (numerical results) that was validated with experimental traction curves. After validation, the model ran ≈ 10000 times varying different operating conditions. These results were then fitted using a custom function based on key parameters, as represented in equation (4.44).

$$\mu(x) = e^{f(SRR,p_0,\nu_0,Ra)} \cdot p_0^{b2} \cdot |SRR|^{b3}\, v_e^{b6} \cdot \eta_0^{b7} \cdot R_X^{b8} \tag{4.44}$$

Different simulations were carried out with a Type C spur gear and an ISO VG

32 mineral base oil without additives. All the formulas for the coefficient of friction between gear teeth are summarized in Appendix E.

This oil was used because the μ_{bl} and μ_{EHD} values were known in advance from the Matsumoto work [122]. On the other side the coefficient of friction of Schlenk, Michaelis and DIN 3990 were derived for a mineral without additives. All the equations except Xu [112] approach were implemented. Xu equation was validated for a PAO and because of that it is not suitable for this comparison. A particular note for Benedict and Kelley equation, where the coefficient of friction was calculated for an average sliding speed along the path of contact. The results are presented in Figure 4.13(a) for constant torque and temperature but with variable rotational speed. It is clear that all the equations are dependent on the rotational speed, but very significant differences are observed on the coefficient of friction predicted by different formulas.

Figure 4.13(b) shows the coefficient of friction for constant rotational speed and temperature and variable torque. Figure 4.13(c) shows the influence of temperature on the coefficient of friction for the different formulas.

In Chapter 6, some of these equations will be compared with experimental results and will allow to calibrate the power loss model.

4.3. Rolling bearing losses

The important role of rolling bearing power loss in machines have attracted many researchers to identify and model the friction mechanisms found in rolling bearings. Several models are currently used to predict the power loss of rolling bearings, as documented in literature [124–128]. Some models are validated by a large number of experimental results, as the ones presented by the major rolling bearing manufacturers in the world, such as SKF [129, 130], FAG [131], NTN [132], NSK [133] and Timken [134, 135].

4.3.1. Mechanisms of friction losses in rolling bearings

Rolling friction

The rolling friction losses in a rolling bearing are identified in literature by the following effects: deformation and elastic hysteresis [136, 137].

The solids in contact in a rolling bearing, usually balls or rollers, are under normal loads to the contact surface. These normal loads cause a deformation at each contact. Because of the deformation and due to the rolling motion of the elements over the raceway, which require a tangential load to overcome rolling resistance, the raceway material is squeezed up to form a bulge in the forward portion of the contact as shown

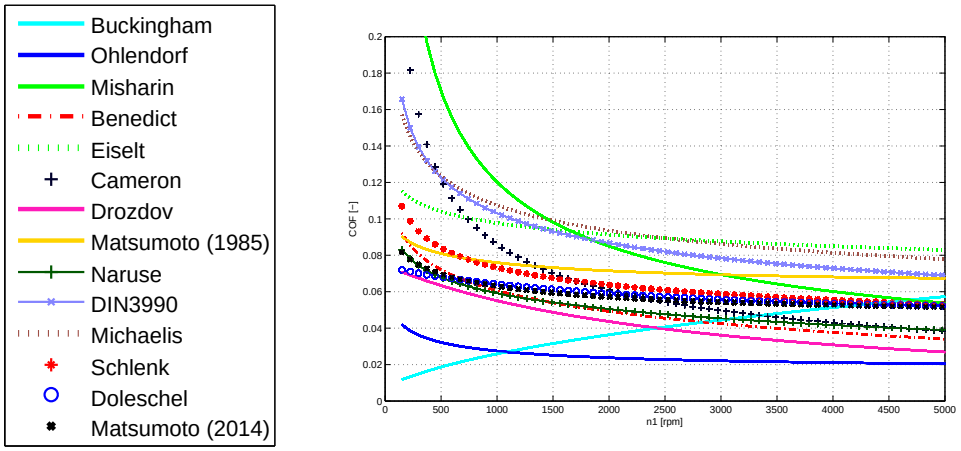

(a) Influence of rotational speed @ 250 Nm and 50 °C.

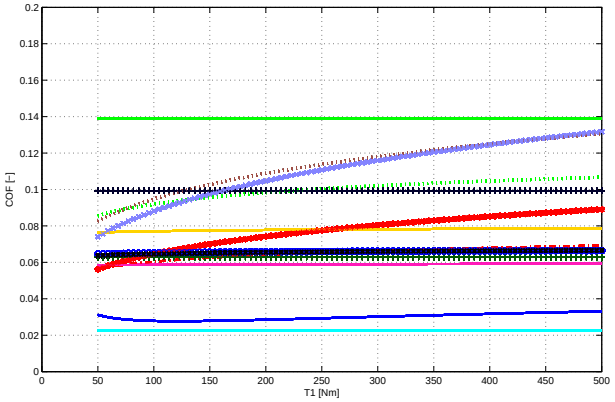

(b) Influence of Torque @ 500 rpm and 50 °C.

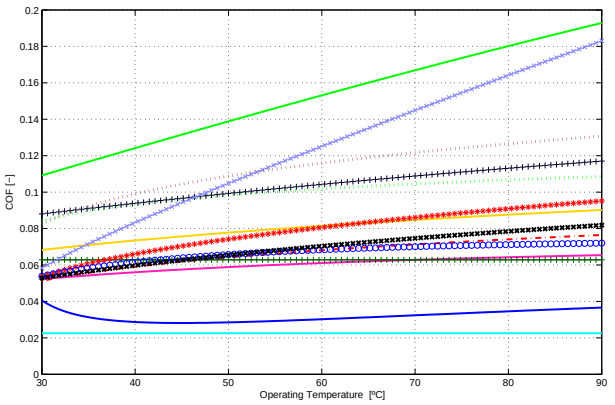

(c) Influence of Temperature @ 250 Nm and 500 rpm.

Figure 4.13.: Coefficient of friction calculated with different formulas for Type C gears lubricated with ISO VG 32 mineral oil witout additives.

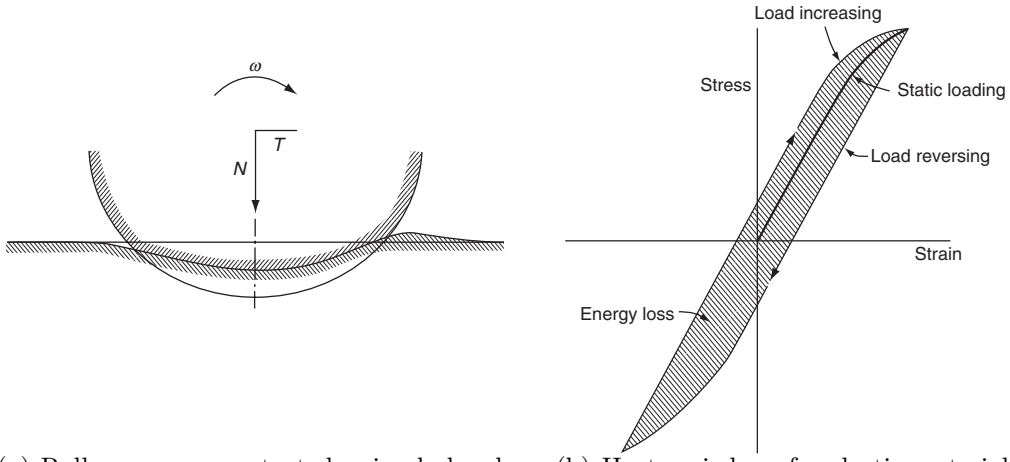

(a) Roller-raceway contact showing bulge due to rolling deformation.

(b) Hysteresis loop for elastic material subjected to reversing stresses.

Figure 4.14.: Rolling torque mechanisms [137].

in Figure 4.14(a). A depression is subsequently formed in the rear of the contact area. Thus, an additional tangential load is required to overcome the resisting force of the bulge.

A rolling element under compressive load travels over a raceway, the material in the forward portion of the contact in the direction of rolling undergoes compression while the material in the rear of the contact is relieved of stress. It is possible to recognize that as load increases, a given stress corresponds to a smaller deflection than when load is decreasing, as presented in Figure 4.14(b). The area between curves in the Figure 4.14(b) is called hysteresis loop, and it represents an energy loss [137].

Sliding friction

Sliding is the major source of friction in a rolling bearing, mainly at low speed. The sliding friction occurs due to microslip and sliding due to rolling motion [136].

If a rolling bearing operates without misalignment under moderate speed, then the total slip of one surface over another would not occur. However, depending on the elastic properties of the contacting bodies and the coefficient of friction between the contacting surfaces, microslip could occur and energy is lost.

A rolling bearing under simple radial load, pure rolling only can occur in points contained in two lines designated “A” as presented in Figure 4.15(a). At all other points along the contact, sliding must occur in a direction parallel to rolling motion. Outside the lines A, sliding occurs in one direction; between points A sliding occurs in the opposite direction. It assumes that the coefficient of friction is not sufficiently

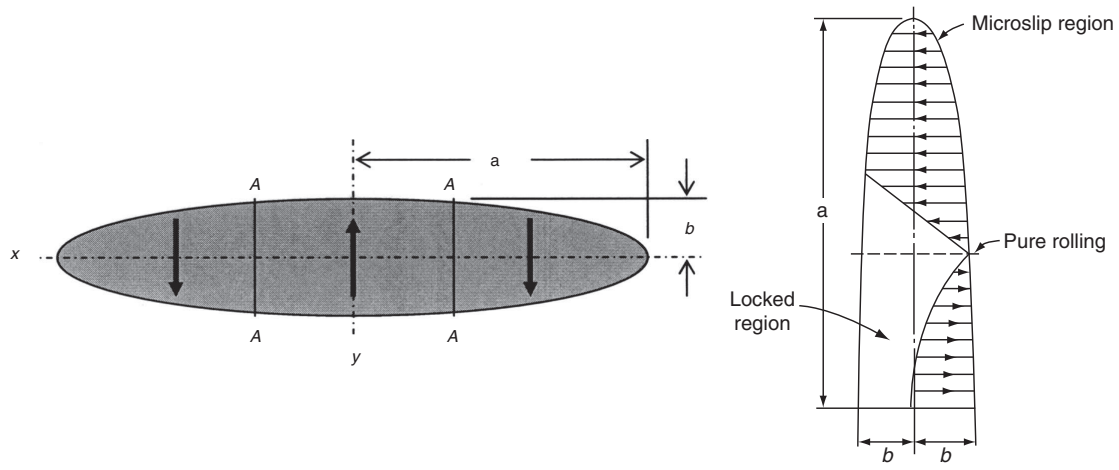

(a) Sliding speed direections. (b) Locked region.

Figure 4.15.: Ball-raceway contact area of a radial bearing with sliding directions presented [137].

great to cause the possibility of a locked region as presented in Figure 4.15(b). In the case of lubricated bearings this never happens because the coefficient of friction is not very high.

Drag friction

As stated by the Elasto-Hydrodynamic Lubrication (EHL) theory [138], the lubricant builds up a film between the raceway and the rolling elements. Usually, from the oil provided to cool and lubricate the contact, only a small portion is used to build up the fluid film. The excess of oil acts as a friction force contrary to the rotational speed of the rolling elements. The power loss due to drag friction is dependent on the viscosity of the lubricant and on the speed.

Rolling bearing seals friction

Seals are used to prevent the bearing to become contaminated with moisture, corrosive media or any other material. Additionally the seal retains the lubricant in the housing. The contact between the rubber of the seal and the shaft generates friction and must be considered as a source of power loss. The loss due to seals friction is mainly dependent on the rotational speed.

4.3.2. Rolling bearing friction torque models

In this section three different friction torque (or power loss) models will be described: Coulomb, Palmgren and New SKF. They are usually used in commercial software's like KissSoft, Powertrain Library and RIKOR to predict friction torque in rolling bearings. RIKOR uses Palmgren model. Powertrain Library uses a modified Coulomb model which includes a viscous term or no-load losses of rolling bearings. KissSoft uses both the Palmgren model and new SKF model as possibilities to estimate the friction torque, so the method chosen for prediction is up to the user.

Some scientific works like the ones of Höhn [66], presented gearbox power loss models whose rolling bearing friction predictions are done with Palmgren model. The Palmgren model is currently known as 'old' SKF model.

Models like the one developed by Biboulet and Houpert [135] or Zhou and Hoeprich [139] showed good agreement with experimental data. However, these models are only valid for unique bearing geometries like ball bearings in the case of Biboulet and Houpert; and tapered roller bearings in Zhou and Hoeprich. These models will be disregarded, because all types of rolling bearings can be found in real gearboxes.

Coulomb model

The friction torque function of Coulomb model [124] is independent of the rotational speed and only depends on the force (F, see equation 4.46), bearing diameter (d_m) and the coefficient of friction (μ), as presented in equation 4.45.

$$M_t = \mu \cdot F \cdot \frac{d_m}{2} \tag{4.45}$$

$$F = \sqrt{{F_r}^2 + {F_a}^2} \tag{4.46}$$

Eschmann performed a large number of rolling bearing tests and determined a reference coefficient of friction for the Coulomb model [124]. Manufacturers like NTN [132] and NSK [133] present in their catalogues a suggestion for the coefficient of friction (μ) for this model, depending on the bearing geometry.

Arvrid Palmgren model (1959)

The Palmgren model, also known as 'old' SKF friction torque model [125], divides the total friction torque in load dependent (M_1) and load independent (M_0) losses, as presented in equation (4.47).

$$M_t = M_0 + M_1 \tag{4.47}$$

The load independent part depends on the kinematic viscosity of the lubricant (ν), on the rotational speed (n) and on the geometry of the rolling bearing (f_0), as shown in equation (4.48).

$$M_0 = f_0 \cdot 10^{-7} \cdot (\nu \cdot n)^{2/3} \cdot d_m^3 \tag{4.48}$$

The load dependent friction torque is given by equation (4.49) and depends on the applied load (F), on the rolling bearing geometry (f_1) and on the coefficient of friction (μ_1).

$$M_1 = \mu_1 \cdot f_1 \cdot F \cdot \frac{d_m}{2} \tag{4.49}$$

Palmgren evaluated the rolling bearing friction torque through experimental tests of different bearing types and sizes. The results allow to determine the f_0, f_1 and μ_1 values [124]. Different values are also suggested by Eschman [124] and FAG [131] and some other rolling bearing manufacturers.

New SKF friction torque model (2004)

The new SKF model [129] considers that the total friction torque is the sum of four different physical sources of torque loss, represented by equation (4.50).

$$M_t = M_{rr}^{'} + M_{sl} + M_{drag} + M_{seal} \tag{4.50}$$

Equations (4.51) and (4.52) define the rolling and sliding torques, respectively.

$$M_{sl} = G_{sl} \cdot \mu_{sl} \tag{4.51}$$

$$M_{rr'} = \phi_{ish} \cdot \phi_{rs} \cdot [G_{rr}(n \cdot \upsilon)^{0,6}] \tag{4.52}$$

The equation (4.53) defines the inlet shear heating and equation (4.54) shows the replenishment/starvation reduction factor.

$$\phi_{ish} = \frac{1}{1 + 1.84 \times 10^{-9} \cdot (n \cdot d_m)^{1.28} \cdot \nu^{0.64}} \tag{4.53}$$

$$\phi_{rs} = \frac{1}{e^{K_{rs} \cdot \nu \cdot n \cdot (d+D) \cdot \sqrt{\frac{K_z}{2 \cdot (D-d)}}}} \tag{4.54}$$

The rolling bearing drag losses are given by equation (4.55) for ball bearings or by equation (4.56) for roller bearings.

$$M_{drag} = 0.4 \cdot V_M \cdot K_{ball} \cdot {d_m}^5 \cdot n^2 + 1.093 \times 10^{-7} \cdot n^2 \cdot {d_m}^3 \cdot \left(\frac{n \cdot {d_m}^2 \cdot f_t}{\nu} \right)^{-1.379} \cdot R_s \tag{4.55}$$

$$M_{drag} = 4 \cdot V_M \cdot K_{roll} \cdot C_w \cdot B \cdot {d_m}^4 \cdot n^2 + 1.093 \times 10^{-7} \cdot n^2 \cdot {d_m}^3 \cdot \left(\frac{n \cdot {d_m}^2 \cdot f_t}{\nu} \right)^{-1.379} \cdot R_s \tag{4.56}$$

The seal losses are defined by equation (4.57).

$$M_{seal} = K_{S1} \cdot {d_s}^{\beta_R} + K_{S2} \tag{4.57}$$

The constants G_{sl}, G_{rr}, K_L, K_Z K_{S1}, K_{S2} and β_R are dependent on the geometry of the rolling bearing.

The sliding friction torque (equation 4.58) is dependent on the weighting factor (equation 4.59) and on the reference values of the coefficient of friction (boundary film coefficient of friction – μ_{bl} and full-film coefficient of friction – μ_{EHD}) of each oil.

$$\mu_{sl} = \phi_{bl} \cdot \mu_{bl} + (1 - \phi_{bl}) \cdot \mu_{EHD} \tag{4.58}$$

$$\phi_{bl} = \frac{1}{e^{2{,}6 \times 10^{-8} (n \cdot \upsilon)^{1{,}4} \cdot d_m}} \tag{4.59}$$

The rolling bearing friction torque model, or torque loss model, only can predict accurate values if the boundary film coefficient of friction μ_{bl} and the full film coefficient of friction μ_{EHD} are representative of the lubricant used and of the operating temperature of the rolling bearing. For mineral oils, whatever the rolling bearing element type, ball or roller, a value of $\mu_{bl} = 0.15$ is suggested. Also for mineral oils a value of $\mu_{EHD} = 0.05$ is proposed for ball element bearings, and a value of $\mu_{EHD} = 0.02$ is proposed for roller element bearings [129].

There are no values of μ_{bl} and μ_{EHD} available for different gear oil formulations, neither for different operating temperatures. These values must be determined experimentally through rolling bearing tests.

A detailed presentation of the new SKF rolling bearing friction torque model is given in Appendix F.

4.3.3. Discussion on friction torque models presented

A simulation was performed using Coulomb, Palmgren and New SKF model for a Thrust Ball Bearing 51107 under different rotational speeds and two types of lubrication conditions: self-induced temperature and a constant temperature of 80 °C. The parameters of interest used for the simulation for each friction torque model are presented in Table 4.3.

The results of the simulation are presented in Figure 4.16(a) for a test performed under self-induced temperature conditions with a thrust ball bearing lubricated with

Table 4.3.: Parameters used to predict the rolling friction torque with different models.

Model	Parameter
Coulomb [124]	$\mu = 0.0012$
Palmgren [124]	$f_0 = 2$; $f_1 = 1.5$ and $\mu = 0.0015 \left(\frac{F}{C_0}\right)^{(1/3)}$
New SKF [129]	$\mu_{bl} = 0.15$ and $\mu_{EHD} = 0.05$

a mineral oil. The results show that the New SKF model has the best prediction for these test conditions. Both Coulomb and Palmgren models show worst correlation with experimental results. Figure 4.16(b) shows the results of the simulation for a rolling bearing running at a constant temperature of 80 °C with a mineral oil. For these conditions the New SKF shows the best correlation for the tests performed at higher speeds. For low speeds the New SKF model predicts a friction torque very different from the one measured. The Coulomb model is closer to the experimental results, but is independent of the rotational speed and also independent of temperature (compare Figure 4.16(a) and 4.16(b)) which is demonstrated to be wrong according to several authors [135, 140]. The Palmgren model follows the behaviour of the experimental friction torque with rotational speed, i.e higher speeds generated higher friction torques. However, the absolute value of the friction torque is not close to the experimental data. The prediction can be calibrated for the experimental data, modifying the parameters presented in Table 4.3. This possibility is valid for all friction torque models presented and will be discussed for each model.

Using Coulomb model it is impossible to predict the friction torque behaviour in function of the rotational speed or temperature. To get a good prediction of the experimental results one should evaluate the coefficient of friction (μ) for each rotational speed, for each oil formulation and for each oil temperature. After performing the calibration for the oil formulation, the same should be done again when a new rolling bearing geometry is considered. This generates a very high amount of possibilities that reduces the possibility of a correct prediction of the rolling bearing friction torque.

The Palmgren model can simulate the influence of the rotational speed and of the temperature through the oil viscosity. A correct prediction of the rolling bearing friction torque can be obtained, adjusting the parameters of the model as mentioned above. However, a different rolling bearing geometry will require a new adjustment of the parameters. This happens because μ_1 is quite different for different rolling bearing geometries.

The New SKF model is able to reproduce, simultaneously, the influence of the

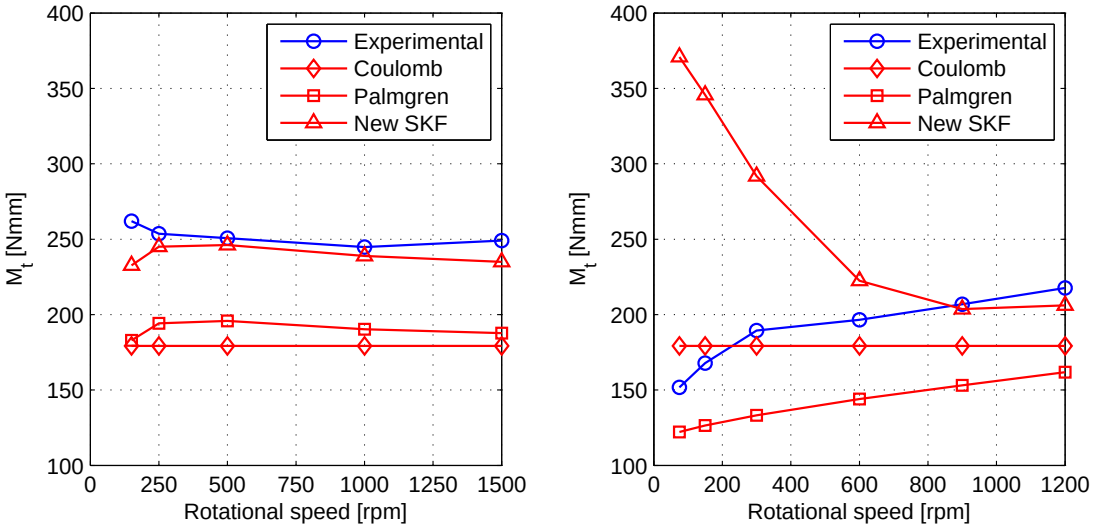

(a) Free temperature.

(b) Constant temperature.

Figure 4.16.: Simulation using different friction torque models against experimental results of MINR oil.

rotational speed and of the lubricant temperature, i.e. the lubrication conditions. The rolling bearing friction torque measured can be effectively determined by adjusting the values of μ_{bl} and μ_{EHD}. The rolling bearing geometry is accounted by the rolling bearing geometric parameters (S_1, R_1, G_{rr}, G_{sl}, etc), known for all SKF rolling bearings (see the SKF catalogue or Appendix F). The results presented showed that the SKF model predicted very well the experimental results under self-induced temperature conditions, because the μ_{EHD} value proposed by SKF is very close to the actual value for a mineral oil. The μ_{EHD} value is the most important parameter for the self-induced temperature conditions since it represents the coefficient of friction under full-film conditions (ϕ_{bl}=0). The experimental results were produced under full-film conditions according to the film thickness predictions. For constant temperature conditions the lubrication regime evolves from boundary film conditions to full-film lubrication when speed increases and, consequently, parameter ϕ_{bl} decreases from 1 to 0. This proves that μ_{bl} has a strong influence at low speeds. Using this type of model, the experimental values can be accurately correlated adjusting the μ_{bl} and μ_{EHD} for each oil, independent of the rolling bearing geometry. This is the most important advantage of the new SKF rolling bearing friction torque model.

4.4. Shaft seal losses

The seal losses were discussed in the rolling bearing losses section, since they are one of the possible contributions to the total power loss of a rolling bearing. However, the use of seals in the shafts are very usual in gearboxes and should be considered in the total power loss.

Seals power loss is due to friction in the contact zone. The friction has been the scope of many researchers but the problem of seal losses is not very well understood yet [141]. The contact zone is very small and the microscopic phenomena is difficult to parametrize. The power loss in this case can be calculated using equations (4.60) and (4.61).

$$P_{VD} = \frac{1}{2} \cdot \mu \cdot F_R \cdot d_{sh} \cdot \omega \tag{4.60}$$

$$F_R = \pi \cdot d_{sh} \cdot t_S \cdot p_S \tag{4.61}$$

However, it is not easy to calculate the interference of the seal in operation, which determines the radial force exerted by the seal on the shaft. To be effective, the lip of a radial shaft seal must always exert a certain radial load on the counter-face. The friction torque resulting from this radial load is only a part of the total friction torque loss at the sealing position. Other contributing factors include the type of medium being sealed, the pressure differential across the seal, the circumferential speed, the ambient temperature, the lubricant and lubrication method and also the condition of the counterface [129]. To calculate the power loss proposed by equation (4.60) it is necessary to know several variables such as, the surface roughness of seal and shaft, the area of contact of the seal, the film thickness and the coefficient of friction. The coefficient of friction is function of the operating temperature, oil viscosity and also the seal/shaft interference.

Freudenberg Simrit performed a large number of measurements and observed that the seal losses are function of seal diameter and rotational speed as presented in Figure 4.17. When the seal diameter is low, the torque loss or power loss is usually very small. However, as the seal diameter increases the seal losses become very significant and cannot be disregarded.

The experimental work of Freudenberg culminated in equation (4.62) to predict seal losses. The formula only takes into account the shaft diameter and the rotational speed while the oil effect is not considered.

$$P_{VD} = 7.69 \times 10^{-6} \cdot d_{sh}^2 \cdot n \tag{4.62}$$

Linke [143] developed a variation of the Simrit equation to take into account different oil viscosities. The Linke's formula is presented in equation (4.63).

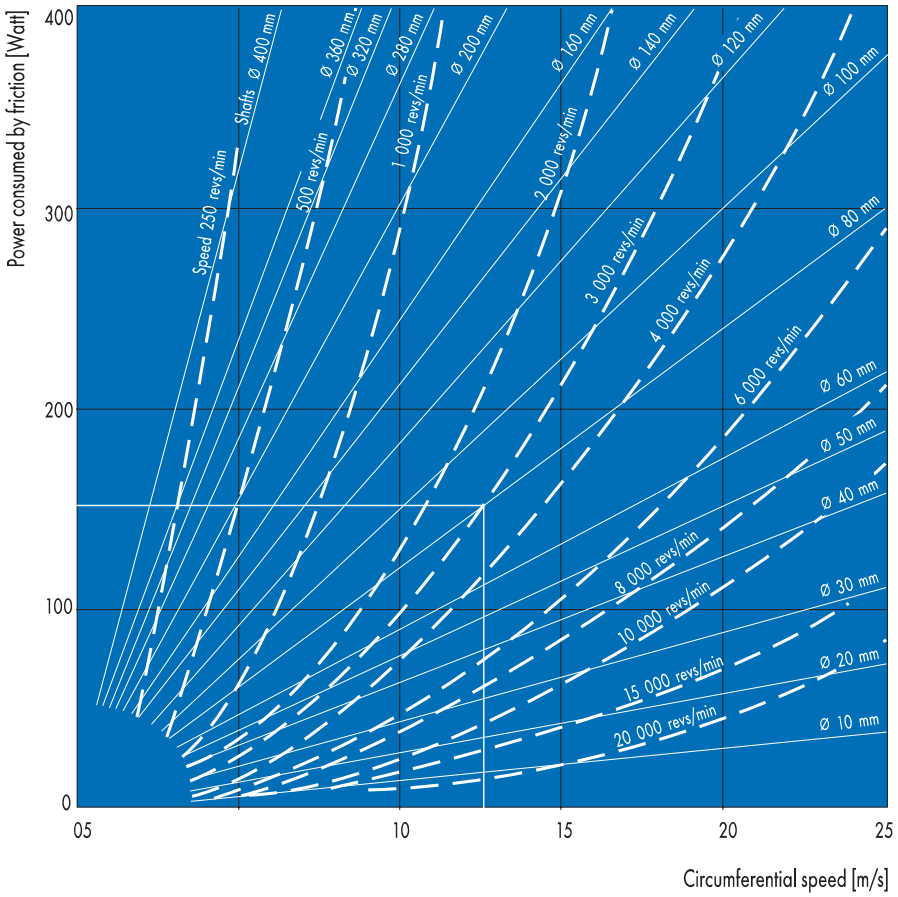

Figure 4.17.: Recommended values for the friction loss on a Simmerring in engine oil SAE 20, at T=100 °C [142].

$$P_{VD} = [145 - 1.6 \cdot \theta + 350 \log \log (\nu_{40} + 0.8)] \times 10^{-7} \cdot d_{sh}^2 \cdot n \tag{4.63}$$

Kettler [144] developed an equation (4.64) to take into account the influence of the oil viscosity.

$$P_{VD} = 7.9163 \times 10^{-6} \cdot F_D \cdot d_{sh}^2 \cdot n \tag{4.64}$$

The factor F_D represents the influence of the temperature on the viscosity.

A simulation was performed with Simrit and Linke models, and the results are presented in Figure 4.18 for a SAE 20 oil at 100 °C and for a mineral ISO VG 320 at 40 °C and 80 °C. It is possible to observe that Simrit and Linke equations give the same result for SAE 20 at 100 °C, which was expected since the Simrit equation was developed with that oil. However, if we use a more viscous oil like an ISO VG 320, the Simrit equation gives the SAE 20 while Linke equation which is dependent

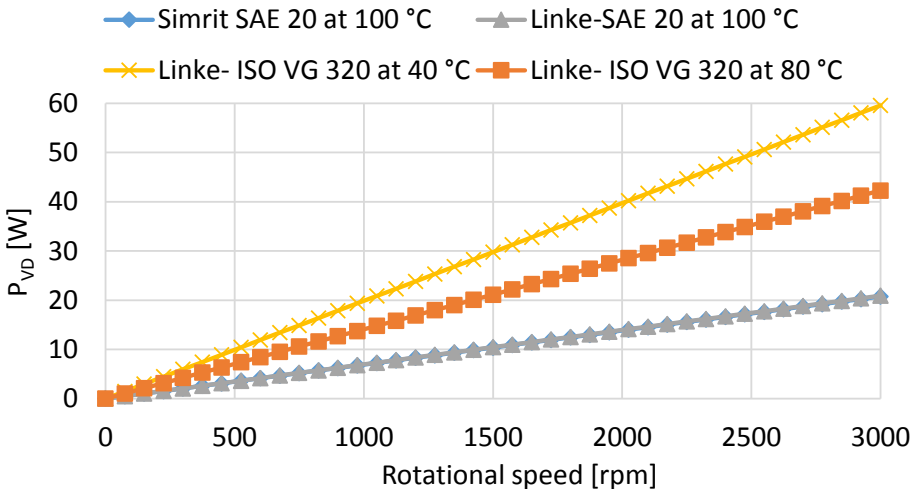

Figure 4.18.: Simulation for 30 mm shaft seals with Simrit and Linke equations.

on the viscosity of the oil at the operating temperature, gives a significantly different prediction.

4.5. Auxiliary losses

The auxiliary losses take into account other dissipative sources that are not generated by gears, bearings or the sealing elements.

4.6. Experimental determination of gear power losses

The power losses occurring in a gearbox are generated by different mechanisms. The seal losses, which are the less important source of power loss will be determined using the Freudenberg equation and the rolling bearing power loss will be predicted using the new SKF friction torque model.

The main objective of this work was to measure and predict accurately the friction power loss in the meshing gears. Since the no-load gear power losses are difficult to predict (see section 4.2.1) they were experimentally measured for each operating speed and gear oil formulation, using a special test procedure.

No-load gear power loss

Depending on the input power and speed, lubricant characteristics and gearbox design, the no-load gear power losses usually are a very important source of energy dissipation. Due to an almost infinite combination of gearbox design possibilities and

operating conditions, it is very difficult to develop a simple and general formulation to evaluate these power loss mechanism, as stated on section 4.2.1.

Assuming that the overall torque loss in a FZG gearbox can be measured at very low input torque (for example, FZG load stage K1=4.95 Nm) and for a wide range of operating speeds, the friction power loss in the meshing gears can be assumed to be null under such conditions . Thus, for a well defined speed and operating temperature, and for any input torque (load stage i) the overall power loss is given by equation (4.65).

$$P_V^i = P_{VZ0}^i + P_{VZP}^i + P_{VL}^i + P_{VD}^i \tag{4.65}$$

For load stage 1 (low input torque, $T_W = 4.95\ Nm$) under the same speed and temperature, equation (4.65) becomes,

$$P_V^1 = P_{VZ0}^1 + P_{VZP}^1 + P_{VL}^1 + P_{VD}^1 \tag{4.66}$$

The term P_V^1 is determined experimentally at load stage K1.

As the concept suggests, the no-load gear losses are independent of the torque, resulting in equation (4.67).

$$P_{VZ0}^i = P_{VZ0}^1 = P_{VZ0},\ \forall\ i \tag{4.67}$$

For load stage K1 it was assumed that,

$$P_{VZP}^1 \approx 0 \tag{4.68}$$

since the corresponding meshing torque loss (T_{VZP}^1) at the operating speed is lower than the precision of the torque cell used to measure the overall torque loss.

The power loss in the rolling bearings (P_{VL}^1) can be calculated using the new SKF model. The power losses in the seals is evaluated using equation (4.69) given in reference [142] by Simrit and is independent of the applied torque.

$$P_{VD}^i = P_{VD}^1 = P_{VD},\ \forall\ i \tag{4.69}$$

Finally, for load stage 1 equation (4.65) becomes

$$P_V^1 = P_{VZ0} + P_{VL}^1 + P_{VD} \tag{4.70}$$

Thus, using this equation (4.70), it is possible to determine the no-load gear loss (P_{VZ0}), stating that,

$$P_{VZ0} = {P_V^1}^{exp} - P_{VL}^1 - P_{VD} \tag{4.71}$$

Load dependent power loss in meshing gears

The load dependent gear losses for any load stage, at the predefined speed and operating temperature, can be calculated according to equation (4.72), subtracting the rolling bearing losses, the seal losses and the no-load losses, known in advance, to the total experimental power loss.

$$P_{VZP}^{i} = P_{V}^{i\,exp} - P_{VL}^{i} - P_{VD} - P_{VZ0} \tag{4.72}$$

4.7. Coupling gearbox power loss models with a thermal equilibrium model

The different power loss mechanisms presented through out this chapter showed that the oil temperature influences the different power loss mechanisms and that the oil temperature depends on the overall power loss of the gearbox.

Höhn *et al.* [66] introduced a model based on the equilibrium between the power loss and heat dissipation, as described in equation (4.73). The model was calibrated using power loss and wall and oil temperatures measured in a FZG machine.

$$Q_{rad} + Q_{conv} + Q_{cond} = P_{VZ0} + P_{VZP} + P_{VL} + P_{VD} \tag{4.73}$$

Based on operating temperature measurements at different load stages on a FZG machine, Martins [80–82, 145–148] calculated the different sources of power loss and was able to determine the coefficient of friction on the meshing gears for different oil formulations.

Figure 4.19 shows the heat transfer balance occurring in a FZG a gearbox, as proposed by Martins *et al.* [80].

The equations used for the heat dissipation are presented on equations (4.74) and (4.75) for radiation.

$$Q_{rad} = \alpha_{rad} \cdot A_{ca} \cdot (\theta_{oil} - \theta_{\infty}) \tag{4.74}$$

$$\alpha_{rad} = 0.23 \cdot 10^{-6} \cdot \epsilon \cdot \left(\frac{T_{oil} + T_{\infty}}{2} \right)^{3} \tag{4.75}$$

The convection and conduction are estimated with equations (4.76), (4.77) and (4.78) developed by Funck [149].

$$Q_{conv} = (\alpha_{conv,v} \cdot A_{v} + \alpha_{conv,h} \cdot A_{h}) \cdot (\theta_{oil} - \theta_{\infty}) \tag{4.76}$$

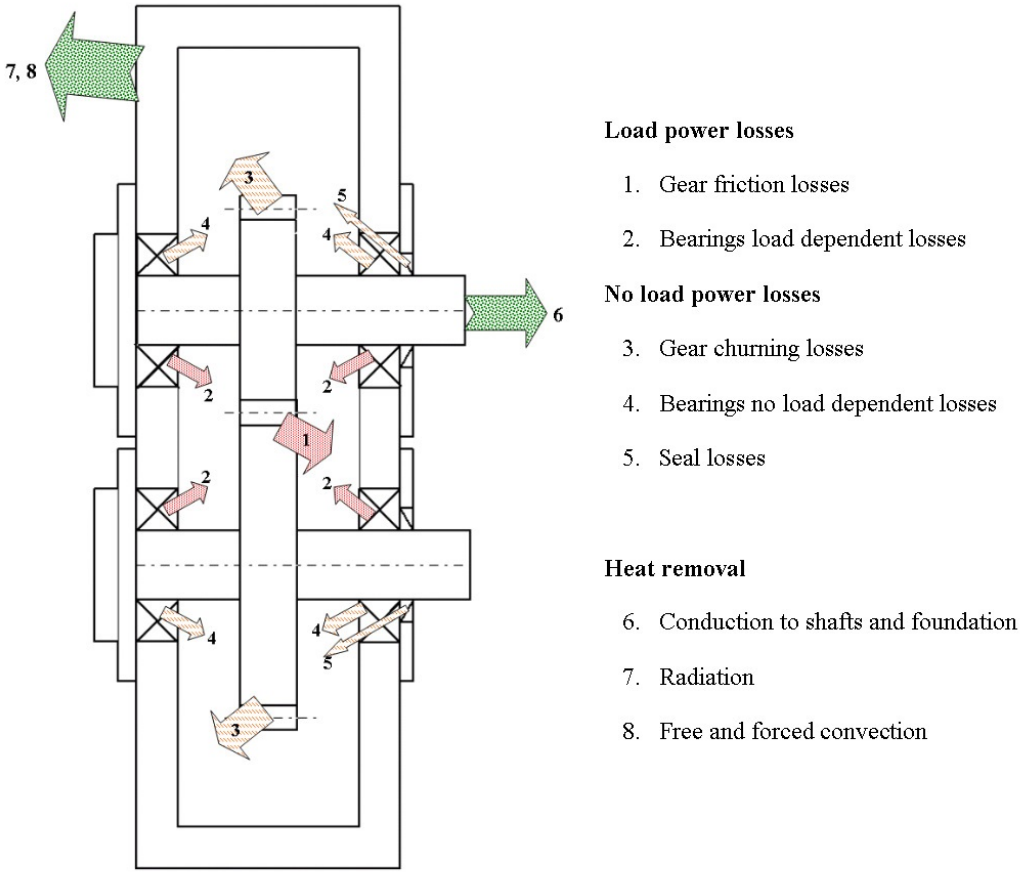

Figure 4.19.: Schematic representation of the different power loss sources and heat removal mechanisms [80].

$$\alpha_{conv,v} = 18 \cdot {h_{ca}}^{-1} \cdot \left(\frac{T_{oil} - T_{\infty}}{T_{\infty}} \right)^{0.3} \tag{4.77}$$

$$\alpha_{conv,h} = 12.87 \cdot (l_{ca} + p_{ca})^{-0.04} \cdot \left(\frac{T_{oil} - T_{\infty}}{T_{\infty}} \right)^{0.32} \tag{4.78}$$

The conduction for the foundation of the gearbox is estimated according to equation (4.79) as function of the radiation and convection existent in the gearbox.

$$Q_{cond} = (Q_{conv} + Q_{rad}) \cdot c_f \cdot \frac{A_{base}}{A_{ca}} \tag{4.79}$$

The conduction factor is usually c_f=1.5.

The total heat dissipated from the the gearbox is given by equation (4.80)

$$Q_T = Q_{conv} + Q_{rad} + Q_{cond} \tag{4.80}$$

More recently Changenet [150, 151] presented a thermomechanic model quite different from that used by Höhn *et al.* [66] and Martins *et al.* [80]. Instead of the isothermal model, that considers isothermic conditions on the gearbox surfaces and components; Changenet uses a thermal network approach that considers nodal temperatures locations along the gearbox. The advantages of Changenet model is to draw the actual distribution of the temperatures inside the gearbox (see Figure 4.20 [151]) and predict the bulk temperature of the oil in each contact. The bulk temperature is of extreme importance because in most of cases, the bulk temperature is much higher than the oil bath temperature, resulting in thinner films and leading to increased risk of gear failure.

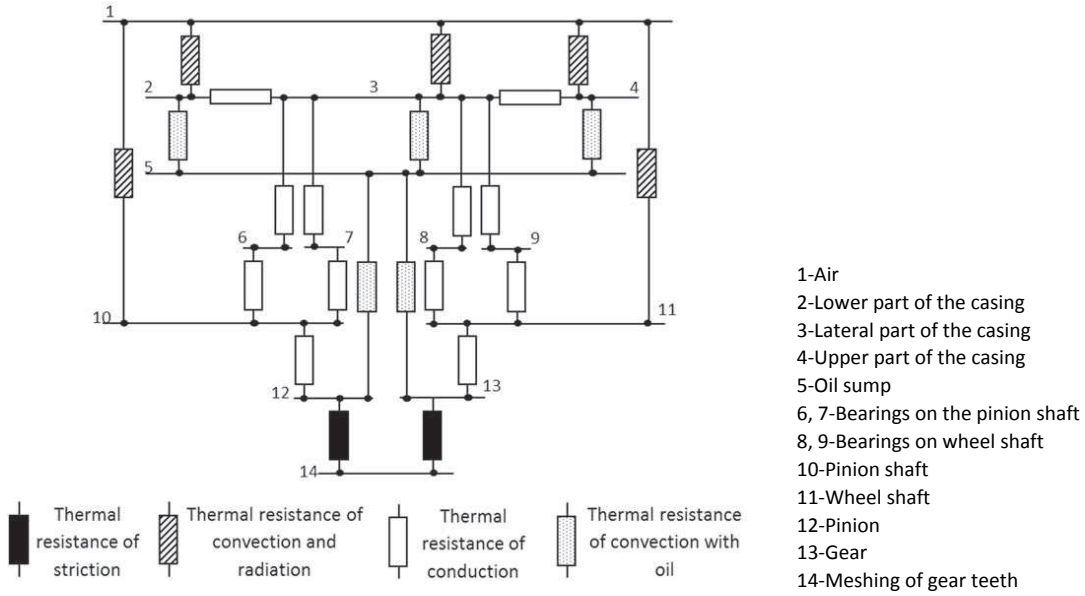

Figure 4.20.: Thermal network of a FZG machine [151].

4.8. Closure

This chapter was dedicated to a literature review of the different power loss mechanisms and corresponding models.

The no-load gear losses are very difficult to generalize and to quantify, for all gearbox designs, operating conditions and lubrication methods (dip or oil-jet lubrication), using the power loss mechanisms known at the moment. Thus, it is more effective to measure the no-load gear power loss than to predict it.

The meshing gear power losses were presented and several approaches compared. An alternative gear loss factor, easy to compute, was proposed, allowing to calculate the load dependent losses for all types of gear geometries. Different coefficient of fric-

tion formulas were also presented, to be discussed later combined with experimental results.

The mechanisms of rolling bearing power loss were presented and several models were discussed and compared, showing the benefits of using the recent model proposed by SKF. This model seems to represent very well the influences of the rolling bearing type and geometry, of the oil formulation and of the lubrication regime.

Finally, the gearbox power loss model is established as:

$$P_V^i = \underbrace{P_{VZ0}}_{P_V^{1\,exp}-P_{VL}^1-P_{VD}} + \underbrace{P_{VZP}^i}_{P_{IN}\cdot H_V\cdot\mu_{mZ}} + \underbrace{P_{VL}^i}_{New\ SKF\ Model} + \underbrace{P_{VD}}_{Simrit\ Equation} \tag{4.81}$$

or

$$P_V^{i\,exp} = \underbrace{P_{VZ0}}_{P_V^{1\,exp}-P_{VL}^1-P_{VD}} + \underbrace{P_{VZP}^i}_{P_V^{i\,exp}-P_{VL}^i-P_{VD}-P_{VZ0}} + \underbrace{P_{VL}^i}_{New\ SKF\ Model} + \underbrace{P_{VD}}_{Simrit\ Equation} \tag{4.82}$$

For prediction purposes the model is based on equation (4.81) while for correlation with experimental results equation (4.82) will be used.

Chapter 5.

Power loss in rolling bearings

5.1. Introduction

The invention of the rolling bearing can be related with the wheel invention. The transition from sliding sledges to rolling was recorded 5000 years ago. The wheel was a breakthrough in friction-reduction [152–154] and there are evidences of different forms of wood rolling bearings used in military machines from Greeks, Celts and Chineses.

The precision rolling bearings such as those used nowadays are a product of the advanced technology of the twentieth century [24]. Their main function is to transmit load at very low friction. However, the rolling bearings friction power loss can reach up to 30% of the total power loss occurring inside a gearbox [155], being a major contribution to the overall energy loss. In machines involving high power density, like wind turbines, the efficiency of the rolling bearings is of extreme importance in achieving an overall efficient machine.

The energy consumption due to rolling bearing power loss is becoming more and more important, keeping the attention of science and industry for the topic. The rolling bearing manufacturers are trying to improve rolling bearing designs in order to reduce the power loss generated, reduce the energy consumption, reduce the operating temperatures and improve the lubrication conditions. At the same time the lubricant manufacturers claim to have new products that increase rolling bearing life, while reducing the energy dissipated [25, 156–158].

Besides the good agreement between model predictions and experimental results that might be obtained, there are several issues that are very difficult to take into account in a power loss model: the evolution of micro-geometry during operation, the particularities of each oil or grease formulation and the evolution of their properties during operation, are examples of such issues. Current models have some limitations regarding the influence of oil formulation in power loss predictions, which can only be overcome through extensive testing.

The measurement of the rolling bearings friction torque has been done by several

authors [126, 135, 136, 140, 159–165] other than rolling bearing manufacturers. There are mainly two groups of test rigs used to measure the friction torque, the ones used by rolling bearing manufacturers and another group mostly dedicated to academic research.

In the industrial field the FAG FE-8 test rig is well known for their wear tests, but can also measure friction torque [23]. The FAG machine is used for preliminary selections and for suitability tests of greases and oils, in accordance with DIN 51819, part of DIN EN 12081. INA [166] developed a test rig that allows to measure friction torque, temperatures and film thickness using cylindrical roller thrust bearings.

In academic research, Blake and Truman [164] developed a new experimental arrangement to test tapper roller bearings. Takabi [160] developed a test rig to investigate the torque loss of different rolling bearing geometries but the system only can test radial loads. Paleu *et al.* [167] developed a test rig to monitor the friction torque in high-speed rolling bearings (up to 120 000 rpm) under oil-mist conditions. Zhou and Hoeprich [139] developed a test rig for tapered roller bearings that allow to measure the torque of cup race, cone race, and rib separately. Recently, Cousseau *et al.* [140] developed a test method to measure friction torque in rolling bearings through the modification of a Four-Ball Machine. The modified Four-Ball Machine was used in this work to measure the torque loss in thrust ball bearings and cylindrical roller thrust bearings.

According to Weigand [168] grease is the most common type of lubricant used in rolling bearings. However, oil is mainly used in gearboxes, where the gears and the rolling bearings are lubricated with the same oil.

This chapter adds some new knowledge about rolling bearings lubricated with wind turbine gear oils. Several tests were performed and a considerable amount of experimental results of power loss in rolling bearings, difficult to find in literature, were obtained. The results presented in this chapter have been published [169–172].

The SKF rolling bearing friction torque model will be calibrated with the experimental results. The model allows a better understanding of the behaviour of different rolling bearing geometries and of the influence of oil formulation. The rolling bearing power loss model will be relevant for the global gearbox power loss model predictions.

5.2. Materials and methods

5.2.1. Rolling bearing assembly

Cousseau *et al.* [140] developed a test method for rolling bearings using a Four-Ball Machine (Cameron-Plint TE 82/7752). The standard four-ball arrangement was replaced by a rolling bearing assembly, as shown in Figure 5.1. The new arrangement

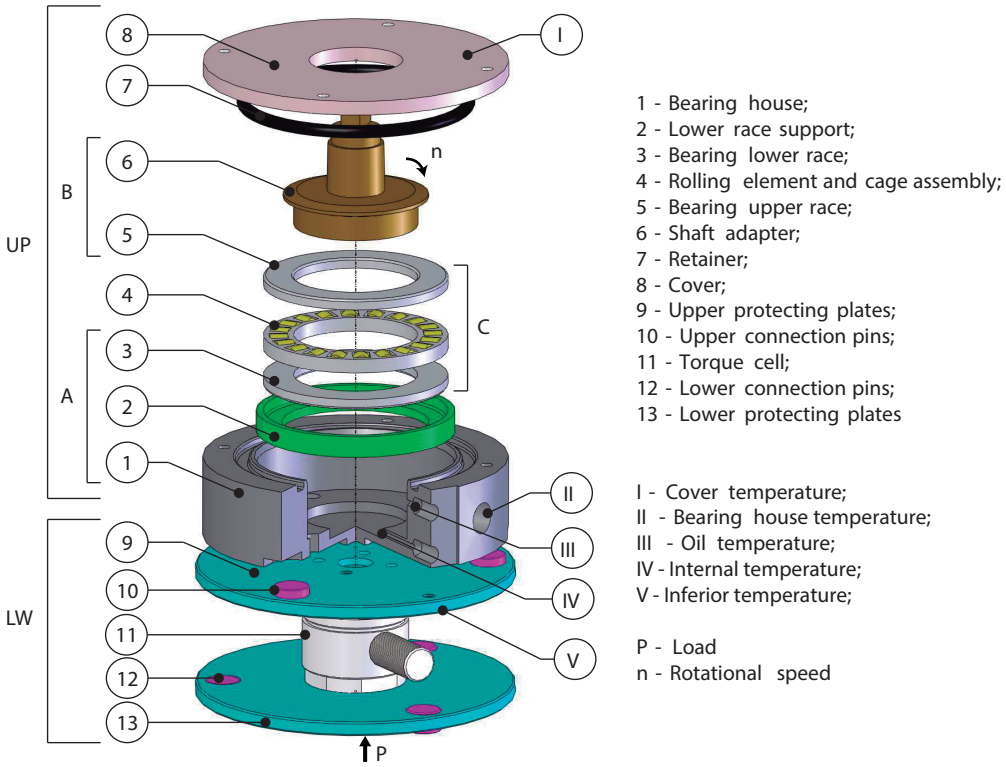

Figure 5.1.: Schematic view of the rolling bearing assembly with a cylindrical roller thrust bearing.

allows to measure the friction torque and the operating temperature in rolling bearings.

The rolling bearing assembly is divided in two parts: the shaft adapter (6), directly connected to the machine shaft and supporting the bearing upper race (5); a lower race support (2) and the bearing lower race (3), both clamped to the bearing housing (1). In operation, the internal bearing torque (or friction torque) is transmitted to the torque cell (11) through the bearing housing (1). The friction torque was measured with a piezoelectric reaction torque sensor $KISTLER$ $9339A$, ensuring high-accuracy measurements ($\pm$ 1 Nmm) even when the friction torque generated in the bearing was very small compared to the measurement range available (please see Table 5.1).

This assembly includes five type K thermocouples (I-V), measuring temperatures at strategic locations (see Figure 5.1), which are used to monitor the temperature inside the bearing assembly (IV), near to the rolling bearing and the lubricant (III) and to evaluate the heat evacuation from the bearing housing into the surrounding environment (I, II and V). The system is also monitored by two thermocouples to monitor the chamber and room temperatures.

Table 5.1.: Technical specifications of the piezoelectric reaction torque sensor KISTLER 9339 A.

Piezoelectric reaction torque sensor KISTLER 9339 A	
Measurement range 100% [Nm]	-10 – 10
Measurement range 10% [Nm]	-1 – 1
Overload [Nm]	-12/12
Linearity [%FSO]	$\leq \pm 0.2$
Hysteresis [%FSO]	≤ 0.3
Accuracy [%]	0.01
Operating temperature range [°C]	-40 – 120
Temperature sensitivity [%/°C]	-0.02

Four types of rolling bearings, of different sizes, can be tested with this assembly, namely: thrust ball bearings (SKF ref. 51103 and ref. 51107), tapper roller bearings (SKF ref. 30302 J2 and ref. 30203 J2), angular contact ball bearings (SKF ref. 7302 and ref. 7302) and cylindrical roller thrust bearings (SKF ref. 81102 TN and ref. 81107 TN).

This assembly can perform two types of tests: one with self-induced temperature, i.e. the temperature is given by the test conditions and consequently heat is generated; the other option is to control the temperature. In order to control the temperature, two heaters were included on the assembly, as shown in Figure 5.2(a). The heaters are controlled with a PID control system with feedback, whose feedback is given by thermocouple (III) (see Figure 5.1). The control system can assure a temperature variation always below than $\pm$ 1 °C as presented in Figure 5.2(b).

5.2.2. Rolling bearings tested

In a wind turbine gearbox as well as in other types of gearboxes, a wide range of rolling bearing geometries might be used. According to "ANSI/AGMA/AWEA 6006-A03 - A standard for design and specification of gearboxes for wind turbines" [26], different types of rolling bearings are usually used for the different shafts of a wind turbine gearbox, as presented in Table 5.2. From the technical point of view it is almost impossible to test all these bearing types. The test rig presented in section 5.2.1 allows to test different rolling bearing geometries but the size of the rolling bearings are much smaller that those used on a full size wind turbine gearbox, i.e. the test rig presented only allows rolling bearings with a maximum outer diameter of 60 mm. Given such limitations, it is important at least to understand the behaviour of different rolling element bearings, understand the lubrication capabilities of different

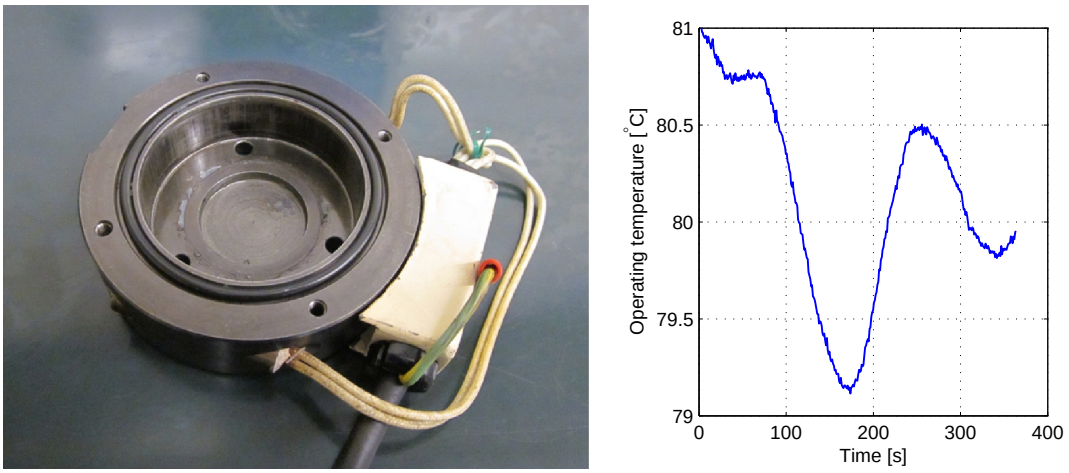

(a) Bearing house.

(b) Control behaviour of operating temperature.

Figure 5.2.: Bearing house with heaters controlled with a PID system.

wind turbine gear oils and try to reduce the power loss in rolling bearings, knowing the influence of several parameters such as speed, load, oil formulation and bearing geometry.

An exploratory test campaign was performed with four rolling bearing geometries lubricated with a PAO oil. The geometries selected were one thrust ball bearing (TBB), one angular contact ball bearing (ACBB), one cylindrical roller thrust bearing (RTB) and one tapper roller bearing (TRB). The tests were performed with free temperature conditions and for different rotational speeds. All rolling bearings were submitted to an axial load of 7000 N and the results are presented in Figure 5.3. The friction torque results show two different behaviours (see Figure 5.3(a)), one for rolling bearings with ball elements (TBB and ACBB) and another for rolling bearings with roller elements (RTB and TRB). The roller bearings generated higher friction torque than the ball bearings. The test performed with tapper roller bearings (TRB) had several problems, for instance, excessive heating of the rolling bearing due to misalignment and poor repeatability of the results. The ball bearings, TBB and ACBB, presented similar friction torque but very different stabilization temperatures, and such behaviour was not expected. The result obtained with the angular contact ball bearing didn't seam acceptable, since they generate the same rolling bearing friction torque but significantly different operating temperatures, which is incompatible with the results reported in literature [66, 151, 173–175].

The exploratory tests showed some problems in the tests performed with the ACCB and TRB. From these observations, two rolling bearing geometries were selected, representing the most common rolling element bearings. A thrust ball

Table 5.2.: Rolling bearing types usually used on wind turbine gearboxes.

Location		Bearing type
High-speed shaft	Fixed-side	SRB, CRB, TRB, BB, 4PCBB
	Free-side	SRB, CRB, BB
Intermediate shaft	Fixed-side	SRB, CRB, TRB, 4PCBB
	Free-side	SRB, CRB
Low-speed shaft	Fixed-side	SRB, TRB
	Free-side	SRB, CRB, FCCRB
Planetary gear		SRB, CRB, FCCRB, TRB
Carrier		FCCRB, SRB, TRB

SRB: Self-aligning Roller Bearing; CRB: Cylindrical Roller Bearing;
FCCRB: Full Complement Cylindrical Roller Bearing ; TRB: Tapered Roller Bearing;
BB: Deep Groove Ball Bearing; 4PCVBB: Four Point Contact Ball Bearing.

bearing, TBB SKF ref. 51107[1] (ball) and a cylindrical roller thrust bearing, RTB SKF ref. 81107[2] (roller) with the geometric characteristics reported in Table 5.3.

5.2.3. Test conditions

Three different test campaigns were designed to test the selected geometries, presented in section 5.2.2.

1. A calibration test campaign was performed under different constant temperatures

2. A test campaign, performed under constant temperature of the oil sump, to match the usual lubrication conditions of a wind turbine gearbox, i.e. 80 °C [176].

3. A test campaign where the oil sump temperature was set free (self-induced temperature), i.e. the oil heat up to a temperature that is function of the generated power loss and corresponding oil thermal properties.

The oils used for these tests were characterized in Chapter 2.

[1]Thrust ball bearing SKF ref. 51107 will be reported from here on as TBB 51107
[2]Cylindrical roller thrust bearing SKF ref. 51107 will be reported from here on as RTB 81107

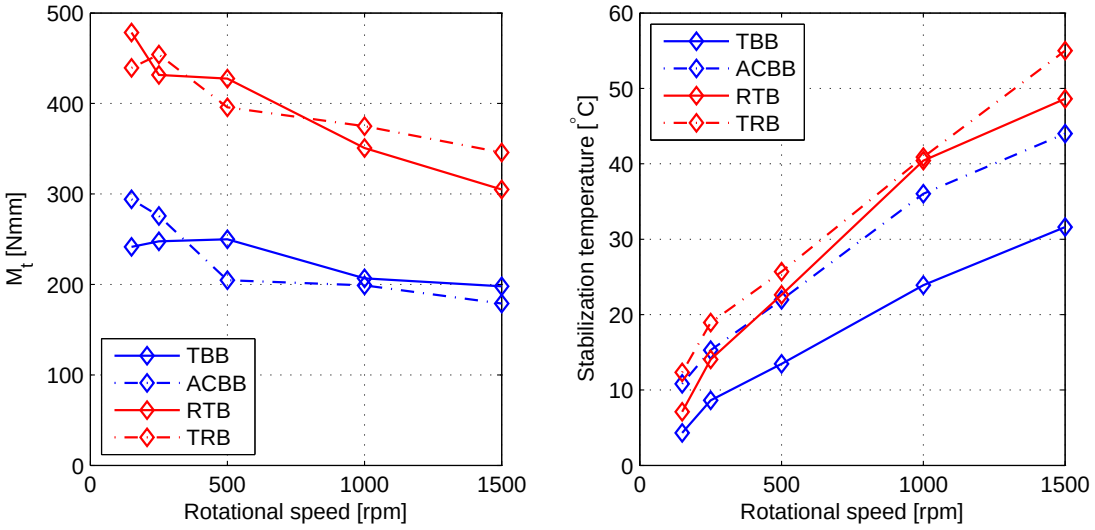

(a) Friction torque.

(b) Stabilization temperature.

Figure 5.3.: Rolling bearing friction torque ans stabilized operating temperature in four different types of rolling bearings: - TBB (thrust ball bearing); - ACBB (angular contact ball bearing SKF ref. 7302); - RTB (cylindrical roller thrust bearing SKF ref. 81107); - TRB (tapper roller bearing SKF ref. 30302 J2); - PAOR oil under self-induced temperature conditions.

The rolling bearing is lubricated by an oil volume of 14 ml. The oil volume was selected so that the oil level reaches the centre of the ball, such as advised by the manufacturer [129].

For each oil tested, a new rolling bearing sample was used in order to reduce the influence of the surface finish and possible chemical interactions between oils tested. The raceway surface finish of different new samples was measured with an absolute stylus probe in a *Hommelwereke T*4000 device. The measurements show a similar finishing on the rolling bearings as presented in Table 5.4.

The rotational speeds were chosen considering the available range of the test machine and also the rotational speeds usually used in wind turbine gearbox rolling bearings. The example presented by KissSoft [176] of a 2.5 MW a wind turbine gearbox where the tangential speed of the rolling bearings go from 0.9 m/s on the LSS (low speed shaft) up to 25 m/s on the HSS (high speed shaft), for a rotational speed on the blades of 20 rpm. Usually the wind turbines start to generate energy with a rotational speed of the blades of 12 rpm, which decrease the circumferential speed up to 0.5 m/s.

The geometries of the rolling bearings used in a 2.5 MW machine are quite different from the rolling bearings used in these tests. So, a simple criterion was developed to

Table 5.3.: Characteristics of TBB 51107 and RTB 81107.

			TBB 51107	RTB 81107
Principal Dimensions	d	mm	35	
	D	mm	52	
	H	mm	12	
Basic load ratings	Dynamic C	kN	19,9	29
	Static C_0	kN	51	93
Speed ratings	Reference speed	rpm	5600	2800
	Limit speed	rpm	7500	5600

Table 5.4.: Average roughness of ring on three different thrust ball bearing samples.

Rolling bearing type	Element	Ra (μm)		
TBB 51107	Raceway	0.0890	0.0978	0.0985
	Ball	≈ 0.1 – not measured		
RTB 81107	Raceway	0.1231	0.1323	0.1002
	Roller	≈ 0.1 – not measured		

compare different geometries, operating conditions and oil formulations.

The SKF friction torque model suggests a weighting function that characterizes the lubrication regime, i.e. the parameter ϕ_{bl} represents the "amount" of boundary film inside the contact. For $\phi_{bl} = 1$ the rolling bearing is under boundary film while for $\phi_{bl} = 0$ lays under full-film lubrication. For a given rolling bearing geometry the ϕ_{bl} parameter is expressed by the average diameter (d_m), rotational speed (n) and operating viscosity (ν) as presented in equation (5.1).

$$\phi_{bl} = \frac{1}{e^{2,6\times10^{-8}\cdot(n\cdot\upsilon)^{1.4}\cdot d_m}} \tag{5.1}$$

When comparing different rolling bearing geometries, the parameter of interest is presented in equation (5.2) which, in the case of constant operating temperature, becomes only the factor LQ (Lubrication Quality) presented in equation (5.3).

$$\phi_{bl} = f((n\cdot\upsilon)^{1.4}\cdot d_m) \tag{5.2}$$

$$LQ = (n\cdot\nu)^{1.4}\cdot d_m \tag{5.3}$$

The criterion is to perform the laboratory tests under the same LQ parameter observed in real applications, as presented in equation (5.4).

$$LQ_{real} = LQ_{test} \; or \; (n_{real} \cdot \nu_{real})^{1.4} \cdot d_{mreal} = (n_{test} \cdot \nu_{test})^{1.4} \cdot d_{mtest} \tag{5.4}$$

For the low speed shaft, the rolling bearing given in reference [176] has a mean diameter of 975 mm and a rotational speed from 12 up to 20 rpm while the HSS (high speed shaft) rolling bearing has a diameter of 230 mm and a rotational speed from 1224.4 up to 2040.6 rpm. So, the factor calculated with equation (5.3) gives the minimum value of LQ_{real}=31 612 and a maximum of LQ_{real}= 9 894 387. The rotational speed of the tests necessary to have the same $LQ_{test} = LQ_{real}$ with an average diameter of d_m=43.5 mm (see section 5.2.2) are,

$$n_{min} = \left(\frac{LQ_{min}}{d_m}\right)^{(1/1.4)} = \left(\frac{31\ 612}{43.5}\right)^{(1/1.4)} = 111\ rpm \tag{5.5}$$

$$n_{max} = \left(\frac{LQ_{max}}{d_m}\right)^{(1/1.4)} = \left(\frac{9\ 894\ 387}{43.5}\right)^{(1/1.4)} = 6704\ rpm \tag{5.6}$$

These calculations were used to define the operating conditions for the tests. The minimum value of the rotational speed selected was 75 rpm, which can assure a lubrication regime similar to that of the 2.5 MW Wind Turbine Gearbox.

The test machine is not able to achieve speeds above 1500 rpm. Although far way from the 6700 rpm specified by the LQ criterion, such rotational speed is enough to reach full-film lubrication regime. So, the tests were performed under speeds in the range 75 rpm to 1500 rpm, allowing to cover all lubrication regimes, from boundary to full-film lubrication.

The rotational speeds selected are those presented in Table 5.5, with the corresponding rolling speeds for tests performed under self-induced temperature conditions or a constant temperature of 80 °C.

The axial loads selected, 700 and 7000 N, generated the maximum Hertzian pressures presented in Table 5.6 for TBB 51107 and in Table 5.7 for RTB 81107.

5.2.4. Test procedure

A new rolling bearing is assembled and lubricated with 14 ml of fresh oil. The rolling bearing assembly is submitted to a continuous air flow, forced by two 38 mm diameter fans, running at 2000 rpm, cooling the chamber surrounding the bearing house.

A running-in period is always required for each rolling bearing and is carried under an axial load of 1000 N and increasing rotational speed from 75 to 1500 rpm during 10 minutes.

Table 5.5.: Rotational speeds used in self-induced and constant temperature tests.

Rotational speed [rpm]	Rolling speed [m/s]	Self-induced	Constant
75	0.171		x
150	0.342	x	x
250	0.569	x	
300	0.683		x
500	1.139	x	
600	1.367		x
900	2.050		x
1000	2.278	x	
1200	2.733		x
1500	3.416	x	

Table 5.6.: Ball-raceway contact parameters of TBB 51107 rolling bearing.

Contact Element	Raceways	Ball
R_{Xi} [m]	∞	3.00×0^{-3}
R_{Yi} [m]	-3.38×10^{-3}	3.00×10^{-3}
Axial Load [N]	700	7000
R_X [m]	6.00×10^{-3}	
R_Y [m]	53.4×10^{-3}	
A_c [μm^2]	57.109	123.87
p_0 [GPa]	1.15	2.48

Table 5.7.: Roller-raceway contact parameters of RTB 81107 rolling bearing.

Axial Load [N]	700	7000
R_X [m]	5.00×10^{-3}	
l [mm]	5.00	
a_H [μm]	13.76	43.50
p_0 [MPa]	318	1004

The machine is then started at the desirable speed and run until it reaches a constant operating temperature (80 °C) induced by the heaters or reaches a stabilization temperature in the case of free conditions tests. When the thermal equilibrium is reached, four friction torque measurements were performed: three

Table 5.8.: Oil operating temperature with a RTB at 1200 rpm.

Oil	MINR	ESTR	PAOR	MINE	PAGD
Oil temperature [°C]	91	88	86	85	83

values are stored and the most dispersed one was disregarded. Due to the "drift effect", which affects the measurements of the piezoelectric sensors after long periods of operation, the friction torque measurements should be made in a short period of time (less than 120 s) and at constant temperature.

5.2.5. Operating temperatures

The operating temperatures are presented in Appendix G for the tests performed under free sump temperature conditions.

For the tests performed under constant temperature conditions, some test conditions went out of the expected operating temperature (80 °C). At 1200 rpm and with a RTB 81107, the oil temperature reaches the values presented in Table 5.8.

5.3. Film thickness inside rolling bearings

The friction torque and the lubrication regime, inside a rolling bearing, are directly linked to each other. In fact the rolling torque depends on operating speed, oil viscosity and applied load and the sliding torque depends on the sliding coefficient of friction, which can be related to the Hersey parameter ($U_S \cdot \eta \cdot \alpha^{1/2} \cdot F^{-1/2}$), as shown by the Stribeck curve [129, 130, 136]. A more detailed description on the different lubrication regimes observed on a lubricated contact is presented in Appendix C.

The central film thickness (h_0) is calculated using Hamrock and Dowson [24] equation, for elliptical contacts or Dowson and Higginson [177] equation for line contacts, presented in detail in Appendix C.

The corrected film thickness (h_{0C}) is given by the product of the thermal correction factor ϕ_T (related to the inlet shear heating) and defined by equations (5.8) and (5.9), by the centre film thickness (h_0), as presented in equation (5.7).

$$h_{0C} = h_0 \cdot \phi_T \tag{5.7}$$

$$\phi_T = \frac{1 - 13.2 \cdot (p_0/E^*) \cdot (L^*)^{0.42}}{1 + 0.213 \cdot (1 + 2.23 \cdot S^{0.83}) \cdot (L^*)^{0.64}} \tag{5.8}$$

$$L^* = \frac{\beta_L \cdot \eta \cdot U_S}{k_L} \tag{5.9}$$

The lubrication regime is usually predicted using the concept of specific film thickness (Λ), introduced by Tallian [121]. The specific film thickness can be calculated with equation (5.10).

$$\Lambda = \frac{h_{0C}}{\sigma_C} \tag{5.10}$$

The composite roughness (σ_c) is calculated with the roughness of the rolling element ($\sigma_{element}$, ball or roller depending on bearing geometry) and the roughness of the race (σ_{race}), according to equation (5.11). The roughness values for each rolling bearing tested are presented in Table 5.4.

$$\sigma_C = \sqrt{{\sigma_{element}}^2 + {\sigma_{race}}^2} \tag{5.11}$$

The concept of specific film thickness (Λ) is well known in machine design, while the viscosity ratio (κ) is widely used in rolling bearing technology [178]. Morales *et al.* [179] and Cann *et al.* [180] presented a critical comparison between the two parameters.

The viscosity ratio κ, proposed by Heemskerk [181] and defined by equation (5.12), is defined as the ratio between the operating viscosity and the viscosity required to provide $\Lambda = 1$.

$$\kappa = \frac{\nu}{\nu_1} \tag{5.12}$$

The viscosity ratio is given by the abacus proposed by SKF on the General Catalogue [129]. Using this abacus it is impossible to select the type of bearing since only the mean diameter (d_m) is considered for the definition of the viscosity ratio. ISO 281 [178] defines the viscosity ratio κ as a function of the specific film thickness, according to equation (5.13).

$$\kappa_{ISO} = \Lambda^{1.3} \tag{5.13}$$

Figure 5.4 shows the viscosity ratio, according to the SKF abacus [129], for each test condition and for each rolling bearing tested. In the case of a TBB, the oil temperature was kept constant and equal to 80 °C, and consequently viscosity ratio increases with increasing speeds. The RTB has the same viscosity ratio of the TBB for the same lubricant and test conditions, up to 900 rpm. Above 900 rpm, the oil temperature was higher than 80 °C and promotes a reduction in the viscosity ratio when compared to the TBB 51107 at 1200 rpm. Another point is that the influence of the load seems to be disregarded in the abacus proposed by SKF. The only difference that can be observed between TBB and RTB, presented in Figures 5.4(a) and 5.4(b) respectively, is that at 1200 rpm the RTB reaches higher temperatures which affects the operating viscosity and in this way decreases the viscosity ratio.

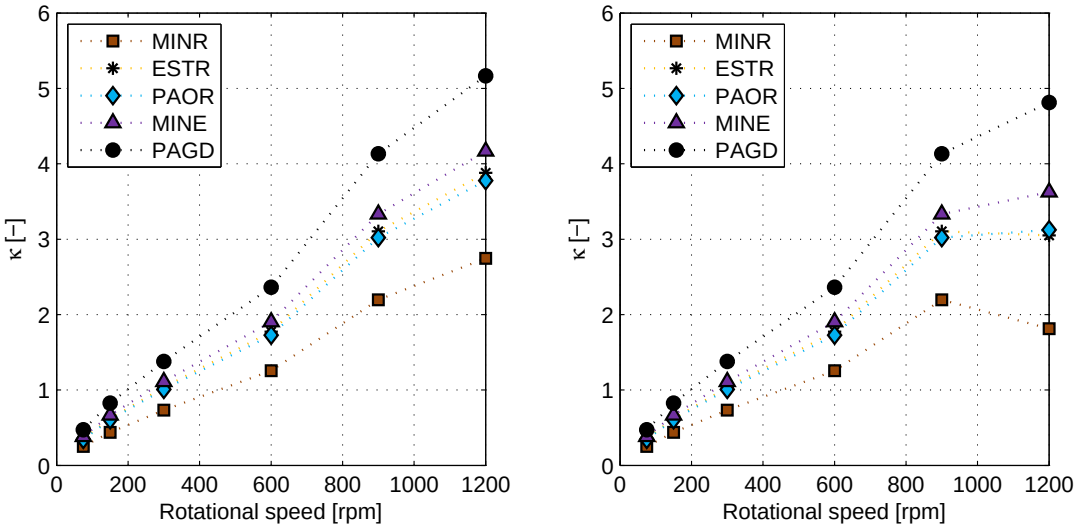

(a) TBB 7000 N.

(b) RTB 7000 N.

Figure 5.4.: Viscosity ratio for a TBB and for a RTB.

A rolling bearing operates under mixed-film lubrication for κ higher than 1 and under full-film lubrication for κ higher than 2. According to the literature, the rolling bearing reaches the boundary film conditions for a viscosity ratio lower than 0.4. The tests performed crossed all the lubrication regimes, no matter the rolling bearing geometry or oil formulation used.

5.4. SKF friction torque model

The torque loss model proposed by SKF [129] considers that the total friction torque is the sum of four different physical sources of torque loss represented by equation (5.14).

$$M_t = M_{rr}^{'} + M_{sl} + M_{drag} + M_{seal} \tag{5.14}$$

The rolling bearings tested, TBB (51107) and RTB (81107), don't have seals and so the M_{seal} torque loss term was disregarded. The drag losses are very small because the operating speeds and the mean diameter of the rolling bearings are also small, consequently, the drag torque loss term was also disregarded.

Figure 5.5 presents the drag losses calculated for different rolling bearings. The results clearly show that the drag losses can be disregarded for such small rolling bearings such as TBB 51107 and RTB 81107.

Thus, the total internal friction torque of the rolling bearings have only two

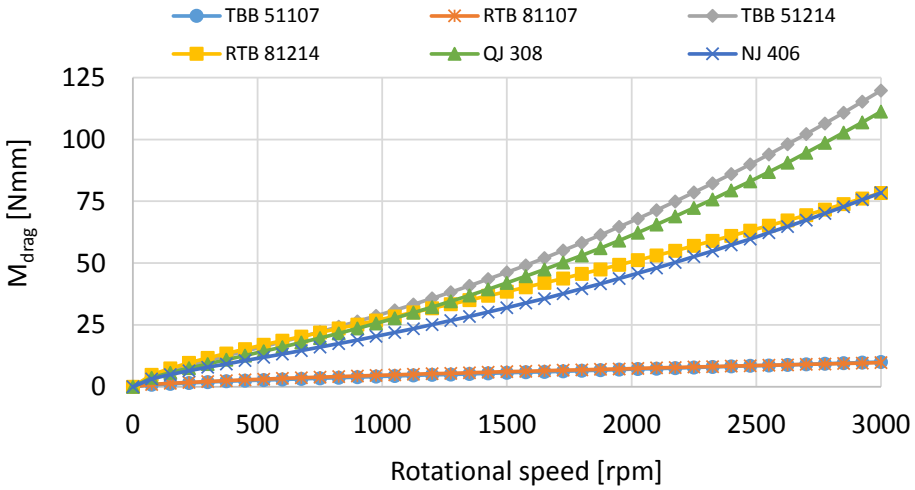

Figure 5.5.: Drag losses calculated for different rolling bearing geometries.

contributions: the rolling and sliding torques, respectively, $M_{rr}^{'}$ and M_{sl}, as presented in equation (5.15).

$$M_t = M_{rr}^{'} + M_{sl} \tag{5.15}$$

Since experimental measurements are available, it is assumed that the total torque loss predicted by the model is equal to the measured torque loss ($M_t = M_t^{exp}$), and equation (5.15) can be written as equation (5.16).

$$M_t = M_t^{exp} = M_{rr}^{'} + M_{sl} \tag{5.16}$$

5.4.1. Sliding coefficient of friction

The rolling torque is then calculated according to the SKF model (equations (4.52) to (4.54), presented in Chapter 4 and in Appendix F). Assuming that the rolling torque is accurately calculated, the sliding torque is obtained using equation (5.17).

$$M_{sl} = M_t^{exp} - M_{rr}^{'} \tag{5.17}$$

The sliding torque is dependent on the coefficient of friction that should be calculated with equation (5.18). The sliding coefficient of friction (μ_{sl}^{exp}) is now considered as an experimental coefficient of friction.

$$\mu_{sl}^{exp} = \frac{M_{sl}}{G_{sl}} = \frac{M_t^{exp} - M_{rr}^{'}}{G_{sl}} \tag{5.18}$$

It is possible to correlate the experimental values of the coefficient of friction (equation (5.18)), μ_{sl}^{exp} with the values of μ_{sl} predicted with equation (5.19).

$$\mu_{sl} = \phi_{bl} \cdot \mu_{bl} + (1 - \phi_{bl}) \cdot \mu_{EHD} \tag{5.19}$$

Where μ_{bl} and μ_{EHD} might be calculated minimizing the difference between μ_{sl}^{exp} and μ_{sl} for each operating temperature and for each type of rolling bearing. The values of μ_{bl} and μ_{EHD} are clearly dependent on the speed range used in the rolling bearing tests, as will be shown later on.

5.4.2. Calibration tests

In order to understand the behaviour of the rolling bearing torque loss model a batch of rolling bearing tests were performed, under significant ranges of operating speeds and temperatures and using two types of rolling bearings, TBB 51107 and RTB 81107, in all cases lubricated with PAOR gear oil. Table 5.9 summarizes the operating conditions used in these calibration tests.

Figure 5.6 shows the torque loss measured for each operating speed and temperature, for TBB (Figure 5.6(a)) and RTB (Figure 5.6(b)). For both rolling bearing types, and as expected [140], when the temperature increases (at constant speed) the torque loss decreases, whithin the temperature range considered (60 °C - 80 °C).

In the case of the TBB 51107 when the speed increases (at constant temperature) the torque loss increases. However, at very high temperature (eg. 135 °C, see Figure 5.6(a)) the opposite trend occurs. This different behaviour is justified by the difference in lubrication regime when the temperature increases from 60 °C - 80 °C to 135 °C. In the case of the RTB 81107 the torque loss decreases when the speed increases (at contant temperature), showing the opposite behaviour of the TBB. Finally, comparing Figure 5.6(a) and Figure 5.6(b), it is clear that the RTB generated significantly higher torque loss than the TBB, for the same operating conditions (eg. 425 N.mm for RTB vs 145 N.mm for TBB, at 75 rpm and 80 °C).

Figure 5.6(c) and Figure 5.6(d) show the sliding coefficient of friction μ_{sl} for TBB and RTB, respectively, obtained using equation (5.18). It is interesting to notice that in all cases, μ_{sl} decreases very slightly when the temperature increases and μ_{sl} also decreases when the operating speed increases. Furthermore, in the case of the

Table 5.9.: Operating conditions of calibration tests performed.

Operating conditions	TBB 51107	RTB 81107
Rotational speed [rpm]	75, 300, 900	75, 300, 600
Temperature [°C]	60, 70, 80, 135	60, 70, 80
Axial load [N]	7000	7000

RTB μ_{sl} is almost temperature independent. Finally, it can be observed that μ_{sl} is smaller in the case of the RTB when compared to the TBB.

The influence of the lubrication regime can be clearly identified analysing Figure 5.6(c) for the oil temperature of 135 °C. At low speed (n=75 rpm), the boundary film lubrication regime prevails, and μ_{sl} reaches high values ($\mu_{sl}^{exp} \cong 0.07$) and at high speed (n=600 rpm) μ_{sl} is very small ($\mu_{sl}^{exp} \cong 0.025$) and the full film lubrication regime prevails.

Figure 5.6(e) and Figure 5.6(f) indicate that when speed and temperature increases the modified Hersey parameter ($Sp = \frac{U_S \cdot \eta \cdot \alpha^{1/2}}{F^{-1/2}}$) increases from 4×10^{-8} to 1×10^{-6} and the sliding coefficient of friction (μ_{sl}^{exp}) decreases from 0.055 to 0.037, in the case of TBB, and from 0.035 to 0.015 in the case of the RTB. These figures give a very good overview of the influence of the operating conditions on the sliding coefficient of friction for both types of rolling bearings, showing the interest of this modified Hersey parameter [182].

Figure 5.6(e) and Figure 5.6(f) also indicate that rolling bearing tests were performed under mixed film lubrication since a clear decrease of the sliding coefficient of friction is observed when the modified Hersey parameter increases.

Using equation (5.19) it is possible to calculate the values of μ_{bl} and μ_{EHD} that minimize the difference between μ_{sl} and μ_{sl}^{exp}, shown in Table 5.10.

The values presented in Table 5.10 demonstrate that equation 5.19 is totally suitable to define accurately the sliding coefficient of friction, for given operating conditions, if the values of μ_{bl} and μ_{EHD} are known for each lubricant, its operating temperature, and a large range of operating speeds. The values presented in Table 5.10 also indicate that μ_{bl} and μ_{EHD} decrease when the temperature increases, as predicted by Brandão [63, 182].

Once again, the μ_{bl} and μ_{EHD} values seem to be reference values of the SKF model which should not be looked in the same way as the values measured on a ball-on-disc or other similar device.

5.5. Tests performed at 80 °C and 7000 N

5.5.1. TBB 51107

The rolling bearing tests were carried under constant temperature and the measured friction torque is presented in Figure 5.7(a), for a TBB carrying an axial load of 7000 N. The total friction torque measured increases when speed increases, but at different rates depending on the oil formulation.

Comparing the friction behaviour of the wind turbine gear oils, inside the thrust ball bearing, it is very clear that MINR oil always produced the highest values of the total friction torque, while oil MINE always generated the lowest corresponding

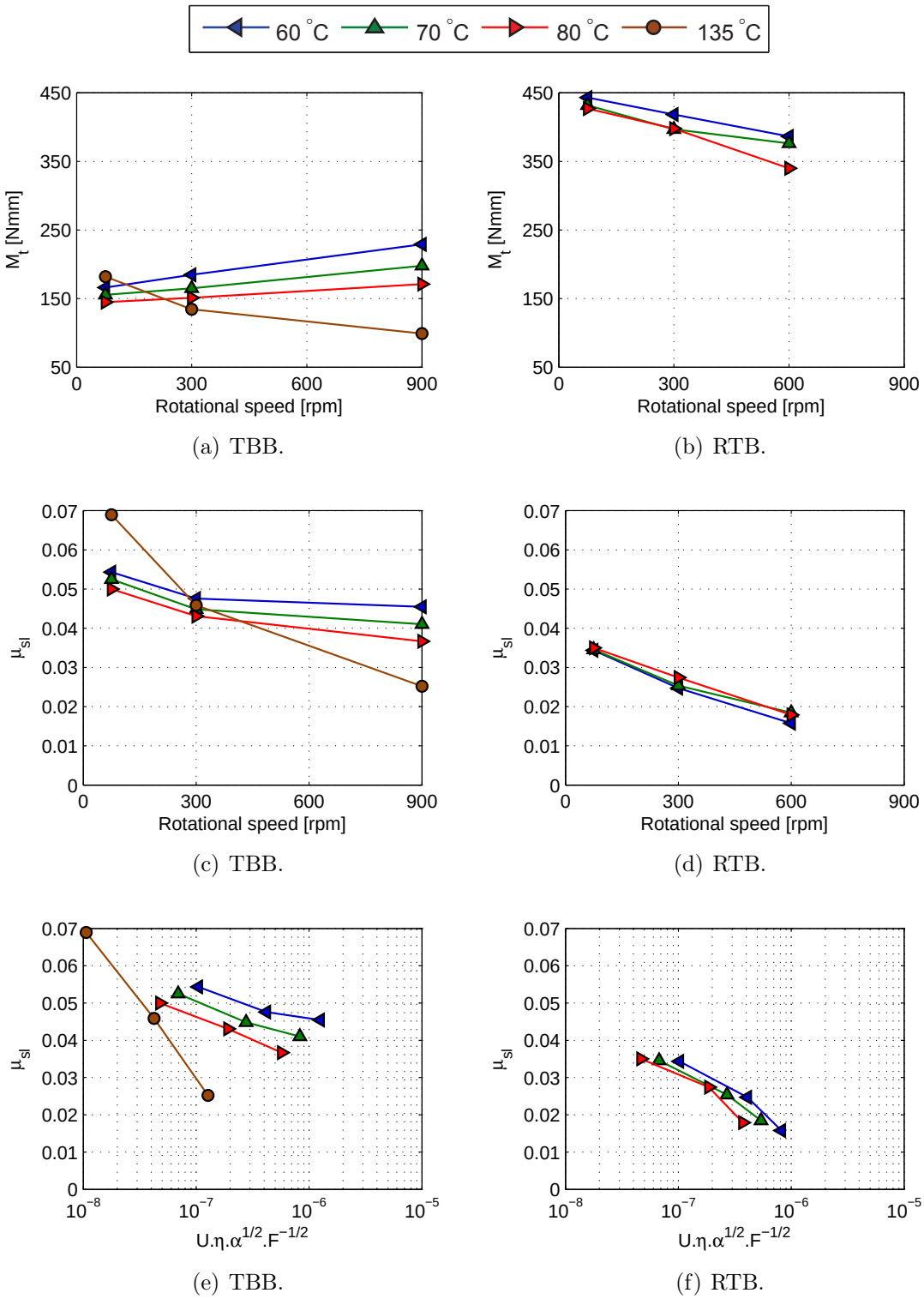

(a) TBB. (b) RTB.

(c) TBB. (d) RTB.

(e) TBB. (f) RTB.

Figure 5.6.: Total friction torque (M_t) and sliding coefficient of friction (μ_{sl}) of a TBB and RTB rolling bearings under constant temperatures and an axial load of 7000 N.

Table 5.10.: Reference values of coefficient of friction, μ_{bl} and μ_{EHD} determined for the calibration tests with PAOR.

	Valid for:	3262.5<n·d_m<39150	3262.5<n·d_m<26100
		Bearing type	
Temperature [°C]	Parameter	TBB	RTB
60	μ_{bl}	0.059	0.044
	μ_{EHD}	0.046	0.016
70	μ_{bl}	0.055	0.046
	μ_{EHD}	0.042	0.015
80	μ_{bl}	0.052	0.043
	μ_{EHD}	0.037	0.014

values (see Figure 5.7(a)). Oils ESTR and PAOR were placed in between of the previous two. PAGD oil exhibited similar values to the ESTR and PAOR at low speed, but it generated the highest friction torques at 900 rpm and above, due to its much higher viscosity at 80 °C.

The rolling torque, presented in Figure 5.7(c), increases with increasing rotational speeds. Analysing the influence of the different oil formulations, the PAGD, with the highest operating viscosity, generated the highest rolling torques, while MINR, with the lowest viscosity, generated the lowest rolling torques.

The sliding torque is presented in Figure 5.7(d). The results indicate that in general the sliding torque decreases slightly with increasing rotational speeds. Such behaviour was expected since for a constant operating temperature the specific film thickness increases with increasing rotational speed, as shown in Figure 5.7(b).

The total friction torque of a TBB 51107 under free temperature conditions was also measured and the results are presented in Appendix G, Figure G.1.

5.5.2. RTB 81107

The measured total friction torque inside a cylindrical roller thrust bearing (RTB 81107), under an axial load of 7000N, is presented in Figure 5.8(a). It is very clear that MINR oil always produced the highest values of the total friction torque above 600 rpm, while PAGD oil always generated the lowest corresponding values below 600 rpm. The much higher kinematic viscosity of PAGD, combined with a typical low coefficient of friction of PAG's resulted in lower total friction torque. Figure 5.8(b) shows that PAGD has a slightly higher specific film thickness for all speed

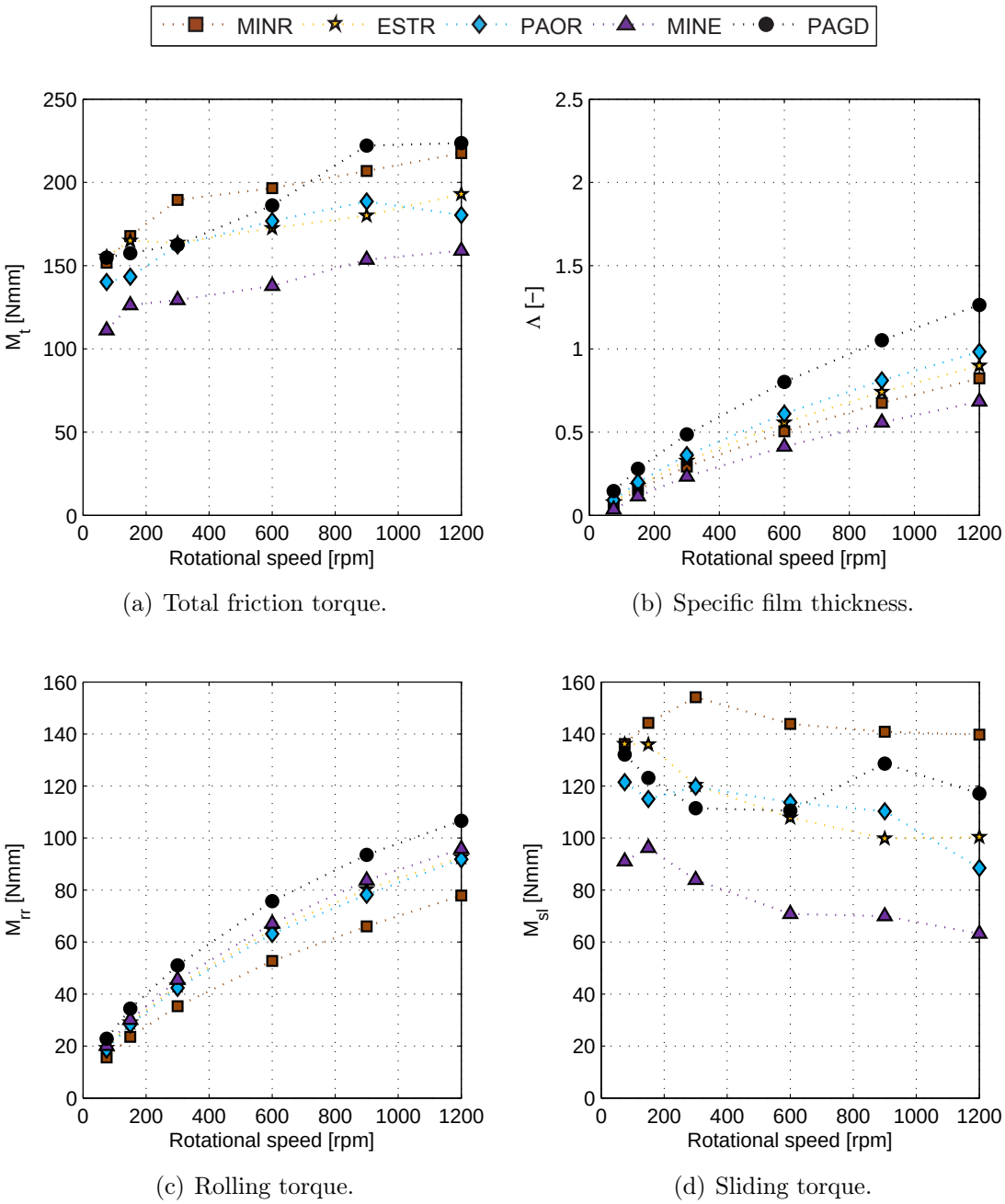

(a) Total friction torque.

(b) Specific film thickness.

(c) Rolling torque.

(d) Sliding torque.

Figure 5.7.: TBB 51107 lubricated at constant temperature of 80 °C with an axial load of 7000 N.

range. Thus, when the speed increases, PAGD generates the highest rolling torque, as shown in Figure 5.8(c).

The sliding torque is presented in Figure 5.8(d). When the rotational speed increases, the sliding torque decreases, which is expected since the sliding torque is dependent on the coefficient of friction, which for mixed film condition should

decrease with increasing Λ, as presented in Figure 5.8(b).

It is very interesting toi observe that the reduction of the sliding torque with increasing speeds, is much more significant in a RTB than in a TBB, as may be noticed comparing Figures 5.8(d) and 5.7(d).

Under constant temperature (80 °C) and constant load (7000 N) the total friction torque decreases when the speed increases, for the case of RTB, while the opposite is observed for a TBB.

The reason for the opposite behaviours of RTB and TBB can be understood with the torque loss model: when the speed increases the sliding torque shows a small reduction in the case of TBB and a very significant reduction in the case ot RTB. For example, in a TBB, lubricated with MINR, the sliding torque is almost constant ($\approx$ 150 Nmm) while in a RTB it decreases from 400 to 200 Nmm when the speed increases from 75 rpm to 1200 rpm, with the same oil.

The same rolling bearing was tested under self-induced temperature and the experimental results are presented in Appendix G, Figure G.2.

5.5.3. Sliding coefficient of friction

Using equation 5.18 and the same procedure described in section 5.4.1, the experimental torque loss (M_t^{exp}) was used to calculate the corresponding sliding coefficient of friction μ_{sl}^{exp}, which is presented in Figure 5.9, both for TBB and RTB, under an operating temperature of 80 °C.

The sliding coefficient of friction (μ_{sl}^{exp}) can also be plotted against the modified Stribeck parameter as shown in Figure 5.10, for both types of rolling bearings, TBB and RTB, and for a constant temperature of 80 °C. As expected when the modified Hersey parameter increases the sliding coefficient of friction (μ_{sl}^{exp}) in general decreases.

As in the previous section, μ_{bl} and μ_{EHD} were calculated minimizing the difference between experimental and numerical values of the sliding coefficient of friction. The values of μ_{bl} and μ_{EHD} are presented in Table 5.11. They were obtained for each gear oil formulation and for each type of bearing, under an operating temperature of 80 °C, an axial load of 7000 N, and for a large range of speed (75 rpm up to 1200 rpm). RTB always generated lower boundary film and full-film coefficients of friction than TBB.

The boundary coefficient of friction, μ_{bl}, depends on the gear oil formulation, as shown in Table 5.11. In the case of the TBB the highest values were obtained with the MINR and PAGD formulations, and the lowest values with the PAOR and MINE formulations. Exactly the opposite trend was obtained in the case of the RTB.

The full-film coefficient of friction, μ_{EHD}, also depends on the gear oil formulation and rolling bearing type. For RTB there is a clear difference between the mineral

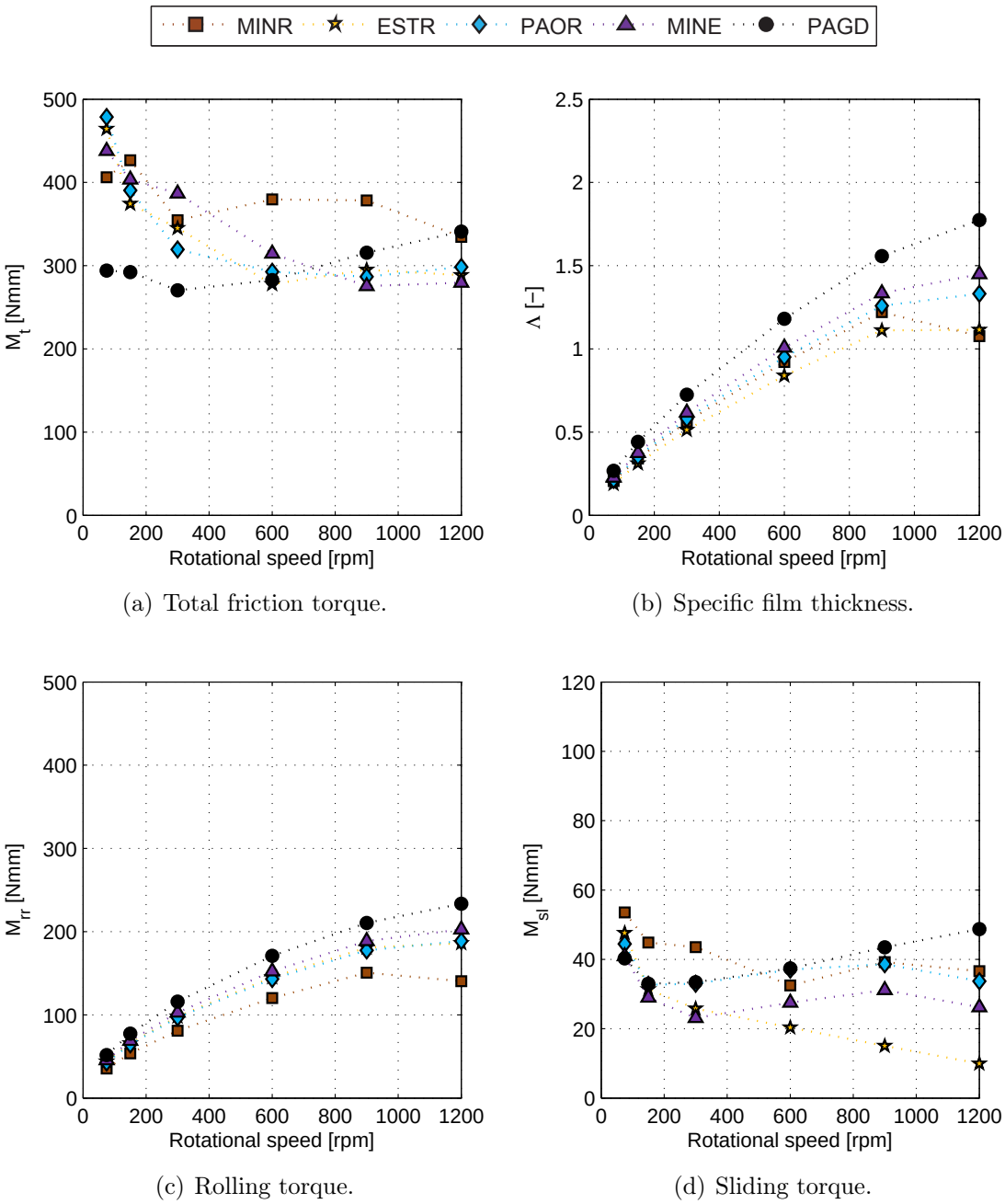

(a) Total friction torque.

(b) Specific film thickness.

(c) Rolling torque.

(d) Sliding torque.

Figure 5.8.: RTB 81107 lubricated at constant temperature of 80 °C with an axial load of 7000 N.

oil (MINR), $\mu_{EHD} = 0.018$, and all the other formulations which have similar μ_{EHD} values, $0.008 \leq \mu_{EHD} \leq 0.010$. In the case of TBB such behaviour of mineral and synthetic formulations is not observed.

In Chapter 2 it was advised that polyalkylene glycol's "provide an especially low coefficient of friction", always lower than PAO's and mineral because its a property

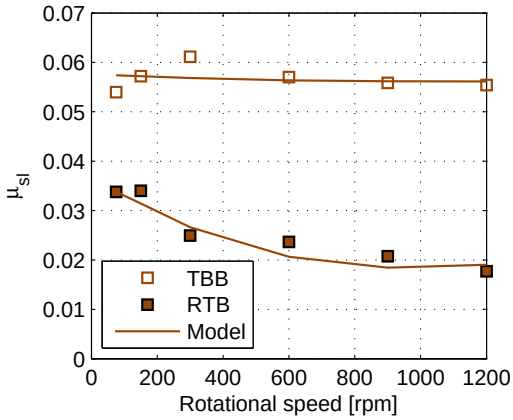

(a) MINR.

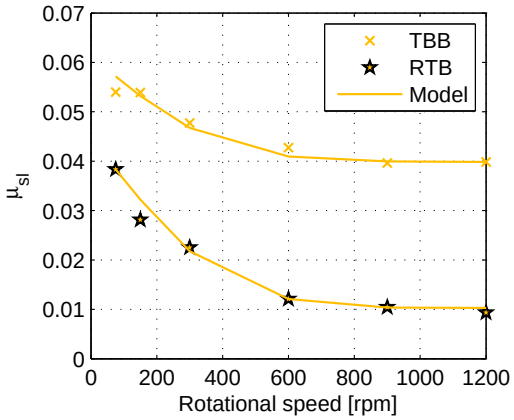

(b) ESTR.

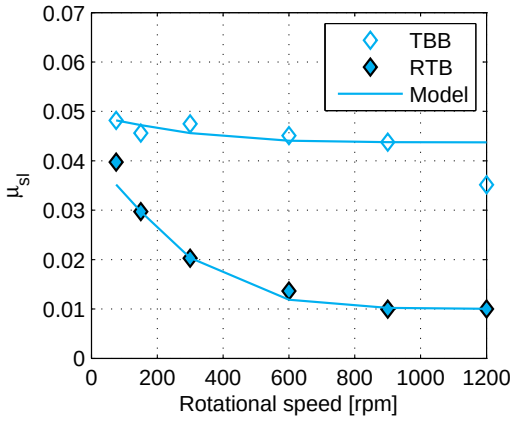

(c) PAOR.

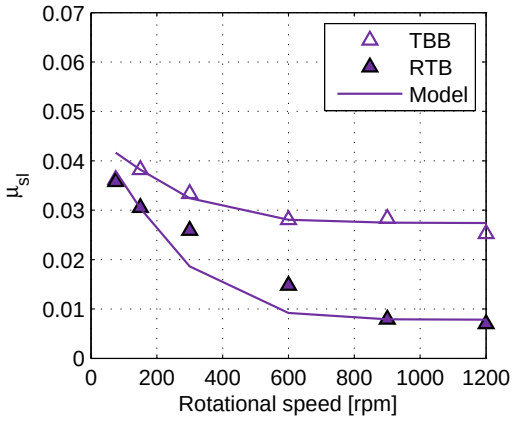

(d) MINE.

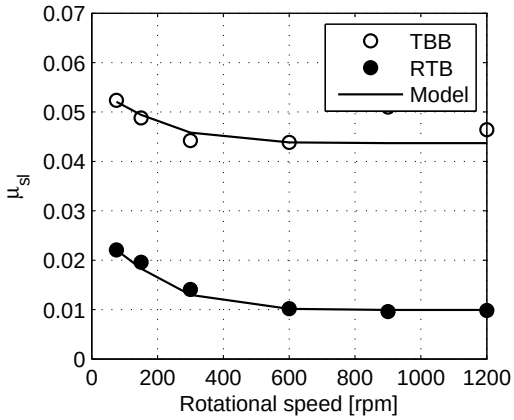

(e) PAGD.

Figure 5.9.: Sliding coefficient of friction against rotational speed for a TBB 51107 and a RTB 81107 and corresponding model simulations with values of Table 5.11 (solid lines).

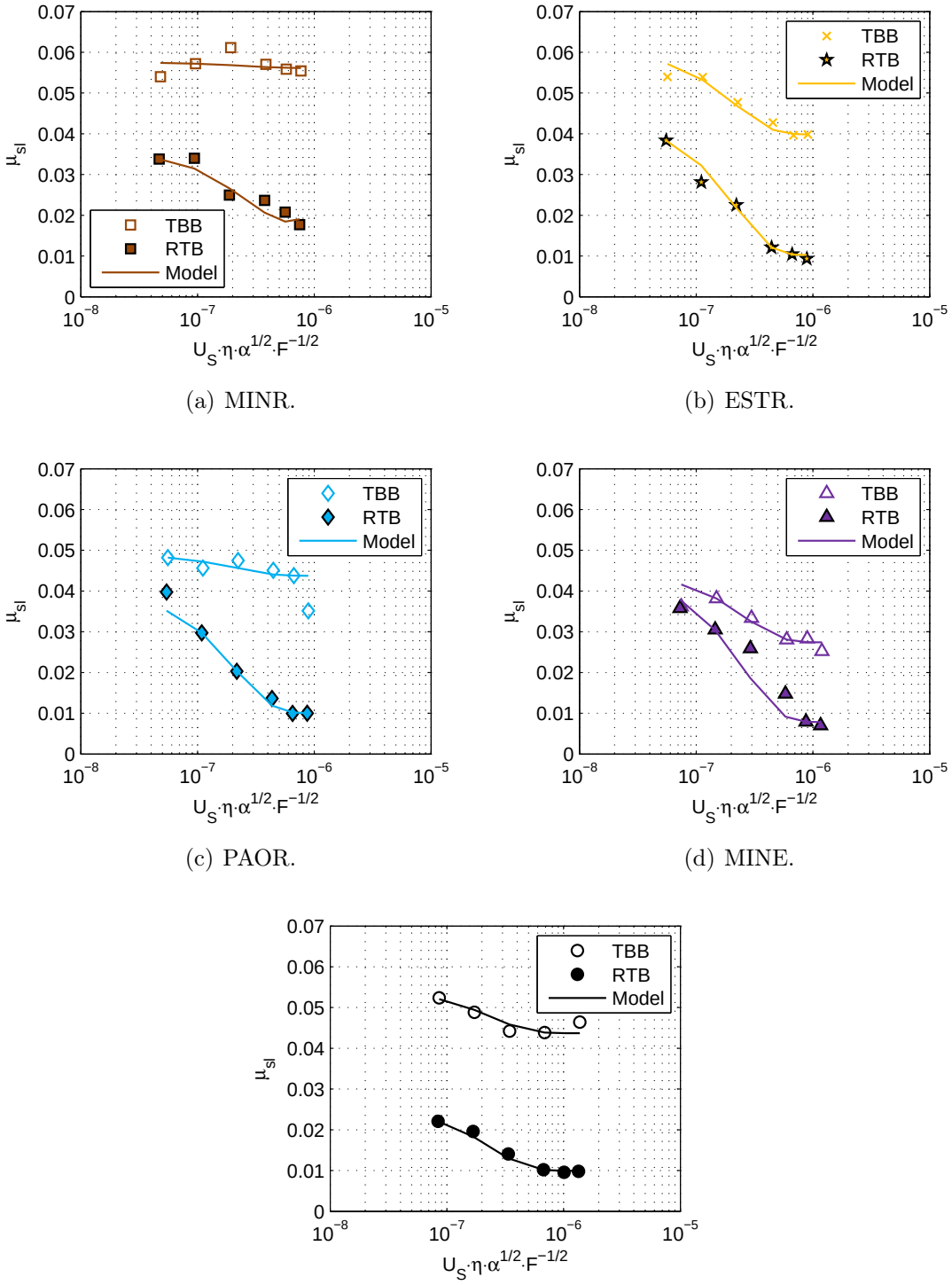

(a) MINR.

(b) ESTR.

(c) PAOR.

(d) MINE.

(e) PAGD.

Figure 5.10.: Sliding coefficient of friction against modified Hersey parameter for the TBB 51107 and RTB 81107 and corresponding model simulations with values of Table 5.11 (solid lines).

Table 5.11.: Coefficient of friction of both TBB and RTB rolling bearings for an operating temperature of 80 °C.

	Valid for:	$3262.5 < n \cdot d_m < 52200$	
		Bearing type	
Oil	Parameter	TBB	RTB
MINR	μ_{bl}	0.058	0.035
	μ_{EHD}	0.056	0.018
ESTR	μ_{bl}	0.060	0.040
	μ_{EHD}	0.043	0.010
PAOR	μ_{bl}	0.049	0.039
	μ_{EHD}	0.044	0.010
MINE	μ_{bl}	0.044	0.044
	μ_{EHD}	0.027	0.008
PAGD	μ_{bl}	0.054	0.025
	μ_{EHD}	0.044	0.010

of the base oil. Such behaviour was not verified in the TBB 51107 measurements which can be related with some grade of incertitude of the SKF model to separate rolling torque and sliding torque components with total accuracy. The accuracy of the model can be a possible reason, but since the coefficient of friction don't represent a measured value, and other sources like rolling torque contributes to the total friction torque, the actual performance of the oil is that measured and defined by the SKF model.

Comparing the influence of the oil formulation, the MINR always generated the highest coefficient of friction which is agreement with the data presented in Chapter 3. The coefficient of friction of both ESTR and PAOR were also similar in the traction coefficient measurements which can be verified with the results presented here (see Figure 5.11). The relative comparison of the oils performance is similar to that verified in the ball-on-disc tests. However, the absolute value determined here should not be compared with the results measured on ball-on-disc tests because the coefficient of friction of SKF model is a reference value of the model which don't represent the actual measured coefficient of friction. Moreover, the bearing geometry is more complex than that used on a simple contact as ball-on-disc shown in Chapter 3.

The geometric influence on the SKF friction torque model is not included in

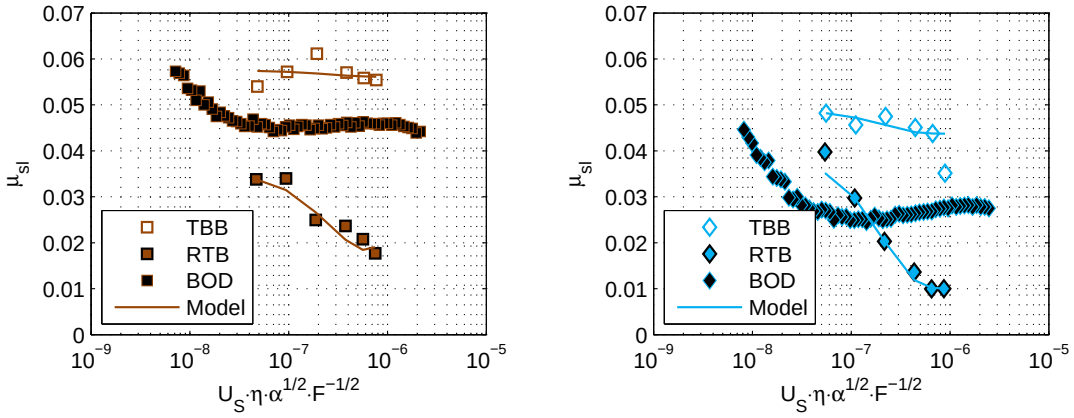

(a) MINR. (b) PAOR.

Figure 5.11.: Sliding coefficient of friction for the TBB 51107 and RTB 81107 and Ball-on-Disc measurements against modified Hersey parameter.

the coefficient of friction value while in ball-on-disc measurements the measured coefficient of friction actually represents also the geometry. Such fact, explains the difference in the absolute value of ball-on-disc measurements and trust ball bearing sliding coefficient of friction. Further investigation is necessary to isolate the influence of the oil from the influence of the geometry on a ball-on-disc experiment. Thus, it is necessary to verify if the values can be related to those found in rolling bearings.

5.5.4. Model validation

The minimization of the differences between μ_{sl}^{exp} and μ_{sl}, allowed the calibration of the coefficient of friction in full-film and boundary conditions, as presented in Table 5.11.

The total friction torque simulations are presented in Figures 5.9 and 5.10 (solid lines) showed a very good correlation between the experimental sliding coefficient of friction and the values predicted by the model (R^2 >0.90).

In the approach developed, the accuracy of the model relies totally on the minimization of the difference between μ_{sl}^{exp} and μ_{sl}. Although this is not necessarily the best procedure, since $M_{rr}^{'}$ is neglected, it was the best compromise considering the "tools" available.

The experimental results as well as the model predictions are presented in Figure 5.12, for TBB and RTB lubricated with MINR at 80 °C. It is clear that the sliding coefficient of friction calculated with the determined μ_{bl} and μ_{EHD} values of Table 5.11 are very reliable to predict the friction torque of rolling bearings under constant

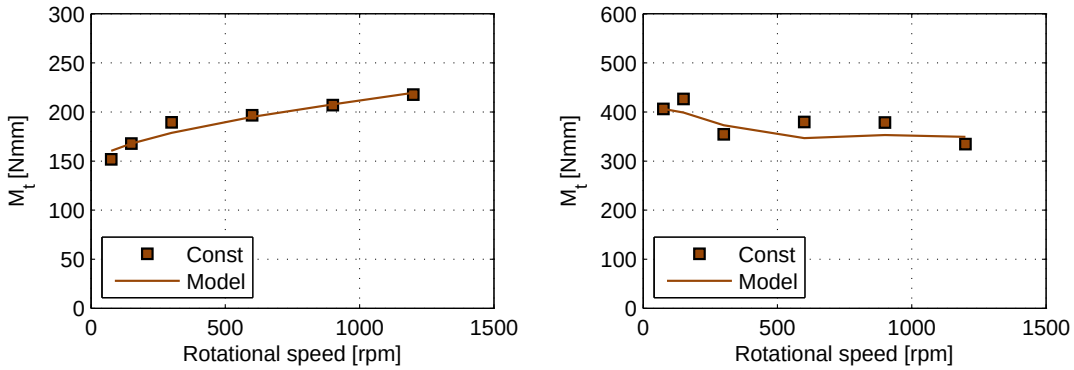

(a) MINR and TBB at 80 °C.

(b) MINR and RTB at 80 °C.

Figure 5.12.: Total friction torque against rotational speed predicted with SKF model for a TBB 51107and a RTB 81107 under 7000 N at 80 °C.

operating temperature.

5.6. Tests performed at 80 °C and 700 N

5.6.1. TBB 51107

The TBB 51107 was also tested under 80 °C and 700 N, a load reduction by 10 times. The total friction torque for a TBB 51107 loaded with 700 N is presented in Figure 5.13(a). The previous results under 7000 N, the oil influence in the total friction torque is similar for all the oils tested except MINE. MINR dissipated the highest power followed by ESTR, PAGD and PAOR. MINE oil seems to show a much better performance as the applied load increases while for lower load presented a performance similar to ESTR.

The total friction torque increased more rapidly with the speed in the previous case. This is caused by the increase of the sliding torque with increasing speed, as shown in Figure 5.13(d). For this lower load, the coefficient of friction is very high with values that do not seem very reasonable, but it should be stressed again that the SKF coefficient friction is a reference value that actually validates the experimental values.

5.6.2. RTB 81107

In the case of RTB 81107 under a load of 700 N, the experimental friction torque increased when speed increased. Comparing the wind turbine gear oils, inside the RTB, it is clear that PAGD oil always generated the highest total friction torque

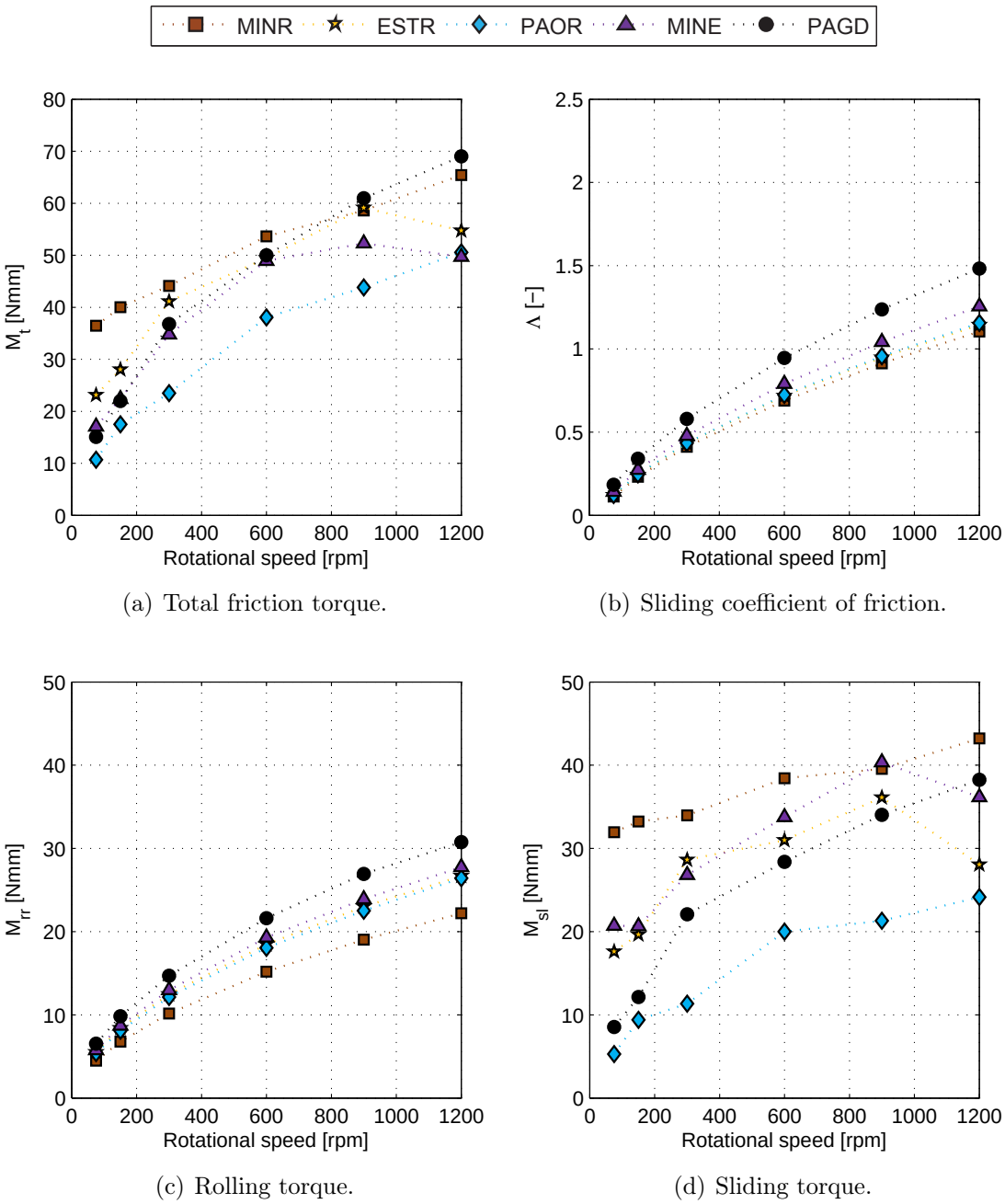

(a) Total friction torque.

(b) Sliding coefficient of friction.

(c) Rolling torque.

(d) Sliding torque.

Figure 5.13.: TBB 51107 lubricated at constant temperature of 80 °C with an axial load of 700 N.

while the other oils produced similar total friction torque, as presented in Figure 5.14(a). The reason for the increase of the friction torque with increasing speed is on the much lower influence of the sliding torque for this level of load. For these particular conditions the influence of the rolling torque is more important as can be observed in Figures 5.14(c) and 5.14(d).

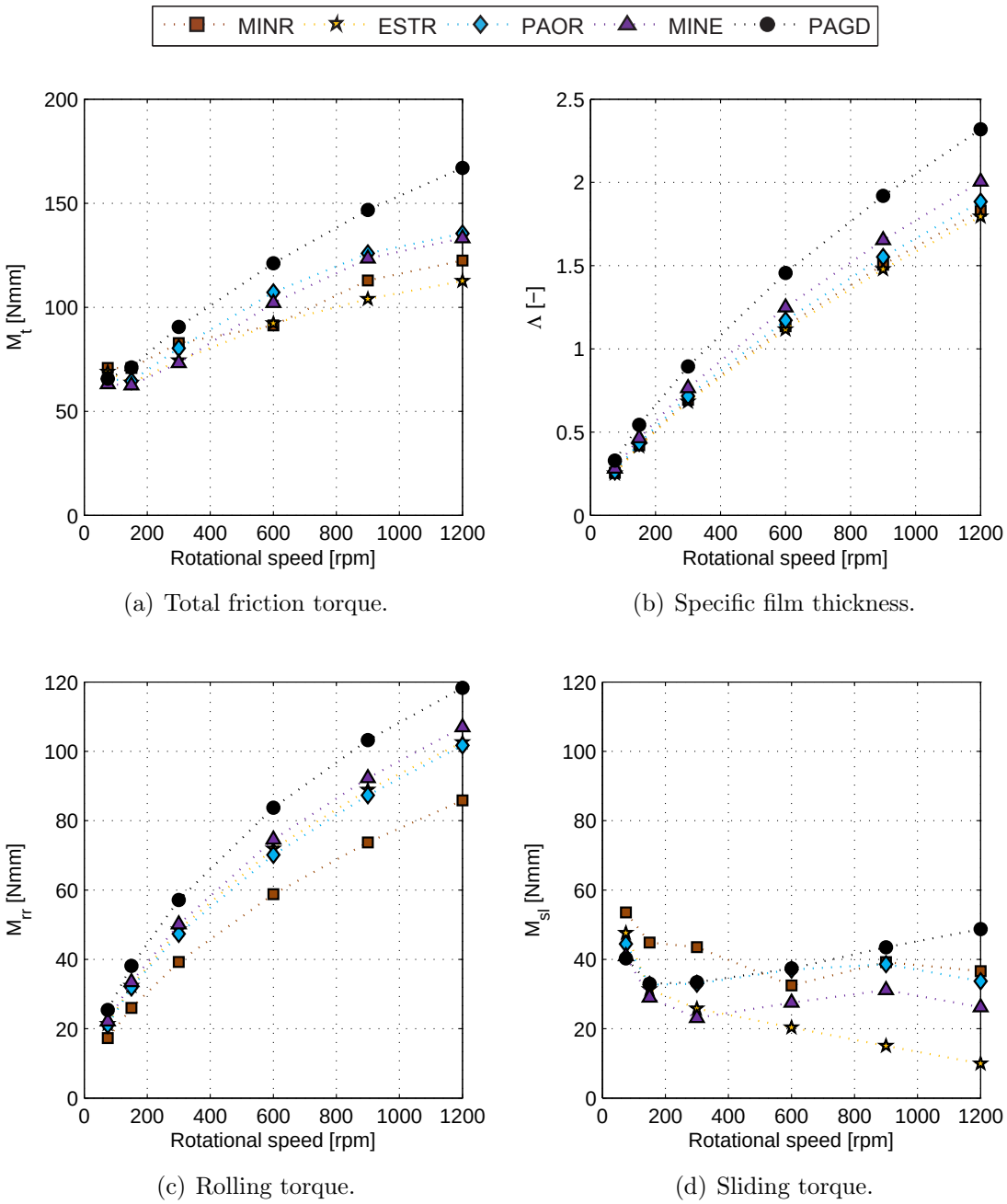

(a) Total friction torque.

(b) Specific film thickness.

(c) Rolling torque.

(d) Sliding torque.

Figure 5.14.: RTB 81107 lubricated at constant temperature of 80 °C with an axial load of 700 N.

5.7. Tests performed under self-induced temperature and 7000 N

Comparing the behaviour of self induced temperature conditions that can be found in Appendix G.2, with the results presented in Figure 5.7(a) for constant

temperature conditions, it can be documented some interesting observations. First, the total friction torque value is higher in the case of self-induced temperature. Second, the friction torque decreases with the rotational speed. This indicates a different influence of the power loss mechanisms, which the model help to understand. In the tests under self-induced temperature, when speed increases, the temperature rises and the rolling torque is approximately constant ($M'_{rr} \propto (n \cdot \nu)^{0.6}$), although always higher than for constant temperature. It is very interesting to observe that between these two types of tests the total friction torque reduces by decreasing the influence of the viscosity on the rolling torque, keeping the dependence on the sliding coefficient of friction the same.

5.7.1. Sliding coefficient of friction

It is interesting to notice that the values of μ_{sl}^{exp} for constant or self-induced temperature conditions are similar, as presented in Figure 5.15. However, the values of self-induced temperature is in many cases, significantly different from 80 °C. Significant differences between constant and self-induced temperature tests were only observed for the TBB lubricated with PAGD gear oil formulation, as shown in Figure 5.15(i).

5.7.2. Model validation

In the case of self-induced temperature conditions the model can predict very well the total friction torque of both TBB and RTB when the operating temperature is not too far way from 80 °C, which is the temperature for which μ_{bl} and μ_{EHD} were determined. For example, the RTB lubricated with MINR under self-induced oil temperature operated at 36.6 °C (see Figure 5.15) and the model is predicting the total friction torque based on reference values at 80 °C. However, the prediction is more accurate than that produced by the original model, as shown in Figure 5.17.

5.8. Prediction of rolling bearings friction torque losses in a FZG gearbox

The values of μ_{bl} and μ_{EHD} (see Table 5.11) and equation 5.20 allow the definition of sliding coefficient of friction for any type of rolling bearing.

$$\mu_{sl} = \phi_{bl} \cdot \mu_{bl} + (1 - \phi_{bl}) \cdot \mu_{EHD} \tag{5.20}$$

In rolling bearings where the races and rolling elements generate elliptic contacts, the values corresponding to the TBB will be used. In the cases where line contacts

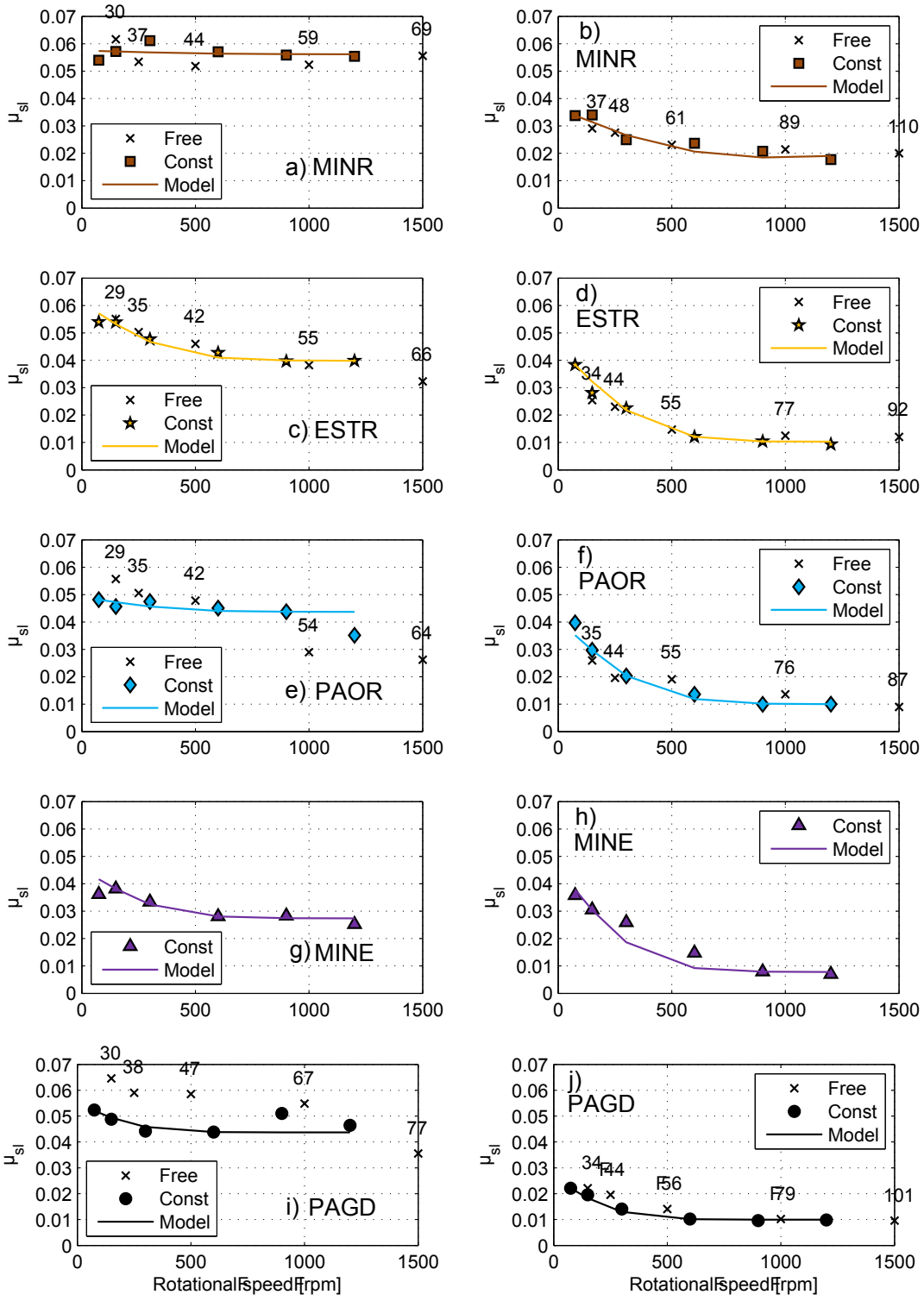

Figure 5.15.: Sliding coefficient of friction against rotational speed for a TBB 51107 (left) and a RTB 81107 (right) - 7000 N.

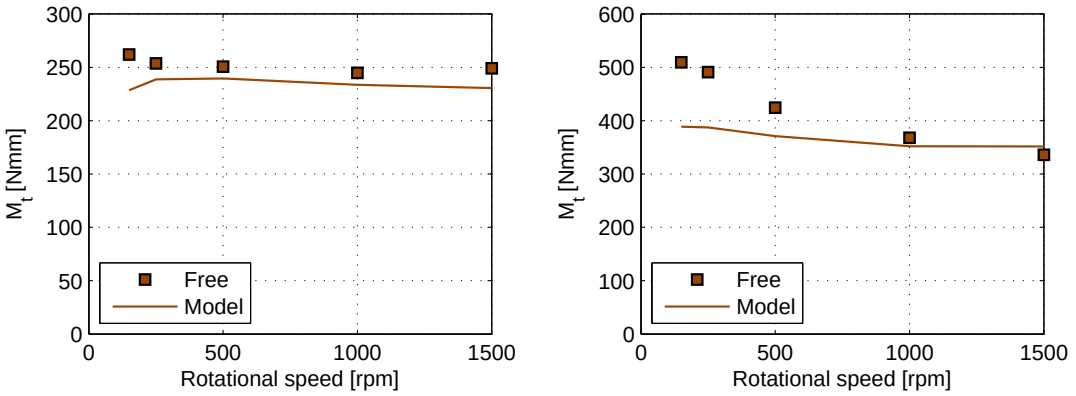

(a) MINR and TBB at self-induced temperature.

(b) MINR and RTB at self-induced temperature.

Figure 5.16.: Total friction torque against rotational speed predicted with SKF model for a TBB 51107and a RTB 81107 under 7000 N under self-induced temperature.

Table 5.12.: Rolling bearings assembled on the slave and test FZG gearboxes.

Gearbox	Rolling bearings
Slave	4 NJ 406 cylindrical roller bearings
Test	2 NJ 406 cylindrical roller bearings + 2 QJ 308 four-point contact ball bearing

are generated the values corresponding to the RTB are considered.

Thus, the torque loss model, may be extrapolated to any type of bearing operating in any type of gearbox. The case of the test gearbox of the FZG machine will be considered as an example .

The FZG machine can test both spur and helical gear geometries. The drive gearbox is mounted with spur gears and cylindrical roller bearings (CRB) and is only prepared to support radial loads. The test gearbox, where both spur and helical gears can be tested, has both cylindrical roller bearings (CRB) and four-point contact ball bearings (FPCB) to balance the axial loads, as presented in Table 5.12.

Using the the torque loss model and the corresponding sliding coefficient of friction determined in section 5.5.3 at 80 °C (see Table 5.11), a simulation was performed for the cylindrical roller bearing and for the four-point contact ball bearing lubricated with each wind turbine gear oil formulation. The equations related to the geometry of the bearings are presented in Appendix F, Table F.1.

This simulation was performed considering the load stage K9 of the FZG machine

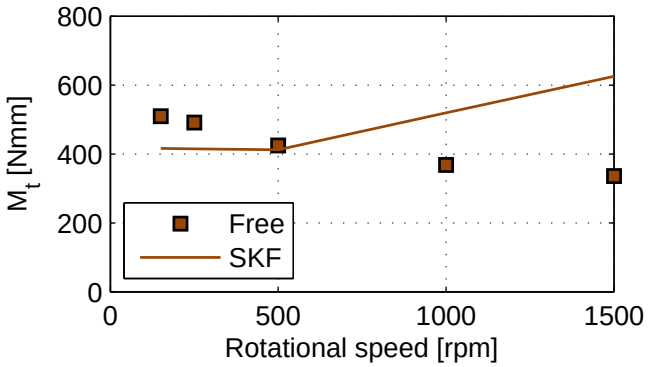

Figure 5.17.: Total friction torque against rotational speed predicted with SKF model for a RTB 81107 under 7000 N under free sump temperature with the original μ_{bl} and μ_{EHD} values.

(load arm length of 0.35 m) corresponding to an applied torque on the wheel of 323 Nm, and oil jet lubrication at 80 °C. In these conditions, the radial load on both rolling bearings (CRB and FPCB) are the same and equal to 2393 N and the axial load on the FPCB is equal to 1594 N. Under these operating conditions and for speeds between 200 rpm and 1800 rpm, the torque loss model together with the μ_{bl} and μ_{EHD} values from Table 5.11, can be used to evaluate the rolling bearing friction torque in each bearing and in the test gearbox, as shown in Figure 5.18.

The four-point contact ball bearing (FPCB) generated higher torque loss (M_t) than the cylindrical roller bearing (CRB) whatever the speed considered. The rolling torque (M'_{rr}) of the FPCB is always lower than the rolling torque generated by the CRB. The major differences are observed on the sliding torque, since the FPCB generates a sliding torque loss that can be up to 20 times higher than the sliding torque generated by CRB.

Regarding the oils, for a constant operating temperature, the MINR promoted the lowest rolling torque for both geometries due to having the lowest viscosity index. At low speed, the four-point contact ball bearing promoted higher torque loss due to the sliding torque contribution, i.e. the sliding torque of that geometry is ten times higher than for a cylindrical roller bearing. Considering the sliding torque, dependent on the coefficient of friction of each oil, the results show a lower value for the mineral oil with viscosity index improver (MINE), while the mineral oil (MINR) promoted the highest torque loss dependent on the coefficient of friction.

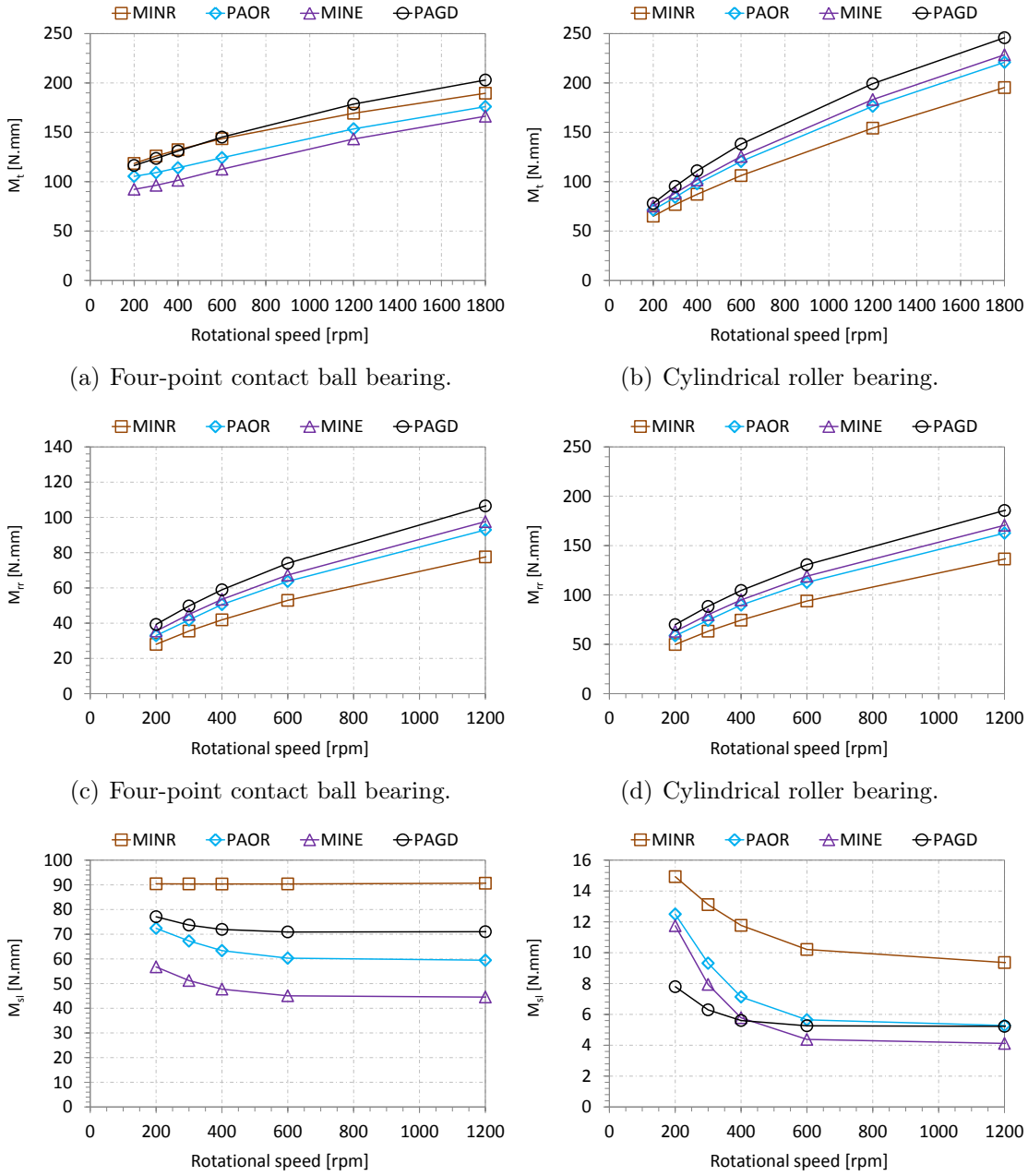

(a) Four-point contact ball bearing.

(b) Cylindrical roller bearing.

(c) Four-point contact ball bearing.

(d) Cylindrical roller bearing.

(e) Four-point contact ball bearing.

(f) Cylindrical roller bearing.

Figure 5.18.: Simulation for torque loss of a rolling bearing of a FZG test gearbox for a load stage K9 (323 Nm) with jet lubrication at 80 °C.

5.9. Closure

Five wind turbine gear oils presented in Chapter 2 were submitted to rolling bearing friction torque measurements.

The experimental results clearly show that the rolling bearing geometry has a great influence in the power loss dissipated. A RTB generated significantly higher friction torque than a TBB. This happens due to the higher energy dissipated in both power loss mechanisms involved, rolling and sliding torque. It is very interesting to note that for the same operating conditions (rotational speed, load and oil properties) a RTB which supports lower contact pressure generates, in some cases, twice the friction torque.

Regarding the performance of each oil formulation, substantial differences were found between oils. The MINR oil always generated the highest friction torque, which is related to its highest sliding coefficient of friction. MINR generated the lowest rolling torque due to lower operating kinematic viscosity.

PAOR and ESTR showed very similar performance, which was also verified in the coefficient of friction measured on a ball-on-disc. These two oils, with very similar kinematic viscosities and consequently similar rolling torque also showed very similar sliding torque for the rolling bearing geometries tested.

The new SKF model was calibrated determining a full-film coefficient of friction (μ_{EHD}) and a boundary film coefficient of friction (μ_{bl}) known for the desired operating temperature and for the gear oil, the friction torque model predicts with high accuracy the friction torque for any type of rolling bearing geometry and operating conditions for each oil formulation.

Chapter 6.

Power loss in FZG gearboxes

6.1. Introduction

In 4th century B.C, Aristotle was the first author to write about gears [183]. The Greeks inventors used gears in water wheels and clocks. However, the involute gear was only proposed by Euler in 1752 [184] and since then, the gears started to be used widely in machines mainly after the invention of the hobbing process patented in 1835 by Whitworth [185].

The first studies of efficiency in gear transmissions were performed by Weisbach [186] and Reuleaux [187] in the 19th century. In the next century, Earl Buckingham [98] measured the power loss in gears and developed formulas to evaluate the friction losses.

Gear tests have been developed to evaluate the capability of candidate blends to avoid the scuffing failure, which was first described in ISO 14635 – part 1 [188] and was recently updated in ISO 14635 – part 3 [189].

FVA suggests the method developed by Doleschel to collect data of efficiency tests on the FZG test rig [190]. However, no standardized method is published by DIN, AGMA or ISO.

Petry-Johnson *et al.* did an experimental investigation of spur gear efficiency with different geometry and different surface finishing [97]. In his work it was shown that lower modules promoted a reduction in the meshing gear power loss. In the same work, he proved that a chemically finished gear had better efficiency than a grounded surface gear.

Yenti *et al.* [191] did an analytical and experimental investigation on the effects of geometry on sliding losses of spur gears. They also showed that decreasing the module can increase the efficiency of a spur gear pair. Additionally, they showed that the pressure angle increase also reduces the meshing gears power loss. The method used to quantify the gearbox power loss was similar to that proposed in Chapter 4. Yenti used the Palmgren model to estimate the rolling bearing losses and concluded that the DIN 3990 coefficient of friction is reliable to predict the

actual gear meshing power loss. The coefficient of friction along the path of contact of gears was discussed in Chapter 4 and several formulas compared .

From the published works it is possible to analyse the influence of the operating conditions on the coefficient of friction. Martins *et al.* showed that the coefficient of friction decreases with increasing rotational speed and increases with increasing load [80]. Naruse showed that the coefficient of friction is insensitive to changes in the surface roughness (R_a) between 0.5 and 3 μm, while Xiao *et al.* suggest that the coefficient of friction is lower for lower surface roughness. However, the Naruse and Xiao works are not tottaly conclusive since they performed only few experimental tests [97].

The experimental results found in literature are usually focused on the general problem of meshing gear power loss, without any particular discussion on commercial available lubricants.

This chapter deals with the measurement of the torque loss in the FZG slave gearbox, lubricated with different wind turbine gear oils. The results allowed to measure the influence of each lubricant on gear efficiency, to characterize the coefficient of friction in meshing gear and, finally, to calculate the power loss in the meshing gear.

6.2. Materials and methods

6.2.1. Test rig

Figure 6.1(a) presents the scheme of the FZG test machine used to test gears. It performs a wide range of standard gear tests such as: scuffing [188, 189, 192, 193], pitting [194] and micropitting [195, 196]. The FZG machine is a gear test rig with circulating power due to a static torque applied [197]. The test pinion (1) and wheel (2) are connected by two shafts to the drive gearbox (3). The shaft connected to test pinion (1) is divided into two parts connected by the load clutch (4). One half of the clutch can be fixed with the locking pin (5), whereas the other can be twisted using the load lever and different weights (6).

The maximum speed of the AC-motor is 3000 rpm. The tests can be performed using dip lubrication or oil jet lubrication. For dip lubrication the oil can be heated using the electrical heaters mounted in the test gearbox. The heater and cooling coil allow the settling of a constant oil temperature measured by the temperature sensor (8). Under oil jet lubrication conditions, the oil is in a reservoir with heaters that can increase the temperature of the oil up to the desired value. After that, the temperature is controlled by the feedback of the temperature sensor in the tube of the reservoir. The reservoir includes an oil pump to put the oil into circulation to the gearboxes and it is possible to select the oil flow.

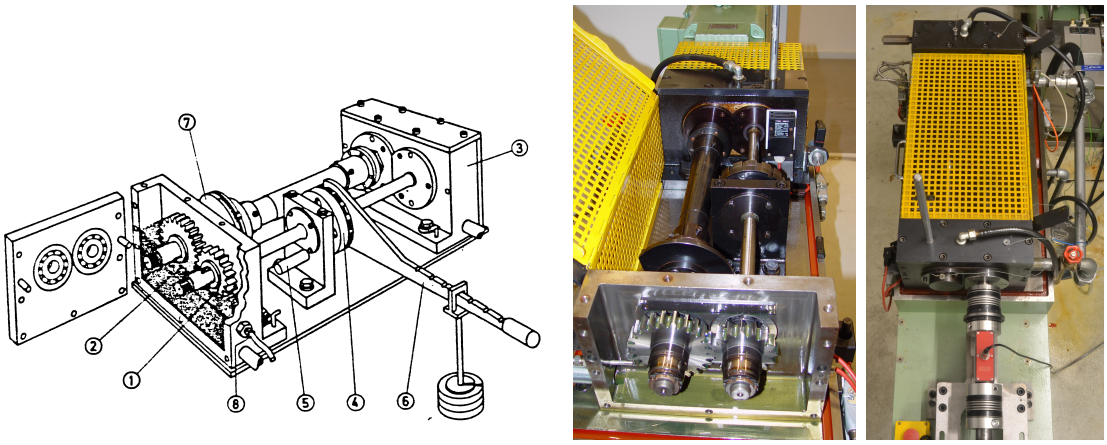

(a) Schematic view. (b) Gears detail. (c) Torque cell.

Figure 6.1.: FZG gear test rig.

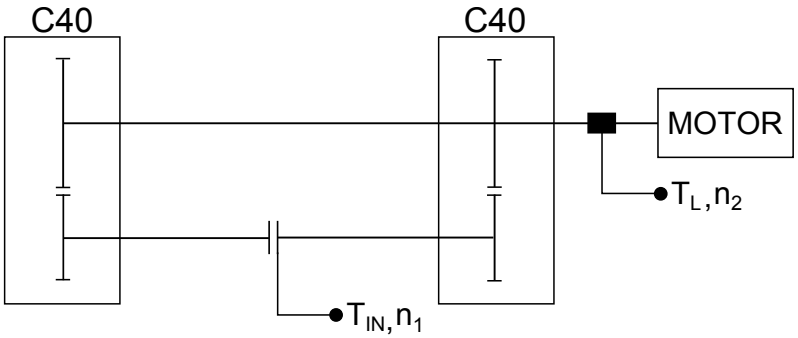

Figure 6.2.: Schematic view of the FZG gear test rig with the torque measuring system.

The torque loss (T_L) is measured using an ETH Messtechnik DRDL II torque transducer assembled on FZG test machine, as shown in Figures 6.1(c) and 6.2. The static torque is applied on the pinion (T_{IN}) which results in a static torque on the wheel according to equation (6.1).

$$T_W = i \cdot T_{IN} \tag{6.1}$$

The technical characteristics of the sensor are displayed in Table 6.1. The system uses a sensor interface Valuemaster$_{Base}$ to communicate with a PC or Notebook with a Ethernet connection with technical specifications detailed in Table 6.2. The integration of the torque cell with the software allows to record the torque values with an adjustable sampling rate (from 1 to 1000 Hz).

The operating temperatures in eight different points of the assembly were also measured, using Type K thermocouples. The temperatures were recorded during

Table 6.1.: Technical specifications of the ETH DRDL torque cell.

Torque Transducer Type DRDL	
Nominal torque [Nm]	50
Measurement range [Nm]	5/10/20/50
Non-linearity [%]	< 0.1
Hysteresis [%]	< 0.1
Accuracy [%]	0.01
Temperature sensitivity [%/°K]	0.01

Table 6.2.: Technical specifications of the torque measuring module.

Torque Measuring Module Type ValueMaster$_{Base}$	
Accuracy [%]	0.02
Non-linearity [%]	0.1
AD converter resolution	11 bit + 1 bit for leading sign

each test using a software and a sampling rate of 1 Hz.

The standard FZG machine is not equipped to measure the torque loss. To do that, some modifications were introduced in the machine to accommodate the torque sensor as well as the coupling of the shafts. The drawings of the modifications are included in Appendix H.

6.2.2. Gears

The torque loss tests performed in this test campaign used type C gears with face width of 40 mm, usually assembled on FZG drive or slave gearboxes. Table 6.3 displays the main geometric properties of the C40 gear set, shown in Figure 6.3.

The same C40 gear set was used for testing all the lubricants. To assure that a similar surface finish was used with all lubricants, the C40 gear was run-in during 48 hours under dip lubrication with a PAO ISO VG 150 gear oil.

The surface roughness was evaluated before and after the run-in period and in the end of the test campaign. Figures 6.4(a) and 6.4(b) display tooth flank profiles measured before run-in, after run-in and at the end of test campaign, in the axial and radial direction, respectively. The surface roughness in the radial direction is considerably larger than that in the axial direction due to the grinding procedure (axial direction, as presented in Table 6.4).

The FZG gears used in this work had worst surface finishing than those proposed

Table 6.3.: Geometric properties of the C40 spur gears.

Property	Symbol	Units	Pinion	Wheel
Number of teeth	z	[-]	16	24
Module	m	[mm]	4.5	
Axis distance	a	[mm]	91.5	
Pressure angle	α_z	[°C]	20	
Working pressure angle	α_{ztw}	[°C]	22.44	
Face width	b	[mm]	40	
Addendum modification coefficients	x_z	[-]	+0.1817	+0.1715
Reference diameter	d	[mm]	72	108
Working pitch diameter	d'	[mm]	82.64	118.54
Tip diameter	d_a	[mm]	82.46	118.36
Base diameter	d_b	[mm]	67.66	101.49
Transverse contact ratio	ϵ_α	[-]	1.44	
Length of path of contact	g_α	[-]	19.099	
Material		[-]	20MnCr5	

by the standards for a Type C micropitting gear with 14 mm width [195–197].

During the test campaign the surface roughness was not measured between oil change in order to avoid assembly variances that are also described in literature as a possible cause of poor repeatability [198].

Since it is of major importance to compare and to score each oil formulation, as well as calibrate the FZG slave gearbox and also the power loss model, the assembly variable was not considered.

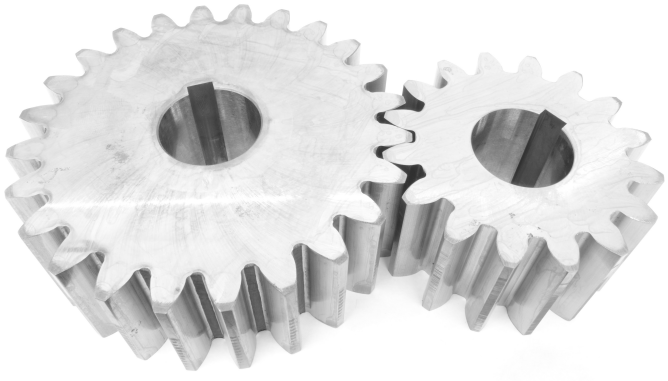

Figure 6.3.: C40 spur gear geometry.

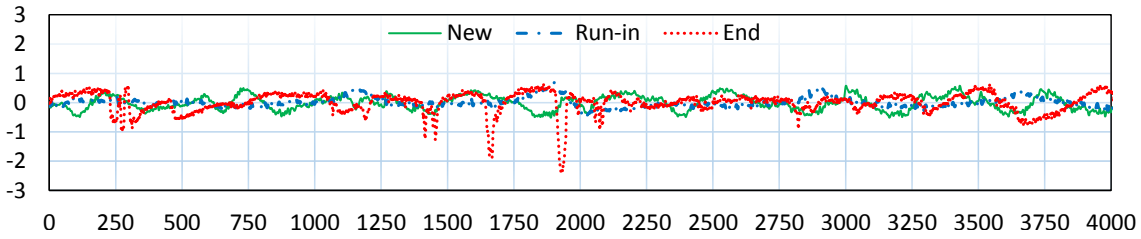

(a) Axial roughness.

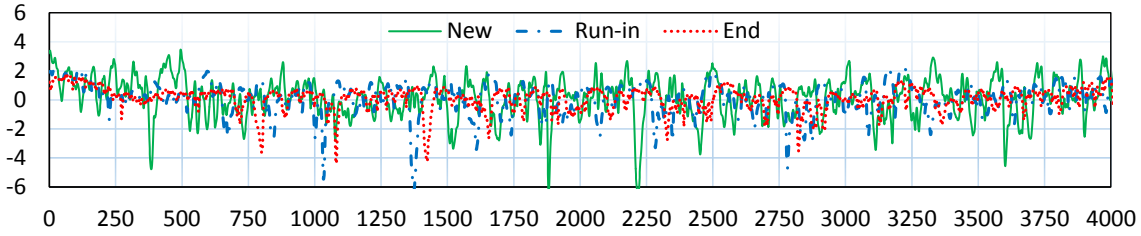

(b) Radial roughness.

Figure 6.4.: C40 pinion absolute average roughness (R_a) in radial and axial directions.

6.2.3. Rolling bearings and seals

The shafts on the test and slave gearbox are supported with cylindrical roller bearings (NJ 406). The rolling bearings have a dynamic load capacity of C=60.5 kN and a static load capacity of C_0=53 kN.

The gearboxes are sealed with four Viton lip seals with an internal diameter of d_{sh}=30 mm. A Viton lip seal is also assembled on the drive gearbox motor shaft (d_{sh}=26 mm).

6.3. Test conditions

The gear load and speed were selected to meet the usual operating conditions of a wind turbine gearbox.

The rotational and tangential speed of each gear mesh of a real wind turbine gearbox are presented in Table 6.5. The tests were designed to have similar tangential speed of the first and second stages, i.e. from 1 to 6 m/s. The third stage was disregarded since it generates low gear power loss due to the low torque transmitted at very high tangential speed. The load conditions produced by a 1.2 MNm torque applied to the input shaft, produced the maximum Hertz pressures presented in Table 6.5.

The operating conditions of the real wind turbine gearbox were used as a reference for the test conditions selected for the FZG gear tests, presented in Table 6.6 (load arm of 0.35 m). It is interesting to notice that the rotational speeds used, 200 rpm

Table 6.4.: Roughness parameters of the C40 spur gear before run-in, after run-in and in the end of the test campaign.

Condition	Element	Direction	R_a	R_q	R_z	R_{max}
New	Pinion	Axial	0.3	0.3	1.5	1.9
		Radial	1.1	1.4	7.8	9.4
	Wheel	Axial	0.2	0.3	1.1	1.9
		Radial	0.8	1.1	4.9	6
Run-in	Pinion	Axial	0.4	0.5	2.5	3.3
		Radial	1	1.3	5.8	8.4
	Wheel	Axial	0.3	0.3	1.8	2.3
		Radial	0.7	0.9	4.5	5.7
End	Pinion	Axial	0.3	0.5	2.5	5.3
		Radial	0.6	0.8	4.3	5.6
	Wheel	Axial	0.1	0.2	1.0	1.9
		Radial	0.5	0.6	3.2	3.9

up to 1200 rpm, simulate very well the operating conditions of stages 1 and 2 of the wind turbine gearbox. Load stages K9 and K7 simulate the Sun/Planet and Planet/Ring contacts, respectively. Load stage K5 is similar to the contact pressure occurring in stage 3 of the wind turbine gearbox.

6.4. Test procedure

The operating conditions used in the torque loss tests are displayed in Table 6.6. The tangential force transmitted by the gears, the radial forces on the rolling

Table 6.5.: Rotational and tangential speed on the gear mesh of a wind turbine gearbox for an input speed of 20 rpm.

		Stage 1		Stage 2		Stage 3
Property	Unit	S/P	P/R	S/P	P/R	P/W
n	[rpm]	111.4	34.9	610.4	190.6	610.4
v_t	[m/s]	1.867	0.974	6.302	3.251	24.933
p_0	[MPa]	1028	699	921	624	567

(S/P – Sun/Planet, P/R – Planet/Ring, P/W – Pinion/Wheel)

Table 6.6.: Operating conditions regarding the torque loss tests.
(load stages with a load lever arm of 0.35 m)

	Gears			Rolling bearings
K_{FZG}	T_W [Nm]	F_{bn} [N]	p_H [MPa]	F_r [N]
K1	4.95	98	111	37
K5	104.97	2069	511	790
K7	198.68	3915	704	1495
K9	323.27	6371	898	2432

bearings and the Hertz pressure in the gears are also included. The oil jet flow was set to 3 l/min at a temperature of 80 ° C.

The test procedure can be summarized as follows:

1. Run load stage Ki and each rotating speed (see Table 6.6) during 3h according to test sequence presented in Figure 6.5.
   - Register the assembly working temperatures;
   - Continuous torque measurement with a sample rate of 1 measurement per second;
2. Repeat procedure till the highest load stage is reached.

The values presented for torque loss and temperature are the average of the last 30 minutes of operation, i.e. only the steady state operating conditions are considered for the average calculation (see Figure 6.6). Between each oil tested the gearboxes were flushed with solvent. The oil reservoir and the injection system are completely drained and cleaned with a solvent (the solvent used depends on the oil base).

In order to be simplify the flushing process, the oils were tested in the following order: PAO 150, MINR, MINE, PAOR, ESTR and PAGD. The PAO 150 is usually used to lubricate the slave gearbox in micropitting and scuffing tests and it is interesting to measure the torque loss associated with this gear oil.

6.5. Film thickness on meshing gears

The centre film thickness in the gears contact was determined using the Dowson and Higginson [24] equation for linear contacts (6.2).

$$h_0 = 1.95 \cdot R_X \cdot U^{0.727} \cdot G^{0.727} \cdot W^{-0.091} \tag{6.2}$$

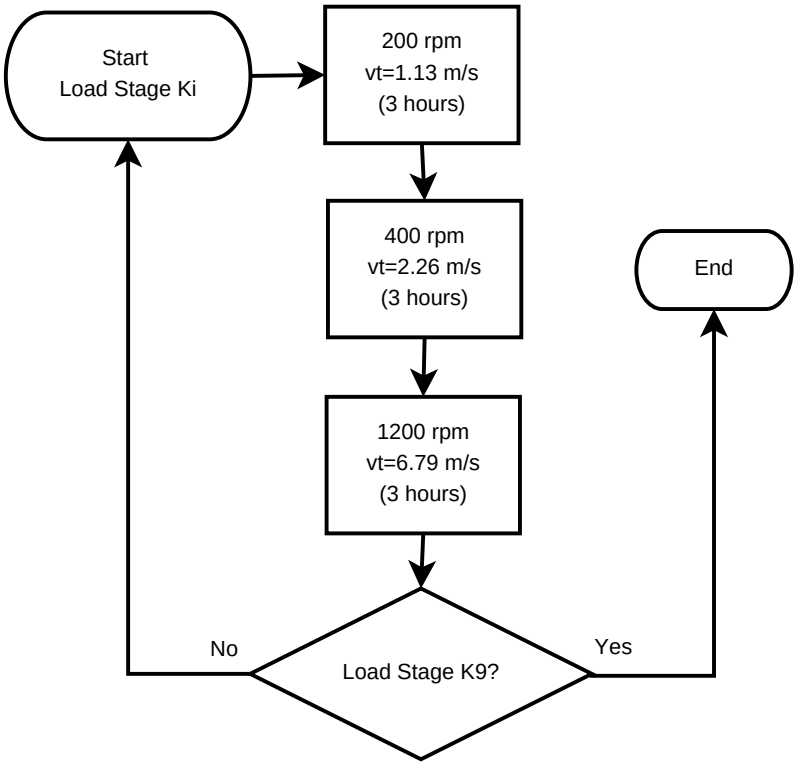

Figure 6.5.: Test procedure sequence.

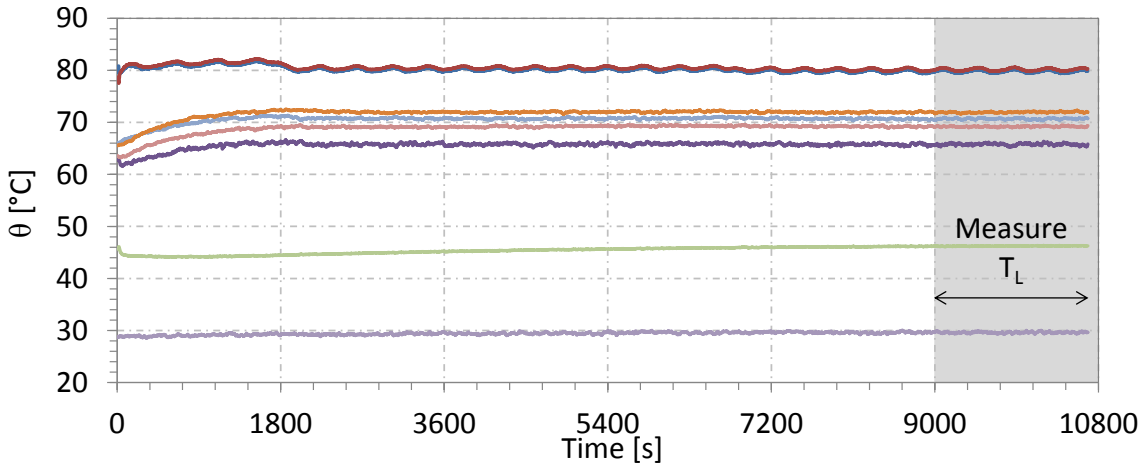

Figure 6.6.: Temperatures behaviour on the test machine during the test.

The parameters U, G and W are detailed in Appendix B.

The theoretical film thickness was calculated at each point of the line of action.

The theoretical film thickness h_0 was then corrected using the thermal reduction factor (ϕ_T, see equations (5.8) and (5.9)) due to inlet shear heating, as shown in equation (6.3).

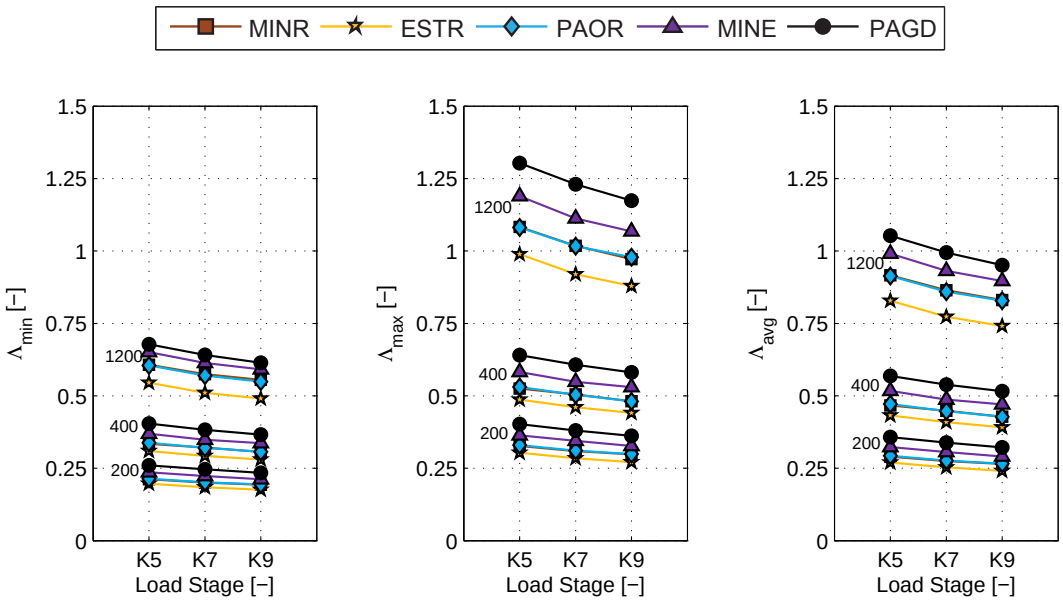

(a) Λ_{min} at beginning of contact.

(b) Λ_{max} at pitch point.

(c) Average specific film thickness Λ_{avg}.

Figure 6.7.: Specific film thickness for each test condition calculated using Gold's constants.

$$h_{0C} = \phi_T \cdot h_0 \tag{6.3}$$

The specific film thickness was calculated with equation (6.4), taking into account the composite roughness of the contact with the values after run-in presented in Table 6.4.

$$\Lambda = \frac{h_{0C}}{\sqrt{R_{a1}^2 + R_{a2}^2}} \tag{6.4}$$

The specific film thickness for each test condition is displayed in Figure 6.7. Figure 6.7(a) shows the minimum film thickness corresponding to the beginning of the contact (point A) while Figure 6.7(b) shows the maximum specific film thickness along the path of contact (pitch point). The average value of the specific film thickness along the path of contact is presented in Figure 6.7(c).

The small differences between oils are due to the operating viscosity, but those differences are not enough to promote a different lubrication regime for the same test condition.

Along the path of contact it is interesting to note that at 1200 rpm the point A is close to boundary lubrication while the pitch point is under mixed lubrication because $\Lambda > 0.7$.

Table 6.7.: Temperature of oil [°C] leaving the test gearbox.

n_2	K_{FZG}	MINR	ESTR	PAOR	MINE	PAGD
200	K1	77.2	78.2	79.6	77.6	79.2
	K5	77.3	77.5	79.2	77.8	78.3
	K7	77.7	78.1	79.5	77.7	78.5
	K9	77.7	78.2	78.9	78.1	78.4
400	K1	78.6	77.8	79.2	78.0	79.0
	K5	78.9	78.1	79.0	78.0	79.2
	K7	78.5	78.4	78.8	78.5	78.9
	K9	78.4	78.8	78.9	78.7	79.0
1200	K1	80.4	79.6	79.9	79.5	79.7
	K5	80.5	79.9	80.1	79.7	79.6
	K7	81.8	81.0	80.5	81.2	80.1
	K9	83.9	82.2	80.7	82.1	80.9

6.6. Results and discussion

6.6.1. Temperatures

The temperature of the oil leaving the test gearbox is displayed in Table 6.7 for all oils and test conditions. These results show that the increase in speed promotes an higher increase of temperature than an increase of load.

It is also interesting to observe the stabilization temperature of the test rig base plate ($\vartheta_{stab,base}$), that is calculated according to equation (6.5).

$$\vartheta_{stab,base} = \theta_{base} - \theta_{\infty} \tag{6.5}$$

It was observed that for the same operating conditions, the difference between the maximum and the minimum stabilization temperature is quite small, usually less than 1 °C, whatever the lubricating oil considered.

6.6.2. Total torque loss

Table 6.8 displays the total torque loss (T_L) measurements of the test and slave gearboxes, for all the lubricants and test conditions.

Figure 6.8(a) displays the torque loss measured for load stage K1 at the input speeds of 200, 400 and 1200 rpm. These test conditions were performed to gather knowledge about the torque loss for a no-load condition, i.e. the total torque loss is

Table 6.8.: Total torque loss [Nm] for each test condition.

n_2	K_{FZG}	MINR	MINE	ESTR	PAOR	PAGD
200	K1	1.16	1.24	1.24	1.22	1.38
	K5	3.72	2.97	3.14	3.12	3.08
	K7	5.92	5.32	4.85	5.08	4.70
	K9	8.88	8.08	7.56	7.73	7.00
400	K1	1.50	1.56	1.53	1.37	1.73
	K5	3.77	3.14	3.30	3.23	3.33
	K7	5.75	5.27	4.85	4.95	4.79
	K9	8.54	7.93	7.33	7.21	6.65
1200	K1	2.13	2.22	2.21	2.13	2.25
	K5	4.22	3.88	4.11	4.06	4.42
	K7	5.86	5.35	5.36	5.55	5.76
	K9	8.08	7.84	7.31	7.34	7.19

mainly promoted by load independent losses.

The torque loss increased with increasing rotational speed which was also verified by Mauz [75] using other lubricating oils.

It is clear that PAGD, with the highest operating viscosity, always promoted higher torque loss under load stage K1, no matter the rotational speed. Such behaviour was expected since the kinematic viscosity is one of the influencing factors for the no-load losses, as discussed in Chapter 4. All the other oil formulations promoted similar torque losses for all speed range. It was observed that PAOR generate lower torque loss at 400 rpm than the other formulations. This seems to affect the behaviour of PAOR in the other load stages, as shown in Figures 6.8(b), 6.8(c) and 6.8(d) for load stages K5, K7 and K9, respectively.

Figure 6.8(b) present the total torque loss under load stage K5. MINE oil generated the lower friction torque loss when load stage K5 was applied, no matter the rotational speed selected. At 200 and 400 rpm the MINR generated much higher torque loss than the other formulations. At 1200 rpm the no-load losses of the PAGD oil are the highest, that together, with the expected high rolling bearing losses (Chapter 5) generate the highest total torque loss. At 200 rpm, MINR oil generated a significantly higher torque loss, 25% higher than MINE for example. However, when the rotational speed increased, the difference is only 9%. ESTR and PAOR shown very similar behaviour no matter the rotational speed.

For the tests performed at load stage K7, Figure 6.8(c), the highest torque loss is achieved using the MINR oil. At low speed (200 and 400 rpm) the higher viscosity index of the PAGD keeps the torque loss lower than other oil formulations. At 1200 rpm all lubricants increase the torque loss and it is interesting to verify that the torque losses generated by PAGD and MINR are very similar (2% lower).

For load stage K9 presented in Figure 6.8(d), the PAGD oil generate much lower torque loss than the other formulations: 22 % less than MINR at 200 rpm and 11 % less than MINR at 1200 rpm. When compared with other synthetic formulations, like PAOR, PAGD generated less 9% torque loss at 200 rpm. As speed increases the differences between the oils become smaller. The MINR benefits of its lowest kinematic viscosity, and the synthetic formulations are penalized.

When the load increased, the influence of the rotational speed on the oil behaviour is modified. For K1 and K5, the no-load losses are still very important in the total torque loss measured, resulting in increasing torque loss with increasing rotational speed. For K7 and K9 load stages the torque loss starts to decrease or remains constant with increasing rotational speed. The film thickness predictions clearly show that increasing from 200 rpm to 1200 rpm promotes lubrication regime transition which affects the meshing gears torque loss mainly when high loads are applied.

6.6.3. Efficiency

The calculation of the gearbox efficiency, in a closed loop test rig, is a function of the torque installed in the system and of the torque applied by the electric motor (designated as torque loss T_L). A static torque was applied on the pinion shaft (T_{IN}) (see Figure 6.9), as a result, the wheel shaft has an higher torque (T_W), function of the pinion torque and of the transmission ratio ($i = z_2/z_1$), as indicated by equation (6.6). The wheel shaft torque values (T_W) tested were already presented in Table 6.6.

$$T_W = i \cdot T_{IN} \tag{6.6}$$

The torque loss (T_L), that is also the torque applied by the electric motor to keep a constant operating speed, was measured on the wheel shaft. Thus, the global efficiency of the test rig is given by equation (6.7).

$$\eta_{global} = \frac{T_W - T_L}{T_W} \times 100 \tag{6.7}$$

During the test, the electric motor will supply to the test-rig the torque loss generated. Each shaft has a torque installed as presented on the diagram of Figure 6.9, where T_1 represents the torque installed on the pinion shaft and T_2 (equation

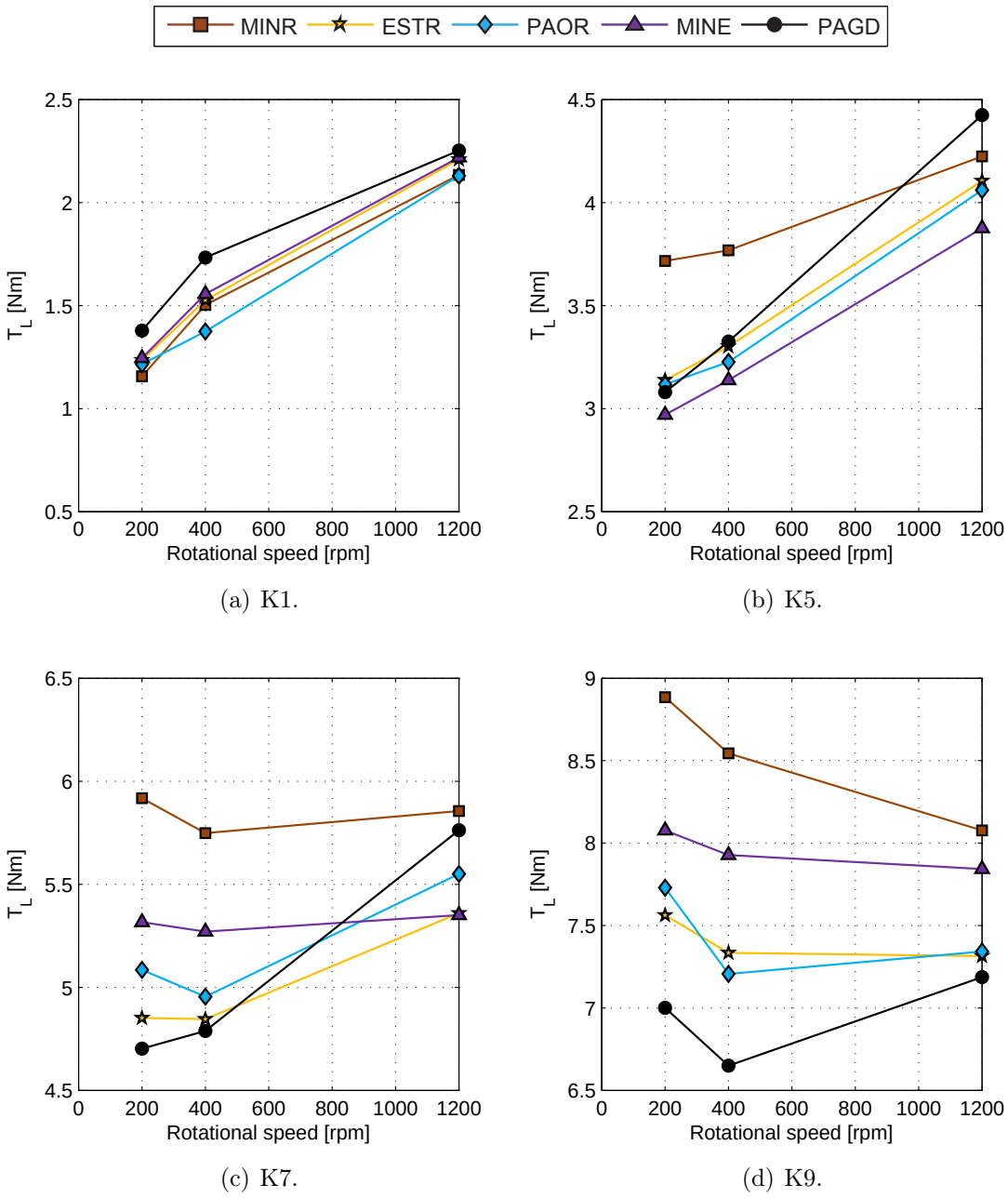

(a) K1.

(b) K5.

(c) K7.

(d) K9.

Figure 6.8.: Total torque loss of the test and slave gearboxes.

(6.8)) represents the torque installed on the wheel shaft. Both T_1 and T_2 are function of the torque loss of the system and the initial static torque applied T_{IN}.

$$T_2 = T_W - T_L \tag{6.8}$$

In order to calculate the efficiency of the slave gearbox, it was assumed that the maximum torque is applied on the motor shaft and is equal to the static torque

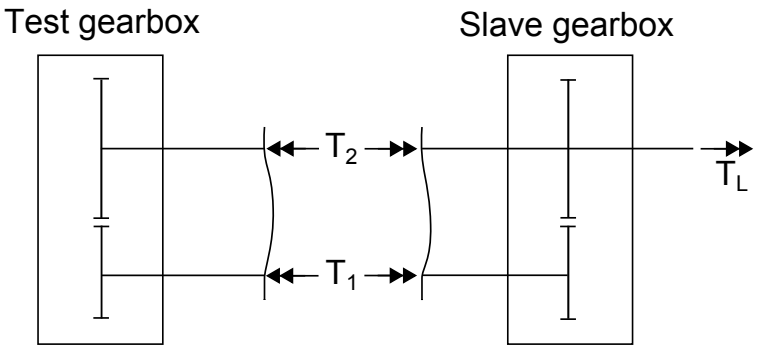

Figure 6.9.: Torques circulating on the test rig.

applied on the test rig. The power equilibrium of the shafts is given by equation (6.9) and the slave gearbox efficiency is given by the equation (6.10).

$$\eta_S \cdot T_W \cdot \omega_2 = T_1 \cdot \omega_1 \tag{6.9}$$

$$\eta_S = \frac{i \cdot T_1}{T_W} \tag{6.10}$$

The power equilibrium of both shafts is presented in equation (6.11) and the efficiency of the test gearbox is expressed on equation (6.12).

$$\eta_T \cdot T_1 \cdot \omega_1 = T_2 \cdot \omega_2 \tag{6.11}$$

$$\eta_T = \frac{T_2}{i \cdot T_1} \tag{6.12}$$

The torque that circulates on shaft 1 is given by equation (6.13).

$$T_1 = \frac{T_W - T_L}{i \cdot \eta_T} \tag{6.13}$$

The torque that circulates on shaft 2 is then given by equation 6.14.

$$T_2 = \eta_S \cdot \eta_T \cdot T_W \tag{6.14}$$

The system operated with equal gear geometry in both gearboxes and for that purpose, the slave and test gearbox efficiencies should be considered as equal. To calculate each gearbox efficiency, the equation (6.15) should be used.

$$\eta_T = \eta_S = \sqrt{\eta_{global}} \tag{6.15}$$

In the case a different test gearbox assembly is used (different gears and different rolling bearings), the efficiency of the test gearbox can be obtained through equation (6.16) if the slave gearbox remains the same.

Table 6.9.: Efficiency values [%] of the slave and test gearboxes for each test condition.

n_2	K_{FZG}	MINR	MINE	ESTR	PAOR	PAGD
200	K1	87.54	86.52	86.63	86.85	84.94
	K5	98.21	98.58	98.49	98.50	98.52
	K7	98.50	98.65	98.77	98.71	98.81
	K9	98.62	98.74	98.82	98.80	98.91
400	K1	83.45	82.80	83.16	84.99	80.62
	K5	98.19	98.49	98.41	98.45	98.40
	K7	98.54	98.66	98.77	98.75	98.79
	K9	98.67	98.77	98.86	98.88	98.97
1200	K1	75.43	74.27	74.41	75.48	73.82
	K5	97.97	98.14	98.02	98.05	97.87
	K7	98.52	98.64	98.64	98.59	98.54
	K9	98.74	98.78	98.86	98.86	98.88

$$\eta_T = \frac{\eta_{global}}{\eta_S} \tag{6.16}$$

Table 6.9 displays the efficiency values of the slave and test gearboxes for all the lubricants tested.

To be easier to understand the influence of the oil formulation on the gearbox efficiency for different operating conditions, a graphic presentation of the results is shown in Figure 6.10. The K1 load stage results were disregarded since the efficiency under no-load conditions is small and should not be compared with the other operating conditions.

Figures 6.10(a) and 6.10(d) show that both MINR and MINE are less influenced by the rotational speed than the other formulations, i.e. when speed increases for the same load, the efficiency doesn't decrease significantly and remains almost constant, mainly at high torque.

In the case of ESTR, PAOR and PAGD the efficiency decreases when the speed increases, for each applied torque, showing the good performance of the synthetic formulations at low speeds.

The influence of torque on the efficiency is similar for all the oils, higher torques generate higher efficiencies.

Regarding the particular use of each oil formulation don't improve the efficiency for all the operating conditions. For lower rotational speed PAGD is the most efficient, no matter the applied torque. ESTR and PAOR are the most efficient for smaller torques and high rotational speeds.

6.7. Coefficient of friction on meshing gears

A bibliographic review about the coefficient of friction on meshing gears was done in Chapter 4. The objective here is to determine a coefficient of friction that is representative of the experimental tests performed, and so, the average coefficient of friction (μ_{mZ}) is more relevant than the coefficient of friction in each point position along the meshing path of contact. For that purpose the different losses in the FZG

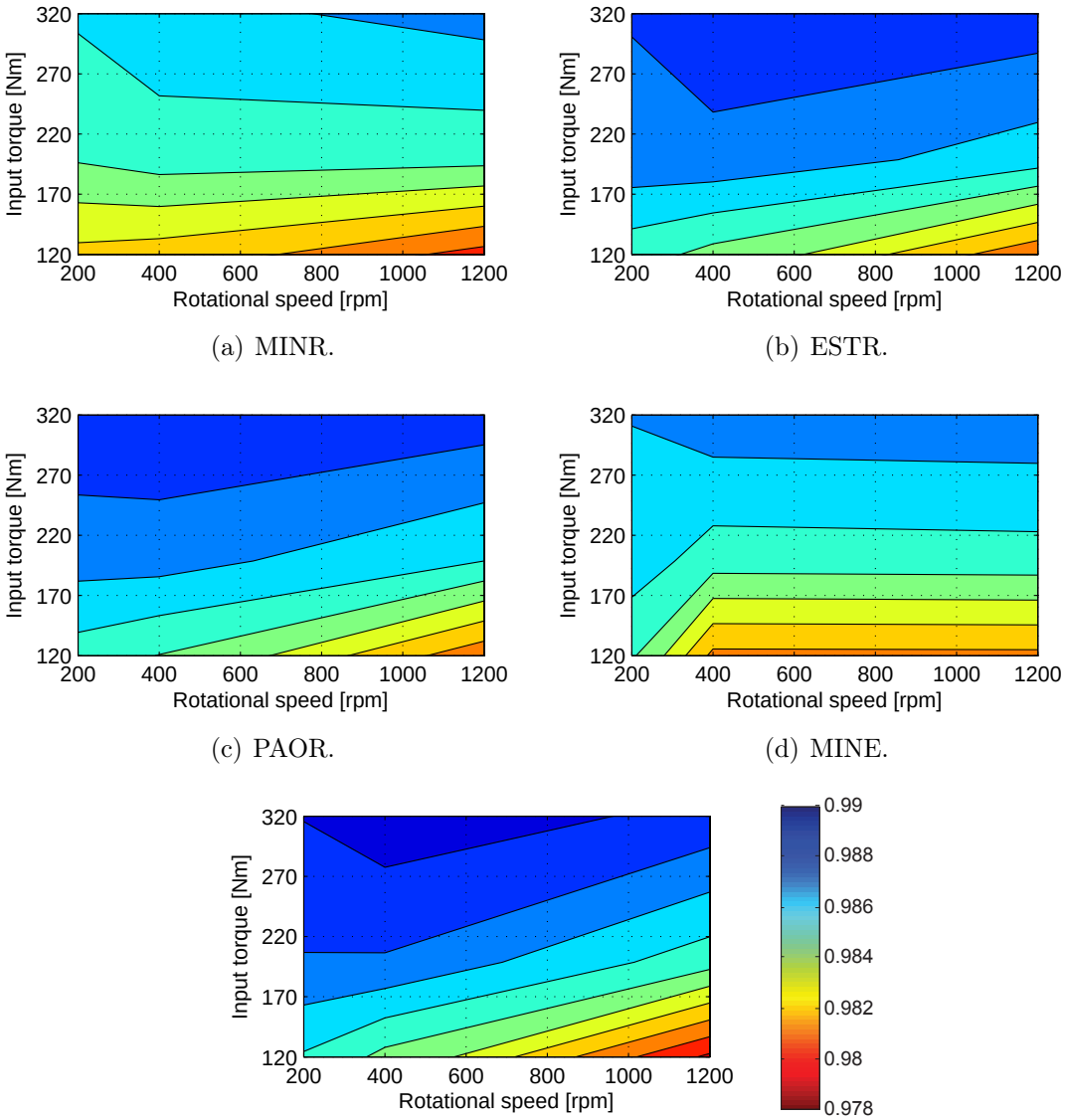

(a) MINR.

(b) ESTR.

(c) PAOR.

(d) MINE.

(e) PAGD.

Figure 6.10.: Efficiency maps for the C40 spur gear tests lubricated with different wind turbine gear oils.

gearboxes, described in Chapter 4, must be quantified.

The gearbox power loss model presented in Chapter 4 is resumed by equation (6.17) where the no-load gear losses are calculated based on the experimental results under K1 load stage.

Some rolling bearing models were discussed in Chapter 4 and the New SKF friction torque model was calibrated in Chapter 5 for each wind turbine gear oil used. The corresponding boundary (μ_{bl}) and full-film (μ_{EHD}) coefficient of friction are known.

The seal losses were calculated using the Simrit equation, also discussed in Chapter 4.

$$P_V^{i\,exp} = \underbrace{P_{VZ0}}_{P_V^{1\,exp}-P_{VL}^1-P_{VD}} + \underbrace{P_{VZP}^i}_{P_V^{i\,exp}-P_{VD}-P_{VZ0}} + \underbrace{P_{VL}^i}_{New\ SKF\ Model} + \underbrace{P_{VD}}_{Simrit\ Equation} \tag{6.17}$$

For each load stage i the experimental power loss is given by equation (6.18).

$$P_V^{i\,exp} = T_L^i \cdot \omega \tag{6.18}$$

6.7.1. No-load gear power loss

The load stage K1 was performed to understand the no-load behaviour of the oils in the FZG gearboxes. For load stage K1 (low input torque, $T_W = 4.95\ Nm$) equation (6.17) becomes equation (6.19).

$$P_V^{1\,exp} = P_{VZ0}^1 + P_{VZP}^1 + P_{VL}^1 + P_{VD}^1 \tag{6.19}$$

Equation (6.19) can be used to determine the no-load gears loss (P_{VZ0}), through equation (6.20), since P_{VZP}^1=0.

$$P_{VZ0} = P_V^{1\,exp} - P_{VL}^1 - P_{VD} \tag{6.20}$$

The no-load gear losses, in fact, also include the power loss generated by the rolling bearing assembled in the clutch shaft (see Figure 6.1(a)). Under no-load situations, the new SKF rolling bearing friction torque model only consider the drag loss mechanism as a source of power dissipation. As discussed in Chapter 5, the predicted drag loss values are sometimes negligible. To be more confident with the quantification of the other power loss sources, the FZG rolling bearing under no-load situation is accounted in P_VZ0, described by equation (6.20).

The results for T_{VZ0} ($= P_{VZ0}/\omega$) are presented in Figure 6.11 for each rotational speed and oil formulation. PAGD promoted the highest no-load gear losses at 200 and 400 rpm. PAOR promoted the lowest no-load torque loss at 400 rpm which only can be attributed to the nature of the base oil, since the operating kinematic

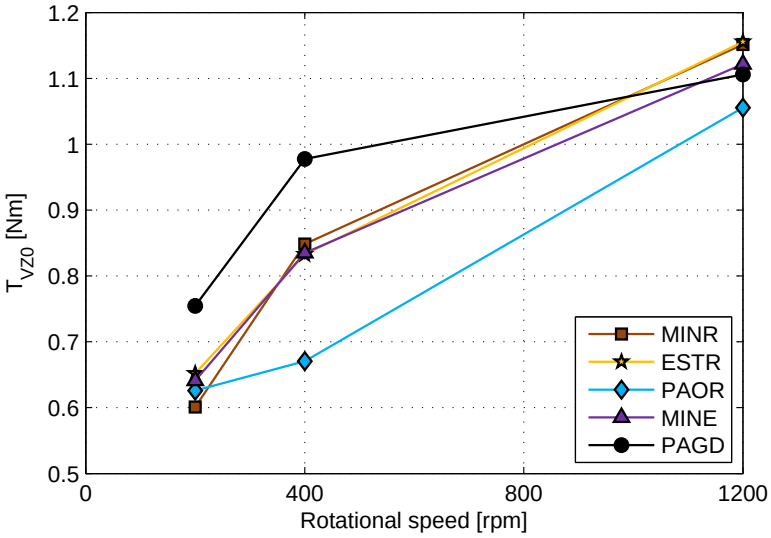

Figure 6.11.: Meshing gears load independent torque loss at K1 (T_{VZ0}).

viscosity is similar to that of ESTR. At 1200 rpm all the formulations show similar no-load losses.

6.7.2. Meshing gear power loss

The gear load dependent losses for any load stage and input speed were calculated, according to equation (6.21), subtracting the rolling bearing losses, the seal losses and the no-load losses previously calculated to the total experimental power loss.

$$P^i_{VZP} = P^{i\ exp}_V - P^i_{VL} - P_{VD} - P_{VZ0} \tag{6.21}$$

The meshing gear torque loss ($T^i_{VZP} = P^i_{VZP}/\omega$) results are presented in Figure 6.12 and as expected, since the tests were performed mainly under mixed film lubrication, the meshing gears torque loss decrease with increasing rotational speed.

PAGD oil, shows a different trend when the speed increase from 400 to 1200 rpm for K5 and K7 load stages. The meshing gears torque loss increase can only be explained with a lubrication transition from mixed film to full-film conditions which is not proved by the film thickness prediction.

With increasing torques, the meshing gears torque loss also increases, which is the expected behaviour.

Considering the influence of the oil formulation, MINR always promoted the highest meshing gear torque loss. PAGD promoted the lowest value for K9 load stage, no matter the rotational speed. In load stage K9, the meshing gear torque loss generated by PAGD is at least 30% lower than the one generated by MINR,

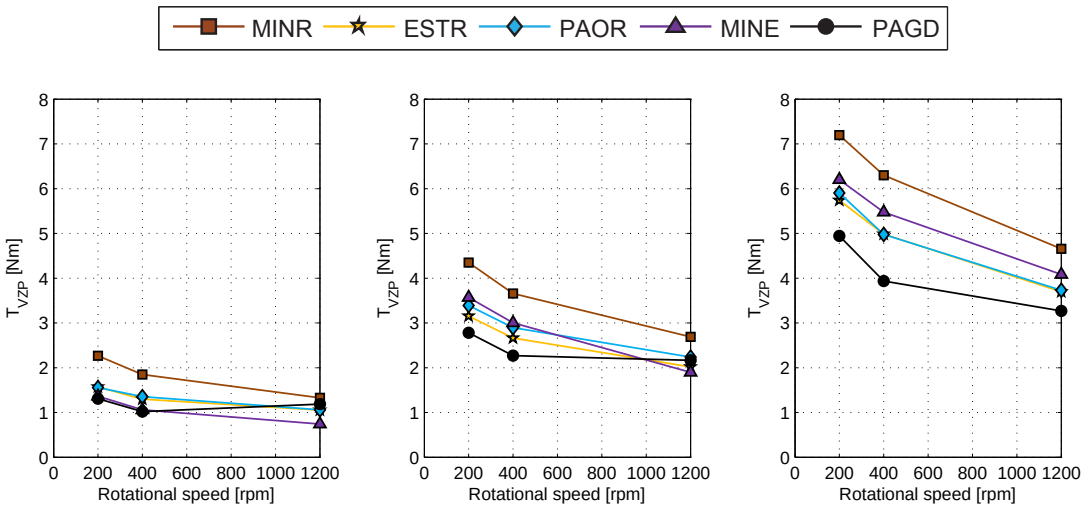

(a) K5. (b) K7. (c) K9.

Figure 6.12.: Meshing gears torque loss: load dependent (T_{VZP}).

Table 6.10.: Gear loss factor of C40 spur gear calculated with different equations.

	Ohlendorf	Velex	Buckingham	Winter	Author	KissSoft
H_V	0.1949	0.2517	0.2522	0.2188	0.1949	0.1946

whatever the rotational speed.

6.7.3. Experimental coefficient of friction

The meshing gear power loss can be used to calculate an average coefficient of friction along the path of contact, according to equation (6.22)

$$\mu_{mZ}^{exp} = \frac{P_{VZP}}{P_{IN} \cdot H_V} \tag{6.22}$$

The gear loss factor was calculated with different equations for the C40 spur gear. As discussed in Chapter 4, all formulas gives similar values to that calculated with the Ohlendorf equation, as presented in Table 6.10.

In Figure 6.13, the average coefficient of friction is given for each load stage and rotational speed. Since the tests were performed under mixed lubrication, the increasing rotational speed promoted a reduction of the average coefficient of friction, as expected. Furthermore, this behaviour was also observed for the sliding coefficient of friction in rolling bearings as well as for the traction coefficient in ball-on-disc tests. The influence of the oil formulation is clear, and no matter the operating

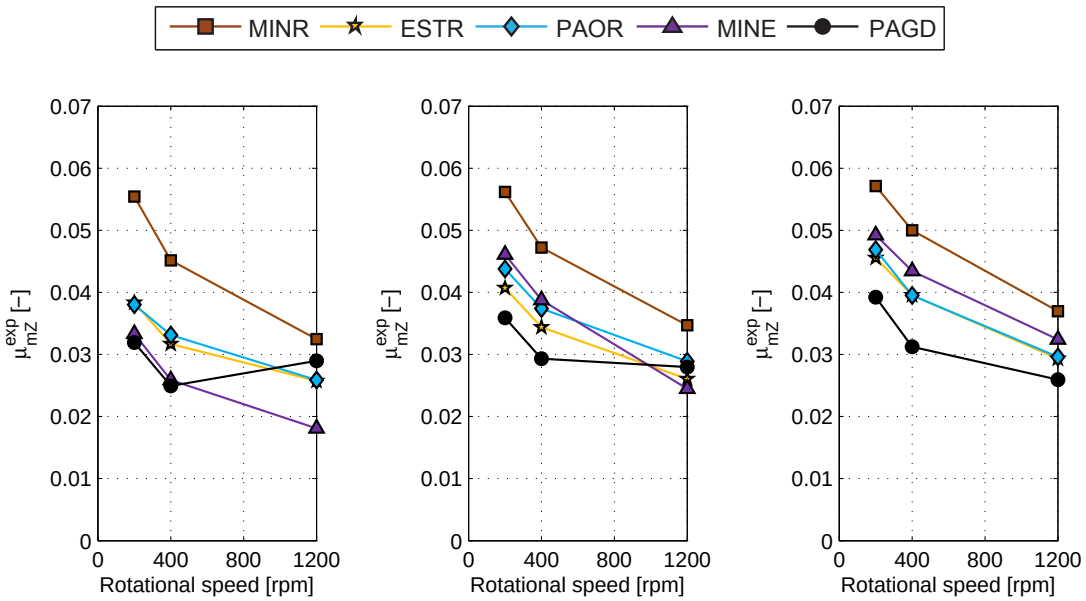

(a) K5. (b) K7. (c) K9.

Figure 6.13.: Coefficient of friction based on experimental results (μ_{mZ}^{exp}) vs. rotational speed for each load stage.

conditions, the MINR always promoted the highest coefficient of friction, confirming previous results.

In Figure 6.14 it can be observed that the PAGD promoted the lowest coefficient of friction mainly at low speeds. Figure 6.14 also shows that increasing the speed, and no matter the load applied, the average coefficient of friction of the oil formulations become similar to all formulations. This Figure also shows that the average coefficient of friction increases with increasing torque. However, the influence of load seems to be less important than influence of the speed.

6.7.4. Schlenk coefficient of friction

Schlenck [120] proposed equation (**??**) to calculate the average coefficient of friction along the path of contact of gears. The equation was derived from twin disc tests lubricated with an additive free mineral oil. For such oil the lubricant parameter (X_L) is equal to 1.

The experimental average coefficient of friction, μ_{mZ}^{exp}, obtained with equation (6.22) can be correlated with those predicted by equation (**??**). The minimization of the difference between these two values, defined by equation (6.23), can be used to determine the X_L lubricant parameter adjusted to each oil formulation.

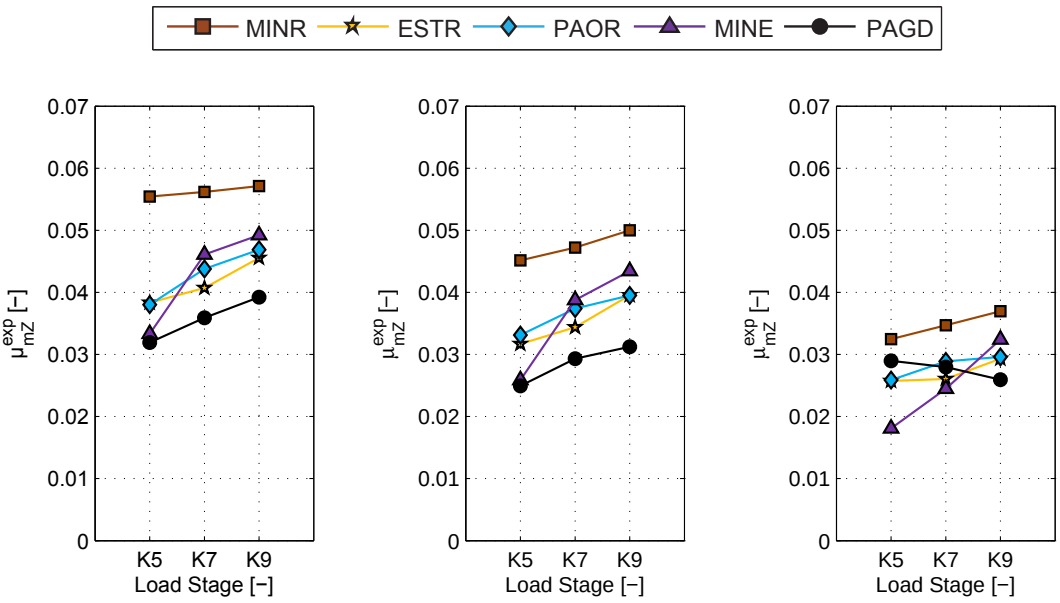

(a) 200 rpm. (b) 400 rpm. (c) 1200 rpm.

Figure 6.14.: Coefficient of friction based on experimental results (μ_{mZ}^{exp}) vs. Load stage for each rotational speed.

$$error = \sum_{i=1}^{n} \left| {\mu_{mZ}^{i}}^{exp} - {\mu_{mZ}^{i}}^{Schlenk} \right| \tag{6.23}$$

To perform the minimization, the following assumption was made: the surface roughness is the mean value of the composite surface roughness, after run-in and at the end of all tests (Table 6.4). The average roughness used for the calculation is presented in equation (6.24).

$$Ra = \frac{\frac{(R_{a2}+R_{a2})^{run-in}}{2} + \frac{(R_{a2}+R_{a2})^{end}}{2}}{2} = \frac{\frac{1+0.7}{2} + \frac{0.6+0.5}{2}}{2} = 0.725 \tag{6.24}$$

Using this minimization approach, the lubricant parameter was calculated for each oil formulation. The results are presented in Figures 6.15 and 6.16.

Figure 6.15 shows the average coefficient of friction, experimental and predicted by Schlenk equation (X_L=0.85), for MINR oil. The correlation is acceptable but the influence of load is not well represented. The high amount of extreme pressure additives on MINR oil can modify the behaviour of the oil when load is applied and this seems to be the case here.

Schlenk's equation shows a much better correlation with the experimental results of ESTR and PAOR, than MINR. For PAGD and MINE the Schlenk formula follow very well part of the experimental results. MINE oil shows the worst correlation

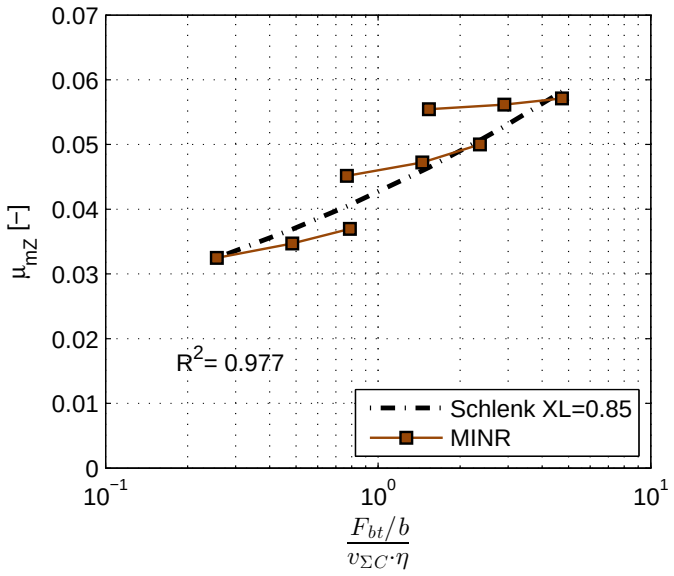

Figure 6.15.: MINR coefficient of friction determined based on experimental results vs. Schlenk equation adjusted as function of hydraulic parameter.

that is related to a different behaviour of the mineral plus PAMA mixture. In the case of PAGD it is possible that full-film lubrication regime occured at 1200 rpm, which can explain the different behaviour for K5 and K7 load stages at 1200 rpm, and Schlenck equation is not suitable under full-film conditions.

Martins *et al.* [80] proposed a different X_L parameter for MINR, as shown in equation (6.25).

$$X_L = \frac{1}{(F_{bt}/b)^{b_1}} \tag{6.25}$$

The minimization procedure presented earlier (equation (6.23)) ended in a value of b_1=0.0346 for MINR. However, the correlation obtained was not significantly better, as shown in Figure 6.17.

A more sophisticated X_L parameter was then tried, based on Martins work, and the influence of the speed was also modified, as shown in equation (6.26). With the minimization process the constants became a_1=1.49, b_1=0.114 and c_1=0.054 for MINR.

$$X_L = \frac{a_1}{(F_{bt}/b)^{b_1} \cdot v_{\Sigma C}^{c_1}} \tag{6.26}$$

It is clear in Figure 6.17 that optimizing the load and speed exponents, b_1 and c_1, the prediction is much better. This more elaborated lubricant parameter gives better

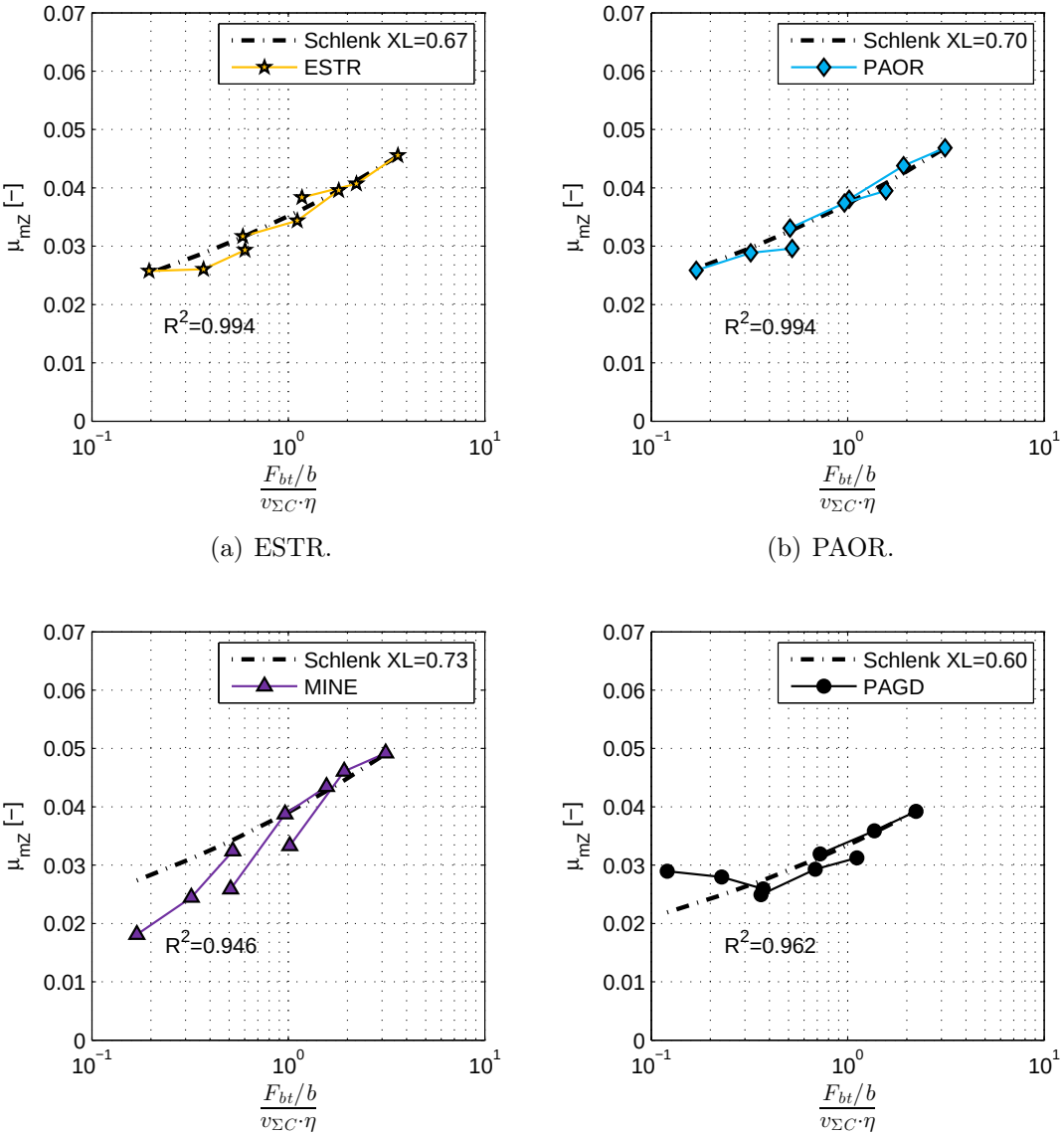

(a) ESTR. (b) PAOR.

(c) MINE. (d) PAGD.

Figure 6.16.: Coefficient of friction determined based on experimental results vs. Schlenk equation adjusted for each wind turbine gear oil as function of hydraulic parameter.

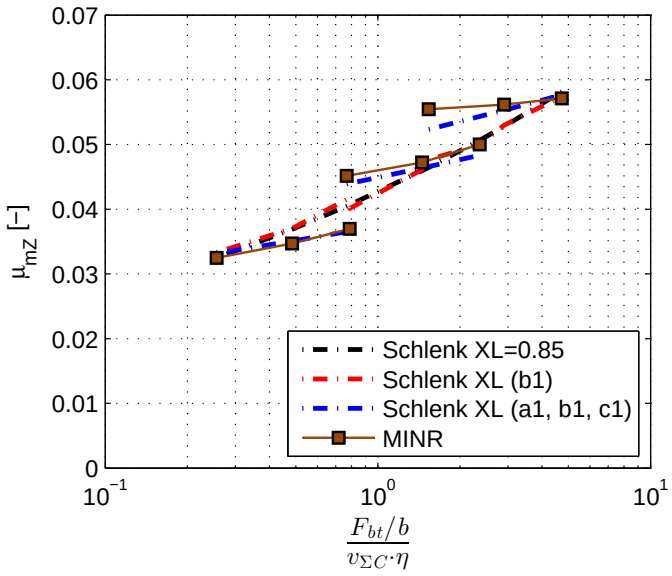

Figure 6.17.: Coefficient of friction determined based on experimental results vs. Schlenk equation adjusted for each wind turbine gear oil asd function of the hydraulic parameter.

predictions of the average coefficient of friction between meshing gears, but it also shows that Schlenk equation has limitations, at least for some gear oil formulations.

Thus, the lubricant parameter shown in Figures 6.15 and 6.16, independent of load and speed, will be considered a quite good first approximation. Additionally, the equation works well for PAOR, ESTR and gives the overall trend for MINR, MINE and PAGD.

6.7.5. New formula for the average coefficient of friction

Brandão [63] performed several traction measurements on a ball-on-disc for gear oils. The results obtained indicate that under mixed film lubrication regime, the coefficient of friction decreases with increasing values of the modified Hersey parameter (S_p). Since the results were presented in a logarithmic scale, the relation between the coefficient of friction and S_p was almost linear.

The traction coefficient measurements presented in Chapter 3, Figure 3.7, also showed the variation of the traction coefficient with S_p parameter. Thus, the experimental average coefficient of friction, based on gear experiments, can also be plotted against the modified Hersey parameter, as shown in Figures 6.18 and 6.19.

It is necessary to recall the modified Hersey parameter, equation (6.27).

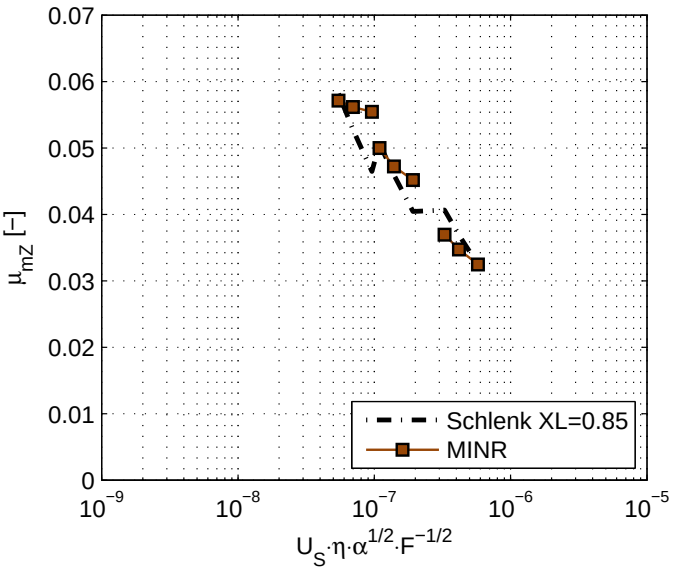

Figure 6.18.: MINR coefficient of friction determined based on experimental results vs. Schlenk equation adjusted.

$$S_p = \frac{U_S \cdot \eta \cdot \alpha^{1/2}}{F^{1/2}} \tag{6.27}$$

The modified Hersey parameter, S_p, was adapted to gears making the following assumptions:

- Velocity U_S, is equal to the sum of the velocities at the pitch point, i.e. $U_S = v_{\Sigma C}$;
- The load F is equal to the tangential force on the base plane, i.e. $F = F_{bt}$.

Thus,

$$S_p{}^{gear} = \frac{v_{\Sigma C} \cdot \eta \cdot \alpha^{1/2}}{F_{bt}^{1/2}} \tag{6.28}$$

Figures 6.18 and 6.19 indicate the same linear trend (on a log scale) for the variation of the average coefficient of friction with S_p parameter. Once more some of the results obtained for PAGD and MINE, are out of this general trend.

The modified parameter gives to the load a square root weight and adds the pressure-viscosity. On the other side, the hydraulic parameter on the Schlenk's equation is directly proportional to the load, consequently gives more importance to the load than what the experimental results indicate.

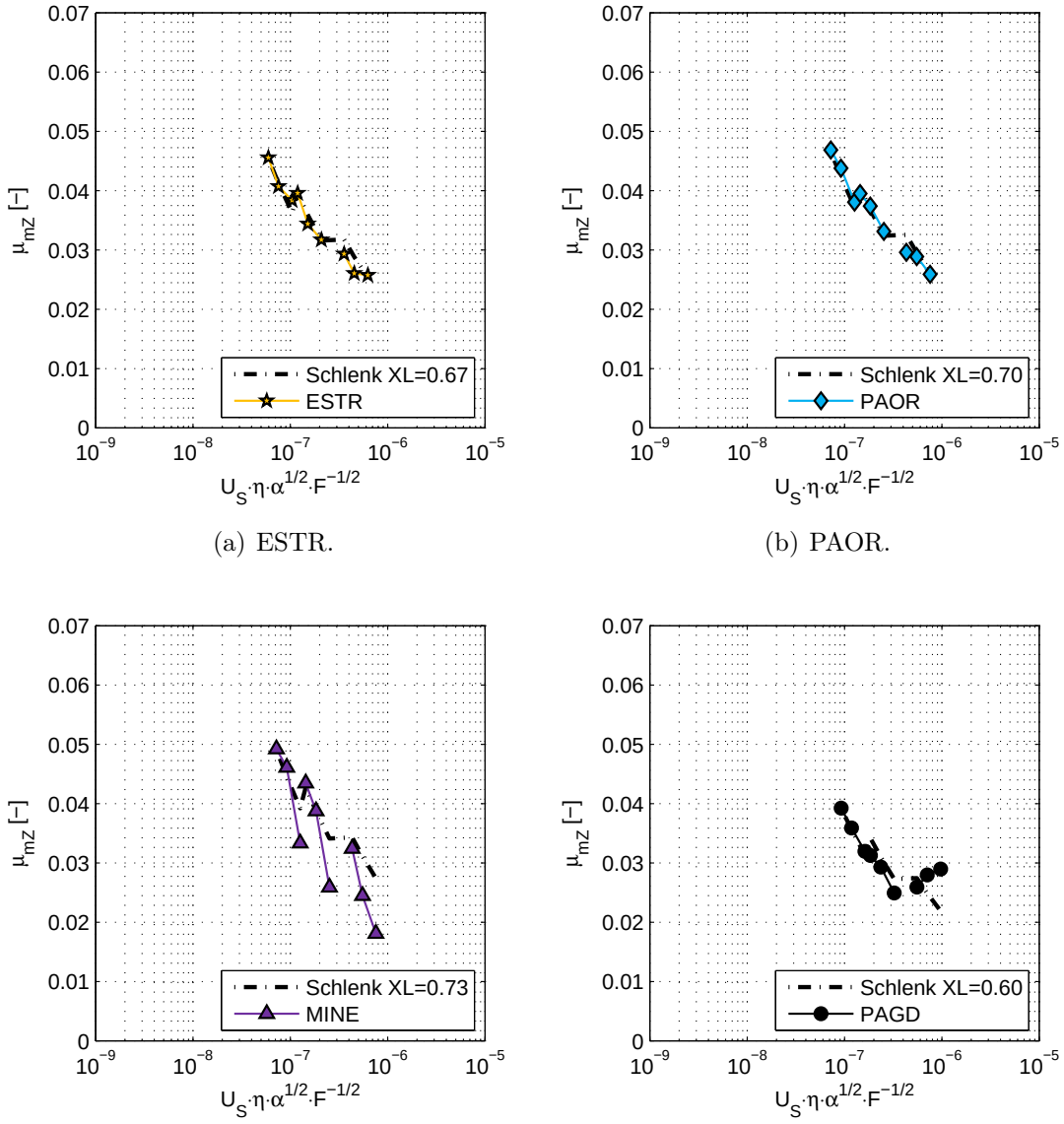

(a) ESTR.

(b) PAOR.

(c) MINE.

(d) PAGD.

Figure 6.19.: Coefficient of friction determined based on experimental results vs. Schlenk equation adjusted for each wind turbine gear oil as function of modified Hersey parameter.

Assuming that a logarithmic line is represented with the topology of equation (6.29) can present the influence S_p on the coefficient of friction.

$$y = m \cdot \log x + b \tag{6.29}$$

Assuming the linear variation of the coefficient of friction with S_p, given by equation (6.30),

$$\mu_{mZ} \propto m \cdot \log\left(S_p\right) + b \tag{6.30}$$

The logarithmic function can be approximated by equation (6.31).

$$\mu_{mZ} \propto A \cdot \left(S_p\right)^B \tag{6.31}$$

However, the modified Hersey parameter (S_p), only takes into account the lubrication conditions and does not consider the influence of the contact geometry. The modified Hersey parameter can describe the influence of the load (F), velocity (U_S), dynamic viscosity (η) and pressure-viscosity coefficient (α). To keep the influence of the geometry in the new coefficient of friction the geometric parameters surface finishing (Ra), face width of the gear (b) and equivalent radius of contact (ρ_{redC}) of Schlenk's equation will be considered.

The influence of roughness is kept the same, since it is not possible for the moment to do a parametric study of the influence of gear geometry in the coefficient of friction. So, the geometric parameter will take the form of equation (6.32).

$$S_g = \frac{R_a^{1/4}}{{\rho_{redC}}^C \cdot \left(\epsilon_\alpha \cdot b\right)^D} \tag{6.32}$$

To assure that the parameter S_g is dimensionless, the π Buckingham theorem implies that that equation (6.33) is verified.

$$C + D = \frac{1}{4} \tag{6.33}$$

On the other side, it will be assumed that $\epsilon_\alpha \cdot b$ should have the same exponent of the load, as in the modified Hersey parameter S_p (see equation (6.27)), which implies the condition of equation (6.34).

$$D = \frac{1}{2} \cdot B \tag{6.34}$$

In section 6.7.4, the lubricant parameter X_L, of Schlenck equation was determined for each wind turbine gear oil. It is of great interest to keep the same parameter on the new equation.

The following system of equations (6.35) will be adjusted to the experimental results to determine A and B.

$$\mu_{mZ} = A \cdot \left(\frac{U_S \cdot \eta \cdot \alpha^{1/2}}{F^{1/2}} \right)^B \cdot \frac{R_a^{1/4}}{\rho_{redC}{}^{\frac{1-2\cdot B}{4}} \cdot (\epsilon_\alpha \cdot b)^{\frac{1}{2}\cdot B}} \cdot X_L \tag{6.35}$$

The minimization process give the following values: A=0.014 and B=0.25. So, the final equation takes the form (6.36), with S_p and S_g given by equations (6.37) and (6.38), respectively. All quantities are expressed in SI units.

$$\mu_{mZ} = 0.014 \cdot \left(\frac{1}{S_p} \right)^{1/4} \cdot S_g \cdot X_L \tag{6.36}$$

$$S_p = \frac{U_S \cdot \eta \cdot \alpha^{1/2}}{F^{1/2}} \tag{6.37}$$

$$S_g = \left(\frac{R_a^2}{\rho_{redC} \cdot \epsilon_\alpha \cdot b} \right)^{1/8} \tag{6.38}$$

The prediction of coefficient of friction using the new equation is presented in Figure 6.20 for MINR and in Figure 6.21 for the other wind turbine gear oil formulations. It is interesting to verify that the new equation follows significantly better the behaviour of the experimental coefficient of friction results.

The new equation includes the influence of the pressure-viscosity coefficient which produces a very interesting effect under constant temperature and operating viscosity: for each rotational speed the slope of the equation will be different (for example: ESTR and PAOR). The highest the pressure-viscosity the lowest is the slope, for the same operating speed. It makes sense, since for the same operating condition and similar operating viscosity, it is expected that the oil with the highest pressure-viscosity generates slightly higher film thickness, and consequently the coefficient of friction is less influenced by the load.

The influence of the viscosity is now more important than in the case of Schlenck equation, since the exponent changes from -0.05 to -0.25. In order to compare the prediction of the coefficient of friction using both equations, Schlenk and the new formula (6.36), Figure 6.22 shows the predictions for twin-disc tests published by Höhn *et al.*, performed at 90 °C with a SRR=10% and a sum of the velocities from 1 to 16 m/s. Three lubricants with mineral base without additives were considered: FVA2 ISO VG 32 ($\nu_{90} = 4.4\ mm^2/s$), FVA 3 ISO VG 100 ($\nu_{90} = 14.5\ mm^2/s$) and FVA4 ISO VG 460 ($\nu_{90} = 46\ mm^2/s$). According to Höhn *et al.* [66], slide-to-roll ratios above 10% do not influence the coefficient of friction.

Figure 6.22 clearly shows that the new formula for the coefficient of friction (6.36) fits very well all experimental results, whatever the viscosity and the lubrication regime.

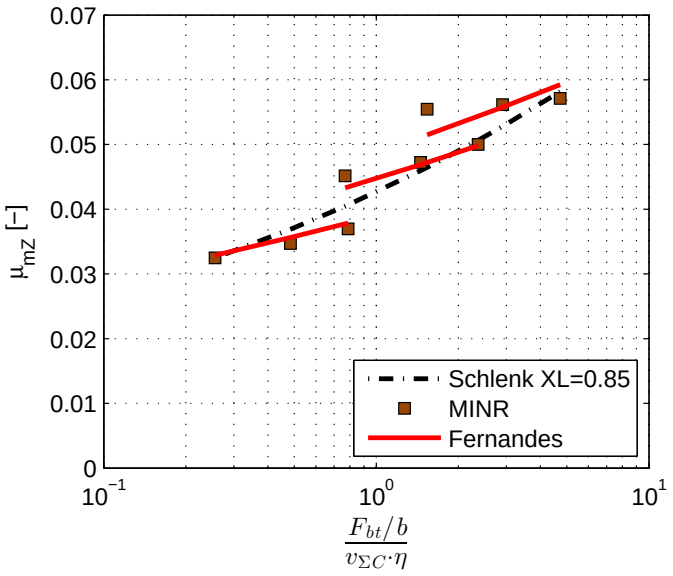

Figure 6.20.: Coefficient of friction determined based on experimental results vs. Schlenk equation adjusted and Fernandes equation, for MINR as function of hydraulic parameter.

Equation (6.36) is more sensitive to the dynamic viscosity which explains the better correlation in the case of FVA 2 oil. The new equation also show an interesting correlation with twin-disc tests performed under mixed lubrication.

In the beginning of this Chapter it was described that a PAO ISO VG 150 oil was also tested in this campaign. For validation purposes, the experimental coefficient of friction was calculated using the procedure described in section 6.7.3. Considering that the X_L parameter obtained for PAOR is valid for this lubricant (X_L=0.7), a simulation was performed and presented in Figure 6.23. It is clear that equation (6.36) predicted quite well the experimental results.

For the moment, equation (6.36) lacks validation for other gear geometries, which will be presented in Chapte r 7. In order to assure that the equation doesn't produce quite large deviations for conditions different from those tested here, Fernandes equation and Schlenck equation are presented in Figure 6.24 for MINR and for a wider range of test conditions. It can be stated that the influence of load was modified in a greater way than the speed influence.

6.7.6. Other coefficient of friction formulas

The experimental results previously presented will be compared with coefficient of friction formulas using load sharing functions.

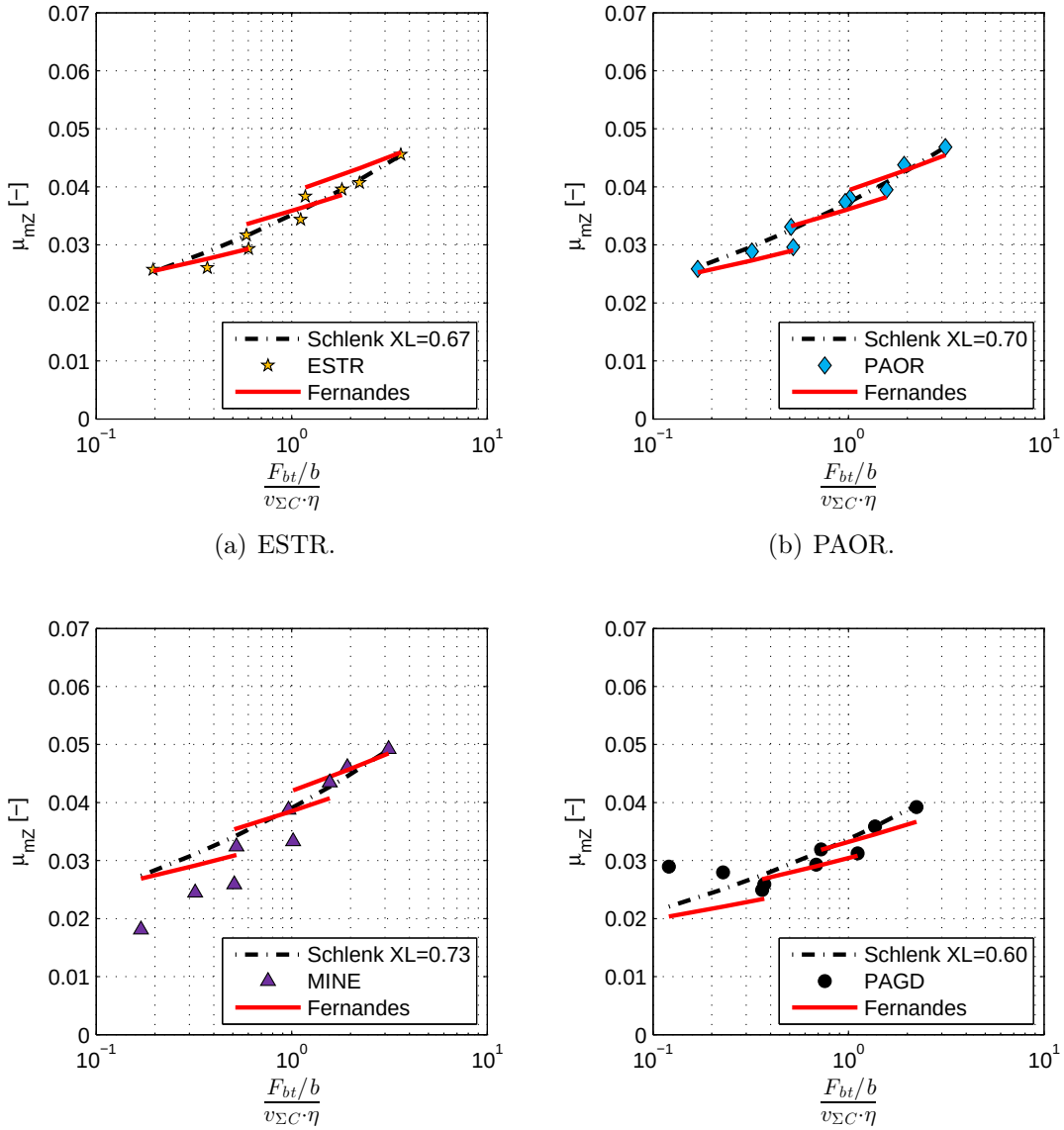

(a) ESTR.

(b) PAOR.

(c) MINE.

(d) PAGD.

Figure 6.21.: Coefficient of friction determined based on experimental results oils vs. Schlenk equation adjusted and Fernandes equation, for each wind turbine gear oil as function of hydraulic parameter.

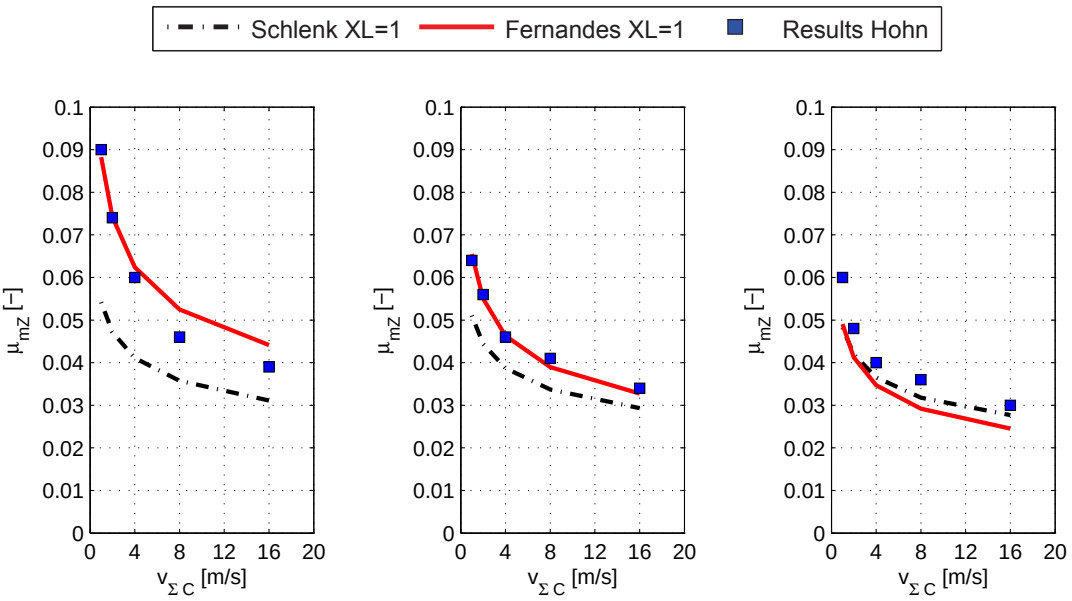

(a) FVA2 @ 90 °C, $\Lambda < 2$. (b) FVA3 @ 90 °C, $\Lambda < 2$. (c) FVA4 @ 90 °C, $\Lambda > 2$.

Figure 6.22.: Fernandes and Schlenk formulas predicting the twin-disc results published by Höhn.

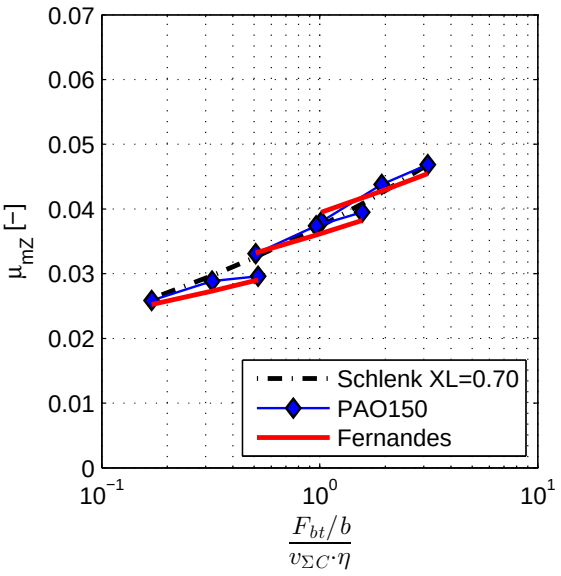

Figure 6.23.: Coefficient of friction determined based on experimental results vs. Schlenk equation adjusted and Fernandes equation, for a PAO 150.

The Doleshchel, Castro and Matsumoto formulas rely on the film thickness prediction and proved to be quite effective [65, 122]. The load sharing functions of Doleshchel, Castro and Matsumoto are presented in Figure 6.25 for a C40 spur

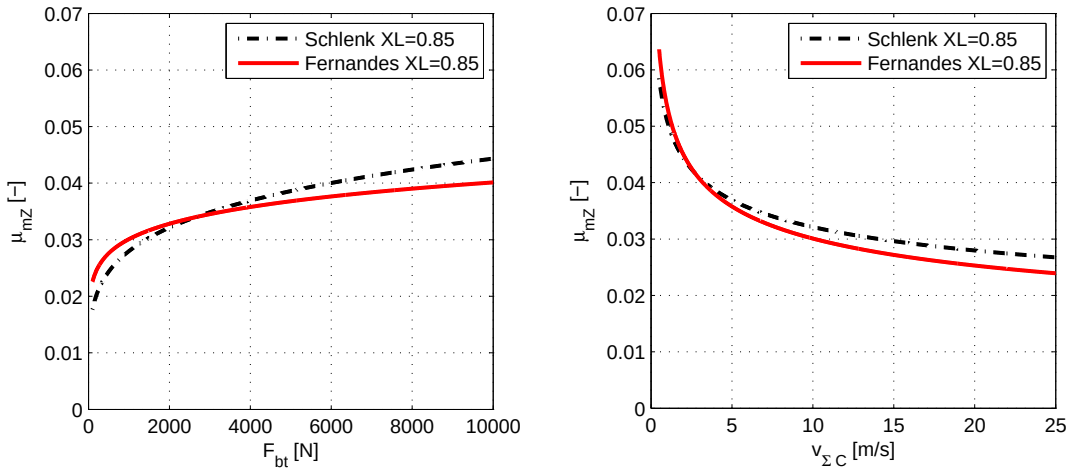

(a) Influence of load.

(b) Influence of speed.

Figure 6.24.: Influence of load and speed on Fernandes and Schlenk formulas.

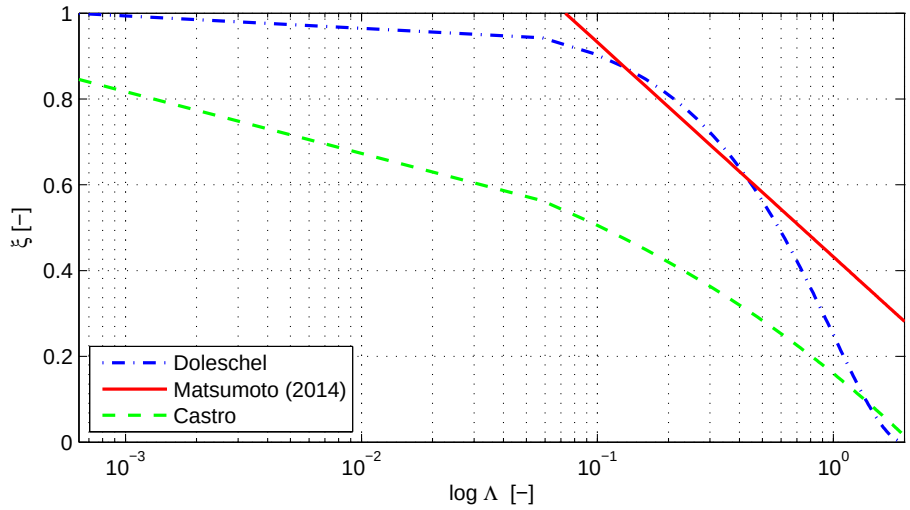

Figure 6.25.: Comparison of load sharing function of Doleschel, Matsumoto and Castro.

gear lubricated with MINR at 80 °C under load stage K9. The range of rotational speed corresponds to operating conditions going from boundary, mixed and full-film conditions.

Castro function gives too much weight to the full film condition than the other approaches, while Matsumoto function gives too much weight to the boundary conditions.

The coefficients of friction predicted for the MINR oil considering each load sharing

Table 6.11.: Coefficients to calculate the μ_{bl} and μ_{EHD} for each test condition (MINR).

Coefficient	$\mu_{bl,R}$	α_{bl}	β_{bl}	$\mu_{EHD,R}$	α_{EHD}	β_{EHD}	γ_{EHD}
Value	0.099	0.62	-0.12	0.026	0.19	-0.05	0.19

function are presented in Figure 6.26. The μ_{bl} and μ_{EHD} values are calculated according to the equations (6.39) and (6.40) proposed by Doleschel [67].

$$\mu_{bl} = \mu_{bl,R} \cdot \left(\frac{p_H}{p_R}\right)^{\alpha_{bl}} \cdot \left(\frac{v_{\Sigma C}}{v_{R,bl}}\right)^{\beta_{bl}} \tag{6.39}$$

$$\mu_{EHD} = \mu_{EHD,R} \cdot \left(\frac{p_H}{p_R}\right)^{\alpha_{EHD}} \cdot \left(\frac{v_{\Sigma C}}{v_{R,EHD}}\right)^{\beta_{EHD}} \cdot \left(\frac{\eta}{\eta_R}\right)^{\gamma_{EHD}} \tag{6.40}$$

The reference values $\mu_{bl,R}$ and $\mu_{EHD,R}$ were calculated in order to have the best possible correlation of the Doleschel formula to the experimental coefficients of friction. The values are presented in Table 6.11.

If the boundary and full-film coefficient of friction are determined using equations (6.39) and (6.40), the load sharing functions are not able to predict the actual coefficient of friction.

The load sharing functions work very well if a full-film coefficient of friction independent of the load is used, since for the same rotational speed, the film thickness is very similar independently of the load applied. The experimental results also show that the variation of coefficient of friction with the operating conditions is significantly smaller than what equations (6.39) and (6.40) predict. If a reference value, independent of load, is used, the predictions improve, but they are not supported by the tribology findings, i.e. the load applied influences the full-film coefficient of friction.

6.8. Calibrated power loss model

The results presented allow to calibrate the power loss model proposed in Chapter 4.

The model was used in the format of equation (6.41) in order to quantify the contribution of each power loss mechanism inside the gearbox. The different losses were quantified and the coefficient of friction was calibrated for each oil formulation.

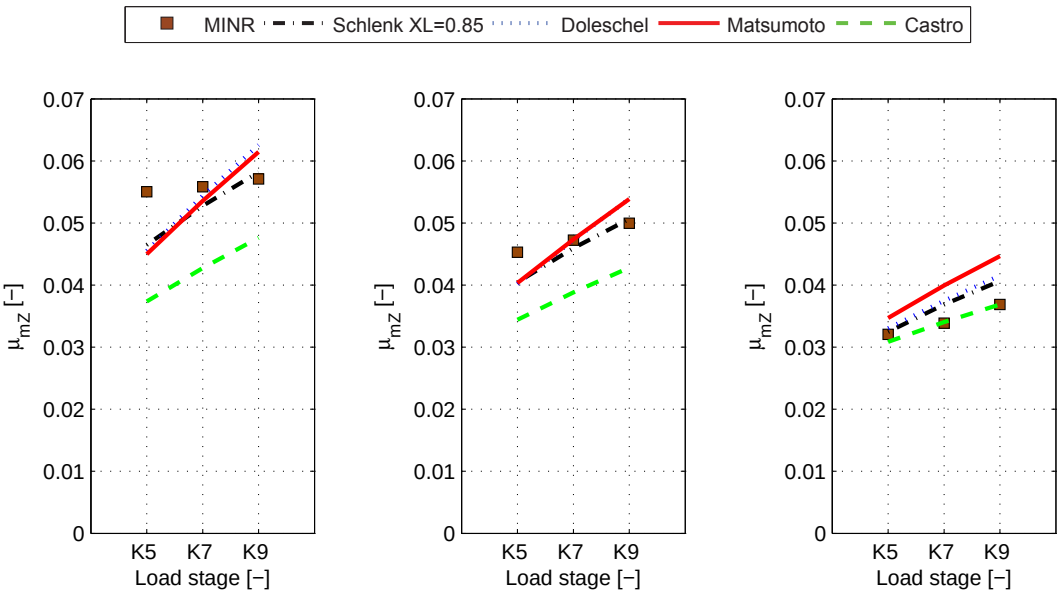

(a) 200 rpm. (b) 400 rpm. (c) 1200 rpm.

Figure 6.26.: Comparison of coefficient of friction formulas.

$$P_V{}^{exp} = \underbrace{P_{VZ0}}_{P_V^{1\,exp}-P_{VL}^1-P_{VD}} + \underbrace{P_{VZP}}_{P_V^{i\,exp}-P_{VL}^i-P_{VD}-P_{VZ0}} + \underbrace{P_{VL}}_{New\ SKF\ Model} + \underbrace{P_{VD}}_{Simrit\ Equation} \tag{6.41}$$

To predict the power loss, the model should be applied as presented in equation (6.42).

$$P_V = \underbrace{P_{VZ0}}_{P_V^{1\,exp}-P_{VL}^1-P_{VD}} + \underbrace{P_{VZP}}_{P_{IN}\cdot H_{VL}\cdot\mu_{mZ}(X_L)} + \underbrace{P_{VL}}_{New\ SKF\ Model} + \underbrace{P_{VD}}_{Simrit\ Equation} \tag{6.42}$$

Take note that the coefficient of friction can be calculated from any approach discussed in the previous sections, with the advantages and disadvantages of each method. However, it will be considered a calibrated power loss model using the Schlenk equation, which is now included on the standards and can be more interesting for design engineers. For each oil formulation the lubricant parameter was determined and is presented in Table 6.12.

The rolling bearing losses were calibrated as discussed in Chapter 5.

To determine the no-load losses is advised to use measurements because the existent models actually are not very accurate to predict the power losses.

Table 6.12.: Lubricant parameter for each oil formulation.

Oil	X_L
MINR	0.85
ESTR	0.67
PAOR	0.70
MINE	0.73
PAGD	0.60

6.9. Closure

FZG gearbox power loss tests were performed using twin gearboxes. The tests allow to understand the power loss behaviour of five wind turbine gear oils and quantify the power loss of the usual FZG slave gearbox which is necessary to measure the power loss when other geometries need to be measured. Furthermore, the results are necessary to calibrate a power loss model.

The results presented clearly identify that the oil formulation is of great importance in the gearbox efficiency. Changing the oil from MINR to PAGD, a reduction of power loss over 20 % was achieved for the lowest speed and highest loads. If PAOR is preferred over MINR, the power loss reduction is higher than 10 %.

A deep study of coefficient of friction was done allowing to calibrate a power loss model.

A lubricant parameter (X_L) that correlate the Schlenk coefficient of friction with the experimental results was determined for each oil formulation.

A new coefficient of friction formula was proposed, changing the usual hydraulic parameter of Schlenck equation by the modified Hersey parameter S_p with promising results.

Chapter 7.

Low loss gears

7.1. Introduction

It is known that the load dependent gear losses are the most relevant source of power loss in a gearbox, when the input torque is high and the speed is low. So, under these operating conditions, gear geometry and lubrication conditions are key parameters for the control of power loss.

In Höhn *et al.* work entitled "Low Loss Gears" [106], it was stated that gear design criteria, such as load capacity or vibration excitation, always predominate over efficiency. Höhn *et al.* proposed the 'low loss' gear tooth geometry in order to replace a standard FZG type C gear with 14 mm width. To do that, he created an helical gear with lower module, higher number of teeth, higher pressure angle and larger width. The gear tooth geometry proposed required non conventional tools with a pressure angle of 40 °.

Magalhães *et al.* worked on the 'low loss' concept and developed three different helical shapes with different modules, but all the gear sets were designed with the same load carrying capacity. The gears developed by Magalhães *et al.* are feasible with conventional tools (α_z=20 °). The results published by Magalhães *et al.* clearly show that the tooth geometry can be modified to improve efficiency without significant change in the safety factors [148, 199].

In gear design, tip relief is often used to prevent premature engagement and stress concentration on the tip of the tooth [200] which is also helpful for increased load carrying capacity. Velex and Ville [201], Frazer *et al.* [202] and Joachim *et al.* [203] proposed the tip relief as a possible way to reduce the power loss of gears. Velex and Ville say that profile relief can reduce the friction losses by suitable combination of tip relief amplitude and extent, and several combinations give similar performances. The tip relief reduces the tooth load at the beginning of the contact path where the sliding speed is very high resulting in more efficient gears.

In this current chapter, three new helical gear geometries based on 'low loss' concept will be presented and tested in a FZG machine. The gears will be lubricated

with wind turbine gear oils, aiming to understand the possible energy savings achievable combining different gear geometries and oil formulations.

The power loss model calibrated in Chapter 6 will be applied for different lubricants, gear geometries and test conditions. Additionally, the power loss model will be used to forecast the oil sump temperature by coupling a thermal model.

7.2. Low loss gears

The power loss along the path of contact, as previously stated in the literature revision of Chapter 4, consists in the product of the sliding velocity, the load and the coefficient of friction at each point along the path of contact, as presented in equation (7.1).

$$P_{VZP}(x) = F_N(x) \cdot v_g(x) \cdot \mu(x) \tag{7.1}$$

The average power loss along the path of contact can be obtained with equation (7.2).

$$P_{VZP} = \frac{1}{p_b} \int_A^E P_{VZP}(x)dx \tag{7.2}$$

Using the average power loss concept, with a constant coefficient of friction along the path of contact, a gear loss factor can be deduced and presented in equation (7.3).

$$H_{VL} = \frac{1}{p_b} \int_0^b \int_A^E \frac{F_N(x,y)}{F_{bt}} \cdot \frac{v_g(x,y)}{v_{tb}} dxdy \tag{7.3}$$

In practice, reduce the gear loss factor is necessary in order to reduce the meshing gears power loss, as stated by the Ohlendorf's equation (7.4).

$$P_{VZP} = P_{IN} \cdot H_{VL} \cdot \mu_{mZ} \tag{7.4}$$

To study the influence of the geometry in the gear loss factor, it will be assumed that the gear geometry will affect the coefficient of friction in a smaller way than oil formulation does, i.e. the coefficient of friction will be disregarded for the moment.

Equation (7.3) gives some insight about how to reduce the gear loss factor. In fact, the gear loss factor decreases if the product $F_N(x) \cdot v_g(x)$ decreases, and if the length of the path of contact (see (7.5)) also decreases.

$$\overline{AE} = g_\alpha = \sqrt{ra_1{}^2 - rb_1{}^2} + \sqrt{ra_2{}^2 - rb_2{}^2} - \sqrt{a^2 - (rb_1 + rb_2)^2} \tag{7.5}$$

For the same centre distance (a) and transmission ratio ($i = z_2/z_1$), the working pitch diameter (d') should be the same, resembling that the path of contact is smaller

for a smaller addendum diameter. This is feasible, introducing a smaller module and a positive profile shift (x_{zi}), since the addendum diameter is given by equation (7.6).

$$da_i = d_i + 2 \cdot m \cdot (x_{zi} + h_{aP} - k_z) \tag{7.6}$$

The reduction of the path of contact will decrease the maximum sliding velocity but also decrease the transverse contact ratio (ϵ_α). A very low contact ratio can produce meshing discontinuity (if $\epsilon_\alpha < 1$), which should never happen in spur gears, and might be overcome for helical gears, selecting an adequate helix angle to produce an overlap contact ratio (ϵ_β).

Theoretically, a smaller module reduces the power loss but also increases the failure risk by root or flank breakage and pitting. A positive effect is the increased resistance to scuffing due to the sliding velocity reduction. Since the safety factors should not be disregarded, some design procedures must be considered.

According to Höhn *et al.* [106] it is expected to reach a low loss geometry by performing the following optimization steps:

- Use high profile shift, always positive, for load reduction in the zones of high sliding speed (beginning and end of contact);
- Reduce the module down to tooth root safety limit;
- Reduce the transverse contact ratio down to the pitting safety limit;
- Use of a root fillet radius as large as possible;
- Increase the pressure angle;
- Increase the face width;
- Introduce a helix angle to produce an overlap contact ratio that compensate the transverse contact ratio reduction.

As stated by Höhn, one of the important steps is to increase the pressure angle. This proves to be quite effective in designing quite efficient gear geometries, but it is also true that the load transmitted to the bearings will increase, which can be a problem for the bearings life. Only 'low loss' gears produced with conventional tools (α_z=20 °) will be studied.

In order to advise the reader for the direct influence of each parameter on the power loss, the local gear loss factor (H_{VL}) will be calculated for different gear geometries, keeping the transmission ratio and the centre distance. A parametric study changing the module, face width, the helix angle and the amount of tip relief was performed. The gears were designed considering positive profile shifts both

in the pinion and wheel, reducing the gear loss factor and maximizing the safety factors.

Figure 7.1(a) shows the influence of the module on the gear loss factor. As expected, a lower module produces a reduction in the gear loss factor.

The influence of the tooth width is not very significant, since the higher the tooth width, the lower will be the load per unit length resulting in almost constant gear loss factor as presented in Figure 7.1(b). However, a higher face width improves the safety factors.

The influence of the helix angle is presented in Figure 7.1(c). The helix angle will not modify significantly the gear loss factor, since a different angle implies different profile shifts. In this case the helix angle is selected in order to produce an adequate mesh (contact ratio) and, at the same time, does not apply very high axial loads on the rolling bearings.

The tip relief influence is presented in Figure 7.1(d). As expected, the higher the tip relief, the lower is the gear loss factor.

7.2.1. Gears designed

Three different helical geometries were developed, based on the standard micropitting FZG type C gear. A standard rack profile was used with properties described in Table 7.1.

Table 7.2 presents the main properties of each gear geometry. The gears were designed imposing a maximum Hertzian pressure similar to that of C14 spur gear and imposing similar safety factors.

Figure 7.2 shows the load distribution and the corresponding local Hertzian pressure along the plane of action of each gear geometry, for an input torque on the wheel equal to 323 Nm, which corresponds to the standard FZG K9 load stage.

It is clear that the maximum Hertzian pressure is very similar for all the gear geometries other than H951. In the case of H951 gear both the load distribution and the Hertzian pressure remain almost constant along the path of contact. In the case of gear H951 the number of teeth simultaneously in contact is almost constant,

Table 7.1.: Basic rack profile used for gear cutting.

Property	Symbol	Value
Pressure angle	α_z	20 °
Root fillet radius	ρ_{fP}	0.3
Dedendum tooth depth	h_{fP}	$1 \cdot$ m
Addendum tooth depth	h_{aP}	$1.25 \cdot$ m

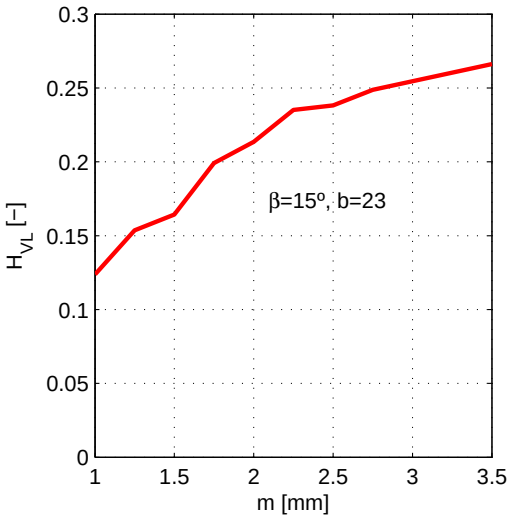

(a) Influence of the module.

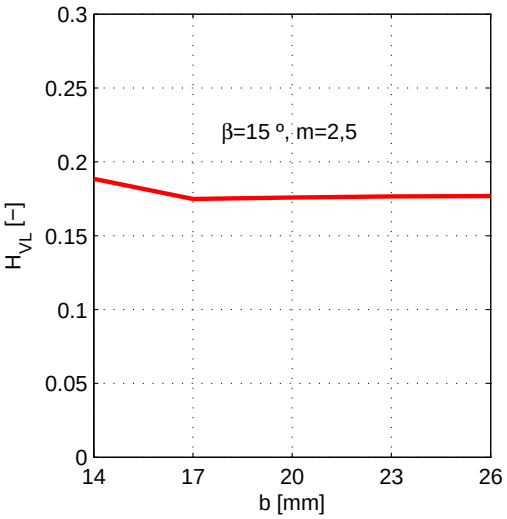

(b) Influence of the face width.

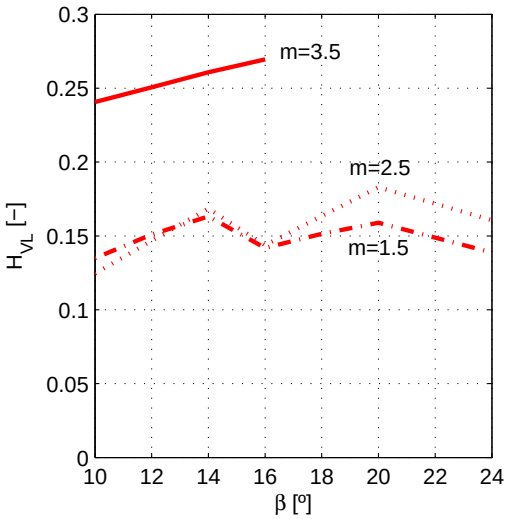

(c) Influence of the helix angle.

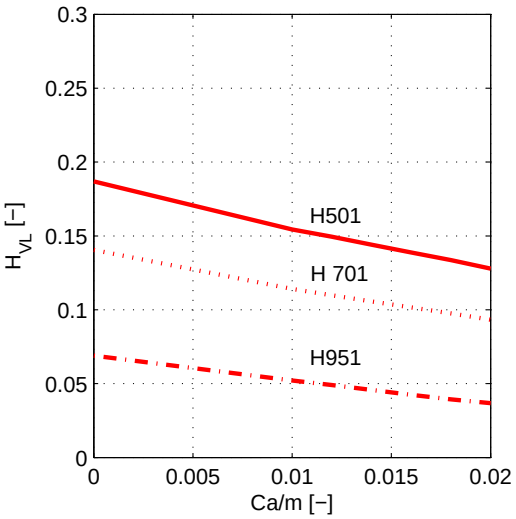

(d) Influence of the tip relief.

Figure 7.1.: Influence of module (m), face width (b), helix angle (β) and tip relief in gear loss factor.

Table 7.2.: Geometric properties of the C14, 501, 701 and 951 gears.

Property	Units	Pinion	Wheel	Pinion	Wheel	Pinion	Wheel	Pinion	Wheel
z	[-]	16	24	20	30	28	42	38	57
m	[mm]	4.5		3.5		2.5		1.75	
a	[mm]	91.5							
α_z	[°]	20							
α_{ztw}	[°]	22.44		22.12		22.12		28.34	
β_z	[°]	0		15					
b	[mm]	14		23		17		23	
x	[-]	+0.1817	+0.1715	+0.1809	+0.0891	+0.2290	+0.1489	+1.6915	+2.0003
d	[mm]	72.00	108.00	72.47	108.70	72.47	108.70	68.85	103.27
d'	[mm]	73.20	109.80	72.47	108.70	73.20	109.8	73.2	109.80
d_a	[mm]	82.46	118.37	80.67	116.27	78.55	114.39	76.23	111.73
d_b	[mm]	67.66	101.49	67.81	101.72	67.82	101.72	64.42	96.64
ϵ_α	[-]	1.438		1.460		1.516		0.934	
ϵ_β	[-]	-		0.541		0.560		1.083	
ϵ_γ	[-]	1.438		2.001		2.076		2.017	
g_α	[-]	19.10		15.55		11.53		4.98	
S_F	[-]	1.15	1.20	1.71	1.72	0.96	0.95	0.97	1.02
S_H	[-]	0.66	0.72	0.92	0.95	0.82	0.84	0.88	0.89
S_S	[-]	1.79		2.65		2.66		3.6	
Material	[-]	20MnCr5							

along the path of contact. The path of contact is slightly smaller than the transverse pitch, which is not the best practice in gear design, but the total contact ratio is similar to the other tooth geometries. The helix angle produces an overlap ratio that assures the correct meshing of the gear set ($\epsilon_\beta > 1$).

It is clear that H501 (Figure 7.2(c) and 7.2(d)) and H701 (Figure 7.2(e) and 7.2(f)) have a smoother load transition than the reference spur gear (Figures 7.2(a) and 7.2(b)). In summary, all the helical gear geometries will result in lower average load per unit length and lower Hertzian pressure and consequently higher flank safety factor.

The load conditions are always better than those of a spur gear, transmitting the same nominal torque. However, some drawbacks are related with the use of helical gears instead of spur: a larger face width is necessary and the helix angle generated axial loads, which imply the use of different rolling bearings.

The gear loss factor equation (7.3), solved with the algorithm detailed in Appendix D, is a dimensionless parameter that represents the product of the load by the sliding velocity, at each point in the plane of action ($F_N(x,y) \cdot v_g(x,y)$). It becomes dimensionless dividing by the normal base force, the tangential base speed, at pitch point, and the transverse pitch ($p_b \cdot F_{bt} \cdot v_{tb}$).

The evolution of the dimensionless parameter given by equation (7.7), along the plane of action, is presented in Figure 7.3 for each gear geometry.

$$h_{VL}(x,y) = \frac{1}{p_b} \cdot \frac{F_N(x,y)}{F_{bt}} \cdot \frac{v_g(x,y)}{v_{tb}} \tag{7.7}$$

At the beginning and at the end of the contact path, points A and E, respectively, the helical gears show a maximum of the h_{VL} parameter. In the case of gears H501 and H701, this maximum is higher than for C14 spur gear. However, the helical gear geometries show a smoother evolution of the h_{VL} parameter along the plane of action, compared to spur gear C14.

The volume below each surface is the actual gear loss factor H_{VL}, for each gear geometry, and it is clear that the helical gears promote a smaller loss factor. The values of the loss factor decrease from gear H501 to H951 (${H_{VL}}^{H501} > {H_{VL}}^{H701} > {H_{VL}}^{H951}$) mainly due to the reduction of the path of contact ($\overline{AE}$). Table 7.3 shows the gear loss factor and the plane of action area, for each gear geometry.

7.3. Torque loss in 'low loss' gears

7.3.1. Materials and methods

The power loss tests were performed using the same test procedure presented in Chapter 6. The low loss gears were assembled in the test gearbox while the slave

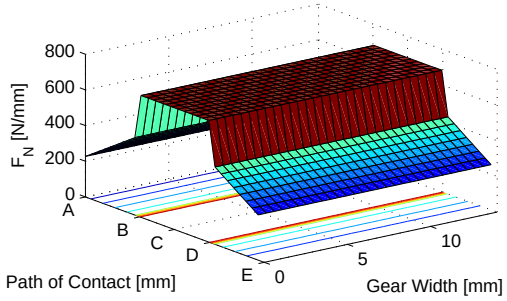

(a) C14.

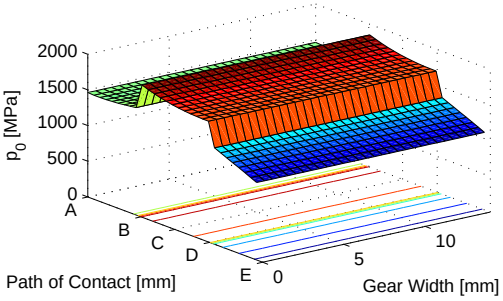

(b) C14.

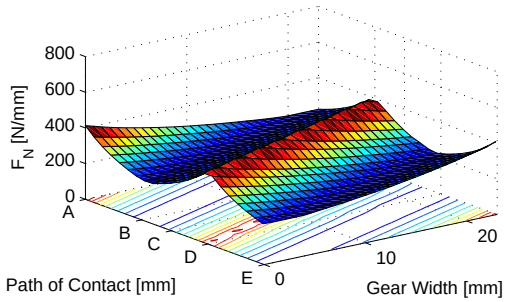

(c) 501.

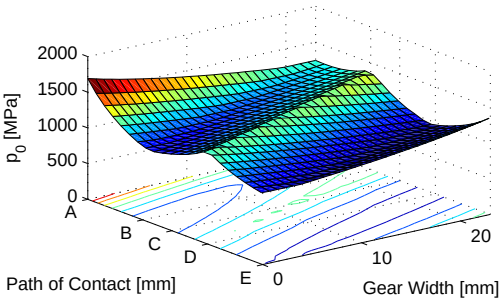

(d) 501.

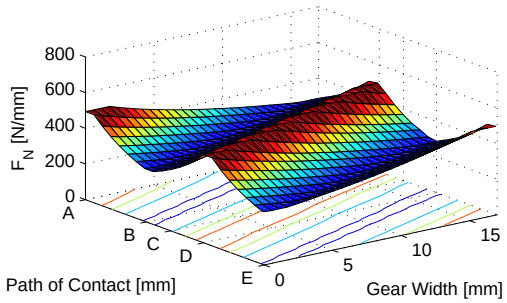

(e) 701.

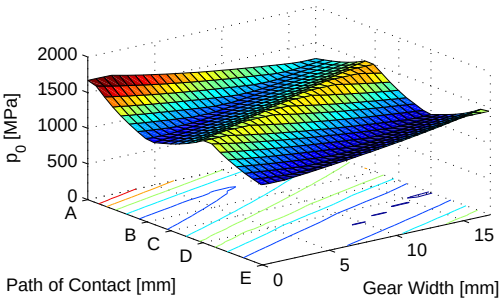

(f) 701.

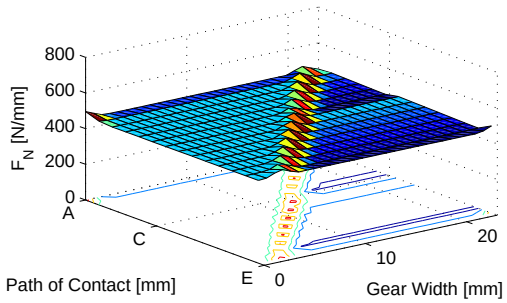

(g) 951.

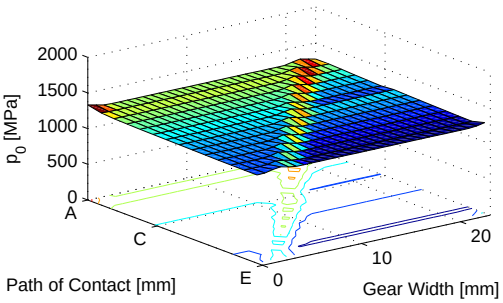

(h) 951.

Figure 7.2.: Load distribution (F_N) and Hertz pressure (p_0) along the path of contact for different gear geometries.

Gear geometry	C14	H501	H701	H951
H_{VL} [-]	0.1949	0.1869	0.1404	0.0689
$\overline{AE} \cdot b$ [mm^2]	267.4	357.7	196.0	114.5

Table 7.3.: Gear loss factors and plane of action area calculated for each gear geometry.

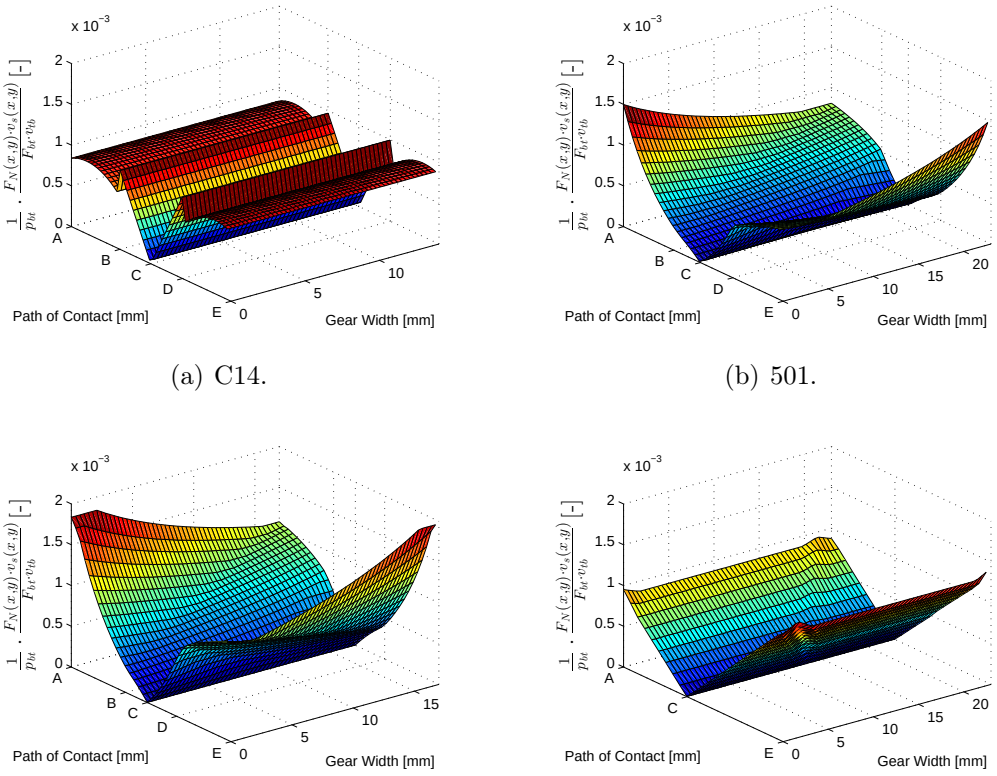

(a) C14.

(b) 501.

(c) 701.

(d) 951.

Figure 7.3.: Dimensionless parameter h_{VL} representative of the instantaneous product of force and sliding velocity along the path of contact.

gearbox remained the same. The new configuration is schematically presented in Figure 7.4.

The operating conditions were the same as for C40 gear tests. However, an additional load stage was included (K11) and the gears operated under the Hertzian pressures and torques presented in Table 7.4. The loads and Hertzian pressures were calculated for H501 gear geometry. It is expected that H701 and H951 produce slightly higher normal loads since the operating pressure angle is higher. The test procedure is resumed in Figure 7.5.

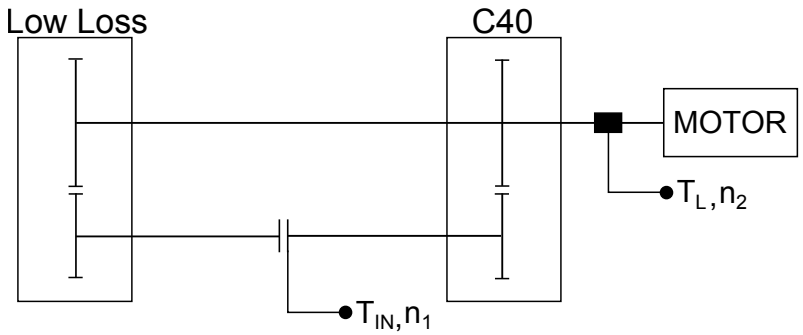

Figure 7.4.: Schematic view of the FZG gear test rig for low loss tests.

Table 7.4.: Operating conditions regarding the torque loss tests.

	Gears			Rolling bearings	
K_{FZG}	T_W [Nm]	F_{bn} [N]	p_H [MPa]	F_r [N]	F_a [N]
K1	4.95	100	171	37	24
K5	104.97	2128	787	777	518
K7	198.68	4027	1083	1471	980
K9	323.27	6553	1382	2393	1594
K11	478.77	8990	1710.2	3653.5	2186.6

Under oil jet lubrication conditions, it is important to guarantee that the pressure inside the gearbox is never lower than the ambient pressure. If the pressure becomes lower than the ambient pressure, the oil acumulates inside the gearbox and a dip lubrication condition is created with consequent abrupt increase of temperature and torque loss. Due to the consequent lower pressure inside the gearbox a lot of foam is created worsening the lubrication ability of the oil.

7.3.2. Film thickness on the meshing gears

The average value of the specific film thickness along the path of contact, for each test condition, is displayed in Figures 7.6(a), 7.6(b) and 7.6(c) for gears H501, H701 and H951, respectively. At 200 and 400 rpm all the gear geometries operate under mixed film lubrication conditions with an oil jet temperature equal to 80 °C. H501 and H701 gears have similar specific film thickness, while H951 gear has a slightly higher specific film thickness due to the highest equivalent radius of contact and also higher sum of velocities. At 1200 rpm the tests run under full-film conditions.

It is possible that the values presented in Figure 7.6 are overestimated as film

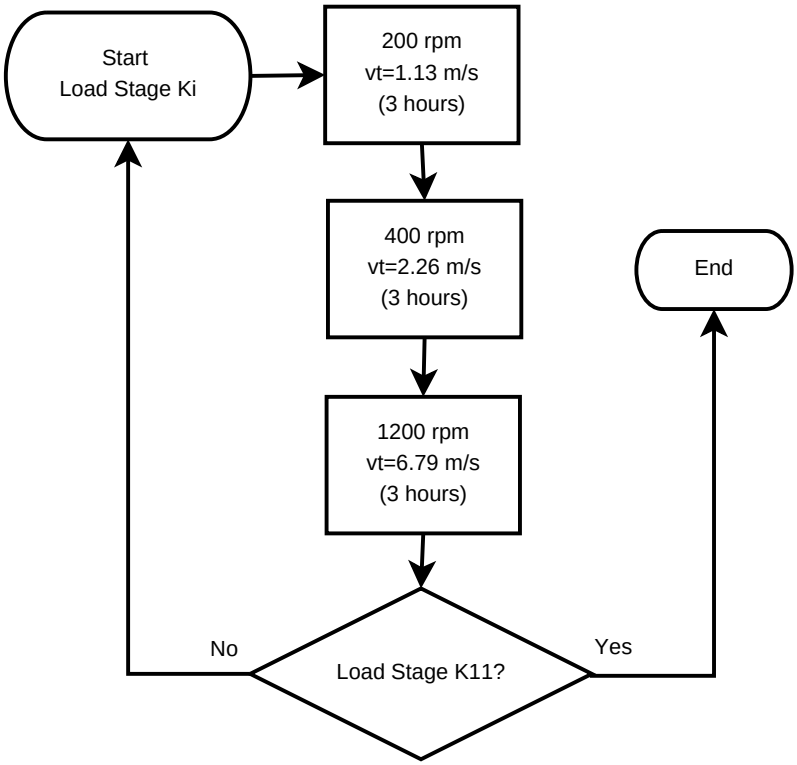

Figure 7.5.: Test procedure sequence.

thickness measurements suggested, but it is not possible to conclude if they are overestimated or not in the case of gears. However, it is clear that mixed and full-film conditions occur.

7.3.3. Experimental Results

The experimental torque loss results are presented in Figure 7.7 for gears H501 and H951, for all load stages (K1, K5, K7, K9 and K11) and for several different wind turbine gear oil formulations. The H701 low loss gear was only tested with MINR and PAGD oil and will be discussed later.

As presented in Chapter 6, load stage K1 was performed to quantify the no-load losses of the gears. It is very interesting to observe that the total torque loss of the test and slave gearboxes, in load stage K1, is higher in the configuration "C40/C40" than in the configuration "Low loss/C40", which put into evidence comparing Figures 7.7(a) and 6.8(a). This was expected since the tooth width and the module of the low loss gears are smaller than in gear C40 which is reported in literature as influencing factors [75, 86]. Comparing the different low loss gear geometries, the H951 generate lower torque loss than H501 in load stage K1.

From load stage K5 up to K9, the torque loss at low speed is clearly influenced by

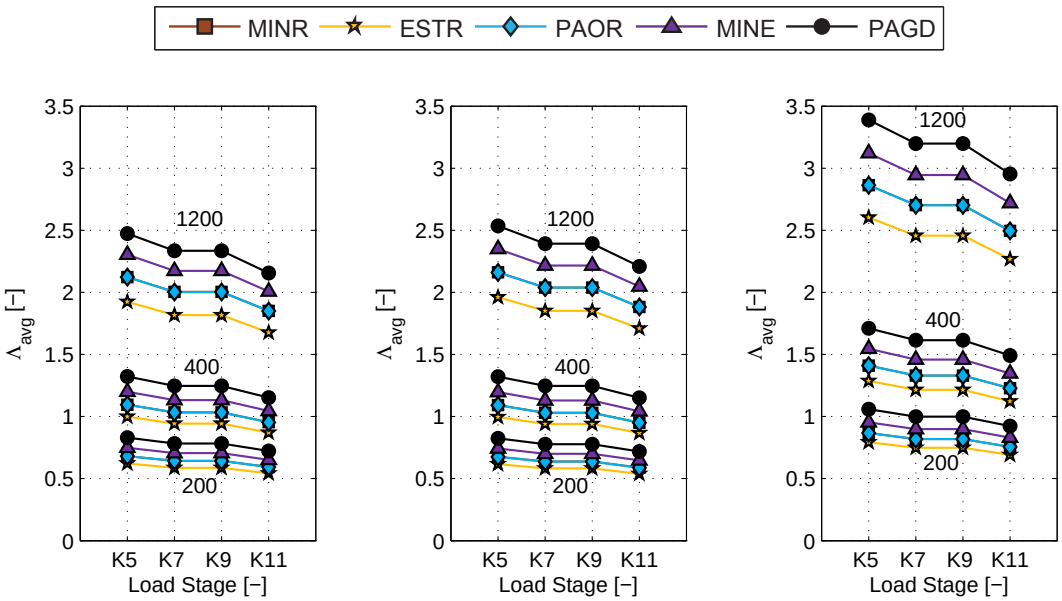

(a) H501. (b) H701. (c) H951.

Figure 7.6.: Average specific film thickness prediction for low loss gears.

the coefficient of friction of each oil. At low speeds, the PAGD oil can reduce the torque loss in comparison with the other formulations. When the speed increases, the PAGD oil has a different behaviour, since its higher viscosity index seems to affect the high speed behaviour, i.e higher speed promoted a reduction of the effect of the coefficient of friction by means of the no-load losses generated.

MINR, with significantly lower operating kinematic viscosity, generated much higher torque loss at lower rotational speeds. However, when speed increases the difference in performance in comparison with other formulations is much lower. The mineral oil with PAMA thickener always generated lower torque loss than the MINR oil.

The friction behaviour of each oil formulation seems to be the same described in Chapter 6 for C40 gears, no-matter what is the gear geometry tested. The gear geometry strongly influences the load dependent losses, as observed comparing Figures 7.7(c) with 7.7(d) for K5, 7.7(e) with 7.7(f) for K7 and 7.7(g) with 7.7(h) for K9. Gear H951, designed to generate low meshing gear losses, by reducing the module and increasing the number of teeth [106, 199], clearly reducers the torque loss of the FZG test gearbox.

It is very interesting to compare Figures 7.7(i) and 7.7(j). The torque loss at 200 rpm for oil MINR, is reduced by 16 %. The same comparison for the MINR oil with gear H501 and PAGD oil with gear H951, shows a torque loss reduction of 29 %.

The influence of the gear geometry, discussed before, is well illustrated in Figure

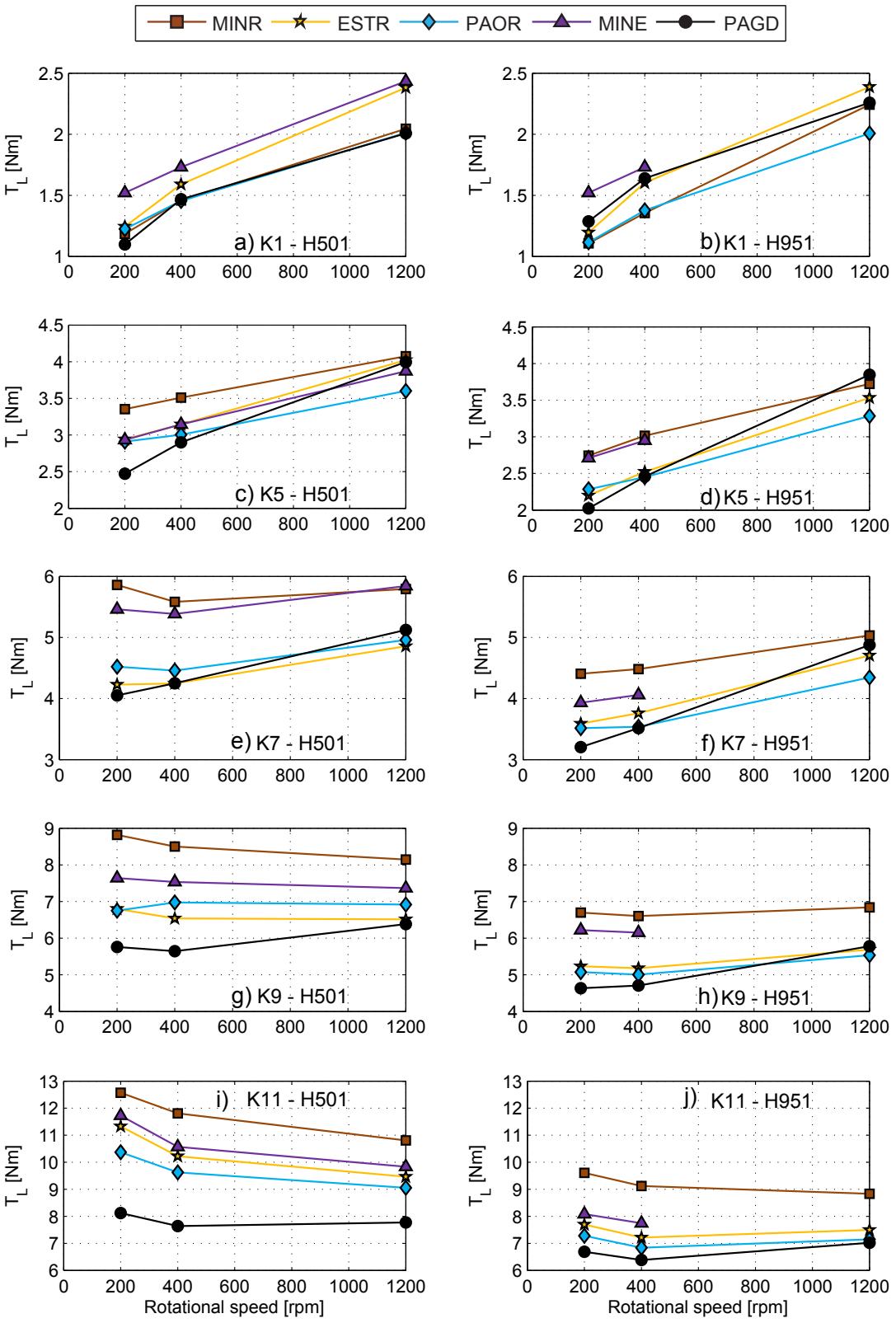

Figure 7.7.: Experimental total torque loss for low loss gears. H501 on left and H951 on right.

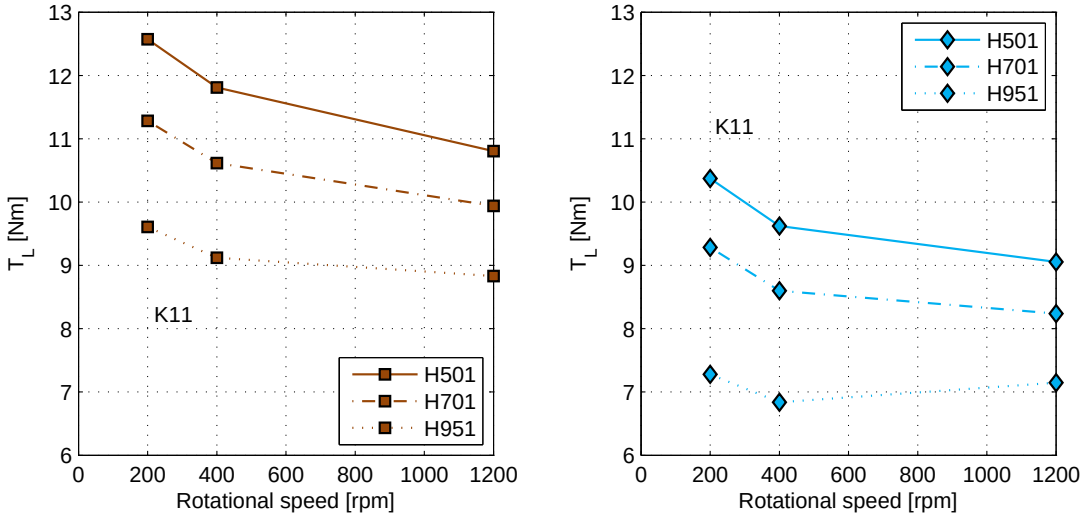

(a) MINR.

(b) PAOR.

Figure 7.8.: Experimental results for load stage K11 for all gear geometries.

7.8, for load stage K11 and with MINR and PAOR gear oils. The influence of the gear geometry is clear and the results follow the expected torque loss reduction predicted by the gear loss factor. It is important to observe that the transition from 400 to 1200 rpm with H951 gear geometry is different from that verified with the other gear geometries. H501 and H701 reduced the torque loss with increasing rotational speed. H951 torque remained very similar from 400 to 1200 rpm, since the specific film thickness of that geometry is much higher at 400 rpm and yet very close to the full-film conditions. When the speed increases from 400 to 1200 rpm the torque loss of H951 remains the same or even increases.

7.4. Power loss model

The power loss model will be applied to predict the torque loss generated by the FZG gearboxes, using the experimental results presented in section 7.3.3. The power loss generated by the rolling bearings was calculated as presented in Chapter 5. The no-load losses were determined using equation (7.8).

$$P_{VZ0} = P_V^1 - P_{VL}^1 - P_{VD} \tag{7.8}$$

The application of the model aims to assess the validity of the coefficient of friction calibrated in Chapter 6, as well as the gear loss factor proposed in this work. In equation 4.37, the gear tooth width, b, was replaced by the minimum of the sum of

the lengths of the contacting lines for the helical gears along the path of contact, keeping the original idea of Schlenck's equation, since b is the minimum length of contact in a spur gear.

$$\mu_{mZ} = 0.048 \cdot \left(\frac{F_{bt}/l_{min}}{\nu_{\Sigma C} \cdot \rho_{redC}} \right)^{0.2} \cdot \eta^{-0.05} \cdot R_a^{0.25} \cdot X_L \tag{7.9}$$

7.4.1. Validation

The model can accurately predict the power loss of the MINR oil, no matter the helical gear used, H501 or H951, as shown by the results presented in Figure 7.9. Figure 7.10 shows the results for PAOR and the quality of the prediction is also very good.

The application of the model for the two different geometries shows the effect of the gear loss factor used, assuming that the rolling bearings power loss as well as the other sources are well estimated. Under this assumption the gear loss factor is reliable. The lubricant parameter (X_L) is also reliable to predict the actual power loss of the gears meshing teeth.

One comment about the lubrication regime is necessary. The tests at 1200 rpm lay under full film conditions, mainly for the synthetic formulations. Schlenck's equation, starts to deviate from the actual coefficient of friction, as advised by Höhn *et al.* [66], when the full-film conditions are reached. So, and since the model produces good results, it is advised to predict the losses for a specific film thickness of the gears, only when Λ <3.

7.4.2. New coefficient of friction formula

The new coefficient of friction formula proposed in Chapter 6 is here again implemented to predict the coefficient of friction of H501 gears lubricated with MINR for 200, 400 and 1200 rpm. The new coefficient of friction follows quite well the coefficient of friction based on experimental results at 200 and 400 rpm, that lay under mixed lubrication. However, at 1200 rpm the tests are performed under full-film conditions and the coefficient of friction starts to deviate from the measured coefficient of friction, as expected and discussed in Chapter 6.

The coefficient of friction worked for these particular cases. However, it would be better to have a much large number of geometries and perform a test campaign with the purpose of calibrate the coefficient of friction based on the modified Hersey parameter. With a dedicated test campaign it is possible to address the influence of the influence and of the lubrication simultaneously.

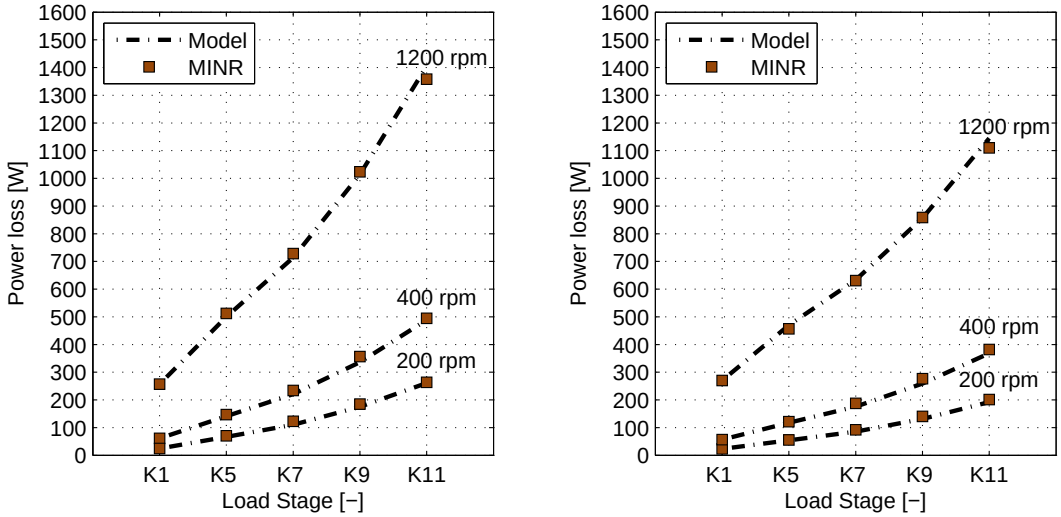

(a) H501. (b) H951.

Figure 7.9.: Power loss model validation for H501 and H951 gear geometries lubricated with MINR.

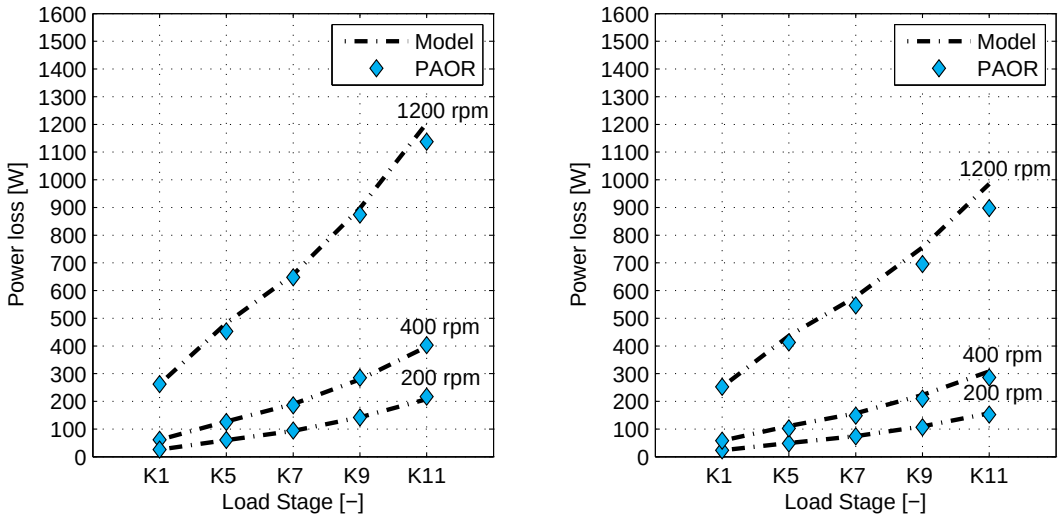

(a) H501. (b) H951.

Figure 7.10.: Power loss model validation for H501 and H951 gear geometries lubricated with PAOR.

7.4.3. Influence of speed and load in each power loss source

The power loss model was calibrated and it allows to predict the actual power loss of the FZG gearbox. The model also allows to verify the weight of each power

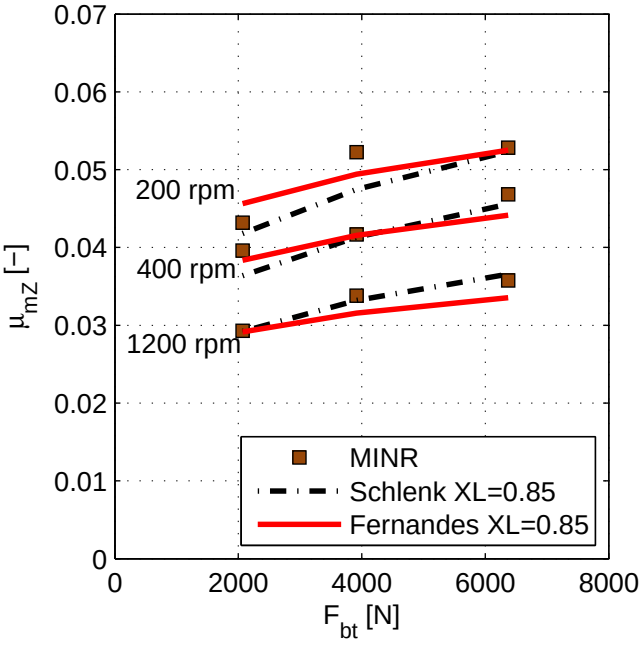

Figure 7.11.: Coefficient of friction determined based on experimental results vs. Schlenck and Fernandes formulas with adjusted X_L.

loss source in the overall gearbox efficiency.

Figures 7.12(a) and 7.12(b) show the power loss predicted by each loss mechanism (P_{VZP}, P_{VZ0}, P_{VL}, P_{VD}) for gears H501 and H951, lubricated with MINR oil, under an applied torque of 300 Nm. In the case of gear H501 all power losses increase with increasing rotational speed, as expected, and the meshing gear power loss (P_{VZP}) is dominant. In the case of gear H951, the rolling bearing losses are dominant in the total power loss, because this gear geometry keeps the meshing gears power loss very low in all speed range.

The influence of the applied torque is presented in Figures 7.12(c) and 7.12(d). The meshing gear power loss increase with the applied torque, as expected, and they are dominant in the case of gear H501.

To better understand the influence of speed and torque on each power loss source and on the global efficiency of the gearbox, the loss degree is presented in Figure 7.13. A high loss degree means a negative influence in the gearbox efficiency, see equation (7.10).

$$\xi_V = 1 - \eta_z \tag{7.10}$$

The loss degree for each meachnism are given by equations (7.11), (7.11), (7.12), (7.13) and (7.14).

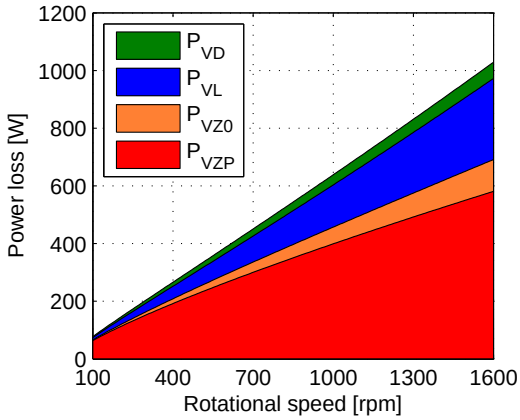

(a) Influence of speed at 300 Nm (501).

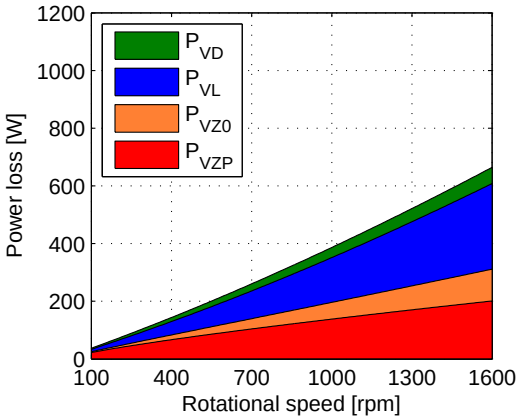

(b) Influence of speed at 300 Nm (951).

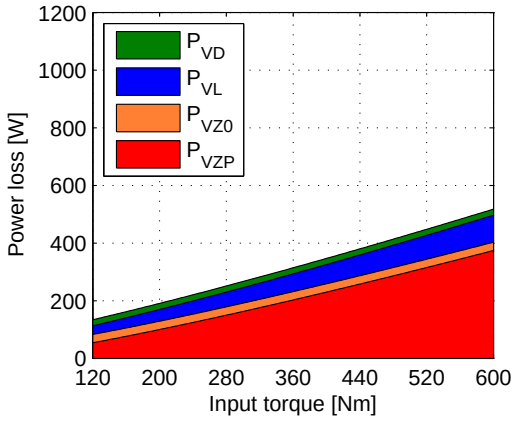

(c) Influence of load at 600 rpm (501).

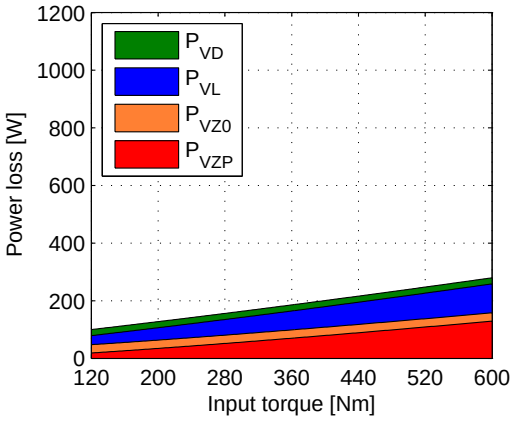

(d) Influence of load at 600 rpm (951).

Figure 7.12.: Evolution of each power loss source with MINR oil for H501 and H951 gear geometries.

$$\xi_{VZP} = \frac{P_{VZP}}{P_{IN}} \tag{7.11}$$

$$\xi_{VZ0} = \frac{P_{VZ0}}{P_{IN}} \tag{7.12}$$

$$\xi_{VL} = \frac{P_{VL}}{P_{IN}} \tag{7.13}$$

$$\xi_{VD} = \frac{P_{VD}}{P_{IN}} \tag{7.14}$$

When speed increases, for a given torque, ξ_{VZP} decreases while ξ_{VD}, ξ_{VL} and ξ_{VZ0} increase. When the torque increases, ξ_{VZP} increases and ξ_{VD}, ξ_{VL} and ξ_{VZ0})

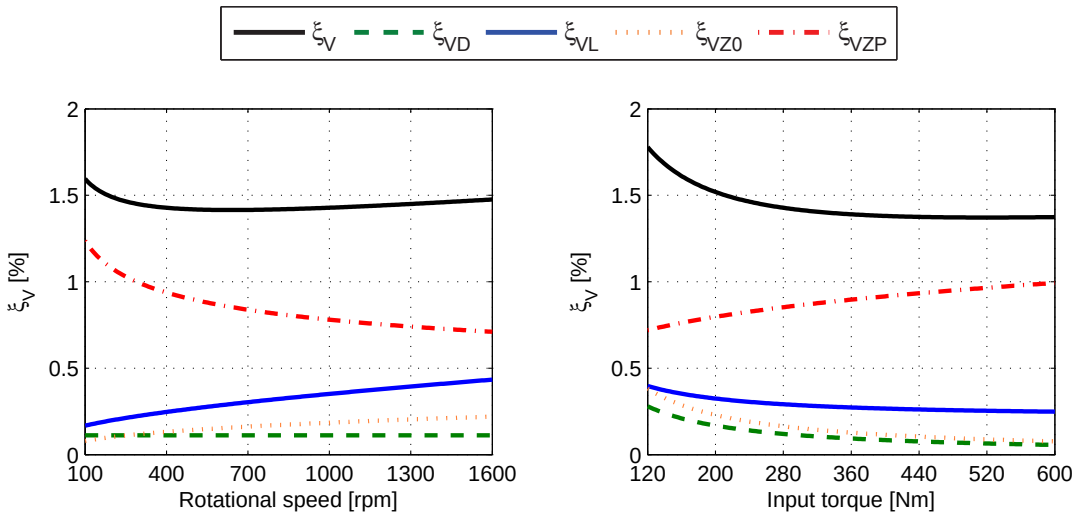

(a) Influence of speed at T_W=300 Nm.

(b) Influence of torque at n_2=600 rpm.

Figure 7.13.: Loss degree of each power loss source for a H501 gear lubricated with MINR.

decrease.

7.4.4. Thermal coupling

In Chapter 4 a brief review about the thermal rating of gearboxes was presented. In the Chapter 6 the coefficient of friction was characterized for different wind turbine gear oils and the power loss model was calibrated.

Furthermore, the power loss model was validated for a large number of torque loss measurements obtained with different gear geometries, different rolling bearings and also different oil formulations. However, the tests were always performed under constant temperature. In real applications the oil temperature is frequently an unknown and engineers need a tool to predict both the power loss and the actual oil temperature.

A test campaign for two different ISO VG 320 candidate blends for wind turbine gear oils, one PAO and a Mineral base oil, were performed. The physical characteristics of the lubricants can be resumed in Table 7.5.

The tests were performed with "C40/H701" FZG configuration and the test procedure described on section 7.3.1 was used. The lubrication method was changed from oil-jet lubrication to dip lubrication, with 1 l of oil in each gearbox. The temperature was kept free and the gearboxes worked for 4 hours under each test condition in order to stabilize the temperature.

The mechanical power loss was measured and modelled, using the lubricant parameters presented in Table 7.6.

Table 7.5.: Physical properties of the candidate Blends.

Property	Unit	Blend A	Blend B
Base oil	[-]	PAO	Mineral
ν @ 40 °C	$[cSt]$	314.8	319.4
ν @ 100 °C	$[cSt]$	39.46	27.8
VI	[-]	178	117
ρ @ 15.6 °C	$[g/cm^3]$	0.851	0.888

Table 7.6.: Oil constants for the power loss model simulation.

	Gears	Ball bearings		Roller bearings	
Oil	X_L	μ_{bl}	μ_{EHD}	μ_{bl}	μ_{EHD}
Blend A	0.70	0.049	0.044	0.039	0.010
Blend B	0.85	0.058	0.056	0.035	0.018

The mechanical power loss model and thermal model (Höhn *et al.* [66]) are defined by equations (7.15) and (7.16), respectively.

$$P_V = \underbrace{P_{VZ0}}_{P_V^{1\,exp} - P_{VL}^1 - P_{VD}} + \underbrace{P_{VZP}}_{P_{IN} \cdot H_{VL} \cdot \mu_{mZ}(X_L)} + \underbrace{P_{VL}}_{New\ SKF\ Model} + \underbrace{P_{VD}}_{Linke\ Equation} \tag{7.15}$$

$$Q_T = \underbrace{Q_{conv} + Q_{rad}}_{(\alpha_{conv} + \alpha_{rad}) \cdot A_{ca} \cdot (\theta_{oil} - \theta_\infty)} \tag{7.16}$$

The conduction influence was disregarded, as suggested by the model proposed by Höhn *et al.* [66].

To determine the oil temperature and the corresponding mechanical power loss it is necessary to solve iteratively equation (7.17). No other input was given to the algorithm, except the initial solution, made equal to the ambient temperature, assumed to be θ_∞=25 °C.

$$P_V\left(\theta_{oil}\right) = Q_T\left(\theta_{oil}\right) \tag{7.17}$$

The gear no-load losses were determined based on the load stage 1 experimental results. The experimental results will be accurate for load stage K1, but when the load increase the temperature will rise and the churning losses will change because of decreasing viscosity and consequent change in the generated losses. The Mauz [75]

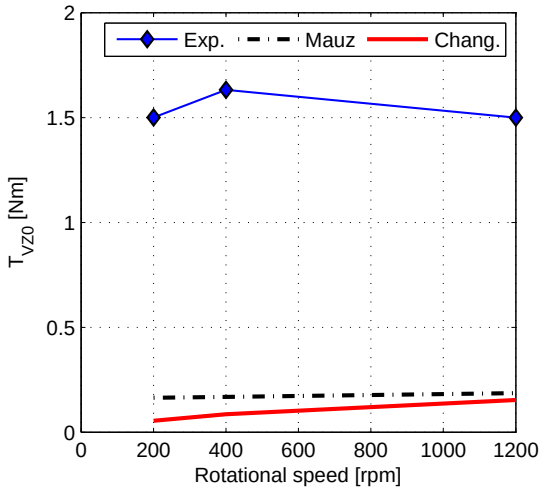

Figure 7.14.: Experimental results vs. Mauz and Changenet model predictions.

and Changenet [86] models were used to predict the actual no-load gear losses. The model proposed by Mauz [75] doesn't consider the oil viscosity.

The measurements performed under load stage K1, were used to compare with Changenet and Mauz predictions. The results are presented in Figure 7.14 and it is clear that any model is able to predict the measured no-load power losses.

The churning loss models were calibrated for tangential speeds much higher than those used in the present work. Furthermore, the gear and gearbox geometries are significantly different. It results in increasing no-load torque loss with increasing speed, which for low rotational speeds will produce negligible results.

The no-load losses may be calculated based on measurements according to equation (7.18). However, the values are only valid for the operating viscosity of the experimental measurement.

$$P^1_{VZ0} = P^{1\,exp}_V - P^1_{VL} - P_{VD} \tag{7.18}$$

Since the operating temperature and viscosity change when the applied torque increases, the no-load losses will change accordingly. Since the models proposed by Changenet or Mauz deviate very much from the experimental results, the measurements under load stage K1 will be considered. The no-load gear losses predictions found in literature are in general related to the lubricant Reynolds number. In this way the no-load losses for each rotational speed can be estimated taking the measurement at load stage K1 as reference according to equation (7.19).

$$P^i_{VZ0} = P^1_{VZ0} \cdot \frac{Re^{i\,-0.21}}{Re^{1\,-0.21}} \tag{7.19}$$

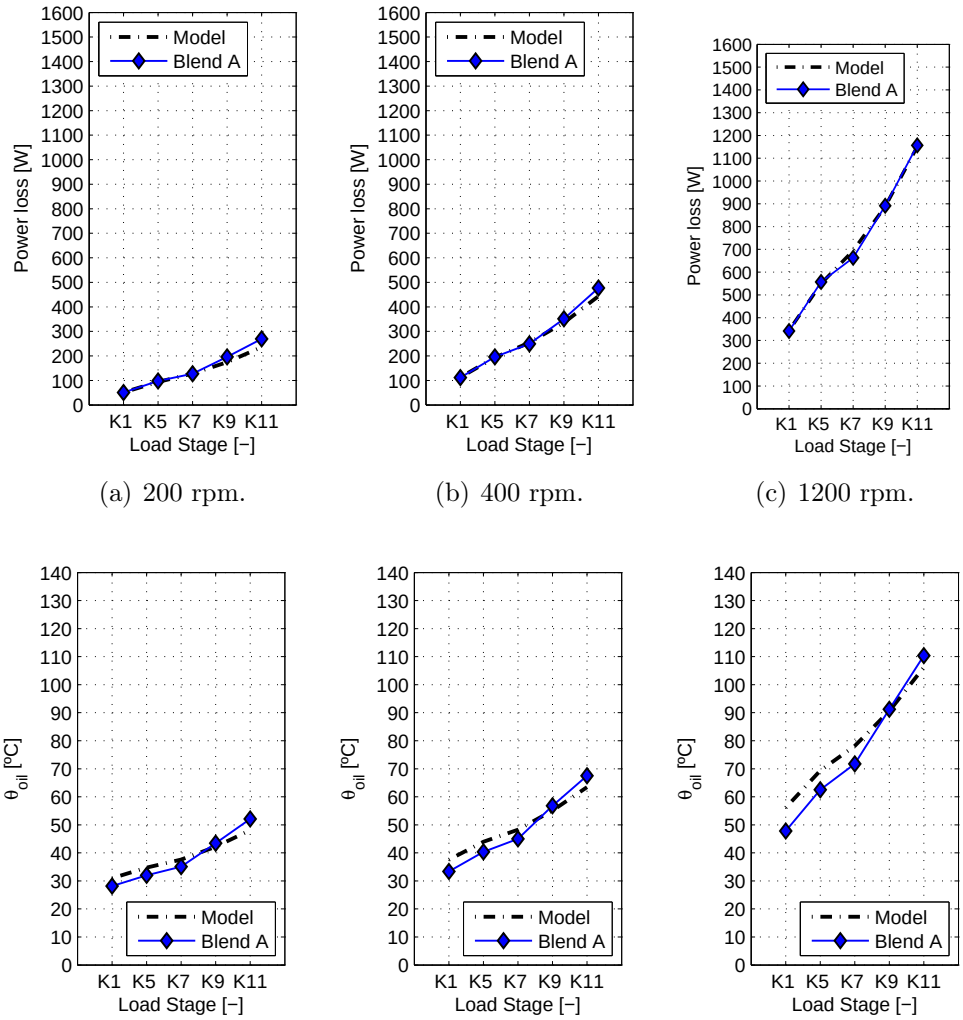

(a) 200 rpm. (b) 400 rpm. (c) 1200 rpm.

(d) 200 rpm. (e) 400 rpm. (f) 1200 rpm.

Figure 7.15.: Power loss and temperature predictions vs experimental results for Blend A.

The Reynolds number takes into account the influence of the flow regime (laminar or turbulent) through the lubricant viscosity, under constant speed.

The power loss as well as the oil temperature were measured during the test campaign. The prediction of the coupled thermo-mechanical model, gave the power loss and oil sump temperature, which are compared to the corresponding experimental measurements in Figure 7.15 for Blend A and in Figure 7.16 for Blend B.

The coupled thermo-mechanical model can actually predict quite well the power loss both for Blend A and Blend B. The relative error is for the majority of the tested conditions lower than 5%. However, for some tests under load stage K11, the

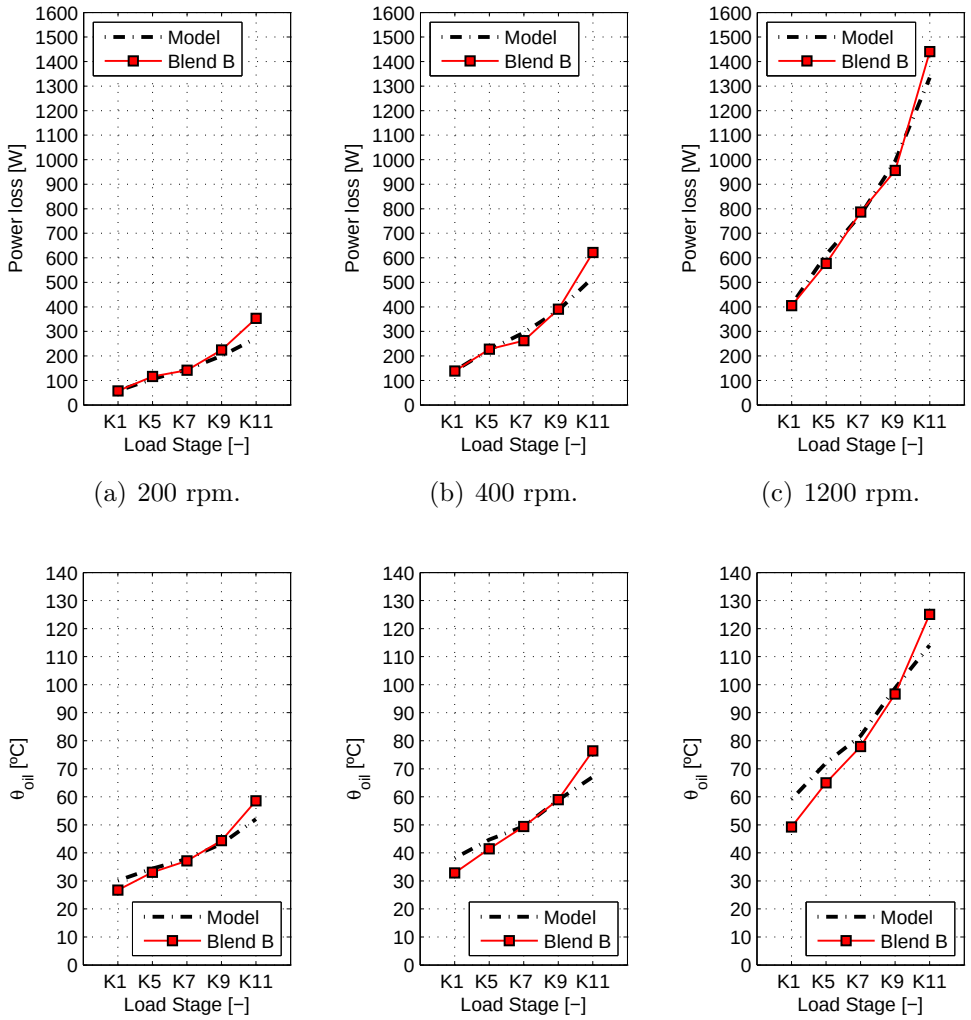

(a) 200 rpm. (b) 400 rpm. (c) 1200 rpm.

(d) 200 rpm. (e) 400 rpm. (f) 1200 rpm.

Figure 7.16.: Power loss and temperature predictions vs experimental results for Blend B.

error is significantly higher. The oil sump temperature predictions are a very good first estimative to forecast a test condition.

7.5. Improving gearbox efficiency

The efficiency was calculated, using the calibrated power loss model, for a wider range of applied torques and rotational speeds than those tested. It was considered only one helical stage, i.e. the test gearbox of the FZG machine lubricated with oil jet lubrication at 80 °C.

The extreme cases of performance will be considered, i.e. MINR with H501 or H951 gears and PAGD with H501 or H951 gears, that were already discussed in section 7.3.3.

7.5.1. Oil formulation

The efficiency maps for a FZG gearbox assembled with H501 gears are presented in Figure 7.17. Figure 7.17(a) shows the map for MINR oil while Figure 7.17(b) present the map for PAGD.

The gearbox efficiency can improve up to 0.5 % when MINR is replaced by PAGD, for the lower operating speeds.

7.5.2. Gear geometry

Figure 7.18 shows again the efficiency of the FZG test gearbox lubricated with MINR oil, when gears H501 and H951 are assembled.

It is interesting to observe that the efficiency maps have different isocurves shape, depending on the gear geometry. Replacing gear H501 by gear H951 can produce an efficiency improvement of about 0.5 %.

It is possible to conclude that, a different oil formulation modifies the influence of the applied torque, mainly at low rotational speeds, while a different gear geometry modifies all the efficiency map.

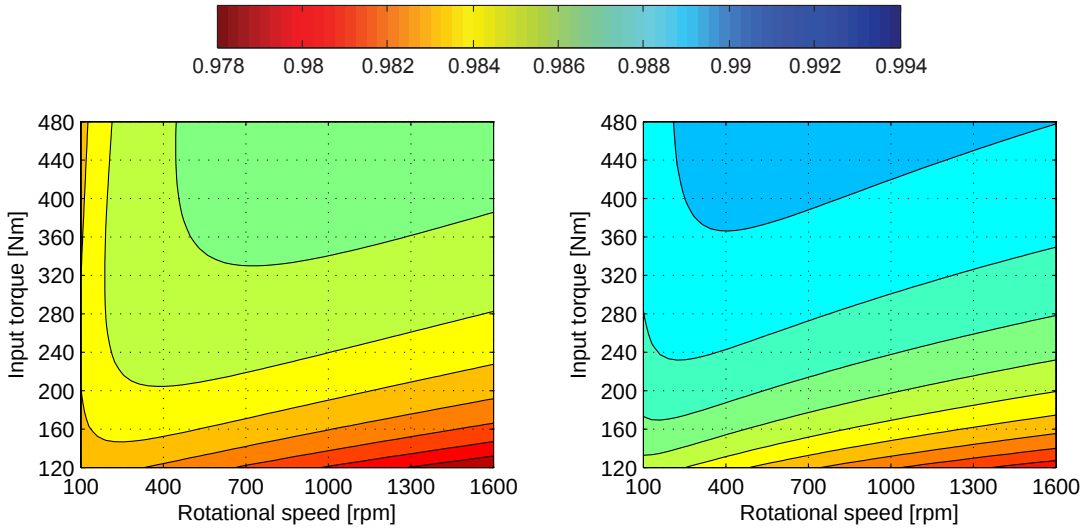

(a) MINR and H501.

(b) PAGD and H501.

Figure 7.17.: Efficiency of a gearbox with H501 gears lubricated with a) MINR and b) PAGD.

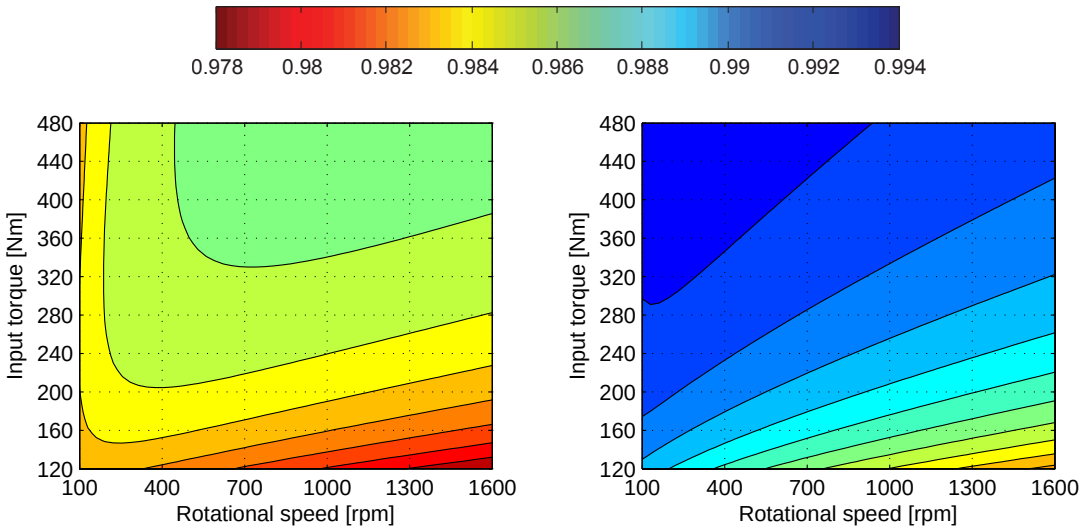

(a) MINR and H501.

(b) MINR and H951.

Figure 7.18.: Efficiency of a gearbox with a) H501 gears b) H951 gears lubricated with MINR.

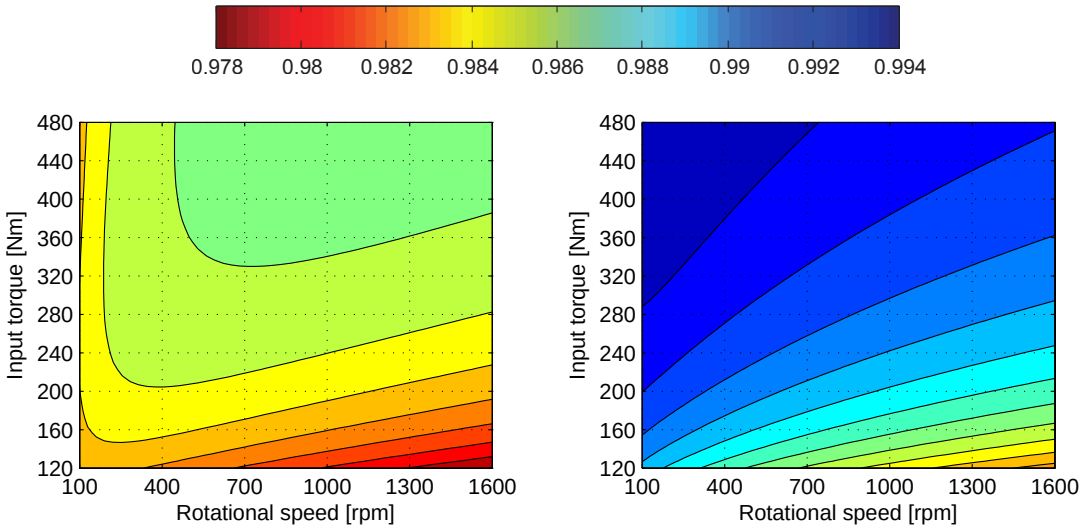

(a) MINR and H501.

(b) PAGD and H951.

Figure 7.19.: Efficiency of a gearbox with a) H501 gears lubricated with MINR and b) H951 gears lubricated with PAGD.

7.5.3. Combine oil formulation and gear geometry

In order to assess the influence of both oil formulation and gear geometry, on gearbox efficiency, Figure 7.19 compares H501 gear lubricated with MINR oil with H951 gear lubricated with PAGD.

Independently of the operating conditions, the efficiency improvement is always higher than 0.5 %. However, for the lower rotational speeds, that improvement can be higher than 1%.

7.6. Closure

The 'low loss' concept for gear geometry design was discussed and three new geometries were proposed.

FZG gearbox power loss tests were performed using a slave gearbox characterized in terms of power loss in Chapter 6, while in the test gearbox were assembled different 'low loss' geometries.

The experimental results clearly show that the gear geometry has an important influence in the gearbox efficiency. The total torque loss measured on FZG machine can be decreased by 20% changing from H501 to H951.

The influence of oil formulation was similar to that verified in spur gear tests, the power loss follows always the following trend: ${P_V}^{MINR} > {P_V}^{MINE} > {P_V}^{ESTR} \approx {P_V}^{PAOR} > {P_V}^{PAGD}$.

The calibrated power loss model was again applied to the experimental results aiming to validate the model for different gearbox geometries both in terms of gears and rolling bearings.

The mechanical model was coupled to a thermal model, aiming to forecast both the power loss and oil temperature of a FZG gearbox. The results are good enough to make a distinction between the power loss and operating temperature of two different gear oil formulations (Mineral and PAO). This step was necessary to validate the power loss model for free sump conditions and dip lubrication.

The outcome was great in terms of efficiency improvement, only with one stage and combining gear oil (PAGD) and gear geometry (H951), 1 % of efficiency improvement is feasible when compared with a MINR lubricating a H501 gear geometry.

Chapter 8.

Testing and prediction of power loss in multi-stage gearboxes

8.1. Introduction

The work presented in the previous chapters aimed to fully characterize wind turbine gear oils in terms of physical properties and friction, on gears and rolling bearings. To do that, dedicated tests were performed, allowing to calibrate each power loss source and then the gearbox power loss model.

The methods developed in chapters 5 and 6 were very effective in characterizing both rolling bearings and gears power losses. In Chapter 7 the model was validated and presented good correlation with experimental results.

This chapter is dedicated to the power loss prediction of full scale gearboxes, in particular wind turbine gearboxes. The main objective is to predict each power loss source and understand how to save energy, either by changing the oil or by modifying gearbox design (gears or rolling bearings).

The model was only validated for FZG gearboxes and it would be a very valuable tool to predict the power loss and efficiency of a gearbox and contribute improve its efficiency.

8.2. Materials and methods

8.2.1. Gearbox test rig

The gearbox test rig (Figure 8.1) follows the principle of recirculating power. This test rig allows the testing of gearboxes of different size and type, given that they fit within the dimensional constraints and allow for reducer/multiplier operation. The two gearboxes are used as speed multiplier and speed reducer, in order to close the circulating power loop. This test rig allows input speeds from 100 to 1900 rpm and input torques from 100 to 1300 Nm. The gearbox oil sump temperature is set free.

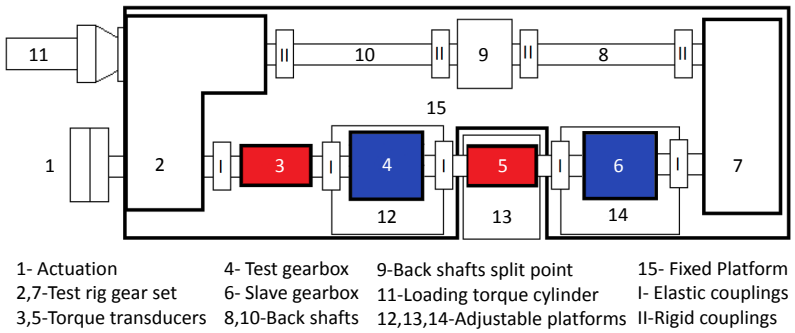

Figure 8.1.: Top view scheme of the gearbox test rig.

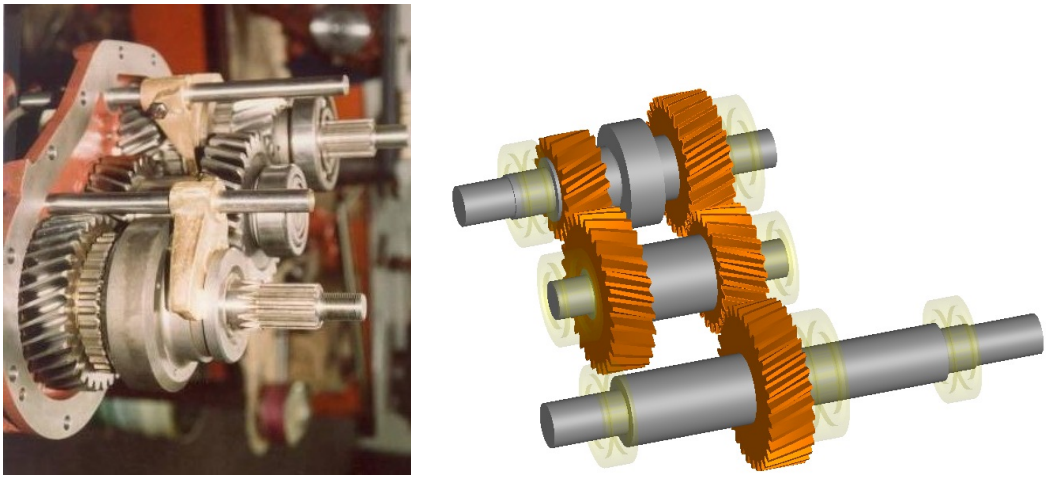

Figure 8.2.: Parallel axis gearbox.

The gearbox test rig allows monitoring and recording several operating parameters, namely: Input and output torque/speed of the test gearbox; Room temperature; Oil sump temperature in the test gearbox in two locations; External wall temperature of the housing on both test and slave gearboxes in various points.

Industrial grade 3 wire $Pt100$ RTD's and Type K thermocouples were used to monitor the temperatures in these points.

8.2.2. Parallel axis gearbox

Figure 8.2 shows a schematic view of the parallel axis gearbox to be tested. This gearbox has three shafts where five pinions are mounted. The gears in the middle shaft are keyed while the gears on the first and third shafts are mounted over needle bearings. All shafts are supported by ball or roller bearings. The test gearbox allows the selection of two different kinematic relations. All tests were conducted with the test gearbox working as speed multiplier ($i \approx 2.3$).

Table 8.1 displays the main geometric properties of the gears used in this transfer

Table 8.1.: Geometrical parameters of the gears in the parallel axis gearbox.

Gears		Parameters							
		z	m	a	α_z	β_z	b	x_z	R_a
		[-]	[mm]	[mm]	[°]	[°]	[mm]	[-]	[μm]
1st stage	Pinion	32	3.5	105.0	20	20	35	+0.3810	
	Gear	23						+0.4150	0.4
2nd stage	Pinion	28	4	95.0	20	20	33.5	-0.2400	
	Gear	17						+0.0510	0.4

Table 8.2.: Rolling bearings in the test gearbox.

Type	Quantity	Reference
Deep Groove Ball	1	RMS 11
Deep Groove Ball	1	RMS 10
Deep Groove Ball	1	6307
Tapper Roller	2	32306
Cylindrical Roller	1	NJ 309E
Needle	1	K38×43×27F

Table 8.3.: Sequence for the experimental tests (parallel axis gearbox).

Test Sequence	Input speed	Input torque	Input Power	Total test time
1		500	5.236	4+4
2	100	750	7.854	4+4
3		1000	10.472	4+4
4		500	10.472	4+4
5	200	750	15.708	4+4
6		1000	20.944	4+4
7		500	20.944	4+4
8	400	750	31.416	4+4
9		1000	41.888	4+4

gearbox for automotive applications. Table 8.2 shows information about the rolling bearings installed in the test gearbox.

The operating conditions and respective test sequence is resumed in Table 8.3. Four wind turbine gear oils were tested: MINR, PAOR, MINE and PAGD.

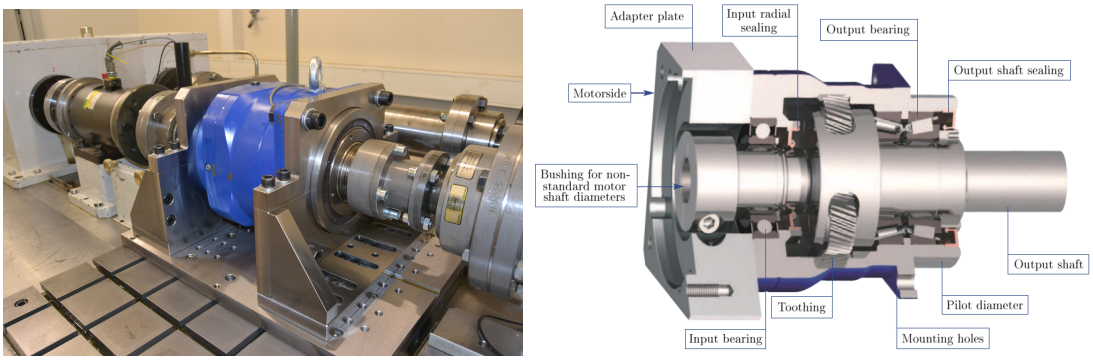

Figure 8.3.: Planetary gearbox installed in the test rig and schematic.

Table 8.4.: Geometrical parameters of the gears in the planetary gegarbox.

Gears	Parameters							
	z	m	a	α_z	β_z	b	x_z	R_a
	[/]	[mm]	[mm]	[°]	[°]	[mm]	[/]	[μm]
Sun	36						-0.0189	
Planet	36	2	74	20	10	42	-0.0189	0.4
Ring	-108						+0.0566	

Table 8.5.: Rolling bearings in the planetary gearbox.

Bearing type	Quantity	Reference
Tapered roller	2	32022 X/Q
Deep groove ball	1	6217-2Z
Needle roller	6	K40×48×4

8.2.3. Planetary gearbox

The planetary speed reducer has a speed ratio of 1/4, n_{out}/n_{in} , a max input speed of 1000 rpm and an nominal output torque of 2500 Nm. This gearbox is suited for heavy industrial applications, therefore it is capable of handling very high loads (axial and transverse) at the output shaft, which is supported by two back-to-back tapered roller bearings. In this work, the planetary gearbox was operating in a multiplier configuration.

Figure 8.3 shows the planetary gearbox installed in the gearbox test rig and a schematic view of the gearbox.

Table 8.6 shows the test sequence and imposed input speed and torques. The tests were conducted at less than 50% of the load capacity of the planetary gearbox (low load).

Table 8.6.: Sequence for the experimental tests (planetary gearbox).

Test Sequence [/]	Input speed [rpm]	Input torque [Nm]	Input Power [kW]	Total test time [h]
1		500	5.236	2+2
2	100	750	7.854	2+2
3		1000	10.472	2+2
4		500	10.472	2+2
5	200	750	15.708	2+2
6		1000	20.944	2+2
7		500	15.707	2+2
8	300	750	23.562	2+2
9		1000	31.416	2+2

8.3. Transfer gearbox results

8.3.1. Experimental results

Figure 8.4 shows the experimental results in terms of stabilized operating temperatures. These results clearly indicate that usually PAGD promotes the lowest power loss and MINR the highest. The test with MINR at the highest load and speed was disregarded due to expected operating temperatures well above 100 °C. PAOR and MINE performed identically, and are positioned between MINR and PAGD.

8.3.2. Power loss modelling

The power loss model presented in Chapter 4 was used to predict the power loss generated in the parallel axis gearbox. In this case the model will be applied considering the lubricant factors X_L calculated in Chapter 6. For the rolling bearings, the new SKF friction torque model with the corresponding coefficients determined in Chapter 5 was implemented.

Recently, Changenet *et al.* [83] presented a gear churning loss model based on a dimensional analysis approach and a series of experimental tests to tune de model.

The model was applied to predict the churning losses [89] but the discrepancies between the experimental and numeric results were overcome by using a different laminar-turbulent transition point.

Figure 8.5 show the predicted power loss as well as each one of its components. For the tested operating conditions the meshing friction losses dominate the power

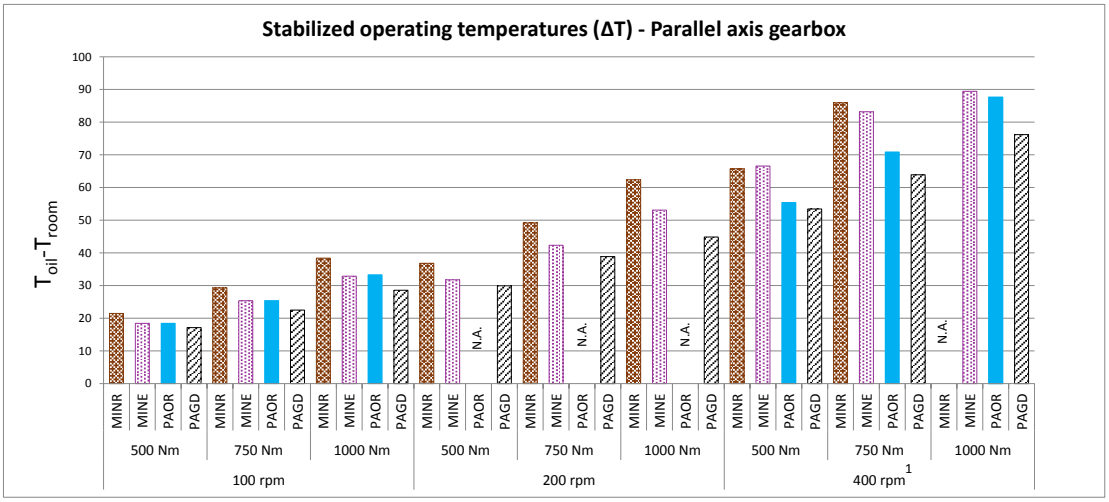

Figure 8.4.: Stabilized operating temperature.

1-MINE tests were performed at 500 instead of 400 rpm

loss. Depending on the oil nature, namely dynamic viscosity, the gear churning losses seem to be higher than the rolling bearings power loss.

Under stabilized conditions the heat that is lost to the environment through the gearbox is equal to the power loss. Equation (8.1) shows the relation between the stabilized operating temperature and the power that is dissipated through the gearbox.

$$Q = \alpha \cdot A \cdot \Delta T \tag{8.1}$$

The global heat transfer coefficient, $\alpha \cdot A$, can be used to verify the general consistency of the power loss model.

Under stabilized operating conditions the global heat transfer behaviour should be more or less independent of the gear oil that is used to lubricate the gearbox (oil sump lubrication). Figure 8.6 shows that $\alpha \cdot A$ follows an almost linear behaviour with temperature, which is also more or less independent of the gear oil. This shows that the model has a consistent behaviour.

8.4. Planetary gearbox results

8.4.1. Experimental results

Figure 8.7 shows the stabilized operating temperatures in the planetary gearbox for the operating conditions presented in Table 8.6. The experimental results indicate that, for a given speed and for a given lubricant, the stabilized operating temperature is almost constant. Under these conditions, the mineral based oil, MINR, has shown

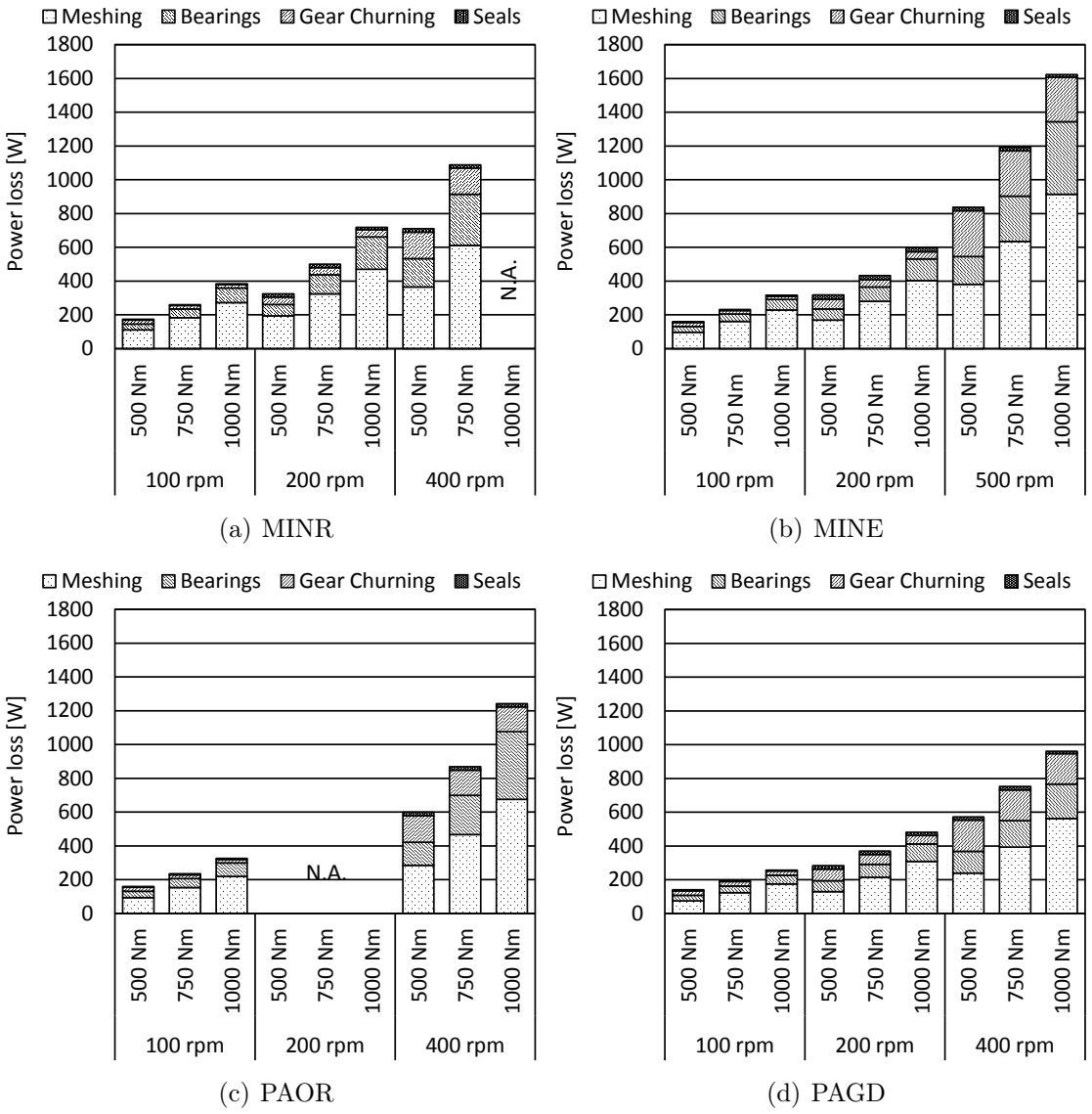

(a) MINR

(b) MINE

(c) PAOR

(d) PAGD

Figure 8.5.: Calculated power loss distribution for the parallel axis gearbox.

the overall lowest operating temperatures. MINE and PAOR performed identical and in between MINR and PAGD. PAGD has shown the highest operating temperatures, specially as speed increases.

The power loss model was applied to the planetary gearbox. In this case, the model lacks the churning loss component, nevertheless the model predictions are allowing to analyse the stabilized operating temperatures.

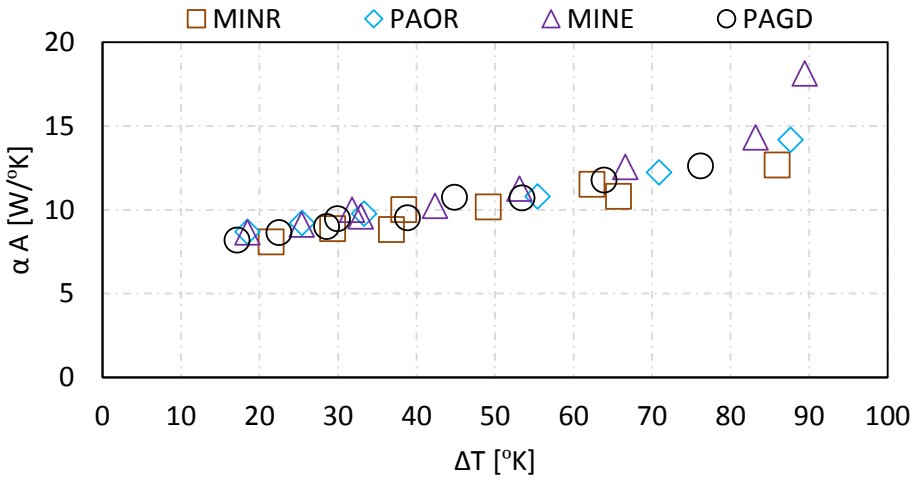

Figure 8.6.: Heat transfer coefficient calculated after the stabilized operating conditions and the predicted power loss.

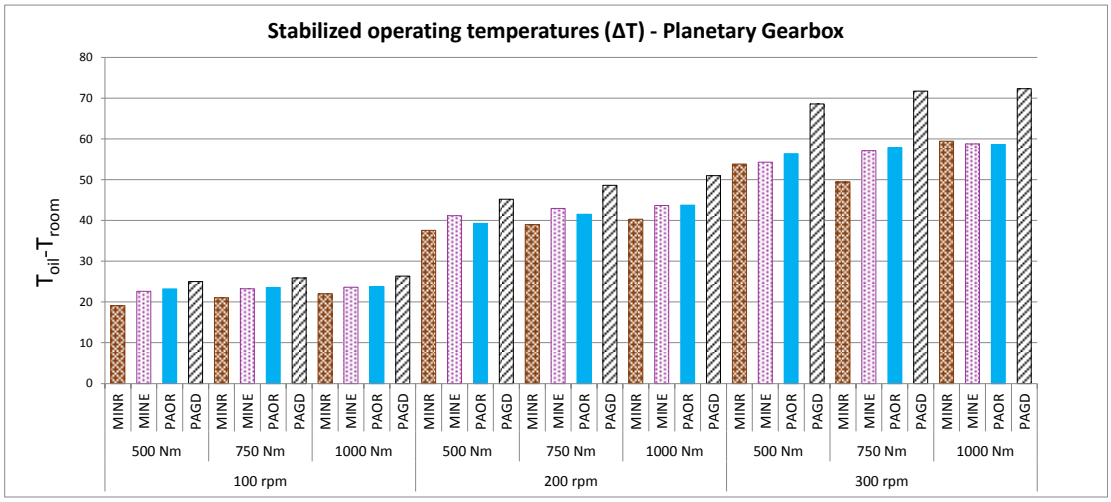

Figure 8.7.: Stabilized operating temperature.

8.4.2. Power loss modelling

The power loss model presented in Chapter 4 was used to predict the power loss generated in the planetary gearbox. The SKF model was used for the rolling bearings.

The no-load gear losses were disregarded due to the lack of models that actually can predict the no-load power loss in the planetary gearbox. Several authors presented studies regarding the prediction of the power loss generated by partly immersed gears. However, in planetary gearboxes, the power loss generated by the air-oil mixture interaction with the moving mechanical elements sets additional difficulties. The planet gears have a rotational movement around their own centre, combined

with another rotational movement around the centre of the sun gear, since the planet carrier is the element that holds the planet gears in place and allows the transport movement of the planets around the sun gear.

In a planetary gearbox in oil sump lubrication several phenomena are prone to create power loss. Consider a planetary gearbox driven by the planet carrier but without the sun and internal gears. The result will be the planet carrier and the planets rotating as a single element. This movement alone is responsible for the majority of the power loss generated due to the air-oil mixture interaction with the moving elements. If the full planetary gearbox is considered, the power loss due to fluid trapping and squeezing as well as pumping effects due to the meshing gears must be considered. The rotation of the planets around its own centre can also create additional power loss.

The model results indicate that the power loss doesn't change that much with increasing torques (for a fixed speed), which is in agreement with the experimental results (Figure 8.8). The model also suggests that all gear oils have similar power loss performance.

Figure 8.8 shows the power loss contribution of each individual power loss source in the planetary gearbox. The main power loss sources are the rolling bearings. The tapered roller bearings have a very high pre-load when compared to the axial loads introduced by the helical gears in the planetary gearbox, which results in approximately constant power loss for a certain operating speed. Since the tapered rolling bearings are the most important power loss source in the gearbox, the overall gearbox follows, more or less, their trend.

The needle roller bearings are very influenced by the input torque and speed, showing an almost direct correlation with the increase of the transmitted power.

None of the power loss sources that were considered seems to be able to explain the much higher operating temperature promoted by the PAGD oil. The only power loss component that wasn't considered was the churning loss. PAGD is the fluid with the highest density and viscosity index, which could have promoted higher churning power losses.

8.5. Power loss of a wind turbine gearbox

8.5.1. Full scale 2.5 MW wind turbine gearbox

A particular wind turbine gearbox design was choosen to perform a power loss simulation. The gearbox is presented in Figure 8.9. It has two planetary stages and a final stage with a parallel helical pair. It is a very common type of configuration used in wind turbine gearboxes as presented in Figure 8.10. The input torque and

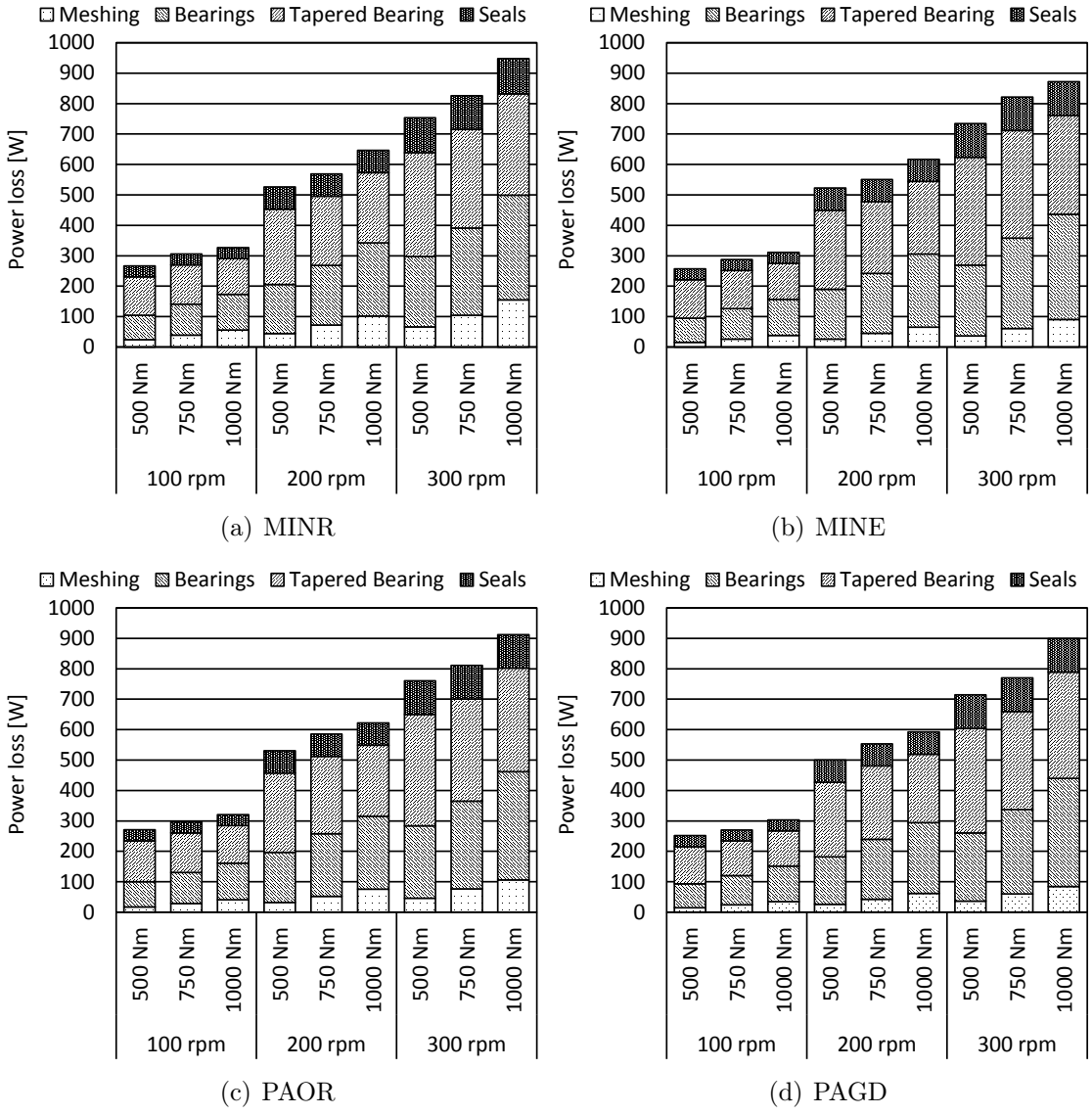

(a) MINR (b) MINE

(c) PAOR (d) PAGD

Figure 8.8.: Calculated power loss distribution for the planetary gearbox.

speed on each planetary stage is made through the planetary carrier and the output in the sun shaft. Thus, a fixed ring configuration is used [176, 204, 205].

The gearbox is designed using helical gears in all stages with an helix angle of 10 °. The total transmission ratio is i ≈ 102. The gear properties are resumed in Table 8.7: all gears have profile shift and the safety factors were calculated for an input torque of 1200 kNm and an input speed of 20 rpm, assuring the necessary life rating of the gears.

The shafts are supported by rolling bearings that are listed in Table 8.8.

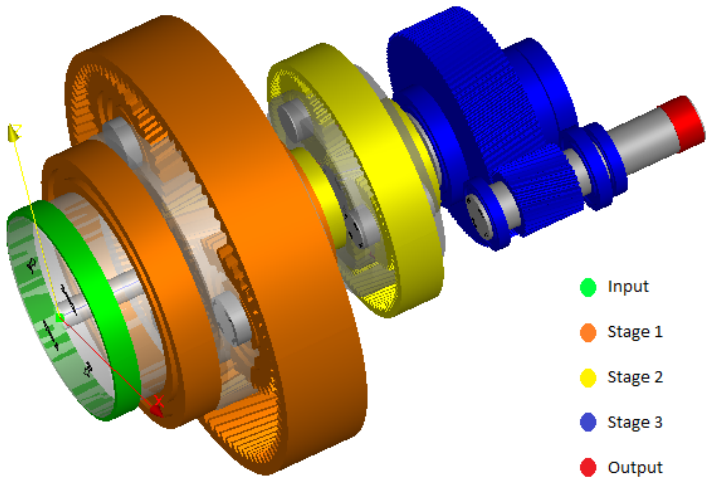

Figure 8.9.: 3D schematic model of a wind turbine gearbox [176].

Table 8.7.: Gear geometric properties of the wind turbine gearbox.

	Stage 1			Stage 2			Stage 3	
Parameter	Sun	Planet	Ring	Sun	Planet	Ring	Pinion	Wheel
z	21	35	-96	23	38	-103	117	35
b	320	320	331.5	168.4	168.4	177.4	245	240
m		16			9		7	
α_z		20			20		20	
β_z		10			10		10	
x_z	0.71	0.8031	0.2093	0.6464	0.7693	-0.0639	0.769	0.7176
S_F	1.68	1.19	1.89	1.98	1.39	2.18	2.74	2.91
S_H	1.09	1.15	1.79	1.18	1.22	2.25	2.02	1.99

8.5.2. Simulation

A simulation was performed for MINR, PAOR and PAGD gear oils. Two different operating temperatures were considered, 60 and 80 °C which is the usual range of operation in a wind turbine gearbox. The test conditions are resumed in Table 8.9.

The no-load gear losses will not be considered for the simulation since the available models don't offer confidence for the predicted values. Furthermore, the experimental and model results presented in Chapter 6 and 7 show a low influence of the no-load

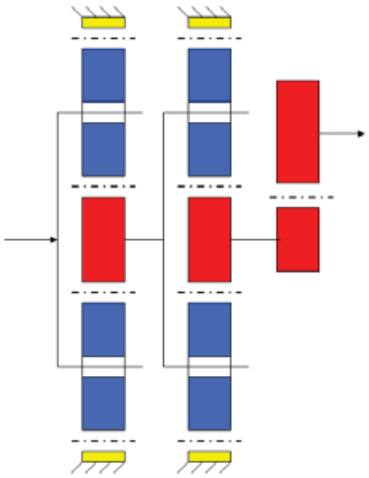

Figure 8.10.: Configuration of the wind turbine gearbox used for the simulation.

Table 8.8.: Rolling bearings of the wind turbine gearbox.

Stage	Rolling bearing	Location	Quantity
Stage 1	SKF NU 20/800 ECMA	carrier	1
	SKF NU 1080 MA	carrier	1
	SKF NU 2340 ECMA	planets	3
	SKF NU 2340 ECMA	planets	3
Stage 2	SKF NU 244 ECMA	carrier	1
	SKF NU 1060 MA	carrier	1
	SKF NNCF 4930 CV	planets	3
	SKF NNCF 4930 CV	planets	3
Stage 3	SKF NU 1060 MA	pinion shaft	1
	SKF 32960	pinion shaft	1
	SKF 32960	pinion shaft	1
	SKF NU 1036 ML	wheel shaft	1
	SKF NUP 236 ECMA	wheel shaft	1
	NSK QJ1036	wheel shaft	1

gear losses on the total torque loss of a gearbox, at low speed. At the same time, the oils used are ISO VG 320 and the differences between them, in terms of no-load losses, are expected to be very small. However, it should be remarked that PAGD prediction, for example, might be optimistic taking into account the results of Figure

Table 8.9.: Wind turbine gearbox conditions for the power loss simulation.

Condition	Value
Input torque	1200 kNm
Input speed	20 rpm
Output speed	2040 rpm
Nominal power	2.5 MW
Operating temperature	60 and 80 °C
Lubrication method (gears)	Oil jet lubrication
Lubrication method (rolling bearings)	Dip lubrication
Oil formulations	MINR, PAOR and PAGD

8.7.

To calculate the meshing gears power losses, the Ohlendorf equation (8.2) was used. The local gear loss factor (H_{VL}, equation (7.3)) was considered as well as the coefficient of friction of Schlenck, with the corresponding lubricant parameter X_L (see Table 6.12).

$$P_{VZP} = P_{IN} \cdot H_{VL} \cdot \mu_{mZ} \tag{8.2}$$

The first and second stage were analysed using the concept of mesh-power, while stage 3 of the wind turbine gearbox, being a parallel helical gear, was analysed using equation (8.2).

The input power on each planetary stage is splitted in 3 planets and the tangential force applied on the base plane is calculated with equation (8.3).

$$F_{bt} = \frac{P_{IN}}{3 \cdot v_t} \tag{8.3}$$

The mesh power in each meshing pair should be calculated as presented in equation (8.4), and so the relative speed was considered. The mesh power (P_M) should be used in equation (8.2) instead of input power (P_{IN}) for the case of planetary gears. Regarding the coefficient of friction the sum velocities in the pitch point ($v_{\Sigma C}$) should also be calculated using the relative velocities.

$$P_M = F_{bt} \cdot v_t{}' \tag{8.4}$$

The input shaft of stage 3 runs at 610 rpm, which corresponds to 25 m/s of tangential speed. Independently of the oil used, the gears will perform under full-film conditions. The Schlenck equation is suitable for mixed film lubrication conditions and the coefficient of friction would decrease ad infinitum if the speed is increased

without care. To avoid the underestimation of the meshing gears power loss, the third stage coefficient of friction was calculated for $\Lambda = 2$, i.e. it was assumed that the coefficient of friction is better estimated if calculated at the speed corresponding to the beginning of full film conditions.

The rolling bearing power losses were calculated using the calibrated power loss model described in Chapter 5. The coefficients of friction (μ_{bl} and μ_{EHD}) determined based on the experimental results are here again used for the simulation performed, assuming that no significant difference is found between 60 °C and 80 °C.

8.5.3. Modeling results

Considering the main sources of power loss in each stage, gears and rolling bearings, antagonistic effects were observed as presented in Figure 8.11. PAGD reduce the gears power loss but slightly increase the rolling bearing losses. The opposite behaviour is observed for MINR.

The temperature has also opposite effects, depending if gears or bearings are considered. Increasing the operating temperature increases the gear losses, as shown in Figures 8.11(c) and 8.11(d). The rolling bearing losses reduce by increasing the temperature and consequently lowering the viscosity. The rolling torque (M_{rr}), in rolling bearings, is the main source of power loss in stage 3 and it is mainly dependent on speed and viscosity. Consequently, the rolling bearings power loss in stage 3 is almost independent on the oil formulation.

Because of the very high Viscosity Index of PAGD, its viscosity at 80 °C is very high compared to the viscosity of the other formulations. Such difference between formulations is higher than at 60 °C. Consequently, at 80 °C PAGD oil generated the highest rolling bearing power loss, as can be observed in figures 8.11(e) and 8.11(f).

The very high speed and the tapper rolling bearings used in stage 3 explain the very high power loss predicted. The losses are even higher those generated by gears in stages 1 and 2.

8.5.4. Modelling results with modified tooth geometry

A different gear geometry was considered for each gearbox stage. The gear loss factor of the original gear mesh's is low, since helical gears were used.

In order to achieve better efficiency, the number of teeth was increased, reducing the module trying to reduce the gear loss factor. A positive profile shift was applied in every gear mesh and the safety factors were slightly reduced, as presented in Table 8.10.

The gear loss factors are presented in Table 8.11 for both the standard (STD) and modified (MOD) teeth.

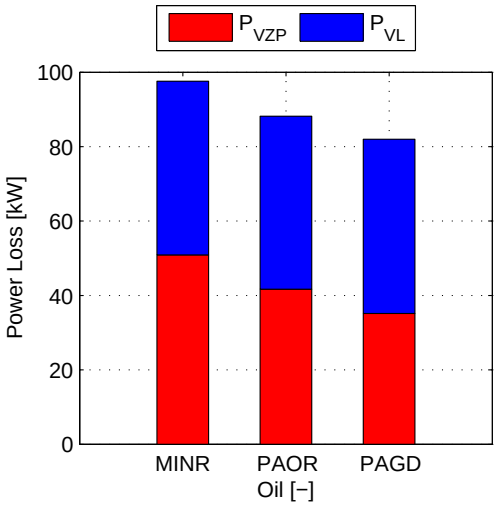

(a) Total Power Loss @ 60 °C.

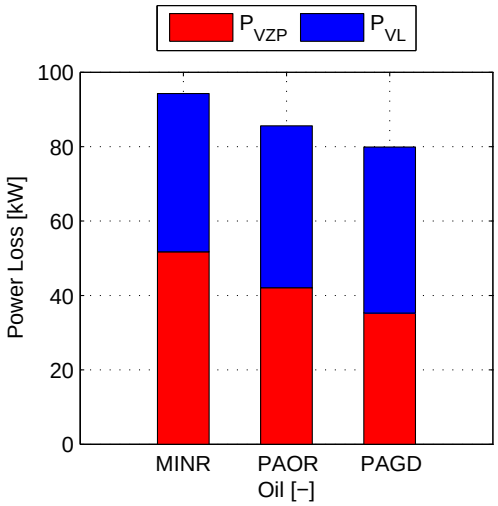

(b) Total Power Loss @ 80 °C.

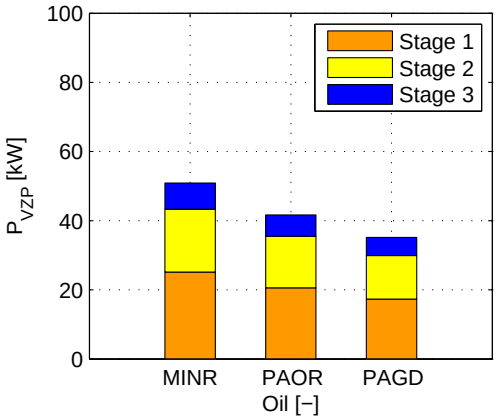

(c) Meshing gears power loss @ 60 °C.

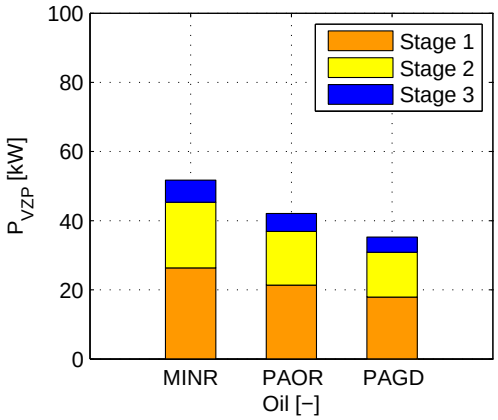

(d) Meshing gears power loss @ 80 °C.

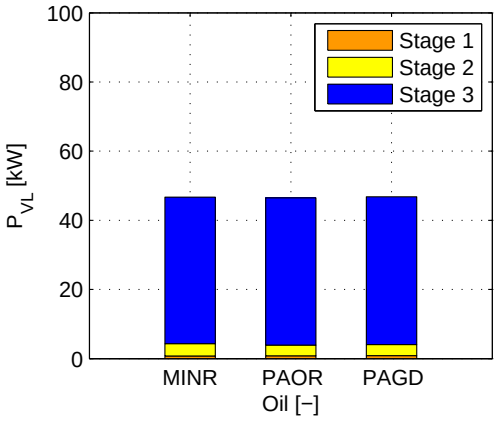

(e) Rolling bearings power loss @ 60 °C.

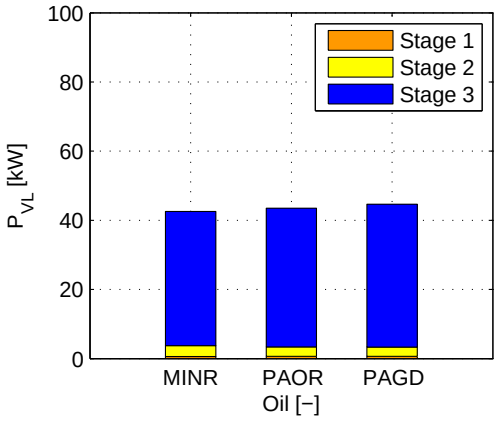

(f) Rolling bearings power loss @ 80 °C.

Figure 8.11.: Power loss prediction for a full wind turbine gearbox.

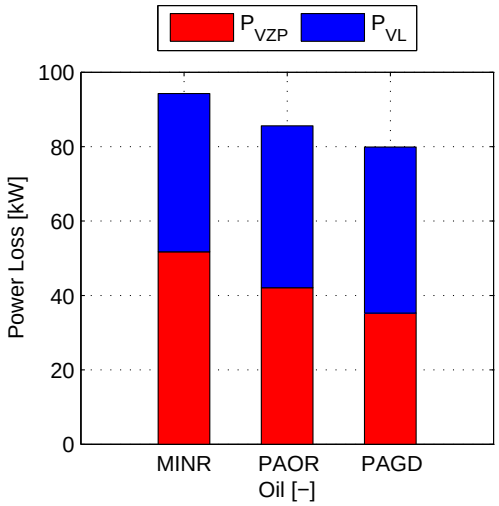

(a) Total Power Loss @ 80 °C (STD).

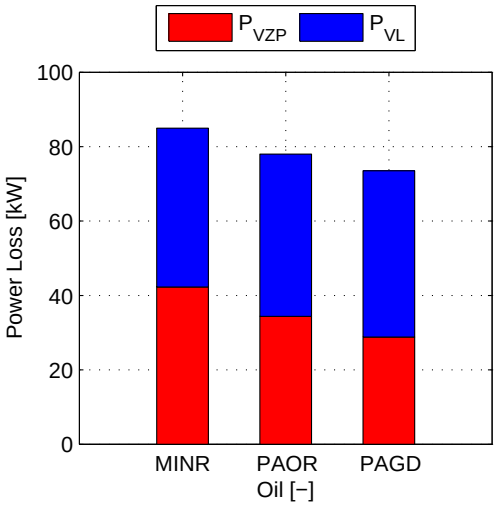

(b) Total Power Loss @ 80 °C (MOD).

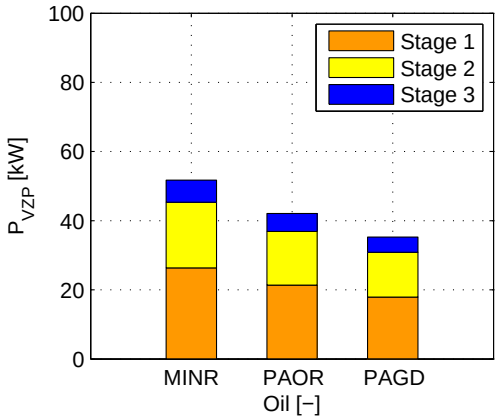

(c) Meshing gears power loss @ 80 °C (STD).

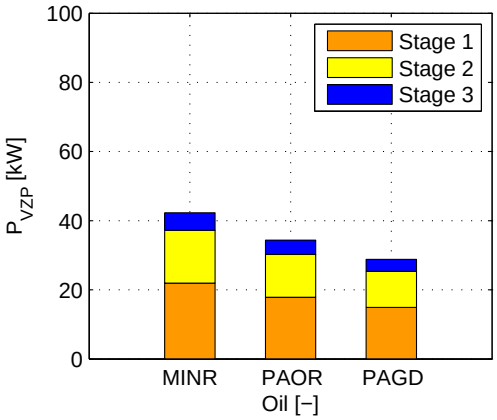

(d) Meshing gears power loss @ 80 °C (MOD).

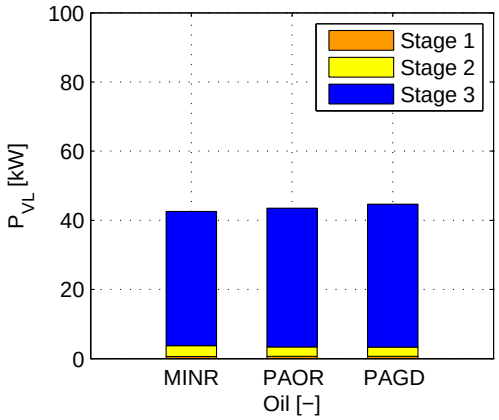

(e) Rolling bearings power loss @ 80 °C (STD).

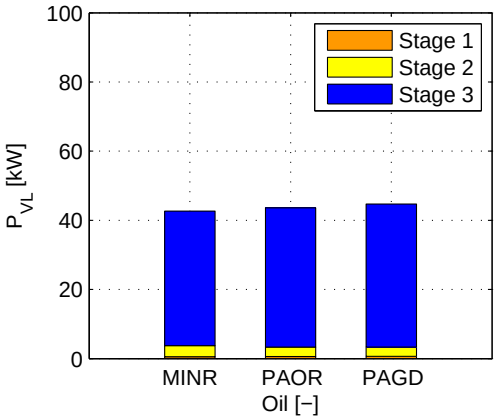

(f) Rolling bearings power loss @ 80 °C (MOD).

Figure 8.12.: Power loss prediction for a full wind turbine gearbox.

The safety factors can be increased by using a larger face width. This was not done in purpose, in order to keep the gearbox dimensions and to show that is possible to reduce the meshing gears power loss in comparison to the original design. The nominal pressure angle and the helix angle were also kept in order to be possible use the same bearings.

Comparing Figures 8.12(a) and 8.12(b) it is clear that the total power loss was decreased and the efficiency increased, for each oil formulation.

The power loss reduction is due to the gear tooth geometry as presented in Figures 8.12(c) and 8.12(d). The meshing gears power loss were reduced by 18 % independently of the oil formulation.

The rolling bearing power losses remain almost the same as presented in Figures 8.12(e) and 8.12(f) which was expected since the applied forces were not increased significantly.

Comparing the original gear geometry lubricated with MINR (Figure 8.12(a)) and the new one lubricated with PAGD (Figure 8.12(b)), the total power loss can decrease 22 %, which corresponds to $\approx$ 21 kW.

Table 8.10.: Gear geometric properties of the modified (MOD) wind turbine gearbox.

	Stage 1			Stage 2			Stage 3	
Parameter	Sun	Planet	Ring	Sun	Planet	Ring	Pinion	Wheel
z	28	47	-128	30	50	-135	150	45
b	320	320	331.5	168.4	168.4	177.4	245	240
m		12			7		5.5	
α_z		20			20		20	
β_z		10			10		10	
x_z	0.7742	1.0280	0.2110	0.4330	0.4342	0.9927	0.7464	0.2850
S_F	1.29	0.94	1.41	1.64	1.14	1.49	2.23	2.29
S_H	1.10	1.16	1.86	1.20	1.24	1.90	2.03	2.00

Table 8.11.: Gear loss factors for the standard (STD) and modified (MOD) wind turbine gearbox.

	Stage 1		Stage 2		Stage 3
	S/P	P/R	S/P	P/R	P/W
H_{VL} (STD)	0.1482	0.1093	0.1391	0.1055	0.0955
H_{VL} (MOD)	0.1132	0.1005	0.1245	0.0676	0.0752

The main problem of stage 3 is due to the rolling bearing dimensions and the high operating speed. For such large bore rolling bearings the only possibility is to be able to replace them by smaller ones. It implies shafts with small diameter, which can not be feasible. The rolling bearing failures are reported in literature [19] as a problem in wind turbine gearboxes, so, the rolling bearing geometry should be addressed with care.

8.5.5. Efficiency

The efficiency of each gearbox stage is presented in Table 8.12 for each gearbox design and for each oil formulation.

Table 8.12.: Wind turbine gearbox efficiency [%] for each oil formulation and gearbox configuration.

Oil	Gearbox design	Stage 1	Stage 2	Stage 3	Global
MINR	Standard	98.93	99.12	98.20	96.25
	Modified	99.10	99.27	98.25	96.62
PAOR	Standard	99.12	99.28	98.20	96.59
	Modified	99.26	99.39	98.23	96.90
PAGD	Standard	99.26	99.38	98.18	96.82
	Modified	99.38	99.48	98.21	97.07

8.6. Closure

The models presented in previous chapters were applied to full gearboxes. Experimental results were presented and the calibrated power loss model was applied successfully to the gearboxes.

The models were then considered able to perform a simulation with a full scale wind turbine gearbox. The model results show the influence of gear meshing and rolling bearing losses. It was found that the rolling bearing losses predominate in very high speed conditions while meshing gear power losses are very important in stage 1 and 2 planetary sets.

The power loss model proved to be a valuable tool to identify the gearbox elements that contribute to energy dissipation. The power loss quantification allows to identify which elements (oil formulation, lubricant viscosity, rolling bearings and gear geometry) that need, redesign or alternative selection.

Chapter 9.

Conclusions and future work

9.1. Conclusions

This thesis, discussed in a systematic and planed way the mechanisms of power loss in gearboxes, based on experimental evidence and modelling.

The methodology presented to test rolling bearings, gears and full gearboxes proved to be effective. A complete characterization of the power loss behaviour of different wind turbine gear oil formulations was included.

In Chapter 2, a physical characterization of different ISO V320 wind turbine gear oils was presented. Viscosity, density and pressure-viscosity were measured.

The tribological performance of the fully formulated oils was revealed with film thickness and traction coefficient measurements, presented in Chapter 3.

The multiple sources of gearbox power loss were discussed in Chapter 4, and a global power loss model structure was proposed to be calibrated through dedicated measurements of bearing and gear power loss.

The power loss of rolling bearings lubricated with wind turbine gear oils was measured in Chapter 5. The results clearly show that the oil formulation has an important influence in power loss. To better understand the results, as well as, to predict the actual rolling bearings power loss, the SKF model was implemented.

The rolling bearing power loss measurements showed that MINR is less efficient than any other formulation, under high loads and low rotational speeds. PAGD is the most efficient formulation for low speeds, because the sliding torque, has great influence. However, for higher speed the sliding torque starts to decrease, no matter the oil formulation, and the rolling torque becomes dominant.

The rolling torque is only dependent on speed, bearing geometry and viscosity, so, the oils with intermediate viscosity index (PAOR, ESTR and MINE) become the most efficient at high speeds, because they have the best balance between power loss dependency on viscosity and sliding coefficient of friction.

Chapter 6 presented power loss results of the FZG gearboxes. The results follow the same trend observed on rolling bearing tests. For load stages above K1, MINR oil promoted the highest power loss, mainly at low speed. PAGD promoted the lowest power loss at low speed, but when speed increases it starts to have a similar performance to that found for PAOR and ESTR.

The rolling bearings showed that for high rotational speed the PAGD is not better than the other formulations. The rolling bearings influence in the total power loss of the FZG gearboxes appeared to be evident for high speeds. The results show that PAGD should only be used for lower or moderate speeds and for the cases, where the gear losses are much higher than all the other power loss sources.

The average coefficient of friction in meshing gears was studied and it is clear that the oil formulations followed the trend: $\mu^{MINR} > \mu^{MINE} > \mu^{PAOR} > \mu^{ESTR} > \mu^{PAGD}$. The results of the average coefficient of friction showed that the PAGD is better for gears under oil jet lubrication but the same is not true for bearings depending on the speed considered.

The meshing gears coefficient of friction was measured and then compared to usual formulations from the literature. A new coefficient of friction was also proposed, which was very useful to complete a calibrated power loss model where the rolling bearing power loss model calibrated in Chapter 5, based on experimental work, takes part.

Chapter 7 studied the influence of gear geometry in the gearbox power loss. Different gear geometries were proposed and tested in a FZG machine. The results showed that it is possible to reduce the module of a gear, improving the efficiency while keeping the safety factors very similar.

The most effective way to improve the gearbox efficiency is to combine gear geometry and oil formulation. That combination can promote up to 1% of efficiency improvement per gear stage.

The power loss model proposed was validated, showing very good correlation with low loss gear experimental results. Afterwards it was then used to study the influence of the operating conditions on each power loss source. It was found that gears and rolling bearings are affected by the speed or load in opposite way. The gears improve the efficiency with increasing speed while the rolling bearings improve the efficiency for increasing load.

All the work carried on was then applied to predict the power loss of a full scale wind turbine gearbox in Chapter 8. It was found that the total power loss is governed by the gears at low speed and the rolling bearings at high speed.

9.2. Future work

Several topics addressed in this thesis, require further analysis and development:

- The influence of the 'low loss' gear geometry on the wear, scuffing and pitting should be addressed in order to assure that the better efficiency is not erased by failure problems.
- The no-load gear power losses should be studied with a specific test-rig developed for such effect. The low rotational speeds should be tested in order to clarify how the models available deal with those particular operating conditions.
- A new coefficient of friction formula was proposed using a different lubrication parameter, a modified Hersey parameter S_p proposed by Brandão *et al.* [63] instead of the usual hydraulic parameter. However, a specific experimental procedure should be done to better calibrate the influence of the geometry. The formula is only valid for the mixed lubrication regime and some additional work is needed to turn the formula better suited for all lubrication regimes.
- A simulation was performed for a wind turbine gearbox. The next step is to apply on the field the suggested changes and try to monitor if the efficiency improvement is measurable after a given time of operation.
- In general, ISO VG 320 are a standard for wind turbine gearboxes. Other viscosity grades and operating temperatures should be analysed (e.g. PAGD ISO VG 220).

Bibliography

[1] E. E. Agency, Europe's onshore and offshore wind energy potential - an assessment of environmental and economic constraints, EEA Technical report No 6 (2009) 91.

[2] B. McNiff, W. Musial, R. Errichello, Variations in gear fatigue life for different wind turbine braking strategies, prepared for AWEA Wind Power '90, Washington, D. C. 24-8 September 1990 (1991) Medium: ED; Size: Pages: (10 p).

[3] L. Winkelmann, Surface roughness and micropitting, National Renewable Energy Laboratory Wind Turbine Tribology Seminar (2011).

[4] M. McDade, Gearbox reliability collaborative (grc) failure database, National Renewable Energy Laboratory - Wind Turbine Tribology Seminar (2011).

[5] M. Jungk, Update on the development of a full life wind turbine gear box lubricating fluid, National Renewable Energy Laboratory Wind Turbine Tribology Seminar (2011).

[6] P. J. Tavner, F. Spinato, G. J. W. v. Bussel, E. Koutoulakos, Reliability of different wind turbine concepts with relevance to offshore application, Presented at the European Wind Energy Conference (April 2008) April.

[7] J. Zellmann, Main types of damage to wind turbine gearboxes, WIND KRAFT JOURNAL Edition 3 (2009) 2–5.

[8] M. Evans, A. Richardson, L. Wang, R. Wood, Serial sectioning investigation of butterfly and white etching crack (wec) formation in wind turbine gearbox bearings, Wear 302 (1-2) (2013) 1573 – 1582, wear of Materials 2013. doi:http://dx.doi.org/10.1016/j.wear.2012.12.031.

[9] J. V. Rensselar, The elephant in the wind turbine, Tribology & Lubrication Technology (June 2010) 2–12.

[10] W. Musial, S. Butterfield, B. McNiff, Improving wind turbine gearbox reliability, National Renewable Energy Laboratory 2007 European Wind Energy Conference, Milan, Italy (May 7-10, 2007) 13.

[11] G. L. Doll, Tibological challenges in wind turbine technology, National Renewable Energy Laboratory Wind Turbine Tribology Seminar (2001).

[12] R. D. Evans, Classic bearing damage modes, National Renewable Energy Laboratory Wind Turbine Tribology Seminar (2011).

[13] H. Uyama, The mechanism of white structure flaking in rolling bearings, National Renewable Energy Laboratory Wind Turbine Tribology Seminar (2011).

[14] M. N. Kotzalas, G. L. Doll, Tribological advancements for reliable wind turbine performance, Philosophical Transactions of the Royal Society A: Mathematical, Physical and Engineering Sciences 368 (1929) (2010) 4829–4850.

[15] K. Tamada, H. Tanaka, Occurrence of brittle flaking on bearings used for automotive electrical instruments and auxiliary devices, Wear 199 (2) (1996) 245–252, cited By (since 1996)50.

[16] M.-H. Evans, A. Richardson, L. Wang, R. Wood, Effect of hydrogen on butterfly and white etching crack (wec) formation under rolling contact fatigue (rcf), Wear 306 (1-2) (2013) 226–241, cited By (since 1996)2.

[17] M. Evans, A. Richardson, L. Wang, R. Wood, Investigations of white etching crack (wec) formation under rolling contact fatigue, Tribology and Lubrication Technology 70 (1) (2014) 16–19, cited By (since 1996)0.

[18] E. Robert, B. Robert, E. Rainer, Investigations of bearing failures associated with white etching areas (weas) in wind turbine gearboxes, Tribology Transactions 56 (6) (2013) 1069–1076, cited By (since 1996)0.

[19] A. Ruellan, F. Ville, X. Kleber, A. Arnaudon, D. Girodin, Understanding white etching cracks in rolling element bearings: The effect of hydrogen charging on the formation mechanisms, Proceedings of the Institution of Mechanical Engineers, Part J: Journal of Engineering Tribology (2014). doi:10.1177/1350650114522452.

[20] F. Sprei, S. Karlsson, Energy efficiency versus gains in consumer amenities—an example from new cars sold in sweden, Energy Policy 53 (0) (2013) 490 – 499. doi:http://dx.doi.org/10.1016/j.enpol.2012.11.017.

[21] U. team, Uk team creates ech2o fuel cell car for efficiency record bid, Fuel Cells Bulletin 2005 (9) (2005) 7 – 8. doi:http://dx.doi.org/10.1016/S1464-2859(05)70746-X.

[22] B.-R. Höhn, K. Michaelis, Influence of oil temperature on gear failures, Tribology International 37 (2) (2004) 103 – 109, austrib 2002. doi:http://dx.doi.org/10.1016/S0301-679X(03)00047-1.

[23] T. Mang, W. Dresel, Lubricants and Lubrication, Wiley, 2007.

[24] B. J. Hamrock, D. Dowson, Ball bearing lubrication, John Wiley & Sons, 1981, 386.

[25] Klüber, Special lubricants for wind turbines, Product selection (2014).

[26] ANSI/AGMA/AWEA 6006-A03 - standard for design and specification of gearboxes for wind turbines (2010).

[27] J. Muller, R. Errichello, Oil cleanliness in wind turbine gearboxes, Machinery Lubrication (2002) July.

[28] J. J. C. Hoo, A. S. for Testing, Materials., Rolling Contact Fatigue Testing of Bearing Steels: A Symposium, no. n.º 771 in ASTM STP 771, American Society for Testing and Materials, 1982.

[29] ISO, Hydraulic fluid power – fluids – method for coding the level of contamination by solid particles, ISO 4406:1999.

[30] P. Dennis A. Lauer, Selecting synthetic gear oil, National Renewable Energy Laboratory - Wind Turbine Tribology Seminar November 15-17, 2011.

[31] API, Engine oil licensing and certification system 1509, 2014.

[32] L. Rudnick, Synthetics, Mineral Oils, and Bio-Based Lubricants: Chemistry and Technology, Chemical Industries, Taylor & Francis, 2005.

[33] R. Mortier, M. Fox, S. Orszulik, Chemistry and Technology of Lubricants, SpringerLink: Springer e-Books, Springer, 2011.

[34] G. Lappin, Alpha Olefins Applications Handbook, Chemical Industries, Taylor & Francis, 1989.

[35] DIN 53019-1: Viscometry - Measurement of viscosities and flow curves by means of rotational viscometers - Part 1: Principles and geometry of measuring system (2008).

[36] ASTM D341 - 09, Standard Practice for Viscosity - Temperature Charts for Liquid Petroleum Products (2009). doi:10.1520/D0341-09.

[37] D. Dowson, G. Higginson, Elasto-hydrodynamic lubrication: the fundamentals of roller and gear lubrication, The Commonwealth and international library, Pergamon Press, 1966.

[38] P. W. Gold, A. Schmidt, Dicke., J. Loos, C. Assmann, Viscosity-pressure-temperature behavior of mineral and synthetic oils, J. Synth. Lubr. 18(1) (2001) 51–79.

[39] S. Mia, S. Mizukami, R. Fukuda, S. Morita, N. Ohno, High-pressure behavior and tribological properties of wind turbine gear oil, Journal of Mechanical Science and Technology 24 (1) (2010) 111–114. doi:10.1007/s12206-009-1179-5.

[40] ASTM D5185 - 09: Standard test method for determination of additive elements, wear metals, and contaminants in used lubricating oils and determination of selected elements in base oils by inductively coupled plasma atomic emission spectrometry (ICP-AES) (2013). doi:10.1520/D5185.

[41] N. Corporation, What you need to know when selecting gear oils, Machinery Lubrication 9.

[42] S. Heston, Basic lubricant identification in the field, Tribology & Lubrication Technology January (2012) 2–6.

[43] Öel Checker, Typical limit values for motor oils from diesel engines (stationary or non-stationary) - wear metals, contaminants and additives, Oel Check Spring (2010) 6–7.

[44] M. Spurlock, Testing new gear oil, Machinery Lubrication 11, 2007.

[45] P. M. Cann, H. A. Spikes, In lubro studies of lubricants in ehd contacts using ftir absorption spectroscopy, Tribology Transactions 34 (2) (1991) 248–256. doi:10.1080/10402009108982033.

[46] D. Pinchuk, E. Akochi-Koblé, R. A. Cocciardi, J. Pinchuk, F. van de Voort, J. Sedman, Demystifying and understanding your lubricants using ft-ir spectroscopic analysis, Thermal-Lube (2014) 14.

[47] P. Anuradha, P. Kumar, New film thickness formula for shear thinning fluids in thin film elastohydrodynamic lubrication line contacts, Proceedings of the Institution of Mechanical Engineers, Part J: Journal of Engineering Tribology 225 (4) (2011) 173–179. doi:10.1177/1350650111399520.

[48] H. P. Jost, Lubrication tribology - education and research, Tech. rep., Department of Education and Science, HMSO, London (1966).

[49] N. Fang, L. Chang, M. Webster, A. Jackson, A non-averaging method of determining the rheological properties of traction fluids, Tribology International 33 (11) (2000) 751 – 760. doi:10.1016/S0301-679X(00)00116-X.

[50] G. J. Johnston, R. Wayte, H. A. Spikes, The measurement and study of very thin lubricant films in concentrated contacts, STLE Tribology Transaction 34 (1991) 187–194.

[51] G. Guangteng, P. Cann, A. V. Olver, H. A. Spikes, Lubricant film thickness in rough surface, mixed elastohydrodynamic contact, Journal of Tribology 122 (2000) 65–76.

[52] P. M. Cann, H. A. Spikes, J. Hutchinson, The development of a spacer layer imaging method (SLIM) for mapping elastohydrodynamic contacts, Tribology Transactions 39 (1996) 915 – 921.

[53] L. Gustafsson, E. Hoglund, O. Marklund, Measuring lubricant film thickness with image analysis, Proceedings - IMechE: J, Journal of Engineering Tribology 208 (1994) 199–205.

[54] M. Hartl, I. Krupka, M. Liska, Differential colorimetry: tool for evaluation of chromatic interference patterns, Optical Engineering 36 (9) (1997) 2384–2391. doi:10.1117/1.601415.

[55] J. A. Greenwood, J. J. Kauzlarich, Elastohydrodynamic film thickness for shear-thinning lubricants, Proceedings of the Institution of Mechanical Engineers, Part J: Journal of Engineering Tribology 212 (3) (1998) 179–191. doi:10.1243/1350650981541994.

[56] H. van Leeuwen, The determination of the pressure-viscosity coefficient of a lubricant through an accurate film thickness formula and accurate film thickness measurements, Proceedings of the Institution of Mechanical Engineers, Part J: Journal of Engineering Tribology 223 (2009) 1143–1163.

[57] R. J. Chittenden, D. Dowson, J. F. Dunn, M. Taylor, C., A theoretical analysis of the isothermal elastohydrodynamic lubrication of concentrated contacts, part i: direction of lubricant entrainment coincident with the major axis of the hertzian contact ellipse., Proc. R. Soc. Lond A397(1813) (1985) 245–269.

[58] B. J. Hamrock, S. R. Schmid, B. Jacobson, Fundamentals of fluid film lubrication, 2nd edition, Dekker, Basel, 2004.

[59] C. Roelands, Correlational aspects of the viscosity-temperature-pressure relationship of lubricating oils, Ph.D. thesis, Delft University of Technology (1967).

[60] P. K. Gupta, H. S. Cheng, D. Zhu, N. H. Forster, J. B. Schrand, Viscoelastic effects in mil-l-7808-type lubricant, part i: Analytical formulation, Tribology Transactions 35 (2) (1992) 269–274. doi:10.1080/10402009208982117.

[61] S. Bair, P. Gordon, Rheological challenges and opportunities for ehl, in: R. Snidle, H. Evans (Eds.), IUTAM Symposium on Elastohydrodynamics and Micro-elastohydrodynamics, Vol. 134 of Solid Mechanics and Its Applications, Springer Netherlands, 2006, pp. 23–43. doi:10.1007/1-4020-4533-6_2.

[62] I. Krupka, S. Bair, P. Kumar, M. Khonsari, M. Hartl, An experimental validation of the recently discovered scale effect in generalized newtonian ehl, Tribology Letters 33 (2) (2009) 127–135. doi:10.1007/s11249-008-9397-z.

[63] A. J. Brandão, M. Meheux, F. Ville, C. M. J., J. Seabra, Traction curves and rheological parameters of fully formulated gear oils, Proceedings of the Institution of Mechanical Engineers, Part J: Journal of Engineering Tribology (in press) 225 (2011) 577–593.

[64] EHD2 Ultra Thin Film Measurement System, Tech. rep. (2014).

[65] B.-R. Höhn, K. Michaelis, M. Hinterstoißer, Optimization of gearbox efficiency, goriva i maziva 48 (4) (2009) 462–480.

[66] B.-R. Höhn, K. Michaelis, T. Vollmer, Thermal rating of gear drives: Balance between power loss and heat dissipation, AGMA Technical Paper, 1996.

[67] K. Michaelis, B. R. Höhn, M. Hinterstoiber, Influence factors on gearbox power loss, Industrial Lubrication and Tribology 63 (1) (2011) 46–55. doi:10.1108/00368791111101830.

[68] S. Seetharaman, A. Kahraman, Load-independent spin power losses of a spur gear pair: Model formulation, Journal of Tribology 131 (2) (2009) 022201. doi:10.1115/1.3085943.

[69] Y. Diab, F. Ville, P. Velex, C. Changenet, Windage losses in high speed gears—preliminary experimental and theoretical results, Journal of Mechanical Design 126 (5) (2004) 903–908. doi:10.1115/1.1767815.

[70] J. Croes, S. Iqbal, D2.1 document 1: Literature survey: gear losses, Tech. rep., ESTOMAD (2009).

[71] H. Mizutani, Y. Isikawa, D. P. Townsend, Effects of lubrication on the performance of high speed spur gears, NASA 1969.

[72] A. S. Terekhov, Hydraulic losses in gearboxes with oil immersion, Vestn. Mashinostroeniya 55 (5) (1975) 13–17.

[73] P. Walter, Anwendungsgrenzen für die tauchschmierung von zahnradgetrieben., Tech. rep., FVA-Forschungsheft Nr. 118 (1982).

[74] E. Lauster, M. Boos, Zum wärmehaushal mechanischer schaltgetriebe für nutzfahrzeuge, VDI-Ber. 488 (1983) 45–55.

[75] W. Mauz, Zahnradsehmierung - Leerlaufverluste, FVA-Forschungsheft Nr. 185, 1985.

[76] R. J. Boness, Churning losses of discs and gears running partially submerged in oil, Procedings of ASME International Power Transmission Gearing Conference 1 (1989) 355–359.

[77] J. W. Daily, R. E. Nece, Chamber dimension effects on induced flow and frictional resistance of enclosed rotating disks, ASME Journal of Fluids Engineering, 1960.

[78] R. W. Mann, C. H. Marston, Friction drag on bladed disks in housings as a function of reynolds number, axial and radial clearance, and blade aspect ratio and solidity, ASME Journal of Fluids Engineering, 1961.

[79] P. Luke, A. V. Olver, A study of churning losses in dip-lubricated spur gears, Proceedings of the Institution of Mechanical Engineers, Part G: Journal of Aerospace Engineering 213 (5) (1999) 337–346. doi:10.1243/0954410991533061.

[80] R. Martins, J. Seabra, A. Brito, C. Seyfert, A. Luther, R.and Igartua, Friction coefficient in fzg gears lubricated with industrial gear oils:biodegradable ester vs. mineral oil, Tribology International 39 (6) (2006) 512–521. doi:10.1016/j.triboint.2005.03.021.

[81] R. Martins, P. Moura, J. Seabra, Power loss in fzg gears: Mineral oil vs. biodegradable ester and carburizedsteel vs. austempered ductile iron vs. mos2-ti coated steel, VDI Berichte 1904.2 (1904 II) (2005) 1467–1486.

[82] R. Martins, N. Cardoso, J. Seabra, Gear power loss performance of biodegradable low-toxicity ester-based oils, Proceedings of the Institution of Mechanical Engineers Part J-Journal of Engineering Tribology 222 (J3) (2008) 431–440. doi:10.1243/13506501jet345.

[83] C. Changenet, G. Leprince, F. Ville, P. Velex, A note on flow regimes and churning loss modeling, Journal of Mechanical Design 133 (12) (2011) 121009. doi:10.1115/1.4005330.

[84] G. LePrince, C. Changenet, F. Ville, P. Velex, C. Dufau, F. Jarnias, Influence of Aerated Lubricants on Gear Churning Losses - An Engineering model, Tribology Transactions 54 (6) (2011) 929–938. doi:10.1080/10402004.2011.597542.

[85] G. Leprince, Pertes mécaniques par frottement et lubrification dans une boîte de vitesses, Ph.D. thesis, L'Institut National des Sciences Appliquees de Lyon (2011).

[86] C. Changenet, P. Velex, A model for the prediction of churning losses in geared transmissions—preliminary results, Journal of Mechanical Design 129 (1) (2007) 128–133. doi:10.1115/1.2403727.

[87] C. Changenet, P. Velex, Housing influence on churning losses in geared transmissions, Journal of Mechanical Design 130 (6) (2008) 062603. doi:10.1115/1.2900714.

[88] C. Changenet, P. Velex, A model for the prediction of churning losses in geared transmissions - preliminary results, Journal of Mechanical Design 1 (2007) 128–133.

[89] P. M. Marques, C. M. Fernandes, R. C. Martins, J. H. Seabra, Power losses at low speed in a gearbox lubricated with wind turbine gear oils with special focus on churning losses, Tribology International 62 (0) (2013) 186 – 197. doi:10.1016/j.triboint.2013.02.026.

[90] F. Concli, C. Gorla, Computational and experimental analysis of the churning power losses in an industrial planetary speed reducer, in: 9th International Conference on Advances in Fluid Mechanics-Advances in Fluid Mechanics IX, WIT Transactions on Engineering Sciences, Vol. 74, 2012, pp. 287–298.

[91] Y. Ariura, T. Ueno, The lubricant churning loss and its behavior in gearbox in cylindical gear systems, Journal of Japan Society of Lubrication Engineers 20, N 3.

[92] L. S. Akin, J. J. Mross, D. P. Townsend, Study of lubricant jet flow phenomena in spur gears, Journal of Tribology 97 (2) (1975) 283–288. doi:10.1115/1.3452576.
URL http://dx.doi.org/10.1115/1.3452576

[93] N. E. Anderson, S. H. Loewenthal, P. L. (U.S.), U. States., Spur-gear-system efficiency at part and full load, National Aeronautics and Space Administration, Scientific and technical Information Office, Washington, D.C., 1980.

[94] P. H. Dawson, Windage loss in larger high-speed gears, Proceedings of the Institution of Mechanical Engineers, Part A: Journal of Power and Energy 198 (1) (1984) 51–59. doi:10.1243/PIME_PROC_1984_198_007_02.

[95] A. A. Lord, Experimental investigation of geometric and oil flow effects on gear windage and meshing losses, Ph.D. thesis, University of Wales Swansea (1998).

[96] R. F. Handschuh, C. J. Kilmain, Preliminary comparison of experimental and analytical efficiency results of high-speed helical gear trains, ASME 2003 International Design Engineering Technical Conferences and Computers and Information in Engineering Conference, 2003.

[97] T. T. Petry-Johnson, A. Kahraman, N. E. Anderson, D. R. Chase, An experimental investigation of spur gear efficiency, Journal of Mechanical Design 130 (6) (2008) 062601–062601. doi:10.1115/1.2898876.

[98] E. Buckingham, Analytical mechanics of gears, Dover Books for Engineers, McGraw-Hill Book Co., 1949.

[99] H. Ohlendorf, Verlustleistung und Erwärmung von Stirnrädern, Ph.D. thesis, Dissertation TU München (1958).

[100] J. A. de Sousa Ferreira Brandão, Gear tooth flank damage prediction using high-cycle fatigue and wear models, Ph.D. thesis, Faculdade de Engenharia da Universidade do Porto (2013).

[101] H. Merrit, Gear Engineering, Pitman, 1971.

[102] G. Henriot, Traité theéorique et pratique des engrenages, Dunod, 1978.

[103] G. Niemann, H. Winter, Maschinenelemente: Band 2: Getriebe allgemein, Zahnradgetriebe - Grundlagen, Stirnradgetriebe, Maschinenelemente /Gustav Niemann, Springer, 1989.

[104] ISO 14179-2: Gears Reducers - Thermal Capacity Part 2: Thermal load-carrying capcity (2001).

[105] A. J. Wimmer, Lastverluste von stirnradverzahnungen, Konstruktive einfüsse, wirkungsgradmaximierung, tribologie, Fakultät für Maschinenwesen der Technischen Universität München (2006).

[106] B. Höhn, K. Michaelis, A. Wimmer, Low loss gears, Gear Technology (2007) 28 – 35.

[107] N. E. Anderson, S. H. Loewenthal, Efficiency of nonstandard and high contact ratio involute spur gears, Journal of Mechanical Design 108 (1) (1986) 119–126. doi:10.1115/1.3260774.

[108] B. R. Höhn, K. Michaelis, A. Wimmer, Gearboxes with minimised power loss, VDI Berichte (1904 II) (2005) 1451–1465.

[109] R. Stribeck, Die wesentlischen eigenschaften der gleit- und rollenlager, pt I, Zeitschrift des Vereines deutscher Ingenieure 46 (37) (1902) 1341–1348.

[110] R. Stribeck, Die wesentlischen eigenschaften der gleit- und rollenlager, pt II, Zeitschrift des Vereines deutscher Ingenieure 46 (38) (1902) 1432–1438.

[111] R. Stribeck, Die wesentlischen eigenschaften der gleit- und rollenlager, pt III, Zeitschrift des Vereines deutscher Ingenieure 46 (39) (1902) 1463–1470.

[112] X. Hai, DEVELOPMENT OF A GENERALIZED MECHANICAL EFFICIENCY PREDICTION METHODOLOGY FOR GEAR PAIRS, Ph.D. thesis, The Ohio State University (2005).

[113] Y. A. Misharin, Influence of the friction condition on the magnitude of the friction coefficient in the case of rollers with sliding, Proceedings International Conference on Gearing, Institute Mechanical Engineers, 1958.

[114] H. Eiselt, Beitrag zur experimentellen und rechnerischen bestimmung der fresstragfähigkeit von zahnradgetrieben unter berücksichtigung der zahnflankenreibung, Ph.D. thesis, TH Desden (1966).

[115] J. P. O'Donoghue, A. Cameron, Friction and temperature in rolling sliding contacts, A S L E Transactions 9 (2) (1966) 186–194. doi:10.1080/05698196608972134.

[116] Y. Drozdov, Y. Gavrikov, Friction and scoring under the conditions of simultaneous rolling and sliding of bodies, Wear 11 (4) (1968) 291 – 302. doi:http://dx.doi.org/10.1016/0043-1648(68)90177-4.

[117] C. NARUSE, S. HAIZUKA, R. NEMOTO, T. SUGANUMA, Studies on limiting load for scoring and frictional loss of hypoid gears of klingelnberg type, Bulletin of JSME 27 (231) (1984) 2053–2060. doi:10.1299/jsme1958.27.2053.

[118] DIN 3990: Tragfähigkeitsberechnung Von Stirnrädern : Anwendungsnorm für Industriegetriebe Detail-Methode, Beuth, 1989.

[119] K. Michaelis, Die integraltemperatur zur beurteilung der fresstragfähigkeit von stirnrädern, Ph.D. thesis, TU München (1987).

[120] L. Schlenk, Unterscuchungen zur Fresstragfähigkeit von Grozahnrädern, Ph.D. thesis, Dissertation TU München (1994).

[121] T. E. Tallian, On competing failure modes in rolling contact, A S L E Transactions 10 (4) (1967) 418–439. doi:10.1080/05698196708972201.

[122] S. Matsumoto, K. Morikawa, The new estimation formula of coefficient of friction in rolling-sliding contact surface under mixed lubrication condition for the power loss reduction of power transmission gears, International Gear Conference, 2014.

[123] G. H. Benedict, B. W. Kelley, Instantaneous coefficients of gear tooth friction, A S L E Transactions 4 (1) (1961) 59–70. doi:10.1080/05698196108972420.

[124] P. Eschmann, L. Hasbargen, K. Weigand, Ball and Roller Bearings - Theory, Design, and Application, John Wiley and Sons, 1985.

[125] A. Palmgren, Ball and roller bearing engineering, SKF Industries, 1959.

[126] V. PALEU, S. CRETU, D. NELIAS, Friction moment in oil and kerosene mist lubricated all-steel and hybrid ball bearings, in: 16th International Colloquium Tribology, 2008.

[127] X. T. Xia, T. M. Lv, Dynamic prediction of rolling bearing friction torque using lyapunov exponent method, Applied Mechanics and Materials 44-47 1120–1124.

[128] V. Wikström, E. Höglund, Starting and steady-state friction torque of grease-lubricated rolling element bearings at low temperatures-part ii: Correlation with less-complex test methods, Tribology Transactions 39 (3) (1996) 684–690. doi:10.1080/10402009608983583.

[129] SKF General Catalogue 6000 EN, SKF, November 2005.

[130] G. Morales-Espejel, Using a friction model as an engineering tool, Evolution SKF 2 (2006) 27–30.

[131] I. FAG, Bearinx - online easy friction, Tech. rep., Shaeffler Group (2011).

[132] NTN, Rolling bearings handbook, Tech. rep. (CAT. No. 9012/E).
URL http://www.ntn-snr.com/portal/it/it-it/file.cfm/Bearing-HB-en.pdf?contentID=8897

[133] NSK, Technical Report CAT. No. E728g.
URL http://www.ntn-snr.com/portal/it/it-it/file.cfm/Bearing-HB-en.pdf?contentID=8897

[134] L. Houpert, Tribology: Numerical and analytical calculations in ball bearings, in: D. Danesy (Ed.), 8th European Space Mechanisms and Tribology Symposium, Vol. 438 of ESA Special Publication, 1999, p. 283.

[135] L. Houpert, Ball bearing and tapered roller bearing torque: Analytical, numerical and experimental results, Tribology Transactions 45 (3) (2002) 345–353. doi:10.1080/10402000208982559.

[136] M. R. D. Balan, V. C. Stamate, L. Houpert, D. N. Olaru, The influence of the lubricant viscosity on the rolling friction torque, Tribology International 72 (0) (2014) 1 – 12. doi:http://dx.doi.org/10.1016/j.triboint.2013.11.017.

[137] T. Harris, M. Kotzalas, Advanced Concepts of Bearing Technology,: Rolling Bearing Analysis, Fifth Edition, Advanced concepts of bearing technology, Taylor & Francis, 2006.

[138] O. Reynolds, On the theory of lubrication and its application to mr. beauchamp tower's experiments, including an experimental determination of the viscosity of olive oil., Proceedings of the Royal Society of London 40 (242-245) (1886) 191–203.

[139] R. S. Zhou, M. R. Hoeprich, Torque of tapered roller bearings, Journal of Tribology 113 (3) (1991) 590–597. doi:10.1115/1.2920664.

[140] T. Cousseau, B. Graça, A. Campos, J. Seabra, Experimental measuring procedure for the friction torque in rolling bearings, Lubrication Science Volume 22, Issue 4 (April 2010) 133–147.

[141] J. Croes, S. Iqbal, D2.1 document 3: Literature survey: seal losses, Tech. rep., ESTOMAD (2009).

[142] Simrit: Radialwellendichtringe, Katalog Nr. 100, 1976.

[143] H. Linke, Stirnradverzahnung, Hanser Verlag, 1996.

[144] J. Kettler, Ölsumpftemperatur von Planetengetrieben: Abschlußbericht ; Forschungsvorhaben Nr. 313: Planetengetriebe-Sumpftemperatur, Forschungsheft: Forschungsvereinigung Antriebstechnik, FVA, 2002.

[145] R. Martins, J. Seabra, C. Seyfert, R. Luther, A. Igartua, A. Brito, Power loss in fzg gears lubricated with industrial gear oils: Biodegradable ester vs. mineral oil, in: M. P. G. D. D. Dowson, A. A. Lubrecht (Eds.), Tribology and Interface Engineering Series, Vol. Volume 48, Elsevier, 2005, pp. 421–430.

[146] R. Martins, J. Seabra, C. Seyfert, R. Luther, A. Igartua, A. Brito, Power loss in FZG gears lubricated with industrial gear oils: biodegradable ester vs. mineral oil, in: Proceedings of the 31th "Leeds-Lyon Symposium" on Tribology, Leeds, UK, 2004.

[147] T. Oliveira, R. Martins, J. Seabra, C. Seyfert, A. Igartua, Efficiency tests of a transfer gearbox: biodegradable non-toxic ester vs.mineral oil, Mecânica Experimental (13) (2006) 45–54.

[148] L. Magalhães, R. Martins, C. Locateli, J. Seabra, Influence of tooth profile and oil formulation on gear power loss, Tribology International 43 (10) (2010) 1861–1871, 36th Leeds-Lyon Symposium Special Issue: Multi-facets of Tribology. doi:10.1016/j.triboint.2009.10.001.

[149] G. Funck, Wärmeabführung bei Getrieben unter quasistationären Betriebsbedingungen, Technische Universität München, 1985.

[150] C. Changenet, X. Oviedo-Marlot, P. Velex, Power loss predictions in geared transmissions using thermal networks-applications to a six-speed manual gearbox, Journal of Mechanical Design 128 (3) (2006) 618–625. doi:10.1115/1.2181601.

[151] J. Durand De Gevigney, C. Changenet, F. Ville, P. Velex, Thermal modelling of a back-to-back gearbox test machine: Application to the fzg test rig, Proceedings of the Institution of Mechanical Engineers, Part J: Journal of Engineering Tribology 226 (6) (2012) 501–515, cited By (since 1996)3.

[152] K. Holmberg, P. Andersson, A. Erdemir, Global energy consumption due to friction in passenger cars, Tribology International 47 (0) (2012) 221 – 234. doi:http://dx.doi.org/10.1016/j.triboint.2011.11.022.

[153] K. Holmberg, R. Siilasto, T. Laitinen, P. Andersson, A. Jäsberg, Global energy consumption due to friction in paper machines, Tribology International 62 (0) (2013) 58 – 77. doi:http://dx.doi.org/10.1016/j.triboint.2013.02.003.

[154] D. Dowson, History of Tribology, Longman, 1979.

[155] C. Attila, M. Kozma, Influence of the oil churning, the bearing and the tooth friction losses on the efficiency of planetary gears, Journal of Mechanical Engineering 56 (2010) 245–252.

[156] E. C. Cabello, Advantages of modified polyalphaolefines for gearboxes in wind power industry, in: LUBMAT, June 2012.

[157] R. Koschabek, C. Wincierz, M. Müller, M. P. Kettunen, S. Dörr, New approaches to wind turbine gear oil formulation, in: 18th International Colloquium Tribology INDUSTRIAL and AUTOMOTIVE LUBRICATION, 2012.

[158] H. Siebert, A.-P. Holm, Protecting gears in wind power applications, Gear Solutions March (2009) 39–44.

[159] S. CRETU, I. DAMIAN, A more accuarate evaluation of the frictional torque in angular contact ball bearings, in: 8th International Tribology Conference, 2003.

[160] J. Takabi, M. Khonsari, Experimental testing and thermal analysis of ball bearings, Tribology International 60 (0) (2013) 93 – 103. doi:http://dx.doi.org/10.1016/j.triboint.2012.10.009.

[161] M. Bercea, M. Bercea, Friction reduction in rolling bearing by using polymer additives, Lubrication Science 21 (8) (2009) 321–330. doi:10.1002/ls.97.

[162] S. Iqbal, F. Al-Bender, J. Croes, B. Pluymers, W. Desmet, Frictional power loss in solid-grease-lubricated needle roller bearing, Lubrication Science 25 (5) (2013) 351–367. doi:10.1002/ls.1195.

[163] T. Hatazawa, T. Kawaguchi, Frictional torque of needle roller thrust bearings, Tribology Transactions 52 (1) (2008) 127–132. doi:10.1080/10402000802561384.

[164] J. J. Blake, C. E. Truman, Measurement of running torque of tapered roller bearings, Proceedings of the Institution of Mechanical Engineers, Part J: Journal of Engineering Tribology 218 (4) (2004) 239–250. doi:10.1243/1350650041762659.

[165] Y. Yang, S. Danyluk, M. Hoeprich, Rolling element skew in tapered roller bearings, Tribology Transactions 43 (3) (2000) 564–568. doi:10.1080/10402000008982379.

[166] N. Geheeb, J. Franke, The effects of lubricant additives on the wear of rolling bearings can be determined on test rigs, Maschinenmarkt, No. 6, February 6, 2000.

[167] V. PALEU, S. CRETU, D. DRAGAN, R. BALAN, Test rig for friction torque measurement in rolling bearings, in: THE ANNALS OF UNIVERSITY "DUNAREA DE JOS" OF GALATI, 2004FASCICLE VIII, 2004, ISSN 1221-4590 TRIBOLOGY.

[168] M. Weigand, Lubrication of rolling bearings - technical solutions for critical running conditions, Machinery Lubrication, January, 2006.

[169] C. M. Fernandes, R. C. Martins, J. H. Seabra, Friction torque of thrust ball bearings lubricated with wind turbine gear oils, Tribology International 58 (0) (2013) 47 – 54. doi:10.1016/j.triboint.2012.09.005.

[170] C. M. Fernandes, R. C. Martins, J. H. Seabra, Friction torque of cylindrical roller thrust bearings lubricated with wind turbine gear oils, Tribology International 59 (0) (2013) 121 – 128. doi:http://dx.doi.org/10.1016/j.triboint.2012.05.030.

[171] C. M. Fernandes, P. M. Amaro, R. C. Martins, J. H. Seabra, Torque loss in thrust ball bearings lubricated with wind turbine gear oils at constant temperature, Tribology International 66 (0) (2013) 194 – 202. doi:http://dx.doi.org/10.1016/j.triboint.2013.05.002.

[172] C. M. Fernandes, P. M. Amaro, R. C. Martins, J. H. Seabra, Torque loss in cylindrical roller thrust bearings lubricated with wind turbine gear oils at constant temperature, Tribology International 67 (0) (2013) 72 – 80. doi:http://dx.doi.org/10.1016/j.triboint.2013.06.016.

[173] R. Martins, New materials, surface coatings and biodegradable oils for industrial gears, Ph.D. thesis, Faculdade de Engenharia da Universidade do Porto (2008).

[174] A. Neurouth, C. Changenet, F. Ville, A. Arnaudon, Thermal modeling of a grease lubricated thrust ball bearing, Proceedings of the Institution of Mechanical Engineers, Part J: Journal of Engineering Tribology, 2014. doi:10.1177/1350650114526387.

[175] F. Pouly, C. Changenet, F. Ville, P. Velex, B. Damiens, Investigations on the power losses and thermal behaviour of rolling element bearings, Proceedings of the Institution of Mechanical Engineers, Part J: Journal of Engineering Tribology 224 (9) (2010) 925–933. doi:10.1243/13506501JET695.

[176] H. Dinner, Wind turbine gearbox calculation, KissSoft.
URL `http://www.kisssoft.ch/english/downloads/KISSsys/Articles/docu_Wind_Turbine_Gearbox_Calculation.pdf`

[177] D. Dowson, G. R. Higginson, Elasto-hydrodynamic Lubrication, SI edition Edition, Pergamon Press, 1977.

[178] I. Standard, ISO 281: Rolling bearings - dynamic load rating and rating life (2007).

[179] G. E. Morales-Espejel, A. Gabelli, E. Ioannides, Micro-geometry lubrication and life ratings of rolling bearings, Proceedings of the Institution of Mechanical Engineers, Part C: Journal of Mechanical Engineering Science 224 (12) (2010) 2610–2626. `doi:10.1243/09544062JMES1965`.

[180] P. Cann, E. Ioannides, B. Jacobson, A. Lubrecht, The lambda ratio - a critical re-examination, Wear 175 (1–2) (1994) 177 – 188. `doi:http://dx.doi.org/10.1016/0043-1648(94)90181-3`.

[181] R. Heemskerk, Ehd lubrication in rolling bearings - review of theory and influence on fatigue life, Stratto da Tribologia e Lubrificazione 4 (1980) 3–7.

[182] A. Brandão, M. Meheux, F. Ville, J. Castro, J. Seabra, Experimental traction and stribeck curves of mineral, pao and ester based fully formulated gear oils, In: Proceedings of the 3rd International Conference on Integrity, Reliability & Failure, Porto, Portugal, 20 - 24 July 2009.

[183] S. Radzevich, Dudley's Handbook of Practical Gear Design and Manufacture, Second Edition, Taylor & Francis, 2012.

[184] L. Euler, De aptissima figura rotarum dentibus tribuenda, Novi Commentarii academiae scientiarum Petropolitanae, 1760.

[185] T. J. Maiuri, Hob tool life technology update, Gear Technology, 2009.

[186] J. Weisbach, L. Gordon, Principles of the Mechanics of Machinery and Engineering, no. vol. 2 in Library of illustrated standard scientific works, H. Bailliere, 1848.

[187] F. Reuleaux, The Constructor - A handbook of machine design, Henry Harrison Suplee, 1893.

[188] ISO 14635-1: FZG test procedures - Part 1: FZG test method A/8,3/90 for relative scuffing load-carrying capacity of oils (2000).

[189] ISO 14635-3: FZG test procedures – Part 3: FZG test method A/2,8/50 for relative scuffing load-carrying capacity and wear characteristics of semifluid gear (2005).

[190] A. Doleschel, Method to determine the frictional behaviour of gear lubricants using fzg gear test rig, FVA Information Sheet N 345, March 2002.

[191] C. Yenti, S. Phongsupasamit, C. Ratanasumawong, Analytical and experimental investigation of parameters affecting sliding loss in a spur gear pair, Engineering Journal, 17, 2012.

[192] ISO 14635-2: FZG test procedures – Part 2: FZG step load test A10/16, 6R/120 for relative scuffing load-carrying capacity of high EP oils (2004).

[193] H. W. K. Michaelis, Scoring tests of aircraft transmission lubricants at high temperatures, Journal of synthetic lubrication, 3, 1986.

[194] H. Winter, P. Oster, Influence of the lubricant on pitting and micro pitting (grey staining, frosted areas) resistance of case carburized gears and test procedures, AGMA, 1987.

[195] FVA Research Project Nr. 54/I-IV, Forschungsvereinigung Antriebstechnik E.V, 1993.

[196] Short test procedure for the investigation of the micropitting load capacityof gear lubricants, DGMK Information sheet, 2002.

[197] H. Winter, K. Michaelis, Fzg gear test rig - desciption and possibilities, In: Coordinate European Council Second International Symposium on The performance Evaluation of Automotive Fuels and Lubricants (1985) 29–42.

[198] M. Andersson, M. Sosa, S. Sjöberg, U. Olofsson, Effect of assembly errors in back-to-back gear efficiency testing, International Gear Conference, August 26-28 2014, Lyon, France.

[199] L. Magalhães, R. Martins, I. Oliveira, J. Seabra, Comparison of tooth profiles and oil formulation focusing lower power losses, Proceedings of the Institution of Mechanical Engineers, Part J: Journal of Engineering Tribology 226 (6) (2012) 529–540. arXiv:http://pij.sagepub.com/content/226/6/529.full.pdf+html, doi:10.1177/1350650112439260.

[200] L. Chang, Y.-R. Jeng, P.-Y. Huang, Modeling and analysis of the meshing losses of involute spur gears in high-speed and high-load conditions, Journal of Tribology 135 (1) (2012) 011504–011504. doi:10.1115/1.4007809.

[201] P. Velex, F. Ville, An analytical approach to tooth friction losses in spur and helical gears - influence of profile modifications, Journal of Mechanical Design 131 (10) (2009) 101008–101008. doi:10.1115/1.3179156.

[202] R. Frazer, B. Shaw, D. Palmer, M. Fish, Optimizing gear geometry for minimum transmission error, mesh friction losses and scuffing risk through computer-aided engineering, Gear Technology, August 2010.

[203] F. Joachim, J. Börner, N. Kurz, How to minimize power losses in transmissions, axles and steering systems, Gear Technology, September 2012.

[204] H. Dinner, Gearing analysis for wind turbine, seen as a process, KISSsoft.
URL http://www.kisssoft.ch/english/downloads/KISSsys/Articles/docu_Showing_the_teeth_at_the_wind.pdf

[205] H. Dinner, Uncertainties in the static calculation of wind turbine gearboxes, KissSoft.
URL http://www.kisssoft.ch/english/downloads/KISSsys/Articles/docu_Uncertainties_in_Static_Calculation_WindTurbine.pdf

[206] L. Rudnick, Lubricant Additives: Chemistry and Applications, Second Edition, Chemical Industries, Taylor & Francis, 2010.

[207] D. Pirro, A. Wessol, Lubrication Fundamentals, Second Edition, MECHANICAL ENGINEERING, Taylor & Francis, 2001.

[208] M. Masuko, H. Sato, A. Suzuki, O. Kurosawa, Prevention of oxidative degradation of zndtp by microcapsulation and verification of its antiwear performance, Tribology International 41 (11) (2008) 1097 – 1102. doi:http://dx.doi.org/10.1016/j.triboint.2008.01.005.

[209] B. S. of Rheology. Conference, R. Wetton, R. Whorlow, Polymer Systems Deformation and Flow: Proceedings of the 1966 Annual Conference, British Society of Rheology, Conference, 1968.

[210] P. J. Carreau, Phd thesis, Ph.D. thesis, University of Wisconsin (1969).

[211] C. Seeton, Viscosity-temperature correlation for liquids, Tribology Letters 22 (1) (2006) 67–78. doi:10.1007/s11249-006-9071-2.

[212] A. Y. Malkin, G. V. Vinogradov, Molecular weight - viscosity relationships of polymers at high rates of shear, Journal of Polymer Science Part B: Polymer Letters 2 (7) (1964) 671–673. doi:10.1002/pol.1964.110020703.

[213] P. M. Lugt, G. E. Morales-Espejel, A review of elasto-hydrodynamic lubrication theory, Tribology Transactions 54 (3) (2011) 470–496. doi:10.1080/10402004.2010.551804.

[214] H. Vogel, The law of the relation between the viscosity of liquids and the temperature, Physikalische Zeitschrift 22 (1921) 645.

[215] D2270-93 - Petroleum products - Calculation of viscosity index from kinematic viscosity (West Conshohocken, PA, 2003). doi:10.1520/D2270-10E01.

[216] C. Barus, Isothermals, isopiestics and isometrics relative to viscosity, American journal of science 45 (266) (1893) 87–96.

[217] B. Hamrock, Fundamentals of fluid film lubrication, McGraw-Hill series in mechanical engineering, McGraw-Hill Higher Education, 1994.

[218] R. Schrader, Zur Schmierfilmbildung von Schmierölen und Schmierfetten im elastohydrodynamischen Wälzkontakt, 1988.

[219] K. Johnson, K. Johnson, Contact Mechanics, Cambridge University Press, 1987.

[220] M. Woydt, R. Wäsche, The history of the stribeck curve and ball bearing steels: The role of adolf martens, Wear 268 (11–12) (2010) 1542 – 1546. doi:http://dx.doi.org/10.1016/j.wear.2010.02.015.

Appendix

Appendix A.

Lubricant additives

A.1. Antioxidant (AO)

One of the most important aspects of lubricating oils is to maximize the oxidation stability. The exposition of hydrocarbons to oxygen and heat will promote the oxidation process. Also, metal parts such copper and iron, act as effective oxidation catalysts. Oxidation produces harmful species, which can compromise the functionality of a lubricant, shortens the service life and in a more extreme point of view, damages the machinery.

The aging of lubricants can be differentiated into two processes: the oxidation process by reaction of the lubricant molecules with oxygen and the thermal decomposition (cracking) at high temperatures [23]. The aged lubricants discolorate and have a burnt odour. In cases of advanced oxidation the viscosity rises significantly, acidic products are generated which promote corrosion and other lubricant problems.

Researchers had verified that some oils provided greater resistance to oxidation than others. The difference was identified as naturally occurring antioxidants which varied depending on crude source or refining techniques. Some of these natural antioxidants were found to contain sulfur or nitrogen-bearing functional groups [206]. The most common oil-soluble organic and organo-metallic antioxidants are compounds of: sulfur; phosphorus; sulphur-phosphorus; phenolic; aromatic amine; hindered phenolic; organo-alkaline earth salt; organo-zinc; organo-copper and organo-molybdenum.

Today all lubricants contain at least one antioxidant for stabilization and other performance-enhancing purposes [206].

A.2. Anti-foam agents (AF)

The foaming of lubricants is a very undesirable effect that can promote additional oxidation by intensive mixture with air, cavitation damage as well as insufficient oil on the lubricating systems [23, 206].

Silicone polymers used at a few parts per million are the most widely used anti-foam agents. These materials are essentially insoluble in oil, and the correct choice of polymer size and blending procedures is critical if settling during long-term storage is to be avoided. Also, these additives may increase air entrainment in the oil. Organic polymers are sometimes used to overcome these difficulties with the silicones, although much higher concentrations are generally required. It is thought that the anti-foam agents droplets attach themselves to the air bubbles and can either spread or form unstable bridges between bubbles, which then coalesce into larger bubbles, which in turn rise more readily to the surface of the foam layer where they collapse, thus releasing the air [207].

A.3. Detergent and dispersant (D/D)

Detergents and dispersants together correspond to 45 to 50 % of the total volume of lubricant additives manufactured.

Detergents neutralize oxidation-derived acids as well as help suspend polar oxidation products in the lubricant.

A.4. Viscosity index improvers (VM)

VI improvers are long chain, high molecular weight polymers that function by causing the relative viscosity of an oil to increase more at high temperatures than at low temperatures. Generally this result is due to a change in the polymer's physical configuration with increasing temperature of the mixture. It is postulated that in cold oil the molecules of the polymer adopt coiled form so that their effect on viscosity is minimized. In hot oil, the oil produces a proportionally greater thickening effect [23, 207].

The absolute increase in viscosity and VI depends on the type, the molecular weight and the concentration of viscosity modifiers in the formulation. Concentrations are usually between 3 and 30%. As a result of their high molecular weight, viscosity modifiers are always dissolved in a base fluid [23].

Apart from their thickening effect that increases with molecular weight, the shear stability is reduced with increasing molecular weight if the polymer concentration remains constant. As will be explained on Appendix B, for the Newtonian fluids the viscosity is independent of the shear rate. The long chain compounds used as VM when subjected to high shear are mechanically broken and depending on the type and duration of the load different molecular sizes are created. This results in reduction of the viscosity of the oil.

A.5. Pour point depressants (PPD)

Certain high molecular weight polymers function by inhibiting the formation of a wax crystal structure that would prevent oil flow at low temperatures [207]. Two general types of pour point depressant are used:

1. Alkylaromatic polymers adsorb on the wax crystals as they form, preventing them from growing and adhering to each other.

2. Polymethacrylates cocrystallize with wax to prevent crystal growth.

With the exception of polyalkylated naphthalenes, pour-point depressants (PPD) are closely linked to a series of viscosity modifiers. The major difference of these polymers is their application concentration and the selection of monomer building blocks . Molecular weight and thickening efficiency only play a subordinate role in a band from 0.1 to max. 2%. An additional thickening effect is always welcome but is usually limited by solubility thresholds [23].

A.6. Rust and corrosion inhibitors (CI)

Rust and corrosion inhibitors are compounds having a high polar attraction that are used in nearly every lubricant to protect the metal surface of any machinery from the attack of oxygen, moisture and aggressive products. The base oil itself creates a protective layer on the metal surface but usually this is not sufficient especially in the case of highly refined oils without natural inhibitors.

A.7. Anti-wear (AW) and extreme-pressure (EP) agents

In practice, the various contact types in a machine, the incidence of operating conditions beyond the design range, and the pressure to improve efficiency results in a oil film thickness below the optimum. In this conditions, the hydrodynamic film is not developed and a mixed or boundary condition is present, the asperities on the interacting surfaces start to contact and the temperature rises. The AW and EP additives react with the surfaces forming tribolayers that prevent direct contact between the sliding surfaces. Usually, anti-wear agents have a lower activation temperature than the extreme-pressure ones.

The distinction between anti-wear and extreme-pressure additives is not very clear. Some are classified as AW in one application and EP in another, and some have both functions [206]. AW additives are designed to deposit surface films under moderate

contact pressures whereas EP additives are much more reactive and are used when the contact pressures are very high in order to prevent modes of failure like scuffing. Typically EP additives increase wear effects due to their high reactivity [23]. Recently it has been suggested to rename the EP additives as anti-scuffing additives, since there is no contact pressure distinction between them and anti-wear additives.

Common AW and EP additives are organo-sulfur and organo-phosphorus compounds; organic polysulfides, phosphates dithiophosphates and dithiocarbamates are frequent [208]. In the 30's the zinc dialkydithiophosphates (ZDDP) was introduced initially to prevent bearing corrosion but later was found to have good antioxidant and anti-wear abilities becoming the most widespread anti-wear additive [23].

A.8. Friction modifiers (FM)

The friction modifiers have to be used to prevent stick-slip oscillations and noises by reducing frictional forces. They work at temperatures where AW and EP additives are not yet reactive [23].

In order to fully understand the function of FM additives, a parallel must be done with AW and EP additives. The AW and EP additives mostly provide good boundary lubrication conditions generating strong layers on the surfaces. The big difference are their mechanical properties. AW/EP are semi-plastic deposits that are difficult to shear off. In turn, FM are build of orderly and closely packed arrays of multi-molecular layers, loosely adhering to one another and with the polar head anchored on the metal surface. The outer layers of the film can be easily sheared off, allowing a reduction of the coefficient of friction [206].

There are different groups of friction modifiers according their function:

- mechanically working FMs with solid lubricating compounds (molybdenum disulfide; graphite; PTFE; polyamide; polyamide; polyimide; fluorinated graphite)
- adsorption layers FMs (long chain carboxylic acids; fatty acid esters; ethers; alcohols; amines; amides; imides)
- tribolayers forming FMs (saturated fatty acids; phosphoric and thiophosphoric acid esters; xanthogenates; sulfurized fatty acids)
- friction polymer-forming FMs (glycol dicarboxylic acid partial esters; dialkyl phthalic esters; methacrylates; unsaturated fatty acids; sulfurized olefins)
- organometallic compounds (molybdenum dithiophosphates; molybdenum dithiocarbamates; copper containing organic compounds).

Appendix B.

Oil rheology

B.1. Newtonian viscosity

Consider an oil placed between two very wide parallel plates as shown in Figure B.1. The bottom plate is fixed and the upper one is readily to move. When the force P is applied, the oil contacting the upper plate will move with a velocity U while the oil contacting the bottom plate has no motion. The oil contained between the two plates moves with a velocity $u = u(y)$. To resist to the applied force the fluid develop a shear stress, τ, that is proportional at the contacting area, $P = \tau A$.

If a load P is applied on the upper plate as shown, a small displacement, δa, occurs. In a time increment, δt, the displacement cause a small rotation, $\delta\beta$, according to equation (B.1).

$$tan\delta\beta \approx \delta\beta = \frac{\delta a}{b} \tag{B.1}$$

The displacement is also $\delta a = U\delta t$ wich gives the equation (B.2).

$$tan\delta\beta \approx \delta\beta = \frac{U\delta t}{b} \tag{B.2}$$

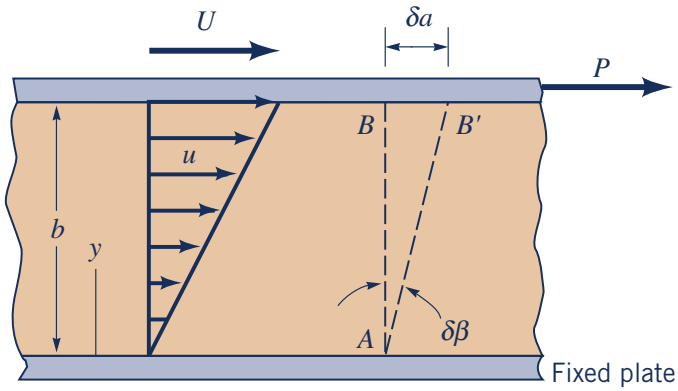

Figure B.1.: Fluid flow between two parallel plates.

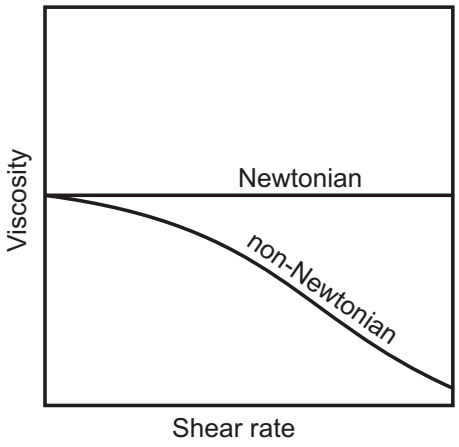

Figure B.2.: Influence of the shear rate on the viscosity of Newtonian and non-Newtonian fluids.

The rate at which $\delta\beta$ is changing with time is defined as rate of shearing strain as presented on equation (B.3).

$$\dot{\gamma} = \lim_{\delta t \to 0} \frac{\delta\beta}{dt} \tag{B.3}$$

The rate of shearing strain can be represented by the variation of the velocity along y as presented on equation (B.4).

$$\dot{\gamma} = \frac{U}{b} = \frac{du}{dy} \tag{B.4}$$

The proportionality constant that is the reason between the shear stress (τ) and the shear rate ($\dot{\gamma}$) as represented by equation (B.5) is called dinamic viscosity [23].

$$\eta = \frac{\tau}{\dot{\gamma}} \tag{B.5}$$

B.2. Non-newtonian viscosity

As presented on the Section B.1, the dynamic viscosity is constant no-matter the shear rate applied for a Newtonian fluid as presented on Figure B.2. In opposite, the dynamic viscosity changes with increasing shear rate for a non-newtonian fluid.

Many author's proposed different analytical equations to describe the flow curves of non-newtonian fluids. The following equations are frequently applied:

- Cross [209], equation (B.6);

$$\eta = \frac{\eta_0}{1 + |\lambda\dot{\gamma}|^m} \tag{B.6}$$

- Carreau [210], equation (B.7);

$$\eta = \frac{\eta_0}{\left[1 + (\lambda\dot{\gamma})^2\right]^{-p}} \tag{B.7}$$

- Yasuda et al. [211], equation (B.8);

$$\eta = \frac{\eta_0}{\left[1 + (\lambda\dot{\gamma})^a\right]^{(n-1)/a}} \tag{B.8}$$

- Vinogradov-Malkin [212], equation (B.9);

$$\eta = \frac{\eta_0}{1 + A\dot{\gamma}^\alpha + B\dot{\gamma}^{2\alpha}} \tag{B.9}$$

The invariant representing the shear rate ($\dot{\gamma}$) presented in previous equations is calculated with equation (B.10).

$$\dot{\gamma} = \sqrt{\frac{2}{3}\left[\left(\frac{\partial u}{\partial x} - \frac{\partial v}{\partial y}\right)^2 + \left(\frac{\partial v}{\partial y} - \frac{\partial w}{\partial z}\right)^2 + \left(\frac{\partial w}{\partial z} - \frac{\partial u}{\partial x}\right)^2\right] + \dot{\gamma}_{xy}^2 + \dot{\gamma}_{yz}^2 + \dot{\gamma}_{xz}^2} \tag{B.10}$$

B.3. Density

The oil density, ρ, is defined as mass per unit volume. The density in case of liquids vary slightly with both temperature and pressure. The equation (B.11) proposed by Dowson and Higginson [37] relates the density with temperature and pressure. The formula applies for mineral and synthetic lubricants, except for silicones, whose compressibility is much higher than for mineral oils [213].

$$\rho = \rho_0 \left(1 + \frac{0.6p}{1 + 1.7p}\right) \tag{B.11}$$

B.4. Kinematic viscosity

The flow of the oils in the capillary tubes is caused by weight effects, thus, the debit through the capillary is proportional to density divided by dynamic viscosity. This ratio, $\frac{\eta}{\rho}$, is called kinematic viscosity, which is given by equation (B.12). Due to practice aspects on the measurement of viscosity, the kinematic viscosity is often used.

$$\nu = \frac{\eta}{\rho} \tag{B.12}$$

B.5. Influence of temperature on viscosity

In 1886, Osborne Reynolds [138] found it necessary to know the viscosity of olive oil as a function of temperature. In a practical point of view, the viscosity of the oils used for lubrication purposes drops significantly when the temperature increases [23]. It is necessary to characterize the behaviour of viscosity with temperature, also known as thermo-viscosity.

For the relation between viscosity and temperature at low pressure, several models exist [211]. These models can be divided in models based on fluid theory and on fitting measured viscosity at a number of temperatures [213].

Based on curve-fitting viscosity-temperature measurements, the equation (B.13), also known as Ubbelohde-Walther equation, has become generally accepted and also is the basis of ASTM D341 [36], ISO and DIN calculation guidelines.

$$\log\ \log(\nu + a_A) = n_A - m_A \cdot \log(T) \tag{B.13}$$

In the equation, a_A and n_A are constants, T is temperature in Kelvin and m_A is the viscosity-temperature (V-T) line slope. The constant a for mineral oils in the V–T equation is between 0.6 and 0.9 [23].

Vogel's [214] equation is also often used and is presented in equation (B.14). To determine the constants k_V, b_V and c_V three measurements at different temperature must be done.

$$\nu = k_V \cdot \mathrm{e}^{\left(\frac{b_V}{\theta + c_V}\right)} \tag{B.14}$$

B.5.1. Viscosity Index

The viscosity index is today accepted as the international description of viscosity-temperature behaviour [23]. According to ASTM D2270-93 standard [215], the viscosity index is used to characterize the variation of viscosity of an oil with temperature. The viscosity index is given by equation (B.15), for fluids with VI<100.

$$VI = \frac{a}{a+b} \times 100 \tag{B.15}$$

For fluids with VI>100, the formula is on equations (B.16) and (B.17).

$$VI = \frac{10^N - 1}{0.0075} + 100 \tag{B.16}$$

$$N = \frac{log_{10}\frac{1}{b}}{log_{10}\nu} + 100 \tag{B.17}$$

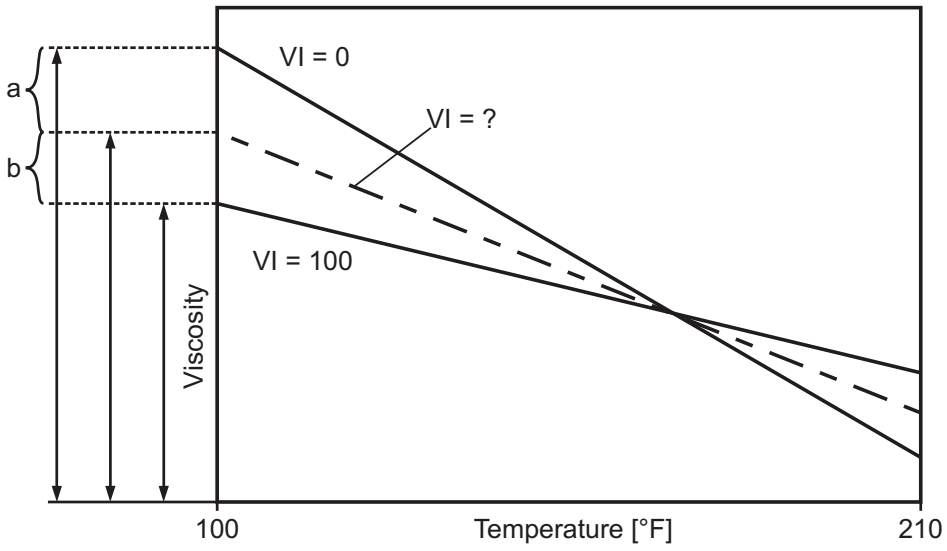

Figure B.3.: Graphic representation of viscosity index (VI).

B.5.2. Viscosity grades

ISO 3448 standard specifies a method to classify industrial lubricants. In this standard are described 18 viscosity grades ranging from 2 to 1500 cSt as presented in Table B.1.

B.6. Influence of pressure on viscosity

The influence of the pressure on viscosity is described by piezoviscosity or pressure-viscosity coefficient.

The influence of viscosity-pressure dependency still is underestimated for numerous lubrication applications. In EHL contacts, pressures are tipically higher than 1 GPa. Under these conditions, the prediction of the film thickness and friction conditions are not independent of the viscosity change with the pressure [23, 213].

In 1983, Barus [216] proposed the equation (B.18) for isothermal viscosity-pressure dependence of liquids, where η_0 is the viscosity at ambient pressure and α_p is the pressure-viscosity coefficient.

$$\eta = \eta_0 \cdot \mathrm{e}^{(\alpha_p \cdot p)} \tag{B.18}$$

As a shortcoming, the Barus equation predicts viscosities that are too high at high pressures [213, 217]. Since then, several isothermal viscosity-pressure formulas have been proposed that usually fit experimental data better than that suggested by equation (B.18). One of the most accurate approaches was introduced by Roelands in 1966, and is presented in equation (B.19)

Table B.1.: Viscosity grades for industrial lubricants, ISO Standard 3448.

Kinematic viscosity at 40 °C, cSt			
Grade	Min.	Max.	Average
2	1.98	2.42	2.20
3	2.88	3.52	3.20
5	4.14	5.06	4.60
7	6.12	7.48	6.80
10	9.00	11.00	10.00
15	13.50	16.50	15.00
22	19.80	24.20	22.00
32	28.80	35.20	32.00
46	41.40	50.60	46.00
68	61.20	74.80	68.00
100	90.00	110.00	100.00
150	135.00	165.00	150.00
220	198.00	242.00	220.00
320	288.00	352.00	320.00
460	414.00	506.00	460.00
680	612.00	748.00	680.00
1000	900.00	1100.00	1000.00
1500	1350.00	1650.00	1500.00

$$\eta(p,T) = \eta_0 \cdot \mathrm{e}^{\left[\{ln(\eta_0)+9.67\}\left\{\left(1+\frac{p}{0.1962}\right)^z\left(\frac{T_0-138}{T-138}\right)^{S_0}-1\right\}\right]} \tag{B.19}$$

Gold et al. [38] performed measurements with a high pressure viscometer. To adapt the experimental data by a mathematical model, Gold used the "Modulus-Equation" presented on equation (B.20) that is based on Barus equation.

$$\eta(p,T) = \eta_0 \cdot \mathrm{e}^{\left(\frac{p}{a_1+a_2\cdot T+(b_1+b_2\cdot T)\cdot p}\right)} \tag{B.20}$$

The a_1 a_2, b_1 and b_2 represent the fluid behaviour and should be calculated with the experimental results. The pressure-viscosity coefficient can be written like in equation (B.21).

$$\alpha(p,T) = \frac{ln\ \eta - ln\ \eta_0}{p-p_0} = \frac{1}{a_1 + a_2\cdot T + (b_1+b_2\cdot T)\cdot p} \tag{B.21}$$

Some author's [38, 218] generalised the viscosity-pressure dependence as presented in equation (B.22), assuming a relation with kinematic viscosity at atmospheric pressure, as can be easily measured without a high pressure viscometer.

$$\alpha = s \cdot \nu^t \times 10^{-8} \tag{B.22}$$

The constants s and t from the equation (B.22) are calculated with experimental results. Gold *et. al* provided results for different base oils [38].

Appendix C.

Elasto Hydrodynamic Lubrication

C.1. Elliptical contacts

The Hertz theory has the following assumptions: the surfaces are continuous and non-conforming

For an elliptical area of contact, with semi-axes a and b, the half-width (a) is calculated with equation (C.1), where $A = 1/R_X$ and $B = 1/R_Y$. The value of C_a is calculated solving the elliptical integrals.

$$a = C_a \cdot \sqrt[3]{\frac{F_n}{(A+B) \cdot E^*}} \tag{C.1}$$

The curvature radius is defined according equation (C.2) in which each term is given by equations (C.3) and (C.4), respectively.

$$\frac{1}{R^*} = \frac{1}{R_X} + \frac{1}{R_Y} \tag{C.2}$$

$$\frac{1}{R_X} = \frac{1}{R_{X1}} + \frac{1}{R_{X2}} \tag{C.3}$$

$$\frac{1}{R_Y} = \frac{1}{R_{Y1}} + \frac{1}{R_{Y2}} \tag{C.4}$$

The effective elastic modulus is calculated from the individual elastic properties of each body, as presented in equation (C.5).

$$\frac{1}{E^*} = \frac{1-{\nu_1}^2}{E_1} + \frac{1-{\nu_2}^2}{E_2} \tag{C.5}$$

If the origin of a coordinate system is placed at the centre of the contact area, with the xy plane coinciding with the common osculating plane of the bodies, the pressure distribution on the surfaces is given by equation (C.6).

$$p(x,y) = p_0 \cdot \sqrt{1 - \left(\frac{x}{a}\right)^2 - \left(\frac{y}{a}\right)^2} \tag{C.6}$$

The maximum Hertz pressure for the elliptical contact is given by equation (C.7).

$$p_0 = \frac{3 \cdot k \cdot F_n}{2 \cdot \pi \cdot a^2} \tag{C.7}$$

According to Hamrock and Dowson [24] the minimum film thickness and centre film thickness is given by equations (C.8) and (C.9), respectively.

$$h_m = 3.63 \cdot R^* \cdot U^{0.68} \cdot G^{0.49} \cdot W^{-0.073} \cdot (1 - \mathrm{e}^{-0.68k}) \tag{C.8}$$

$$h_0 = 2.69 \cdot R^* \cdot U^{0.67} \cdot G^{0.53} \cdot W^{-0.067} \cdot (1 - 0.61\mathrm{e}^{-0.73k}) \tag{C.9}$$

The dimensionless speed (U), material (G) and load (W) parameters are given by equations (C.10), (C.11) and (C.12), respectively.

$$U = \frac{\eta_0 \cdot U}{E^* \cdot R^*} \tag{C.10}$$

$$G = \alpha \cdot E^* \tag{C.11}$$

$$W = \frac{F_n}{E^* \cdot R^{*2}} \tag{C.12}$$

The ellipticity parameter is given by equation (C.13), considering the the ellipse semi axis in transverse (a) and motion (b) directions.

$$k = \frac{a}{b} \tag{C.13}$$

C.2. Line contacts

The previous section described the Hertz's theory applied to an elliptical contact. However, this can be extended to cover the case of line contact [219].

While the shape of the contact area is already known, with a width b given by the contacting bodies, its half-width a needs to be computed with equation (C.14).

$$a = \sqrt{\frac{2 \cdot F_n \cdot R_X}{\pi \cdot l \cdot E^*}} \tag{C.14}$$

For line contact, the effective radius of curvature is given by equation (C.15).

$$\frac{1}{R_X} = \frac{1}{R_{X1}} + \frac{1}{R_{X2}} \tag{C.15}$$

If the origin of a coordinate system is placed at the centre of the contact area, the pressure distribution on the surfaces is according equation (C.16).

$$p(x) = p_0 \cdot \sqrt{1 - \left(\frac{x}{a}\right)^2} \tag{C.16}$$

The maximum Hertz pressure for a line contact is given by equation (C.17).

$$p_0 = \frac{2}{\pi} \frac{F_n}{a \cdot b} \tag{C.17}$$

According to Hamrock and Dowson [24] the minimum film thickness and centre film thickness for a line contact is given by equations (C.18) and (C.19), respectively.

$$h_m = 2.65 \cdot R_X \cdot U^{0.70} \cdot G^{0.54} \cdot W^{-0.13} \tag{C.18}$$

$$h_0 = 1.95 \cdot R_X \cdot U^{0.727} \cdot G^{0.727} \cdot W^{-0.091} \tag{C.19}$$

The dimensionless speed (U), material (G) and load (W) parameters for a line contact are given by equations (C.20), (C.21) and (C.22), respectively.

$$U = \frac{\eta_0 \cdot U}{E^* \cdot R_X} \tag{C.20}$$

$$G = \alpha \cdot E^* \tag{C.21}$$

$$W = \frac{F_n}{E^* \cdot R_X \cdot b} \tag{C.22}$$

C.3. Specific film thickness and lubrication regimes

Tallian [121] introduced the concept of specific film thickness (Λ) given by the ratio of the corrected centre film thickness (h_{0C}) and the composite roughness (σ_C) of the surfaces, as presented in equations (C.23) and (C.24).

$$\Lambda = \frac{h_{0C}}{\sigma_C} \tag{C.23}$$

$$\sigma_C = \sqrt{{\sigma_1}^2 + {\sigma_2}^2} \tag{C.24}$$

The correction of film thickness (equation (C.25)) is necessary due to the presence of a sufficiently thick lubricant layer on the raceway, and inlet shear heating will be produced reducing the viscosity and the film thickness.

$$h_{0C} = h_0 \cdot \phi_T \tag{C.25}$$

C.3.1. Hydrodynamic or fluid-film lubrication

When a lubricant film is thick enough to fully separate the surfaces is called fluid-film lubrication. This type of lubrication is considered an ideal form of lubrication since it promotes low friction and wear protection [23, 24]. The friction is generated due to the rheological properties of the lubricant. The surfaces finish effects are neglected since the film thickness is thicker than roughness.

C.3.2. Elastohydrodynamic lubrication (EHL)

Elastohydrodynamic lubrication is a form of hydrodynamic lubrication where the elastic deformation of the contacting bodies surfaces as well as the oil pressure-viscosity are relevant. It can be hard or soft EHL. The hard EHL is usually related to metals. Good examples of this are machine components like rolling bearings and gears. The soft EHL is associated with materials of low elastic modulus like rubber and elastomer's.

C.3.3. Boundary lubrication

In boundary lubrication the surfaces have asperity contact and in this way the fluid-film effects are negligible. The properties of the lubricants have little influence on the friction behaviour of boundary lubrication. Thus, the contact is governed by the properties of the surfaces as well as the chemical properties of thin surface films of molecular size [23, 24, 217].

The coefficient of friction is independent of fluid viscosity [217]. However, Brandão *et al* [63] shown the influence of base oil and additives on the coefficient of friction under boundary lubrication.

C.3.4. Mixed lubrication

Mixed lubrication is the existence of both boundary and hydrodynamic lubrication. In this lubrication condition the contact between asperities may occur due to high pressures or low speeds causing the penetration of the film by the asperities. In this situation the interaction between molecular layers of boundary films also occurs.

C.3.5. Stribeck curve

The friction or lubrication behaviour of the transition from boundary until hydrodynamic lubrication is presented on a Stribeck curve as shown on Figure C.1. The graphs of friction force reported by Stribeck stem from a carefully conducted, wide-ranging series of experiments on journal bearings. They clearly showed the minimum

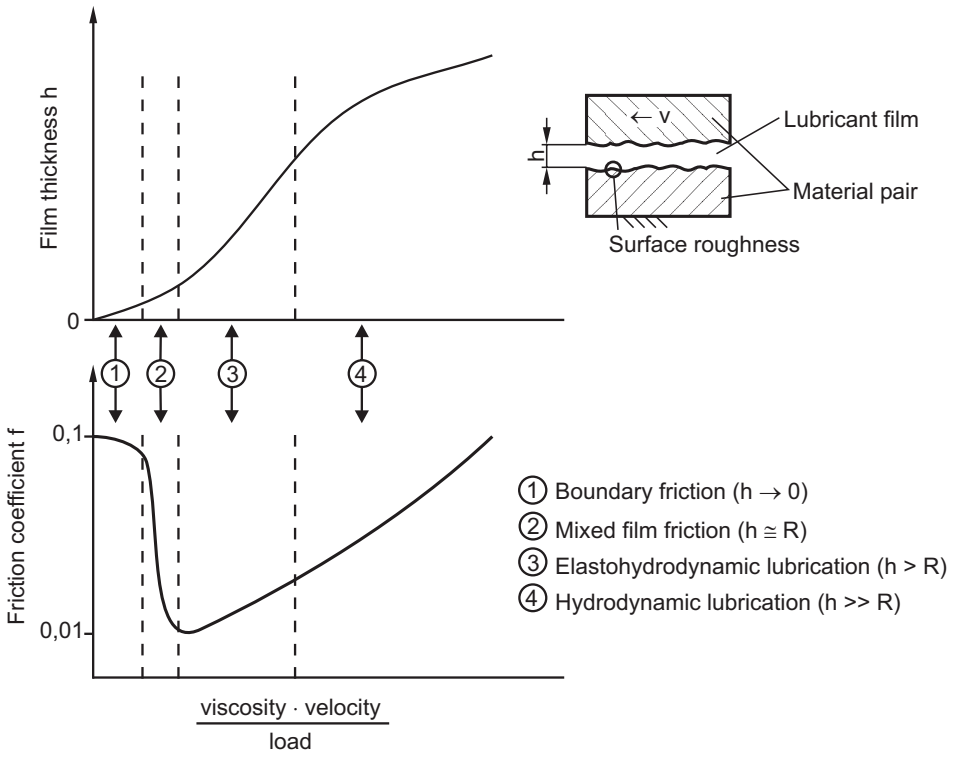

Figure C.1.: Stribeck diagram.

value of friction now known as the transition between mixed and elastohydrodynamic lubrication [220].

Appendix D.

Load distribution along path of contact

Before enter the contact zone of a gear, or the path of contact which value is given by equation (D.1), a teeth line has the representation of Figure D.1(a).

$$\overline{AE} = \epsilon_\alpha \cdot p_{bt} \tag{D.1}$$

When the contact starts, the length of the contacting line increases proportionally to the coordinate of the path of contact, represented by the first condition of equation (D.2) (Figures D.1(a) and D.1(b)). The contact then continues to increase up to the situation of a full line of contact, that occur at the coordinate $x = \epsilon \cdot p_{bt} = b \cdot \tan \beta_b$ up to the end of contact at $x = \epsilon_\alpha \cdot p_{bt}$ which is given by second row of equation (D.2) (Figure D.1(c)). Then, the teeth start to go out from the contact and the line length start to decrease as shown in the third row of equation (D.2) and Figure D.1(d).

$$\begin{cases} l(x) = \frac{x}{\sin\ \beta_b} & 0 < x < \epsilon_\beta \cdot p_{bt} \\ l(x) = \frac{b}{\cos\ \beta_b} & \epsilon_\beta \cdot p_{bt} < x < \epsilon_\alpha \cdot p_{bt} \\ l(x) = \frac{b}{\cos\ \beta_b} - \frac{x - \epsilon_\alpha \cdot p_{bt}}{\sin\ \beta_b} & \epsilon_\alpha \cdot p_{bt} < x < (\epsilon_\alpha + \epsilon_\beta) \cdot p_{bt} \end{cases} \tag{D.2}$$

The equation (D.2) previously presented is valid for the length of a single line along the path of contact. The other tooth have the same behaviour of the single line yet presented but at the distance of a transverse pitch, which is the distance between the tooth along the path of contact as represented in Figure D.1.

The same equations deduced for a single line can be used, but the coordinates should be transformed according to equation (D.3). The value i of the equation (D.3) is calculated with equation (D.4) that represents the lines screened from the single line with value $i = 0$, from behind and behead in integer steps.

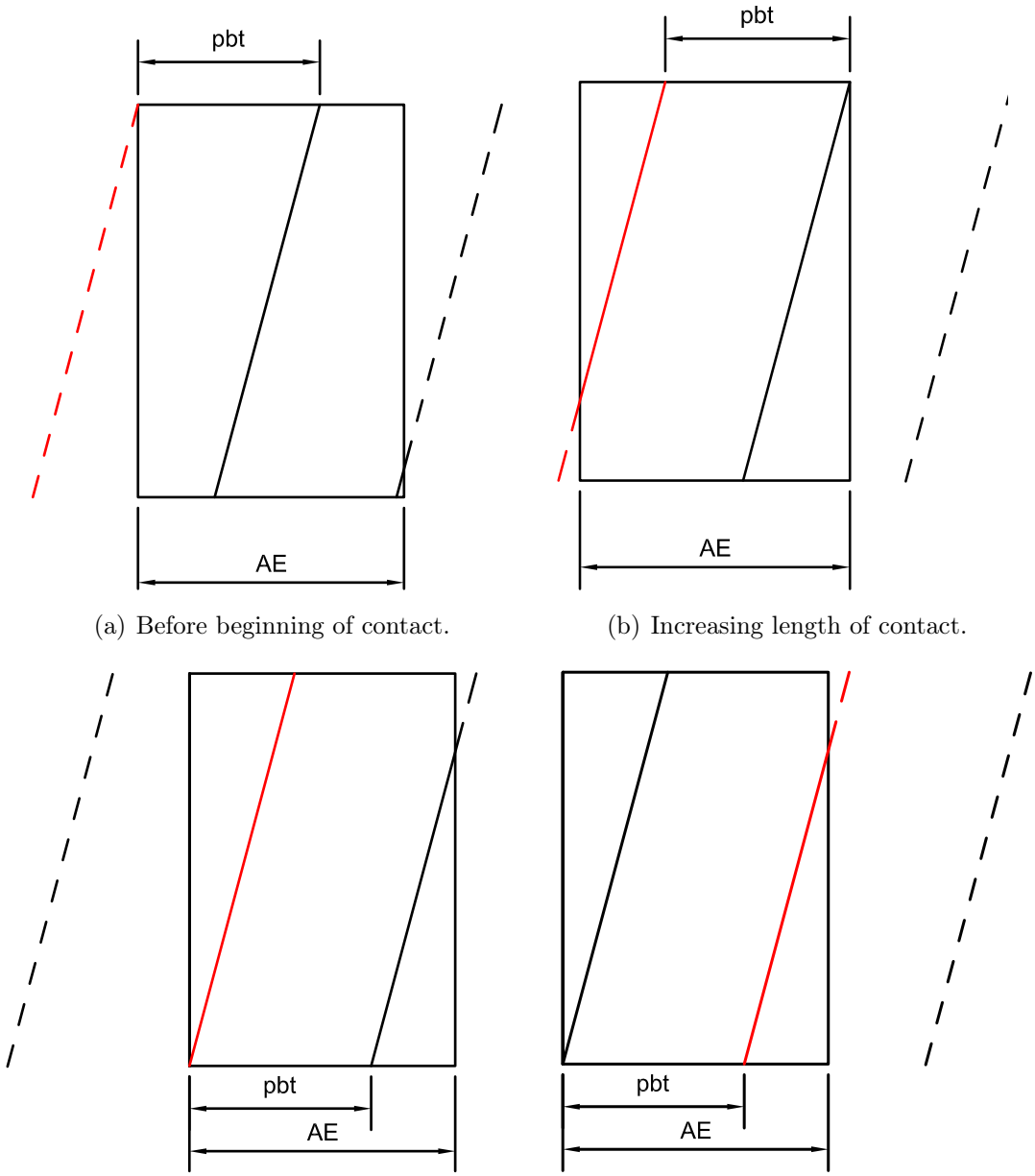

(a) Before beginning of contact.

(b) Increasing length of contact.

(c) After full line contact.

(d) Decreasing length of contact.

Figure D.1.: Evolution of a single line along the path of contact

$$x^*(x) = x + i \cdot p_{bt} \tag{D.3}$$

$$i = -ceil(\epsilon_\alpha + \epsilon_\beta) : 1 : ceil(\epsilon_\alpha + \epsilon_\beta) \tag{D.4}$$

It is also possible to a 3D representation of the line length as function of x, but also y. To do that, the y coordinate representing the tooth width that changes from

0 up to b as presented in equation (D.5). Since the tooth line of contact of a helical gear has a helix angle the y coordinate is function of the x coordinate which can be expressed with equation (D.6).

$$y = [0; b] \tag{D.5}$$

$$b^* = y \cdot \tan \beta_b \tag{D.6}$$

Applying the coordinate transformation of equation (D.7) and the formulas of equation (D.2), the line length of each tooth screened from the teeth i is presented in equation (D.8).

$$x^*(x, y) = x + i \cdot p_{bt} + b^* \tag{D.7}$$

$$\begin{cases} l^i(x,y) = \frac{x^*}{\sin\ \beta_b} & 0 < x^* < b \cdot \tan\ \beta_b \\ l^i(x,y) = \frac{b}{\cos\ \beta_b} & b \cdot \tan\ \beta_b < x^* < \epsilon_\alpha \cdot p_{bt} \\ l^i(x,y) = \frac{b}{\cos\ \beta_b} - \frac{x^* - \epsilon_\alpha \cdot p_{bt}}{\sin\ \beta_b} & \epsilon_\alpha \cdot p_{bt} < x^* < (\epsilon_\alpha + \epsilon_\beta) \cdot p_{bt} \end{cases} \tag{D.8}$$

The formulation presented is valid for gears with a contact ratio ($\epsilon_\alpha > \epsilon_\beta >$), i.e. one complete line contact exists during the meshing period.

For the case that one complete line is not in contact, the cycle of meshing is slightly different and the path of contact is smaller than the transverse pitch. In such cases usually the overlap contact ratio is $\epsilon_\beta > \epsilon_\alpha$.

The equation is slightly different from that presented before because the domains change in a different way as presented in equation (D.9).

$$\begin{cases} l^i(x,y) = \frac{x^*}{\sin\ \beta_b} & 0 < x^* < \epsilon_\alpha \cdot p_{bt} \\ l^i(x,y) = \frac{\epsilon_\alpha \cdot p_{bt}}{\sin\ \beta_b} & \epsilon_\alpha \cdot p_{bt} < x^* < \epsilon_\beta \cdot p_{bt} \\ l_i(x,y) = \frac{\epsilon_\alpha \cdot p_{bt}}{\sin\ \beta_b} - \frac{x^* - \epsilon_\beta p_{bt}}{\sin\ \beta_b} & \epsilon_\beta \cdot p_{bt} < x^* < (\epsilon_\alpha + \epsilon_\beta) \cdot p_{bt} \end{cases} \tag{D.9}$$

The total sum of lines can be easily done with equation (D.10). It is important to note that the algorithm also calculate the line contact length of spur gears using only the second row of equation (D.2).

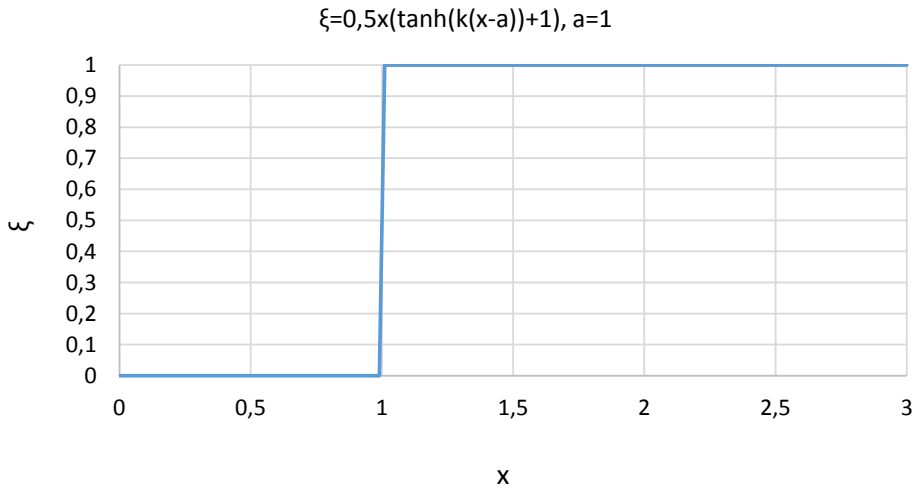

Figure D.2.: Step function tanh with a=1.

$$L(x,y) = \sum_{-ceil(\epsilon_\alpha+\epsilon_\beta)}^{ceil(\epsilon_\alpha+\epsilon_\beta)} l_i(x,y) \tag{D.10}$$

D.1. Step functions

The algorithm previously presented is based on the identification of different domains in the meshing cycle of helical gears. However, the different domains can be combined using stepwise functions like Heaviside (equation (D.11)) or hyperbolic tangent (equation (D.12)) and presented in Figure D.2.

$$\xi = \frac{1}{1+e^{-2k(x-a)}} \tag{D.11}$$

$$\xi = \frac{1}{2}\cdot(\tanh(k\cdot(x-a))+1) \tag{D.12}$$

The coordinate a is the point when the step is desired.

Using the hyperbolic tangent equation, the three domains can be expressed in equation (D.13) for the beginning of contact ($x=0$), equation (D.14) for a complete line ($x=\epsilon_\beta \cdot p_{bt}$) and equation (D.15) for a line going out from the contact ($x=\epsilon_\alpha \cdot p_{bt}$). The constant k changes the precision of the algorithm. For the case it was considered $k=1000$.

$$\xi_1 = \frac{1}{2}\cdot(\tanh(k\cdot x)-\tanh(k\cdot(x-(\epsilon_\alpha+\epsilon_\beta)\cdot p_{bt}))) \tag{D.13}$$

$$\xi_2 = \frac{1}{2}\cdot(\tanh(k\cdot(x-\epsilon_\beta\cdot p_{bt}))+1) \tag{D.14}$$

$$\xi_3 = \frac{1}{2} \cdot (\tanh(k \cdot (x - \epsilon_\alpha \cdot p_{bt})) + 1) \tag{D.15}$$

For each single line the length along the path of contact is given by equation (D.16).

$$l(x) = \frac{1}{\sin \beta_b} \cdot \xi_1 \cdot (x - \xi_2 \cdot (x - \epsilon_\beta \cdot p_{bt}) - \xi_3 \cdot (x - \epsilon_\alpha \cdot p_{bt})) \tag{D.16}$$

For spur gears the length for each line is given by equation (D.17).

$$l(x) = b \cdot \xi_1 \tag{D.17}$$

For the lines screened from the one considered the length is computed with equation (D.3) previously explained which results in equation (D.18).

$$l_i(x, y) = l(x^*(x, y)) \tag{D.18}$$

The total sum of lines is then given by equation (D.19).

$$L(x, y) = \sum_{-ceil(\epsilon_\alpha + \epsilon_\beta)}^{ceil(\epsilon_\alpha + \epsilon_\beta)} l_i(x, y) \tag{D.19}$$

Using such type of function or other stepwise function is great to get a continuous function. However, the computational time can increase due to the expense of computing the tanh.

D.2. Load distribution

The algorithms presented are particularly useful to quantify the load distribution along the path of contact that is expressed in equation (D.20)

$$Fn(x, y) = F_{bt} \frac{l_0(x, y)}{L(x, y)} \tag{D.20}$$

Appendix E.

Formulas for the coefficient of friction in meshing gear

E.1. Average coefficient of friction along the path of contact

E.1.1. Buckingham (1949)

$$\mu_{mZ} = \frac{0.050}{e^{0.125 \cdot v_s}} + 0.002 \cdot \sqrt{v_s} \tag{E.1}$$

E.1.2. Ohlendorf (1958)

$$\mu_{mZ} = 0.001 \cdot \frac{f_h}{H_V} \sqrt{\eta_m \cdot v_{tw} . \frac{b}{F_{bt}} \cdot \frac{F_{bt,h}}{F_{bt}}} + \mu_F \cdot \left(1 - \frac{F_{bt,h}}{F_{bt}}\right) \tag{E.2}$$

$$f_h = 4.16 \cdot \sqrt{\frac{\sin^3 \alpha_{tw}}{\cos^2 \alpha_{tw}} \cdot \epsilon_\alpha} \cdot \left[1 + 1.36 \cdot \left(\frac{\epsilon_\alpha}{z_1 \cdot \tan \alpha_{tw}} \frac{u+1}{u}\right)^2\right] \tag{E.3}$$

$$\eta_m = \frac{\eta_{oil}}{1 + \sqrt{\frac{F_{bt}}{b} \cdot \frac{v_{tw}}{29.43}}} \tag{E.4}$$

$$\frac{F_{bt}}{F_{bt}} = \left[1 + \frac{0.5418 \cdot {R_p}^{0.5} \cdot {\eta_{oil}}^{0.8}}{\sin \alpha_{tw} \cdot \epsilon_\alpha . \eta_m \cdot v_{tw}}\right]^{-1} \tag{E.5}$$

E.1.3. Misharin (1958)

$$\mu_{mZ} = 0.325 \cdot [v_s \cdot v_r \cdot \nu_k]^{-0.25} \tag{E.6}$$

E.1.4. Eiselt (1966)

$$\mu_{mZ} = \frac{2.068}{\sqrt[3]{\rho_{red,m}}} \cdot \left\{ \log \left[\left(\frac{F_{bt}}{b \cdot v_{\Sigma C}} \right)^{0.02075} \cdot {\eta_{oil}}^{-0.00325} \right] + 0.05415 \right\} \tag{E.7}$$

E.1.5. O'donoghue and Cameron (1966)

$$\mu_{mZ} = 0.6 \cdot [(Ra + 22)/35] \cdot \left[{\nu^{1/8} \cdot v_g}^{1/3} {v_r}^{1/6} \cdot \rho_{redC}^{1/2} \right]^{-1} \tag{E.8}$$

E.1.6. Drozdov and Gavrikov (1967)

$$\mu = \left[0.8 \cdot \sqrt{\nu} \cdot v_g + v_r \cdot \phi + 13.4 \right]^{-1} \tag{E.9}$$

$$\phi = 0.47 - 0.13 \cdot 10^{-4} P_{max} - 0.4 \cdot 10^{-3} \cdot \nu \tag{E.10}$$

E.1.7. Matsumoto (1985)

$$\mu_{mZ} = 0.01; \; D \leq 1 \tag{E.11}$$

$$\mu_{mZ} = 0.01 \cdot (5 \cdot \log D + 1) \, ; \; 1 < D \leq 10 \tag{E.12}$$

$$\mu_{mZ} = 0.01 \cdot (2.5 \cdot \log D + 3.5) \, ; \; D > 10 \tag{E.13}$$

$$D = \frac{(R_{z1} + R_{z2})}{h_0} \tag{E.14}$$

E.1.8. Naruse (1984)

$$\mu_{mZ} = \ln \left({v_{gm}}^{-0.0126} \right) + 0.0569 \tag{E.15}$$

E.1.9. DIN 3990 (1987)

$$\mu_{mZ} = 0.12 \cdot \left(\frac{F_{bt}/b \cdot Ra}{v_{\Sigma C} \cdot \rho_{redC} \cdot \eta} \right)^{0.25} \tag{E.16}$$

E.1.10. Michaelis (1987)

$$\mu_{mZ} = 0.045 \cdot \left(\frac{F_{bt}/b}{v_{\Sigma C} \cdot \rho_{redC}} \right)^{0.2} \cdot \eta^{-0.05} \cdot X_R \tag{E.17}$$

$$X_R = 3.8 \cdot \sqrt[4]{\frac{Ra}{d_1}} \tag{E.18}$$

E.1.11. Schlenk (1995)

$$\mu_{mZ} = 0.048 \cdot \left(\frac{F_{bt}/b}{\nu_{\Sigma C} \cdot \rho_{redC}} \right)^{0.2} \cdot \eta^{-0.05} \cdot Ra^{0.25} \cdot X_L \tag{E.19}$$

E.1.12. Doleschel (2002)

$$\mu_{mZ} = \xi \cdot \mu_{bl} + (1 - \xi) \cdot \mu_{EHD} \tag{E.20}$$

$$\xi = \begin{cases} 1 + 0.25 \cdot \Lambda^2 - \Lambda, \ for\ \Lambda < 2 \\ \\ 0, \ for\ \Lambda \geq 2 \end{cases} \tag{E.21}$$

$$\mu_{bl} = \mu_{bl,R} \cdot \left(\frac{P_H}{P_R} \right)^{\alpha_F} \cdot \left(\frac{V_\Sigma}{V_{R,F}} \right)^{\beta_F} \tag{E.22}$$

$$\mu_{EHD} = \mu_{EHD,R} \cdot \left(\frac{P_H}{P_R} \right)^{\alpha_{EHD}} \cdot \left(\frac{V_\Sigma}{V_{R,EHD}} \right)^{\gamma_{EHD}} \tag{E.23}$$

The exponents in equations (E.22) and (E.23) are derived from experimental results in FZG-VA tests [65].

E.1.13. Matsumoto (2014)

$$\mu_{mZ} = \xi \cdot \mu_{bl} + (1 - \xi) \cdot \mu_{EHD} \tag{E.24}$$

$$\xi = 0.5 \cdot \log D \tag{E.25}$$

$$D = \frac{(R_{z1} + R_{z2})}{h_0} \tag{E.26}$$

E.2. Variable coefficient of friction along the path of contact

E.2.1. Benedict and Kelley (1961)

$$\mu_{mZ} = 0.0127 \cdot \log\left(\frac{F_{bt}}{b} \cdot \frac{29652}{\eta_{oil} \cdot v_g \cdot {v_\Sigma}^2}\right) \tag{E.27}$$

E.2.2. Xu Hai (2005)

$$\mu(x) = e^{f(SRR,P_0,\nu_0,Ra)} \cdot P_0^{b2} \cdot |SRR|^{b3}\, v_e^{b6} \cdot \eta_0^{b7} \cdot R^{b8} \tag{E.28}$$

$$f(SRR, P_0, \nu_0, Ra) = b_1 + b_4 \cdot |SRR| \cdot P_0 \cdot \log(\nu_0) + b_5 \cdot e^{-|SRR| \cdot P_0 \cdot \log(\nu_0)} + b_9 \cdot e^{Ra} \tag{E.29}$$

Table E.1.: Range of the parameters used in the parametric study [112].

Lubricants	75W90 gear oil
Inlet temperature, ° C	50 - 110
Radius of curvature (R), m	0.005 - 0.08
Entraining velocity (V_e), m/s	1 - 20
Slide-to-roll ratio (SR)	0.005 - 1.0
Surface roughness (S), μm	0 - 0.4
Maximum Hertzian pressure (P_h), GPa	0.5-2.5

Table E.2.: Coefficients for the EHL based formula.

b_1	-8.916465
b_2	1.03303
b_3	1.036077
b_4	-0.354068
b_5	2.812084
b_6	-0.100601
b_7	0.752755
b_8	-0.390958
b_9	0.620305

Appendix F.

Rolling bearing friction torque

F.1. SKF rolling friction torque model

A summary of the SKF friction torque model information available in [129] and [130] is presented here. Therefore, all constants and equations presented should be used for different bearings discussed in the main text, considering the lubrication methods or assembly arrangements.

The total internal friction torque of a rolling bearing is composed by the rolling (M_{rr}), sliding torque (M_{sl}), drag torque (M_{drag}) and seals torque (M_{seals}) components, according to Equation (F.1).

$$M_t = M_{rr}^{'} + M_{sl} + M_{drag} + M_{seals} \tag{F.1}$$

F.1.1. Rolling torque - M_{rr}

The rolling frictional moment is calculated from Equation (F.2),

$$M_{rr} = G_{rr}(n \cdot \nu)^{0,6} \tag{F.2}$$

where ν is the kinematic viscosity of the lubricant at the operating temperature in mm^2/s, n is the rotational speed in rpm and G_{rr} represents the influence of the bearing load on the rolling resistance and depends on the bearing type, the bearing mean diameter and the axial load. The load distribution in the different rolling element contacts is added all together. G_{rr} is presented in Table F.1 for different rolling bearing geometries.

The centrifugal force F_g is given by equation (F.3), with $R_3 = 1.40 \times 10^{-12}$.

$$F_g = R_3 \cdot {d_m}^4 \cdot n^2 \tag{F.3}$$

Bearing	G_{rr}	R_1	R_2
TBB 51107	$R_1 \cdot {d_m}^{1.83} \cdot {F_a}^{0.54}$	1.03×10^{-6}	-
RTB 81107	$R_1 \cdot {d_m}^{2.38} \cdot {F_a}^{0.31}$	2.25×10^{-6}	-
NJ 406	$R_1 \cdot {d_m}^{2.41} \cdot {F_r}^{0.31}$	1.09×10^{-6}	-
FPCB QJ 308	$R_1 \cdot {d_m}^{1.97} \cdot [F_r + F_g + R_2 \cdot F_a]^{0.54}$	4.78×10^{-7}	2.42

Table F.1.: Bearing load constant G_{rr} influencing the rolling friction torque for different rolling bearing geometries

On the equations of Table F.1, d_m is the bearing mean diameter in mm; F_a is the axial load in N; F_r is the radial load in N and F_g is the inercial forces load in N.

The rolling friction resistance is also affected by two reduction factors, the inlet shear heating (ϕ_{ish}) and the kinematic replenishment/starvation (ϕ_{rs}):

Inlet shear heating - ϕ_{ish}

Inlet shear heating occurs because not all the lubricant present at the inlet of the contact manages to get inside; some of it will recirculate in the inlet because of the reverse flow. This recirculation produces heat, since the viscosity of the lubricant is highly reduced by the temperature; lower viscosity at the inlet of the contact means lower film thickness and, therefore, lower rolling resistance. This effect is taken into account in the SKF friction model by means of the reduction factor ϕ_{ish}, which is calculated by Equation (F.4).

$$\phi_{ish} = \frac{1}{1 + 1,84 \times 10^{-9}(nd_m)^{1,28}\nu^{0,64}} \tag{F.4}$$

Kinematic replenishment/starvation - ϕ_{rs}

The kinematic replenishment/starvation occurs when high speeds or high lubricant viscosities hamper the replenishment of lubricant in the raceway after a rolling element has passed, since the lubricant will not have sufficient time to flow back from the sides to the centre of the raceway. This is kinematic starvation, which will produce a reduction of the lubricant availability in the inlet of the contact and reduce the film thickness and the rolling resistance. The replenishment/starvation effect is considered in the SKF friction model by means of the multiplication factor ϕ_{rs}. This factor is a function of the lubricant supply mechanism as well and is calculated by

$$\phi_{rs} = \frac{1}{e^{K_{rs}\nu n(d+D)\sqrt{\frac{K_z}{2(D-d)}}}} \tag{F.5}$$

Rolling bearing	K_Z
TBB	3.8
RTB	4.4
CRB	5.1
FCBB	3.1

Table F.2.: Geometry constant K_Z.

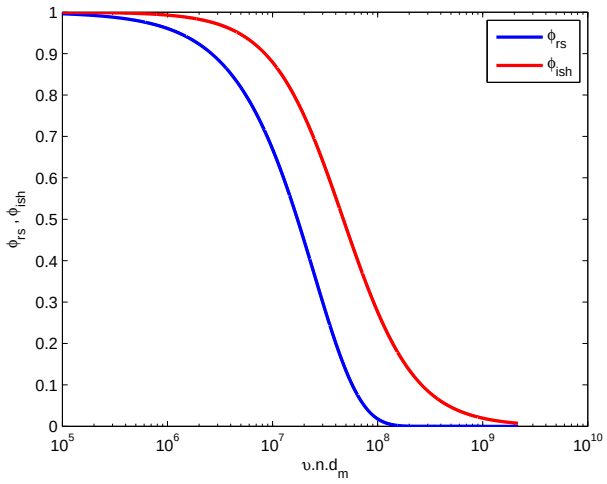

Figure F.1.: Typical variation of the reduction factors ϕ_{ish} and ϕ_{rs} with the operating parameter $\nu \cdot n \cdot d_m$.

where K_{rs} is the replenishment/starvation factor with value of 3×10^{-8} for low level oil bath and oil jet lubrication; and 6×10^{-8} for grease and oil-spot lubrication. K_Z is a bearing type related geometry. The values are presented in Table F.2 for different rolling bearing geometries.

The typical curve of ϕ_{ish} and ϕ_{rs} for the same inputs of speed, viscosity and bearing geometry are shown in Figure F.1

This figure clearly shows that the kinematic replenishment/starvation factor (ϕ_{rs}) has a greater influence on the rolling torque that the inlet shear heating factor (ϕ_{ish}) at the same operating condition.

Including the inlet shear heating and the kinematic replenishment/starvation effects, the rolling resistance can be expressed by Equation (F.6).

$$M'_{rr} = \phi_{ish} \cdot \phi_{rs} \cdot G_{rr}(n \cdot \nu)^{0,6} \tag{F.6}$$

The typical behaviour of the rolling torque is shown in Figure F.2 including (M'_{rr})

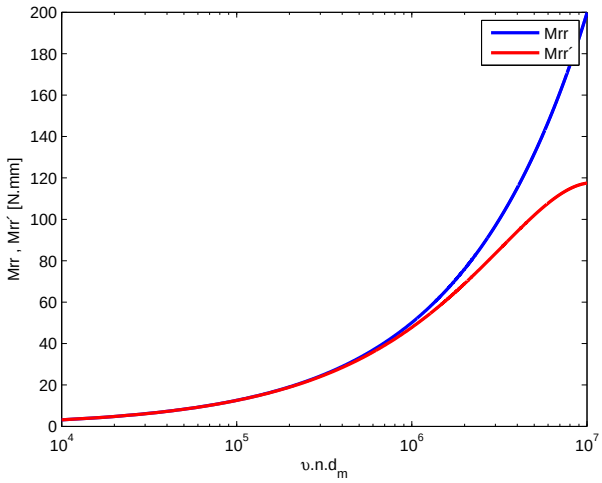

Figure F.2.: Typical variation of the rolling torque M'_{rr} and M_{rr} with the operating parameter $\nu \cdot n \cdot d_m$.

Rolling bearing	G_{sl}	S_1	S_2
TBB 5107	$S_1 \cdot {d_m}^{0,05} \cdot {F_a}^{4/3}$	1.6×10^{-2}	-
RTB 81107	$S_1 \cdot {d_m}^{0.62} \cdot F_a$	0.154	-
CRB NJ 406	$S_1 \cdot {d_m}^{0.9} \cdot F_a + S_2 \cdot d_m \cdot F_r$	0.16	-
FPCB QJ 308	$S_1 \cdot {d_m}^{0.26} \cdot \left[(F_r + F_g)^{4/3} + S_2 \cdot F_a^{4/3}\right]$	1.2×10^{-2}	0.9

Table F.3.: Bearing load constant G_{sl} influencing the sliding friction torque for different rolling bearing geometries

and not including (M_{rr}) the reduction factors.

F.1.2. Sliding torque - M_{sl}

The sliding frictional moment is calculated from Equation (F.7)

$$M_{sl} = G_{sl}.\mu_{sl} \tag{F.7}$$

where G_{sl} represents the influence of the bearing load on the sliding resistance and depends on the bearing type, the bearing mean diameter and the axial load. The load distribution in the different rolling element contacts is added together and it is given in Table F.3 for different rolling bearing geometries.

The centrifugal force F_g is given by equation (F.8), with $S_3 = 1.40 \times 10^{-12}$.

$$F_g = S_3.{d_m}^4.n^2 \tag{F.8}$$

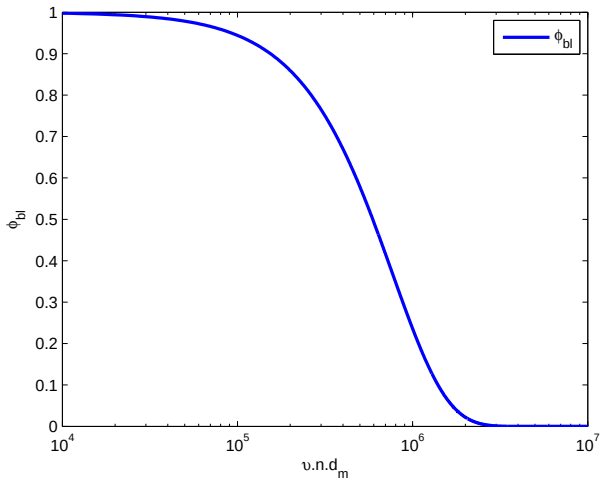

Figure F.3.: Typical variation of the weighting factor (ϕ_{bl}) with the operating parameter $\nu \cdot n \cdot d_m$.

where S_1 is a geometry constant for sliding frictional moment. μ_{sl} is the global coefficient of friction of the rolling bearing (lubricant shearing - μ_{EHL} plus asperity contacts - μ_{bl}). It strongly depends on the lubrication regime, which is defined here by ϕ_{bl}. For full film lubrication μ_{sl} mostly depends on lubricant shearing and for boundary lubrication on asperity contacts. It is given by

$$\mu_{sl} = \phi_{bl}.\mu_{bl} + (1 - \phi_{bl}).\mu_{EHL} \tag{F.9}$$

where μ_{bl} is the coefficient of friction in boundary lubrication and therefore strongly depends on lubricant additive package; and μ_{EHL} is the coefficient of friction in full film lubrication and therefore strongly depends on lubricant rheology and contact area. ϕ_{bl} is the weighting factor for the influence of asperity contact and lubricant shearing mechanisms and is determined by Equation (F.10).

$$\phi_{bl} = \frac{1}{e^{2{,}6\times10^{-8}(n.\nu)^{1,4}d_m}} \tag{F.10}$$

The typical curve of ϕ_{bl} for the same inputs of speed, viscosity and bearing geometry are shown in Figure F.3

Figure F.3 indicates that the transition from full film lubrication to mixed lubrication starts when $\phi_{bl} \neq 0$. For the given example, it happens when $\nu \times n \times d_m \leq 2 \times 10^6$.

SKF recommends μ_{bl} =0,15 and μ_{EHL} =0,05 for mineral oils and μ_{EHL} =0,04 for synthetic oils.

Rolling bearing	K_L	K_Z
TBB 51107	-	3.8
RTB 81107	0.43	4.4
CRB NJ 406	0.65	5.1
FPCB QJ 308	-	3.1

Table F.4.: Geometry constant K_L and K_Z.

F.2. Drag friction torque

The rolling bearing drag losses are given by equation (F.11) for ball bearings or by equation (F.13) for roller bearings.

$$M_{drag} = 0.4 \cdot V_M \cdot K_{ball} \cdot {d_m}^5 \cdot n^2 + 1.093 \times 10^{-7} \cdot n^2 \cdot {d_m}^3 \cdot \left(\frac{n \cdot {d_m}^2 \cdot f_t}{\nu} \right)^{-1.379} \cdot R_s \quad \text{(F.11)}$$

with,

$$K_{ball} = \frac{i_{rw} \cdot K_Z (d + D)}{D - d} \times 10^{-12} \quad \text{(F.12)}$$

where i_{rw} is the number of ball rows.

$$M_{drag} = 4 \cdot V_M \cdot K_{roll} \cdot C_w \cdot B \cdot {d_m}^4 \cdot n^2 + 1.093 \times 10^{-7} \cdot n^2 \cdot {d_m}^3 \cdot \left(\frac{n \cdot {d_m}^2 \cdot f_t}{\nu} \right)^{-1.379} \cdot R_s \quad \text{(F.13)}$$

with,

$$K_{roll} = \frac{K_L \cdot K_Z (d + D)}{D - d} \times 10^{-12} \quad \text{(F.14)}$$

The constants K_L and K_Z are presented in Table F.4.
The C_w factor is given by equation (F.15) and l_D given by equation (F.16).

$$C_w = 2.789 \times 10^{-10} \cdot {l_D}^3 - 2.786 \times 10^{-4} \cdot {l_D}^2 + 0.0195 \cdot l_D + 0.6439 \quad \text{(F.15)}$$

$$l_D = 5 \frac{K_L \cdot B}{d_m} \quad \text{(F.16)}$$

Equations (F.17), (F.18), (F.19), (F.20) and (F.21) define f_t, R_s, t, and f_A quantities, respectively.

$$f_t = \sin(0.5 \cdot t),\ if\ 0 \leq t \leq \pi \tag{F.17}$$

$$f_t = 1,\ if\ \pi < t < 2 \cdot \pi \tag{F.18}$$

$$R_s = 0.36 \cdot {d_m}^2 \cdot (t - \sin t) \cdot f_A \tag{F.19}$$

$$t = 2 \cdot \cos^{-1}\left(\frac{0.6 \cdot d_m - H}{0.6 \cdot d_m}\right),\ when\ H \geq d_m,\ use\ H = d_m \tag{F.20}$$

$$f_A = 0.05 \frac{K_Z \cdot (D + d)}{D - d} \tag{F.21}$$

F.3. Seal friction torque

The seal losses are defined by equation (F.22).

$$M_{seal} = K_{S1} \cdot {d_s}^{\beta_R} + K_{S2} \tag{F.22}$$

The constants K_{S1}, K_{S2} and β_R are dependent on the geometry of the rolling bearing.

Appendix G.

Friction torque of rolling bearings at free temperature conditions

G.1. TBB 51107

Figure G.1(a) shows the total friction torque measured in a TBB 51107 for different rotational speeds and wind turbine gear oils characterized in Chapter 2. The operating temperature is the one measured in the thermocouple (III), shown in Figure G.1(c).

The results clearly show that operating temperatures increase while the friction torque decreases with the bearing speed. The behaviour found was the same verified by Cousseau in a TBB 51107 lubricated with grease [140].

Concerning the oil formulation, the TBBs lubricated with MINR and PAGD oils always generated the highest friction torques. Depending on the operating speed, the friction torques generated by TBBs lubricated with ESTR and PAOR oils were close in value. However, PAOR generated lower friction torque for the highest rotational speeds. This oils are similar in viscosity index, as presented in Chapter 2, which results in similar operating kinematic viscosity due their similar operating temperatures, as shown in Figure G.1(d).

The lowest friction torque found for ESTR and PAOR oils are in accordance to the lowest operating and corresponding stabilization temperatures achieved.

G.2. RTB 81107

The internal friction torque of the RTB 81107, measured at different rotating speeds (150 - 1500 rpm) and for each wind turbine gear oil tested is plotted in Figure G.2(a). The friction torque inside the RTB decreased when the operating speed increased whatever the gear oil considered.

The RTB lubricated with MINR oil always generated the highest friction torque followed closely by the RTB lubricated with PAGD oil. The RTB lubricated with

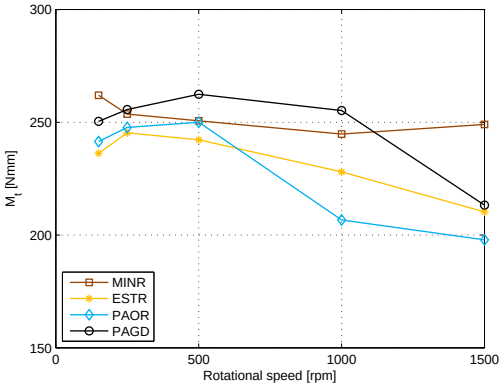

(a) Friction torque.

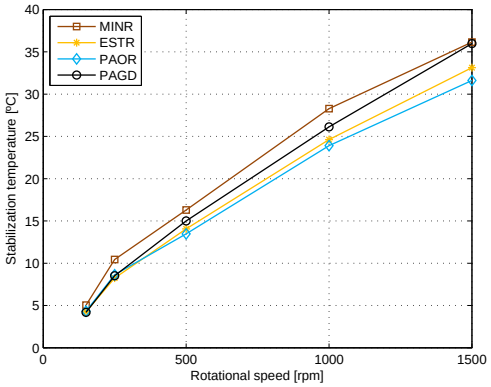

(b) Stabilization temperature.

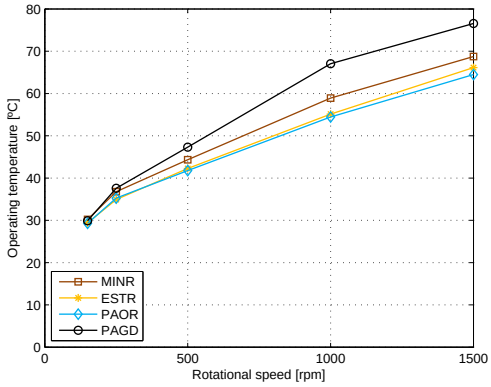

(c) Operating temperature.

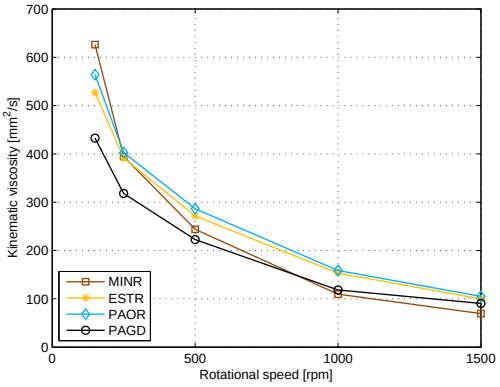

(d) Kinematic viscosity.

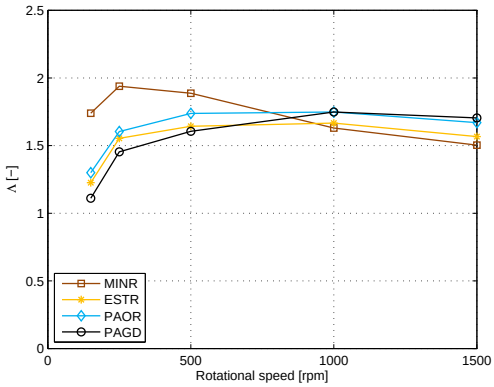

(e) Specific film thickness.

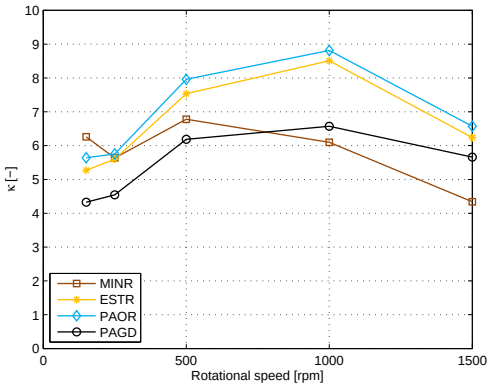

(f) Viscosity ratio.

Figure G.1.: Results for a TBB 51107 lubricated at free temperature conditions.

ESTR oil has the lowest friction torque. The RTB lubricated with PAOR oil generated the lowest friction torque at 1500 rpm.

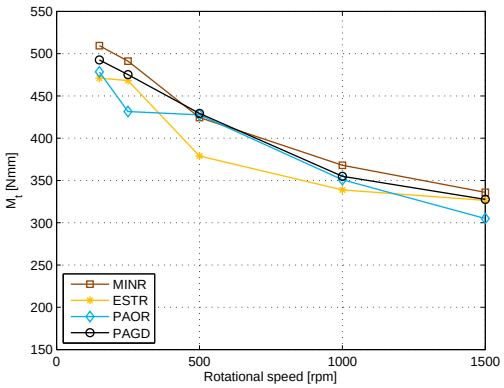

(a) Friction torque.

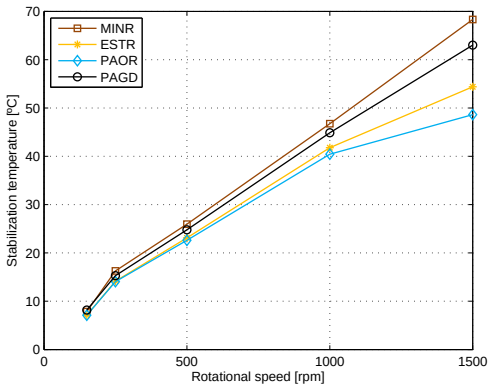

(b) Operating temperature.

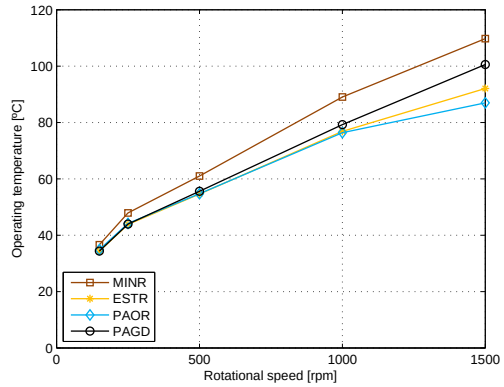

(c) Operating temperature.

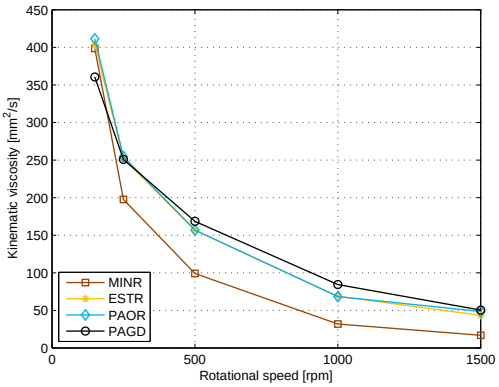

(d) Kinematic viscosity.

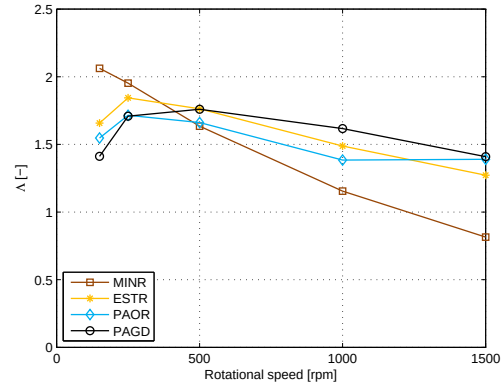

(e) Specific film thickness.

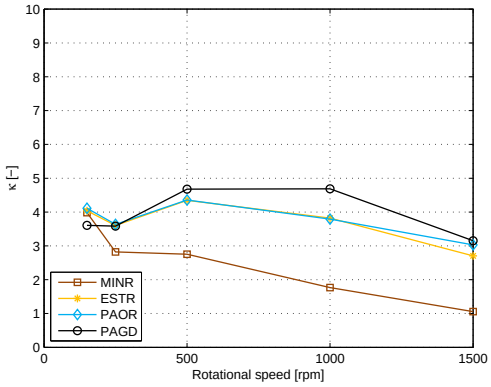

(f) Viscosity ratio.

Figure G.2.: Results for a RTB 81107 lubricated at free temperature conditions.

Appendix H.

FZG machine modifications

The FZG machine was subjected to several modifications in the motor positioning in order to assemble a torque transducer. In 'Assembly' it is presented the plate to support the motor, the support for the plate and the sensor assembly.

The drawing 'Assemby sensor' it is presented the torque transducer and two couplings to connect the sensor between the motor and the FZG slave gearbox. The coupling assure that the sensor is not damage for an applied torque higher than 80 Nm.

The next drawings are detailed views of the 'Support sensor', 'Motor plate' and 'Support plate' that should be machined.

ITEM NO.	PART NUMBER	DESCRIPTION	QTY.
1	Motor plate	Plate to support motor	1
2	Support plate	Support for the plate	4
3	ISO 4762 M10 x 25 --- 25N		8
4	ISO 4762 M12 x 45 --- 45N		4
5	Support sensor	Support for the sensor	1
5	Assembly sensor	See next drawing	1

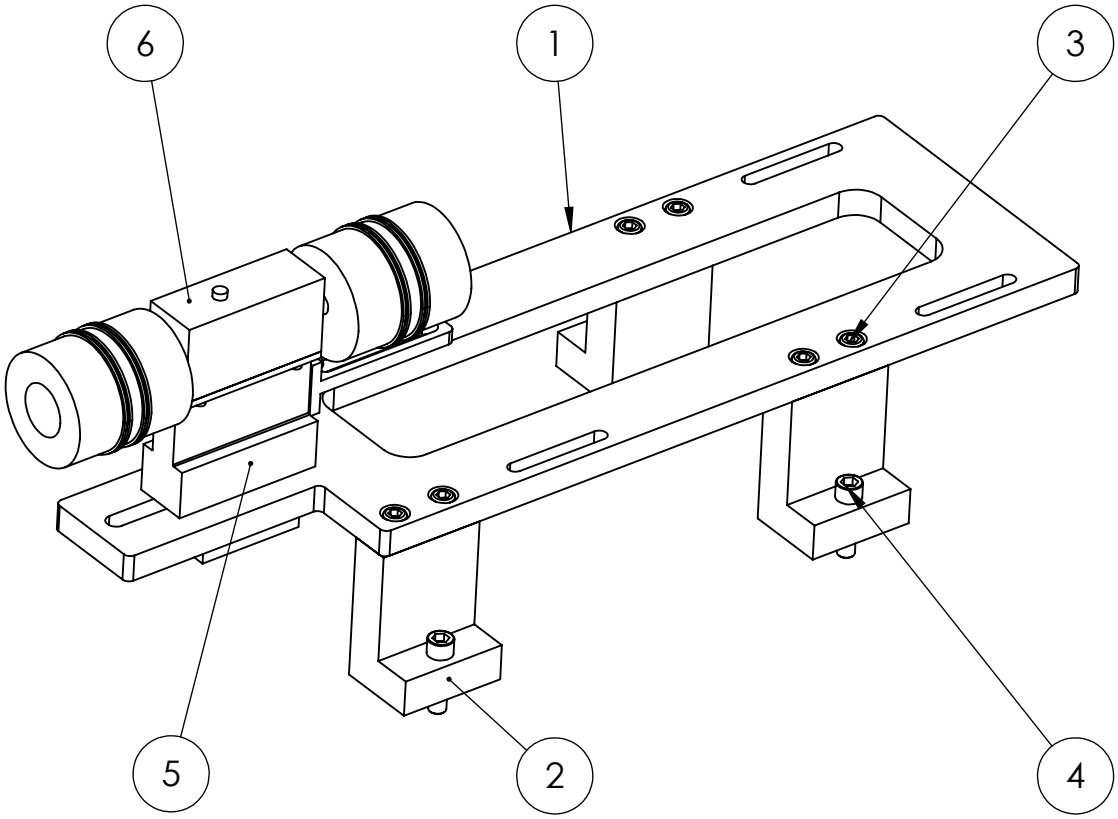

UNLESS OTHERWISE SPECIFIED: DIMENSIONS ARE IN MILLIMETERS SURFACE FINISH: TOLERANCES: LINEAR: ANGULAR:		FINISH:		DEBUR AND BREAK SHARP EDGES		DO NOT SCALE DRAWING	REVISION
	NAME	SIGNATURE	DATE			TITLE:	
DRAWN							
CHK'D							
APPV'D							
MFG							
Q.A				MATERIAL:		DWG NO. Assembly	A4
				WEIGHT:		SCALE:1:10	SHEET 1 OF 1

ITEM NO.	PART NUMBER	DESCRIPTION	QTY.
1	ETH DRDL-II 50/10	Torque sensor	1
2	ETH BK2/80	Coupling motor shaft	1
3	ETH BK5/80	Coupling gearbox shaft	1

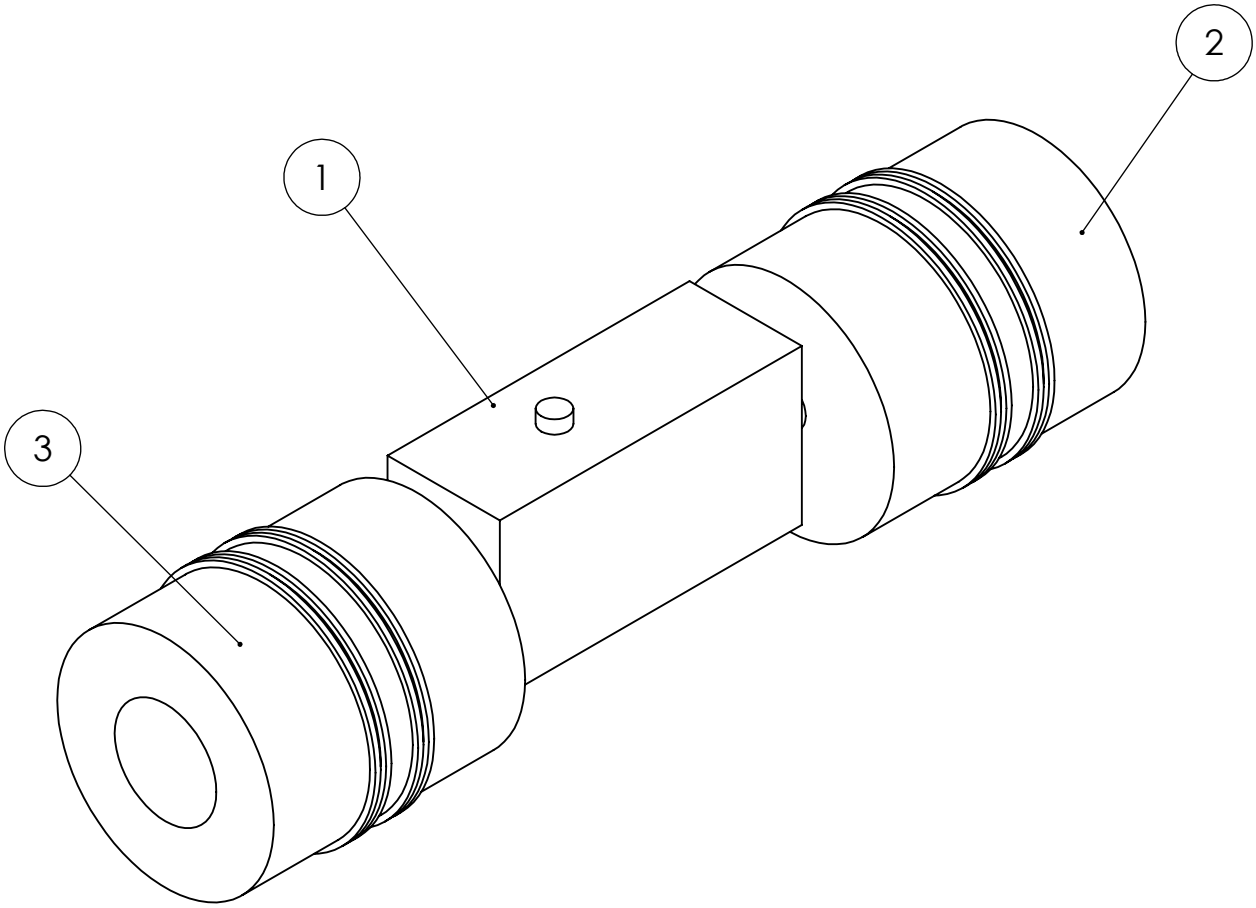

UNLESS OTHERWISE SPECIFIED: DIMENSIONS ARE IN MILLIMETERS SURFACE FINISH: TOLERANCES: LINEAR: ANGULAR:	FINISH:		DEBUR AND BREAK SHARP EDGES		DO NOT SCALE DRAWING	REVISION
	NAME	SIGNATURE	DATE			TITLE:
DRAWN						
CHK'D						
APPV'D						
MFG						
Q.A				MATERIAL:	DWG NO.	A4
					Assembly sensor	
				WEIGHT:	SCALE:1:5	SHEET 1 OF 1

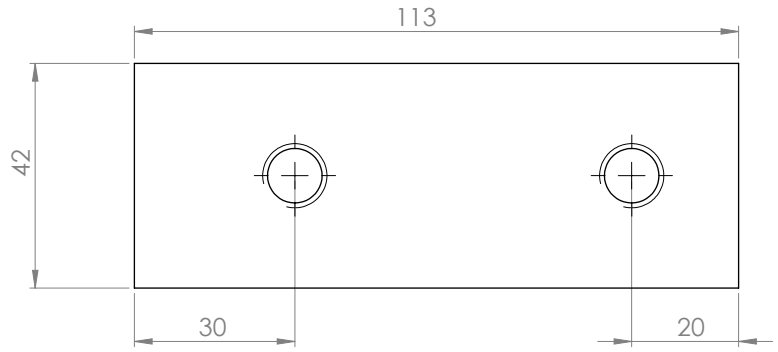

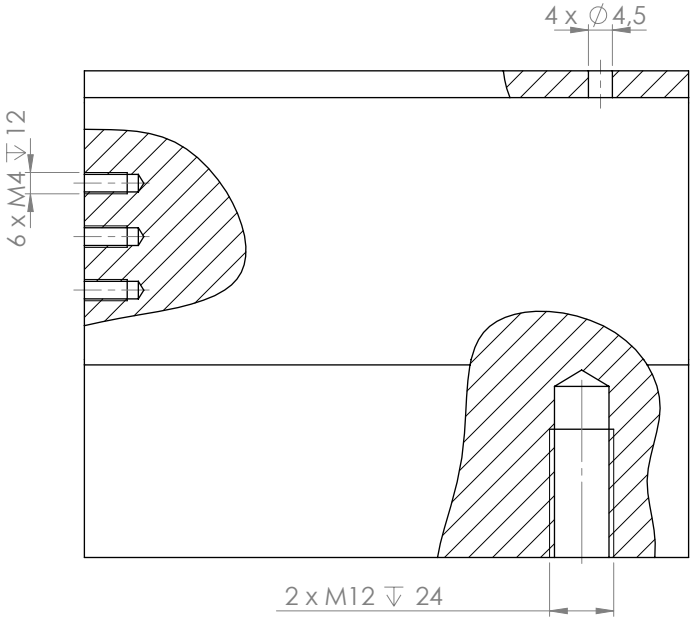

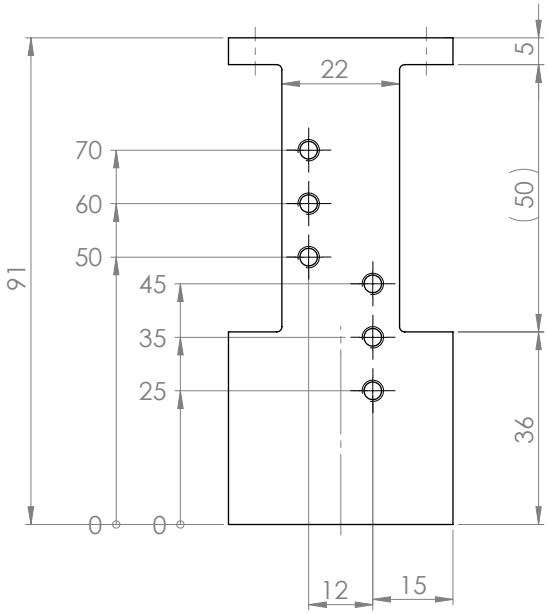

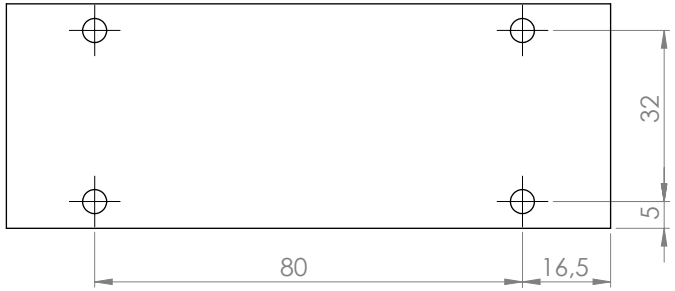

UNLESS OTHERWISE SPECIFIED: DIMENSIONS: mm SURFACE FINISH: TOLERANCES: ISO 2768mK ISO 8015	FINISH:		DEBUR AND BREAK SHARP EDGES		DO NOT SCALE DRAWING	REVISION
	NAME	SIGNATURE	DATE		TITLE:	
DRAWN					Support sensor	
CHK'D						
APPV'D						
MFG						
Q.A				MATERIAL: Aluminio	DWG NO.	A3
				WEIGHT:	SCALE:1:1	SHEET 1 OF 1

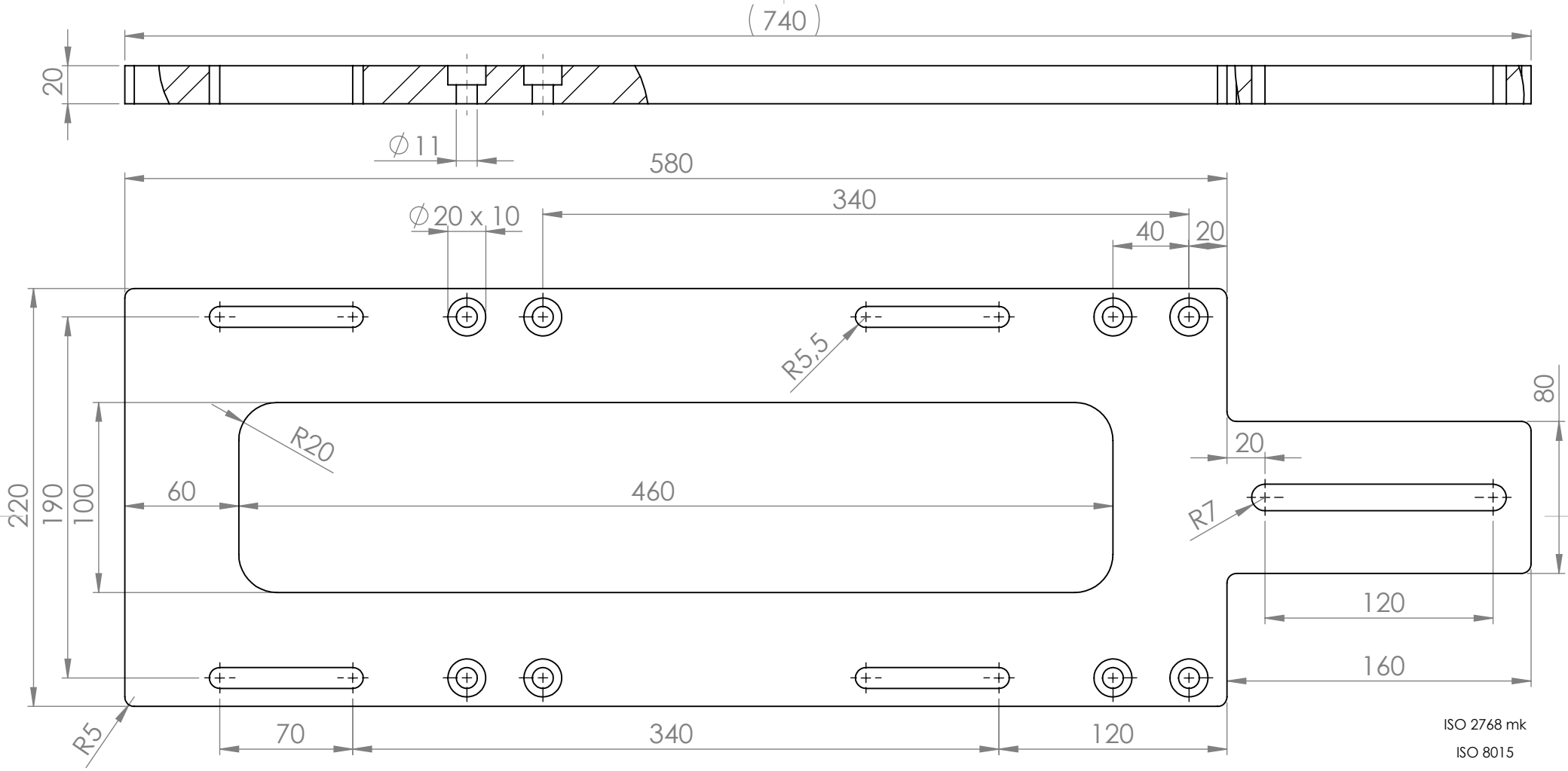

UNLESS OTHERWISE SPECIFIED: DIMENSIONS ARE IN MILLIMETERS SURFACE FINISH: TOLERANCES: LINEAR: ANGULAR:	FINISH:		DEBUR AND BREAK SHARP EDGES		DO NOT SCALE DRAWING	REVISION
	NAME	SIGNATURE	DATE		TITLE:	
DRAWN					Motor plate	
CHK'D						
APPV'D						
MFG						
Q.A				MATERIAL:	DWG NO.	A4
				WEIGHT:	SCALE:1:10	SHEET 1 OF 1

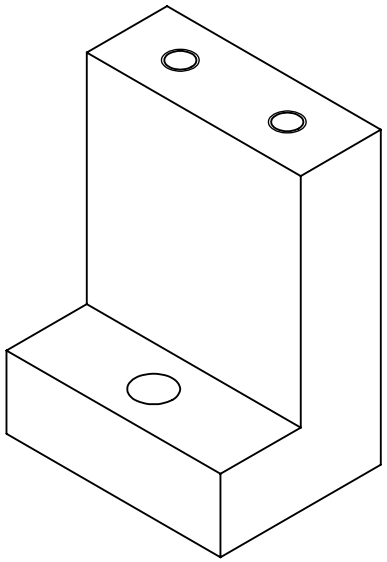

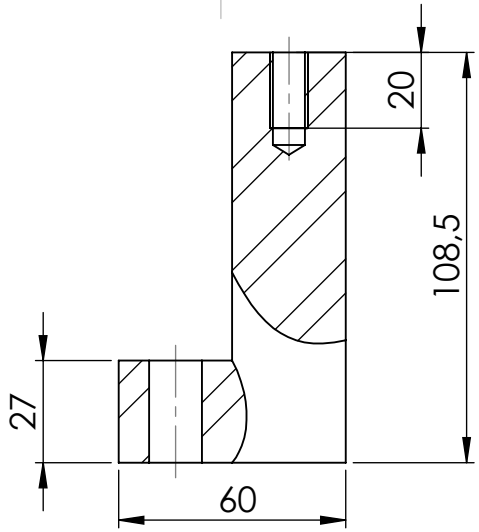

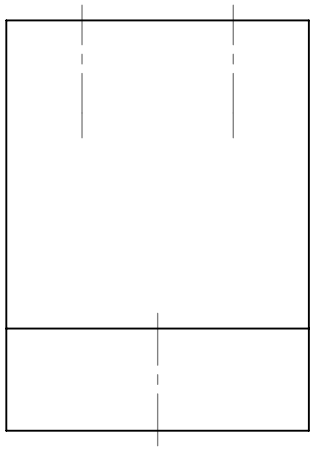

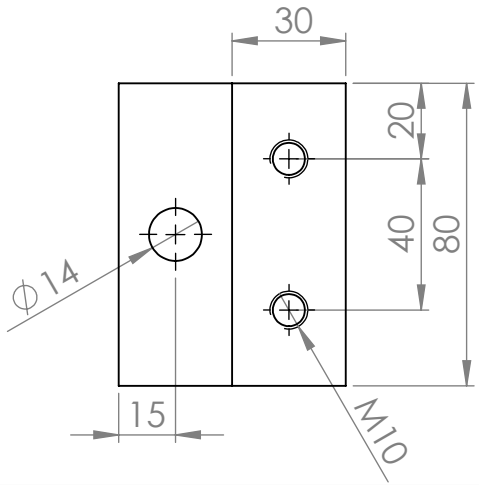

ISO 2768 mK
ISO 8015

UNLESS OTHERWISE SPECIFIED: DIMENSIONS ARE IN MILLIMETERS SURFACE FINISH: TOLERANCES: LINEAR: ANGULAR:		FINISH:		DEBUR AND BREAK SHARP EDGES	DO NOT SCALE DRAWING	REVISION
	NAME	SIGNATURE	DATE		TITLE:	
DRAWN					Support plate	
CHK'D						
APPV'D						
MFG						
Q.A				MATERIAL:	DWG NO.	A4
				WEIGHT:	SCALE:1:2	SHEET 1 OF 1